Evaluation of Glaciothermal Engines for the Generation of Polar Renewable Energy

By

Zane Smith

Bachelor of Applied Science (Geology)

School of Engineering and ICT

Submitted in fulfilment of the requirements for Master of Engineering Science

University of Tasmania, January, 2016

Declaration of Originality

This thesis contains no material which has been accepted for a degree or diploma by the University or any other institution, except by way of background information and duly acknowledged in the thesis, and to the best of my knowledge and belief no material previously published or written by another person except where due acknowledgement is

Zane Smith

Date: 29 January 2016

Statement of Authority to Access

This thesis may be made available for loan and limited copying and communication in accordance with the Copyright Act 1986 .

Zane Smith

Date: 29 January 2016

Statement of Co-Authorship

The following people and institutions contributed to the publication of work undertaken as part of this thesis:

Name and School	**Zane Smith, School of Engineering and ICT**
Name and institution	**Prof Michael Negnevitsky, University of Tasmania**
Name and institution	**Dr Xiaolin Wang, University of Tasmania**
Name and institution	**Dr Kelvin Michael, University of Tasmania**

Author details and their roles:

Paper 1, Cold Climate Energy Production:
Located in chapter 1
Candidate was the primary author and with author 3 (10%), author 1 (5%) and author 2 (5%) contributed to the idea, its formalisation and development

Paper 2, Glaciothermal Power Generation in Cold Climate Regions:
Located in chapters 2 and 3
Candidate was the primary author and with author 2 (10%), author 1 (5%) and author 3 (5%) contributed to the idea, its formalisation and development

We the undersigned agree with the above stated "proportion of work undertaken" for each of the above published (or submitted) peer-reviewed manuscripts contributing to this thesis:

Signed: _

(Name)	*(Name)*
Supervisor	*Head of School*
School of Engineering and ICT	*School of Engineering and ICT*
University of Tasmania	University of Tasmania

Date: 29.01.16

Abstract

Providing reliable power services to remote Arctic and Antarctic locations presents a formidable task. Delivery of fossil fuel poses expensive logistical challenges, especially for sites subject to restricted seasonal access. Locally renewable wind and solar energy resources help to supplement diesel and other hydrocarbon fuels, but the search continues for viable energy alternatives. Latent heat from freezing seawater or meltwater can be used to boil a high pressure organic working fluid and drive a fluid expander to generate electrical power. The extreme chill of cold polar air provides the essential heat sink to recondense the exhaust vapour. These sources provide an opportunity to generate power from seawater using glaciothermal power cycles.

Ambient temperatures may fall below -80 °C during winter at elevated interior sites, and as low as -60 °C at high latitude ice shelf sites. A large amount of heat is released when water freezes (~335 MJ per tonne of ice formed) – equivalent to energy released from a liquid water heat source with a temperature difference of 80 °C. Nett thermal efficiencies of 9—11% at interior sites could be achieved if ice-slurry and tube-fin condenser technologies are properly adapted for use in glaciothermal power cycles.

This thesis reviews earlier research work and proposes specific designs for a practical glaciothermal engine that can generate power from freezing water. The performance of a 250 kW engine was studied and the feasibility of using such an engine to provide power at remote cold climate sites was investigated. The conceptual device provides a convenient way to explore the behaviour of various processes intrinsic to the operation of a glaciothermal engine cycle.

The analysis includes investigation of underlying physical processes and device working principles, heat transfer modelling, and optimisation of an ice-in-tube glaciothermal boiler,

twin-screw expander, tube-fin condenser and associated devices. Year-round performance of the glaciothermal power generator was investigated around Antarctica, providing an overview of potential applications of such a device in Antarctica. Mean annual temperatures across the Antarctic continent were mapped using regression analysis of ice sheet temperature data.

The analysis demonstrates that glaciothermal power generation can potentially contribute to providing sustainable energy in very cold climate conditions.

Acknowledgements

As a mature age student I am fortunate to be able to draw on accumulated life, travel and work experiences. It is quite impossible to recall the full list of family, friends, colleagues, work mates, fellow students and teachers who have contributed in so many different ways to my education over the years, and unfair to single out individual names. Please know that my gratitude is real. I have been very privileged to have met and worked with so many skilled and dedicated people.

I very much appreciate the camaraderie of my fellow post graduate colleagues and staff at the School of Engineering and ICT. The completion of this thesis is due in no small part to your expert guidance and encouragement. I am ever grateful to Prof. Michael Negnevitsky for agreeing to oversee my candidature, for extending me and getting the best out of me, but in fewer words. I owe a special debt to Dr Xiaolin Wang for taking much time to advise me on thermal engineering aspects. I now know the difference between what might work, what does work and what best practice actually becomes. It is rewarding to learn the technical aspects of engineering and be able to find solutions to things. Engineering solutions in Antarctica are tempered by stark realities and so I appreciate the guidance of Dr Kelvin Michael whose Antarctic expertise has been very reassuring.

As a first time researcher, I am struck by the enormous enterprise of fellow researchers all around the globe in adding to our combined human knowledge. I look forward to contributing at least one article to one of the 20,000 or so journals that are published every year. I salute the authors of all the papers I have read, and for those papers that contribute materially to this thesis I sincerely hope that I have been able to properly represent your work and ideas.

In compiling this thesis and accompanying conference papers I gratefully acknowledge the support of colleagues at the Australian Antarctic Division, the Institute for Marine and Antarctic Studies and the CSIRO Division of Marine and Atmospheric Research for providing a wealth of materials and advice. Thanks also to the Australian Bureau of Meteorology for your assistance in collating time series datasets. Research is only possible with real data. As a researcher I am grateful to those organisations that make their data freely available over the web. In particular: the University of

Wisconsin-Madison Automatic Weather Station Program for your Antarctic meteorology data sets, data display, and information; the National Snow and Ice Data Centre, University of Colorado, Boulder for your RAMPDEM topographic datasets and 10m ice temperature data; the National Institute of Standards and Technology for your thermophysical fluid properties reference software; the Joint Committee on the Properties of Seawater for your publications on the TEOS-10 seawater reference; and to the Australian Antarctic Data Centre for your *MRV Aurora Australis* voyage tracks and underway data. Particular thanks also to our always amicable University of Tasmania librarians who have tracked down and procured so many articles on my behalf.

During the course of my candidature I have had opportunity to view some power engineering first hand through various field trips around Tasmania. Thank you to Tas Networks, Hydro Tasmania and the Department of State Development for granting me access and acquainting me with different aspects of the engineering legacy of our mountainous state. Tassie can certainly claim its fair share of engineering innovation.

For all the above riches though, I reserve my most heartfelt gratitude to my family. I will ever remain grateful to Mum and Dad who gave me the greatest freedom and opportunity as a child to explore and learn about the world. To my own children Kyle and Ashlyn I can only hope you have been so lucky, and that you might forgive me for so many absences over the years in pursuit of yet another one of Dad's projects. If there is no value in this thesis then I have no defence. If you have been so lucky I know that it is because of your Mum's care and attention.

To the love of my life, Leanne, it is only through you that this work is possible. You have been my principle sponsor, confidant and project manager through these past years. I love most that you have faith in me at those times when I struggle myself. You must know that my appreciation of your own work as a teacher only grows with each passing year. It is to you that I owe the most.

Table of Contents

Abstract i

Acknowledgements iii

Table of Contents vii

List of Figures xiii

List of Tables xix

List of Appendices xx

List of Acronyms xxi

List of Symbols xxiii

Greek Symbols xxiv

Subscripts xxv

Boolean arguments xxvii

String arguments xxvii

Literature models xxviii

Chapter 1 – Introduction 1

1.1 Background: Challenges of power production in cold climate regions 1

1.1.1 Deployment and reliability of equipment in the field 4

1.1.2 Utilisation of renewable energy captors 6

1.1.3 Potential renewable energy sources 7

1.2 Evolution of renewable energy systems in cold climate regions 8

1.2.1 Wind energy 8

1.2.2 Solar energy 13

1.2.3 Hybrid systems 18

1.2.4 Thermal energy 25

1.3 Glaciothermal power generation 32

1.3.1 Glaciothermal boiler 33

1.3.2 Two-phase vapor expander 36

1.3.3 Condenser 37

1.3.4 Existing device models 39

1.4 Project objectives 40

1.5 Thesis structure 41

Chapter 2 – Mathematical Model of a Basic Glaciothermal Engine 42

2.1 Introduction 42

2.2 Engine summary 42

2.3 Working fluid 43

2.4 Tube fin condenser 45

2.4.1 Tube-fins 45

2.4.2 Horizontal in-tube condensing film 48

2.4.3 Condenser panel scaling 58

2.4.4 Condenser fan work 59

2.5 Condensate injection pump 60

2.6 Ice slurry loop 61

2.6.1 Ice-slurry pump 63

2.6.2 Ice-slurry mixer 64

2.7 Ice-in-tube boiler 67

2.7.1 Condensate preheater 67

2.7.2 Glaciothermal heater 68

2.7.3 Boiler tube bundle scaling 73

2.7.4 Flooded evaporator 73

2.8 Two-phase expander 74

2.9 Component scaling 77

Chapter 3 – Performance Evaluation of the Basic Glaciothermal Engine 78

3.1 Introduction 78

3.2 The working fluid cycle 78

3.2.1 Thermodynamic efficiency of glaciothermal cycles 78

3.2.2 Selection of working fluid species 80

3.3 Parametric analysis 81

3.3.1 Tube-fin condenser configuration 81

3.3.2 Glaciothermal boiler configuration and operation 87

3.3.3 Turbine and generator 93

3.3.4 Engine parasitic losses 93

3.4 Performance curves and device dimensions 96

3.5 Critical operating points 96

3.5.1 Maximum nett thermal efficiency 96

3.5.2 Maximum power output 97

3.5.3 Zero power output 98

3.6 Conclusions 99

Chapter 4 – Potential Year-Round Power Output of the Basic Glaciothermal Engine 101

4.1 Introduction 101

4.2 Modelling of ambient conditions for glaciothermal engine 104

4.2.1 Ambient air temperature data processing 105

4.2.2 Ambient seawater temperature modelling 106

4.3 Year round glaciothermal engine performance 111

4.3.1 Potential glaciothermal power locations 111

4.3.2 Year round performance at potential locations 115

4.4 Conclusions 119

Chapter 5 – Conclusions and Future Work 120

5.1 Major findings of this thesis and conclusions 120

5.2 Potential augmentation methods and future work 121

References 123

Appendices 131

2-A Working fluid thermophysical properties 132

2-B Liquid refrigerant pump 133

2-C Seawater thermophysical properties 134

2-D Characteristic salinity 135

2-E Continuous properties model 136

2-F Ice slurry loop control 137

2-G Ice-slurry classifier 141

2-H Ice crystal nucleation 143

2-I Ice crystal growth 146

2-J Glaciothermal heater 148

2-K Vapour bubble nucleation 154

2-L Twin screw expander 158

2-M Glaciothermal engine summary 160

5-A Potential augmentation methods 162

5-B Year round augmented power 168

5-C Potential large scale augmentation methods 171

5-D Minor findings 175

5-E Miscellaneous future work 176

List of Figures

Figure 1.1	Mean monthly and mean annual temperatures at selected polar stations	1
Figure 1.2	Katabatic winds over Ross Ice Shelf	2
Figure 1.3	Main powerhouse 125 kW diesel generators at Casey Station	3
Figure 1.4	Two 300 kW horizontal axis wind turbines at Mawson Station	5
Figure 1.5	Inferred tracks for extra-tropical cyclones and anticyclones	9
Figure 1.6	Three-hourly wind direction and temperature data for Mawson Station	10
Figure 1.7	Vertical axis and horizontal axis wind turbines	11
Figure 1.8	Aerowatt UM-70X wind turbine and performance curve	12
Figure 1.9	Daily-average insolation at the top of the atmosphere	14
Figure 1.10	Solar chimneys at Syowa Station	15
Figure 1.11	Solar concentrator for snow melting	15
Figure 1.12	An automated geophysical observatory employing wind and PVs	16
Figure 1.13	Diesel hybrid heat and power system	19
Figure 1.14	Renewable energy penetration with diesel power regulation	24
Figure 1.15	Two-phase closed thermosyphons help keep permafrost frozen	26
Figure 1.16	Ground loops and solar collectors for a hybrid GSHP in Fairbanks, Alaska	27
Figure 1.17	Absorption heat transformer for space heating	28
Figure 1.18	Multi-effect ammonia-water absorption system for combined heat and power	28
Figure 1.19	Polar renewable energy evaluation studies 1980 – 2013	29
Figure 1.20	Thermo-mechanical engine as proposed by Le Goff et al	31
Figure 1.21	Mechanical scraper, rotating slab, and fluidised bed ice slurry generators	36
Figure 1.22	Proprietary ‘N’ screw rotor profile for twin screw expander	37
Figure 1.23	Dynamometer testing of twin screw expander running R-113	37
Figure 1.24	Cold wind flux meter and tube fin condenser	39

Figure 2.1	The basic glaciothermal engine prototype	43
Figure 2.2	Algorithm for air-side tube fin condenser HTC	47
Figure 2.3	Flow regimes for film condensation in long tubes	48
Figure 2.4	Condensing film model for smooth condenser tube	50
Figure 2.5	Schematic of a fan-forced tube fin condenser	50
Figure 2.6	Algorithm summary for horizontal tube condensing film	51
Figure 2.7	Thermal resistance layers for horizontal tube condensing film node	54
Figure 2.8	R134a condensing film HTC Cavallini et al comparisons	57
Figure 2.9	CO_2 condensing film HTC Kim et al comparisons	58
Figure 2.10	Algorithm summary for integrated tube-fin condenser	60
Figure 2.11	Schematic of ice slurry loop for an ice-in-tube glaciothermal boiler	61
Figure 2.12	Ice slurry mixer equilibrium temperature	62
Figure 2.13	Pumping efficiency for centrifugal pump	63
Figure 2.14	Algorithm summary for ice slurry mixer heat and mass flows	67
Figure 2.15	Freezing ice slurry model for an ice-in-tube glaciothermal heater	70
Figure 2.16	Summary of algorithm for ice-in-tube glaciothermal boiler	71
Figure 2.17	Thermal resistance layers for ice-in-tube glaciothermal boiler node	72
Figure 2.18	Vapour density ratios of various working fluids	75

Figure 3.1	T-S diagram of basic glaciothermal and ORC Rankine cycles	79
Figure 3.2	Performance curves for nominal basic glaciothermal engine	80
Figure 3.3	Theoretical performance of natural refrigerant working fluids	80
Figure 3.4	Tonnes Cu per MW nett power for 3 and 12 mm condenser tubes	82
Figure 3.5	Overall horizontal condenser tube HTC's as a function of vapour quality	83
Figure 3.6	Condenser HTC and nett thermal efficiency of engine	84
Figure 3.7	Condenser HTC and HTC / pressure drop as a function of fin spacing	84
Figure 3.8	Cut length of ethane and CO_2 horizontal condenser tubes	85
Figure 3.9	Tube-fin condenser temperature glides at 100 and 500 kg/m^{2}s	86
Figure 3.10	Glaciothermal boiler HTC as a function of ice slurry velocity	88
Figure 3.11	Ice slurry HTC as a function of tube diameter, supercooling and velocity	88
Figure 3.12	Glaciothermal boiler HTC as a function of seed ice mass fraction	89
Figure 3.13	Apparent heat capacity and ice slurry forced convective HTC	89
Figure 3.14	Glaciothermal boiler tube HTC as a function of feed temperature	90
Figure 3.15	Cut length of boiler tubes as a function of ice slurry flow velocity	90
Figure 3.16	Glaciothermal boiler temperature glides for 10% seed ice fraction	92
Figure 3.17	Glaciothermal boiler temperature glides for 30% seed ice fraction	93
Figure 3.18	Ice slurry HTC and HTC / pump work as a function of ice slurry velocity	94
Figure 3.19	Ice slurry pump parasitic losses as a proportion of engine efficiency	94
Figure 3.20	Condensate injection ratios demonstrate relative pumping effort	95
Figure 3.21	Condenser fan parasitic losses as a proportion of engine efficiency	95
Figure 3.22	Basic glaciothermal engine performance curves	96

Figure 4.1	Surface gradient map of Antarctica	101
Figure 4.2	Density curves for freshwater and ice-shelf water	102
Figure 4.3	Southern Ocean circulation to the coast from Antarctic divergence	103
Figure 4.4	Ice shelf water of uniform salinity around 34.65 g/kg	103
Figure 4.5	Wind glaze areas on East Antarctic plateau	104
Figure 4.6	Year round air temperature percentiles for selected Antarctic stations	105
Figure 4.7	Ambient air temperature calendars for selected Antarctic sites	106
Figure 4.8	Seawater surface temperatures from *MRV Aurora Australis* voyage tracks	107
Figure 4.9	Seawater surface temperature versus salinity from selected voyages	108
Figure 4.10	Seawater surface temperature versus salinity showing ice shelf water	108
Figure 4.11	Daily aggregates of 1 minute seawater temperature data	109
Figure 4.12	Year round seawater salinity estimate using polynomial regression	110
Figure 4.13	Year round seawater temperature estimate using polynomial regression	110
Figure 4.14	Map of mild coastal, cold ice-shelf and frigid interior type locations	111
Figure 4.15	Histograms of year round ambient air temperatures for interior sites	112
Figure 4.16	Histograms of year round ambient air temperatures for ice-shelf sites	113
Figure 4.17	Histograms of year round ambient air temperatures for coastal oases	113
Figure 4.18	Year round ambient air temperature data for high elevation interior site	114
Figure 4.19	5-year 5-pt moving average air temperatures for selected Antarctic sites	114
Figure 4.20	Year round nett efficiency of basic glaciothermal engine	115
Figure 4.21	Manning velocities for finished concrete tunnels	116
Figure 4.22	Performance of basic glaciothermal engine including seawater pump losses	117
Figure 4.23	Nett efficiency of glaciothermal system on East Antarctic Plateau	117
Figure 4.24	Comparative efficiency of glaciothermal systems including pumping losses	118
Figure 4.25	Comparative efficiency of glaciothermal systems on the Windmill Coast	118

Figure 5.1 Meltwater bell provides heat source for year round power generation 122

Figure 2A-1	Latent heat of fusion for natural working fluids	132
Figure 2A-2	Working fluid densities for vapour and condensate	132
Figure 2D-1	Characteristic salinity curves for seawater brine	135
Figure 2E-1	Salinity liquidus curve for seawater brine	136
Figure 2F-1	Operating range for an ice slurry loop showing wide set point	137
Figure 2F-2	Ice slurry freezing curves for temperature and brine salinity	139
Figure 2H-1	Supercooling degree for scraped-tube ice nuclei	143
Figure 2H-2	Radius and critical radius of homogeneous ice nuclei in seawater brine	144
Figure 2H-3	Free energy of heterogeneous ice nucleation	144
Figure 2K-1	Critical radius for homogeneous nucleation of vapour bubble nuclei	154
Figure 2K-2	Indicative dimensions of some structured and porous EBS's	156
Figure 2K-3	SEM images of micro-nano cones formed by electro-deposition of nickel	157
Figure 5A-1	Glaciothermal capacity and thermal storage efficiency of meltwater bells	163
Figure 5A-2	Proposed ground source thermal storage device	165
Figure 5A-3	Shear strain rates for low temperature ice	166
Figure 5A-4	Control logic for operation of ice sheet thermal storage	167
Figure 5B-1	Seawater and ground source thermal storage on iceshelf	169
Figure 5B-2	Exponential growth of engine components, feedwater and thermal storage	170
Figure 5C-1	Phase equilibrium for CO_2 clathrate hydrates	172
Figure 5C-2	Illustration of potential 10,000 MW vaporjet expander concept	173
Figure 5C-3	Qualitative model of power output from vaporjet expander	173
Figure 5C-4	Map of Antarctica showing 5 million km^2 of icesheet colder than -40 °C	174

List of Tables

TABLE I HIGH PRESSURE NATURAL WORKING FLUIDS 44

List of Appendices

2-A	**Working fluid thermophysical properties**	**132**
2-B	**Liquid refrigerant pump**	**133**
2-C	**Seawater thermophysical properties**	**134**
2-D	**Characteristic salinity**	**135**
2-E	**Continuous properties model**	**136**
2-F	**Ice slurry loop control**	**137**
2-G	**Ice slurry classifier**	**141**
2-H	**Ice crystal nucleation**	**143**
2-I	**Ice crystal growth**	**146**
2-J	**Glaciothermal heater**	**148**
2-K	**Vapour bubble nucleation**	**154**
2-L	**Twin screw expander**	**158**
2-M	**Glaciothermal engine summary**	**160**
5-A	**Potential augmentation methods**	**162**
5-B	**Year round augmented power**	**168**
5-C	**Potential large scale augmentation methods**	**171**
5-D	**Miscellaneous findings**	**175**
5-E	**Future work**	**176**

List of Acronyms

AAD	Australian Antarctic Division
AGL	Above Ground Level
AMTD	Arithmetic Mean Temperature Difference
ASL	Above Sea Level
ATS	Antarctic Treaty System
AWS	Automated Weather Stations
BFP	Butane Freezing Process
BGC	Basic Glaciothermal Cycle
BGE	Basic Glaciothermal Engine
BPMED	Bi-Polar Membrane Electro-Dialysis
BoM	Bureau of Meteorology (Australia)
CEE	Comprehensive Environmental Evaluation
CFD	Computational Fluid Dynamics
CSIRO	Commonwealth Scientific and Industrial Research Organisation
DAC	Direct Air Capture (of carbon dioxide)
DEG	Diesel Electric Generator
DSD	Department of State Development
EBS	Enhanced Boiling Surface
EIA	Environmental Impact Assessment
EN	Electroless Nickel
FEA	Finite Element Analysis
GFE	Gibbs Free Energy
GSHX	Ground Source Heat Exchange
GWP	Global Warming Potential
HTC	Heat Transfer Coefficient
HFE	Hydrofluoroether
HX	Heat Exchange, Heat Exchanger

IFP	Incipient Freezing Point
INC	Ice Nucleation Coatings
ISG	Ice Slurry Generator
ISW	Ice Shelf Water
LMTD	Logarithmic Mean Temperature Difference
MTD	Mean Temperature Difference
MWB	Melt Water Bell
NFE	Nucleation Free Energy
ODP	Ozone Depletion Potential
ORC	Organic Rankine Cycle
OTEC	Ocean Thermal Energy Conversion
RAMPDEM	Radarsat Antarctic Mapping Project Digital Elevation Model
RAPS	Remote Area Power Systems
SAB	Special Antarctic Blend (diesel)
SFE	Surface Free Energy
SRM	Svenska Rotor Maskiner
TD	Temperature Difference
TFC	Tri-lateral Flash Cycle
TPCT	Two-Phase Closed Thermosyphon
TR	Thermal Resistance
TSE	Twin Screw Expander
UTC	Coordinated Universal Time
UW-M	University of Wisconsin, Madison
VFE	Volume Free Energy

List of Symbols

A	m^2	**area**
A_c	m^2	**cross-sectional area**
A	N	**force of adhesion**
ΔC	-	**boundary layer concentration changes**
C_m	-	**ice mass fraction**
C_p	J/kg·K	**isobaric heat capacity**
C_v	-	**ice volume fraction**
D	m, mm	**diameter**
D_h	m	**hydraulic diameter**
D	$kg/s \cdot m^3$	**boundary layer diffusion coefficient**
G	$kg/m^2 \cdot s$	**condensing fluid mass flux**
L	m, mm	**length**
P	bar	**pressure**
Q	J	**total heat**
R	K/W	**thermal resistance**
S	g/kg	**salinity**
S_{100}	g/kg	**characteristic salinity**
T	°C	**temperature**
U	$W/m^2 \cdot K$	**overall heat transfer coefficient**
V	m/s	**velocity**
W	J	**total work**
h	J/kg	**enthalpy**
k	W/m·K	**thermal conductivity**
k_i	$kg/m^2 \cdot s$	**molecular incorporation mass transfer coefficient**
m	kg	**mass**

$\dot{m}$	**kg/s**	**mass flow rate**
m_c	**kg**	**mass of ice crystal**
p	**m**	**perimeter**
q	**J**	**heat (per kg of working fluid)**
$\dot{q}$	**J/s**	**heat flow rate**
r	**m, mm**	**radius**
r	**-**	**surface roughness factor**
s	**m, mm**	**spacing**
t	**m, mm**	**thickness**
t	**s**	**time**
v	**m^3**	**volume**
w	**J**	**work (per kg of working fluid)**
z	**m**	**length of incremental condenser tube segment**

Greek Symbols

α	**$W/m^2 \cdot K$**	**heat transfer coefficient**
γ	**N/m^2**	**surface tension**
δ	**m**	**boundary layer thickness**
δ	**K**	**range of temperature glide**
η	**-**	**process efficiency**
θ	**°**	**solid smooth surface contact angle**
θ'	**°**	**solid rough surface contact angle**
μ	**Pa·s**	**dynamic viscosity**
ν	**m^2/s**	**kinematic viscosity**
λ	**W/m·K**	**thermal conductivity**
ρ	**kg/m^3**	**density**
ϕ	**K**	**degree of superheating**

χ	**K**	**initial temperature difference**
ψ	**K**	**degree of supercooling**

Subscripts

1	**inlet of working fluid control volume**
2	**outlet of working fluid control volume**
air	**ambient air**
$alloy$	**ice-brine alloy (ice slurry)**
$bare$	**exposed area of tube between adjacent condenser fins**
$base$	**base of condenser fin**
$boil$	**working fluid vaporisation conditions**
$brine.\ B$	**liquid phase of ice-brine alloy**
c	**condensate, condensation**
cf	**carrier fluid (brine phase in the case of ice slurry)**
$cold$	**thermal layers on cold side of heat exchanger**
$cond$	**condenser outlet conditions**
$duct$	**rectangular cross-section formed by adjacent tubes and fins**
EBS	**enhanced boiling surface**
ext	**extended fin surface area of tube-fin condenser**
f	**freezing**
fan	**condenser fan**
$feed$	**seawater or meltwater entering the ice slurry mixer**
$film$	**condensate film in contact with boiler or condenser**
fin	**condenser fin**
$fluid$	**working fluid species**
gap	**bond/air gap between condenser tube and fins**
gas	**incompressible gas fraction of condensing vapour**
$glacio$	**glaciothermal boiler (ice slurry + evaporator sides)**

$glaze$	**ice fouling layer on internal condenser tube surface**
hot	**thermal layers on hot side of heat exchanger**
i	**iteration number**
$ice,\ I,\ Ih$	**solid phase of ice-brine alloy (hexagonal ice)**
is	**ice slurry**
$inlet$	**inlet to boiler or condenser tube**
l	**liquid**
m	**melting**
mat	**matrix material of enhanced boiling surface**
mix	**ice slurry mixture leaving ice slurry mixer**
n	**number of objects**
$node$	**node within boiler or condenser flow model**
$pitch$	**spacing between adjacent condenser tubes**
$press$	**cold condensate from condenser injected to boiler pressure**
$prime$	**ice mass fraction entering the ice slurry mixer**
$pump$	**mechanical pump**
$rime$	**ice/snow fouling layer on external condenser fins**
s	**solid**
sat	**working fluid phase at saturated equilibrium**
sea	**seawater**
$seed$	**seed ice mass fraction**
$segment$	**segment within boiler or condenser flow model**
$skin$	**top coat of internal boiler tube surface**
$spent$	**ice slurry mixture leaving glaciothermal boiler**
sub	**substrate of internal boiler tube surface**
$suction$	**working fluid inlet port to condenser**
$throw$	**spacing between adjacent condenser tube rows**

tp	**two phase**
$tube$	**boiler or condenser tube**
v	**vapor, vaporisation**
$wall$	**boiler or condenser tube wall**
wf	**working fluid species**

Boolean arguments

$inline$	**in-line or staggered condenser tube array**

String arguments

$cond$	**type of condenser**
EBS	**type of enhanced boiling surface**
fan	**type of condenser fan**
$fluid$	**working fluid species**
is_{pump}	**type of ice slurry pump**
M_{glace}	**material fouling inner surface of ice slurry tube**
M_{skin}	**material lining ice slurry tube**
M_{sub}	**material forming substrate of ice slurry tube lining**
M_{wall}	**material forming ice slurry tube wall**
M_{mat}	**material forming matrix of enhanced boiling surface**
M_{film}	**vaporising film = working fluid condensate**
M_{glaze}	**ice fouling inner surface of condenser tube**
M_{tube}	**condenser tube material**
M_{gap}	**bonding material or air gap between condenser tube and fins**
M_{fin}	**condenser fin material**
M_{rime}	**ice/snow fouling external condenser fin surfaces**

Literature models

DV	**author for ice slurry dynamic viscosity model**
	Jeffrey (1972), Einstein (1906), Thomas (1965), Meewisse (2004)
HITCF	**author for horizontal in-tube condensing film model**
	Cavallini et al (2006), Dobson & Chato (1998)
ST	**author for seawater brine surface tension model**
	Nayar et al (2014), IAPWS (1994)
TC	**author for ice slurry thermal conductivity model**
	Jeffrey (1973), Eucken (1940), Tareef (1973)
TCI	**author for ice thermal conductivity model**
	Landeur & Plumb (1956), Handbook
TCB	**author for seawater brine thermal conductivity model**
	Sharqawy et al (2010), Jamieson & Tudhope (1970)

Chapter 1 – Introduction

The high level of scientific research activity in the Arctic and Antarctic territories has fuelled ongoing demand for reliable heat and power services in cold climate regions. Expeditioners are faced with the dilemma of how to deal with the environmental impacts of their activities, but at the same time provide for their own reasonable survival needs. Provision of reliable heat and power services to research stations is a constant challenge for modern visitors seeking to support comfortable living conditions and customary energy intensive practices. Reliability is the foremost consideration for station operators who face constant challenges from the remote and extreme environments.

1.1 Background: Challenges of power production in cold climate regions

Conditions atop the ice caps are extreme. Monthly mean temperatures for selected Antarctic stations are plotted in Fig. 1.1 and show the dramatic difference between coastal and interior sites where monthly mean temperatures reach down to -70 °C in winter. Around 5 million square kilometres of the high plateau endure mean annual surface temperatures below -40 °C with the coldest weather station at Dome Argus averaging -58 °C.

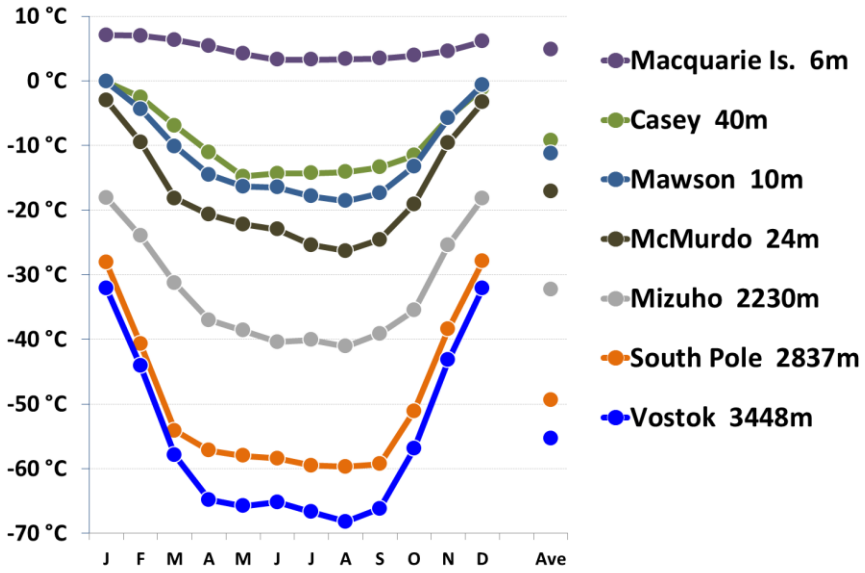

Fig. 1.1. Mean monthly and mean annual temperatures at selected polar stations. ***Data BoM, ACE-CRC [1, 2]***

Mizuho, South Pole, and Vostok stations are situated high on the plateau and remain frigid year-round due to the elevation and latitude. Low seasonal temperature variations at Macquarie Island demonstrate the thermal inertia inherent in the sub-polar Southern Ocean. Antarctic mainland coastal stations such as Casey and Mawson also benefit from the moderating effect of the ocean, although average monthly temperatures only rise above freezing briefly in summer. McMurdo also occupies a low-level coastal site, but its higher latitude leaves it more exposed to the cold interior. Mean summer and winter temperatures for the Greenland ice-cap summit are similar to those at Mizuho station.

Cold polar air contains almost no water vapor, so residual heat from ice and snow surfaces can radiate directly into space through an open infra-red window. Ground-level air becomes dense upon cooling and flows under gravity to form locally intense and persistent katabatic streams. These converge with strong regional synoptic winds at the coast to create fearsome winter conditions at many sites, Fig. 1.2. Wind-blown ice and snow and almost total darkness through the polar winter restrict visibility and limit the mobility of expeditioners for much of the year.

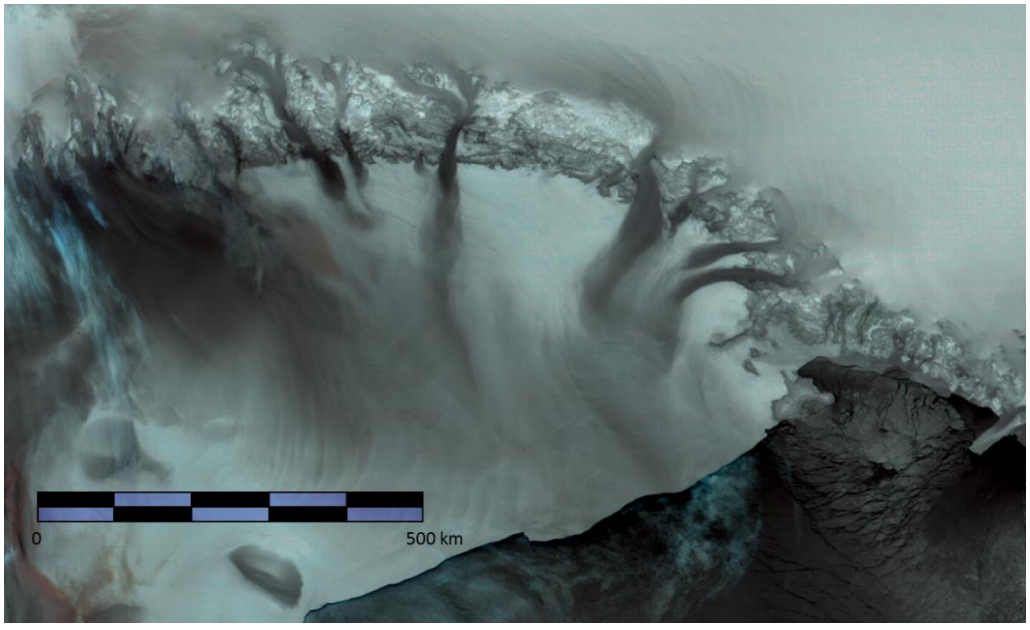

Fig. 1.2. Katabatic winds (dark grey) over Ross Ice Shelf are ~10 °C warmer than low level air (lightest grey).
Image: EUMETSAT Metop-A, Advanced Very High Resolution Radiometer, 27 May 2008, 18:49 UTC

It was not until the 1950's and 60's that diesel generators and oil-fired boilers made it possible to survive year-round on or near to the frigid ice sheets. Dependence upon regular delivery of bulk

volumes of liquid fuel places considerable constraints on the operation of polar stations. Three coastal Australian Antarctic stations (Casey, Davis and Mawson) between them support 200 expeditioners in summer, and 62 in winter, and were consuming around 2.1 million litres of diesel per annum by 2000 [3]. Running out of fuel has severe consequences and seasonal access restrictions pose a real threat to these stations. If a summer resupply were to fail, most stations hold enough reserves to get them through another winter, but a second failure would likely result in crisis with the prospect of some stations being abandoned if their heat-traced pipes or related infrastructure were to freeze.

As with domestic power systems, most remote area power supplies in cold climate regions remain largely dependent upon fossil fuels, Fig. 1.3. Strict controls apply to the use, transport and handling of liquid fuels and other chemicals. Particulate emissions and potential spillages raise the risk of adverse environmental impacts in sensitive areas. The finite nature of fossil fuels, ongoing concern over escalating CO_2 emissions, and a continual desire to improve local air quality are all good reasons to justify a search for alternative clean energy sources. These issues along with the high cost of shipping and logistical support provide ample reasons to reduce our dependence upon fossil fuels.

Fig. 1.3. Main powerhouse 125 kW diesel generators at Casey Station.
Photo © Colin Lee-Hong / Australian Antarctic Division

It would appear desirable to replace diesel and other finite fossil fuels entirely. However, this should not prevent a search for the most effective way to manage the impacts of fossil fuel use, especially where proven systems continue to perform well in other respects. Clean solutions with small footprints and transitory impacts are optimal.

1.1.1 Deployment and reliability of equipment in the field

Before any new energy devices or systems are proposed it is worth considering what impact extreme cold climate conditions might have upon the reliable operation of equipment. This section identifies some typical issues that have been encountered in the past.

Numerous alternative energy systems have been investigated for use in cold regions. Only recently though have suitable wind and solar technologies been developed that are sufficiently robust and reliable for routine deployment. Operators face a range of logistical problems in attempting to deliver, install and operate their power systems.

Remote sites by definition only have access to limited infrastructure. Even with a suitable window for delivery of supplies in summer equipment may not easily be offloaded from ships. Large wind turbine components weigh many tonnes. Masts for the 300 kW units installed at Mawson Station had to be shortened to permit erection with a small 100 tonne crane because there are no port facilities to unload a larger one [4], Fig. 1.4. Smaller wind turbines previously erected at Syowa station were cantilevered into position using a small winch and gin-pole [5].

Special methods are also needed for foundation works. Conditions at coastal sites may be mild enough in summer to permit pouring of concrete footings if the ground has thawed, but this is not the case for many sites. Permafrost conditions need to be considered. The ground at Ross Island is perpetually frozen and strict environmental guidelines apply. During construction of their wind farm, prefabricated concrete footings were transported and placed above ground for each of eight legs comprising the base of the wind turbine towers [6].

Frigid conditions provide many operational challenges as well. Low temperature lubricants are typically required for cold running equipment such as gearboxes, transmissions and hydraulics. A small horizontal axis wind turbine at Casey Station went offline a number of times during early testing due to gearbox lubrication, oil seal and pitch control problems [7]. Concerns over similar issues were subsequently addressed at Mawson station by selecting a gearbox-less variable pitch turbine model [4].

Fig. 1.4. Two 300 kW horizontal axis wind turbines provide 35% of Mawson Station energy needs.
Photo © Leslie Frost / Australian Antarctic Division

Strong winds create various problems for wind turbines and other energy captors. Early wind turbine models suffered a variety of problems under such conditions, but continuous improvement over the decades has led to modern designs that are robust and reliable under the most adverse conditions. Commercial wind turbines today can furl their blades during high winds and reduce power output to ride through severe storms.

Icing is a serious problem for sub-Arctic wind turbines due to high humidity air masses that originate over warm northern oceans. Falling ice poses a significant risk to people and equipment [8]. Anti-icing strategies have been investigated, including antifreeze coatings, black paint, mechanical shivering, resistance heaters on blade surfaces, hot air inside blades, and inflatable mechanical de-icing methods as used in aviation. Commercial wind turbine manufacturers advertise blade heating solutions with sensors to detect when atmospheric conditions are prone to icing. Icing conditions may vary dramatically with height. At Pori in western Finland in-cloud icing was measured to be 7 times as frequent at 84 m as at 62 m. Blade heaters typically consume 1—5% of generated power and lightning strikes are an issue for wind turbines that use resistance heating elements rather than warm air fans for blade heating [8].

By contrast, the winds that descend from the Antarctic plateau are exceedingly dry. Icing conditions do occur with onshore winds around Antarctica, but absolute humidity is lower for air masses that originate over cold ocean waters or atop the vast sea-ice domain in winter. Electrostatic discharge is more of a problem with dry winds and turbines need to be properly earthed [4]. Build-up of drift snow, mechanical damage and abrasion from wind-blown sand, ice and snow also pose a problem for wind turbines, photovoltaic panels and other captor devices, especially those located at low level coastal sites.

Extreme cold presents a range of problems for many different devices and manufacturers typically need to develop purpose-built models. A significant proportion of commercial wind turbines are deployed in cold climate regions and standard models are invariably modified. The Arctic design of 100 kW Northwind turbines installed in Kotzebue Alaska is rated to -50 °C [9].

Electrical equipment and batteries that operate reliably under mild conditions will very often fail in the extreme cold. Electronic circuitry required for ambient operation at frigid interior sites will need special purpose-built low temperature components. Custom built devices are very expensive and time consuming to deploy. One way around this problem is to provide heated compartments so that affordable standard electronics can be used instead [10]. Batteries also often fail at low temperature. For electrolyte at -30 °C, the relative capacity of a lead acid battery is only about 30% of that at 30 °C [11].

The above issues regarding operation of appliances in cold climate conditions do not represent an exhaustive list. Specific challenges will arise for any project and contingencies need to be planned. Critical systems must be robust and reliable enough for continuous stand-alone operation.

1.1.2 Utilisation of renewable energy captors

Regardless of the durability of a device, the foremost economic consideration that affects the selection of a suitable renewable energy captor at a given location is the actual utilization. The *capacity factor* is the ratio of mean average power output of a device throughout the year, compared to its rated maximum capacity. This is a product of the captor performance curve, and of energy

availability at that location. Capacity factors may vary between different captor devices at the same site, and between different sites for the same captor device.

Capacity factor is the critical economic metric when assessing the renewable energy potential of an installation. Intermittency of wind or solar energy is a critical factor. The power or efficiency rating of an installed captor is of little concern if the wind at the chosen site is typically weak or calm, or if the sun is often blocked by clouds. Finding ways to improve captor efficiency under very low ambient energy conditions is the main aim. Operators have explored different strategies to improve the capacity factor of various renewable energy captors, including wind turbines, photovoltaic cells, solar thermal and wind thermal devices. Key factors that impact utilization include resource intermittency, energy conversion efficiency across the full range of ambient conditions and device configurations, device availability, reliability, survivability and maintainability [7].

Intermittency is the primary economic constraint so it is essential to develop a sound understanding of the nature of different renewable energy resources that are available.

1.1.3 Potential renewable energy sources

The Earth's Polar Regions contain a variety of local renewable energy sources. Obvious wind and solar resources are accompanied by other less familiar forms. Le Goff identified air pressure, wind velocity, temperature and humidity as potential sources of energy inherent in the atmosphere. He calculated time dependent fluctuations in the energy content of a cubic meter of air at selected field locations in France [12]. The thermal and dryness energy components were found to be 100 to 1,000 times larger than the kinetic energy of the wind. Although it is impractical to exploit variations in barometric pressure for energy production, various thermal methods might be devised to exploit heat flows from ambient and seasonal temperature differences and evaporative humidity effects.

The following section describes the natural polar energy sources that exist and some of the energy captors that have been installed.

1.2 Evolution of renewable energy systems in cold climate regions

Numerous alternative energy systems have been conceived over several decades to help supplement fossil fuels for the provision of reliable heat and power services at remote sites. Many early systems struggled to achieve reliable operation under the extreme conditions but persistent adaptations and technological improvements have delivered excellent results.

Recent developments have seen the emergence of wind power as a key component of hybrid energy systems for the delivery of heat and power services at permanently manned polar research stations. Dual thermal and electrical carrier systems have evolved that enable high penetration of wind energy, and to a lesser extent summer-only solar energy, into the station energy mix. Modern energy management systems permit intermittent sources to be captured and promptly diverted to thermal and other dump loads. Renewable captors are scaled to match the thermal inertia inherent in thermal carrier systems and thus balance the varying supply loads. Sites of low wind availability require too much electrical storage to achieve the same results.

High penetration of renewables has also been achieved at interior summer-only stations using advanced energy management systems. Integrated wind, solar thermal and photovoltaic systems with warm battery storage are able to provide up to 100% of heat and power needs without burning any fossil fuels. Diesel generators provide start-up and emergency backup power only. Solar thermal systems typically enjoy very good payback periods, and new photovoltaic devices are also very affordable.

Specific strategies that different operators have explored in attempting to improve the utilization of various renewable energy captors are described in the following sections.

1.2.1 Wind energy

Constant strong winds are a well-known feature of the Antarctic coast. Cold dense air masses above the ice-sheet spill slowly downward under the influence of gravity, are deflected to the west of the fall-line by 20° to 50° due to the Coriolis force, and collect into fast-moving katabatic air streams near the coast. At the same time, equally powerful synoptic winds associated with cyclonic

depressions circumnavigate the continent, as clearly depicted by the inferred storm tracks shown in Fig. 1.5 (a). The synoptic winds are further deflected by the topography of the continent and often coincide with and reinforce katabatic flows to produce notoriously strong and persistent winds along the Antarctic coastline [13]. The strongest winds at most stations have a predominant direction, Fig. 1.6.

Numerous concepts have been devised to harness the energy of the wind. Except for an assortment of wind tether devices, most practical designs consist of rotating blade configurations that can be broadly grouped as either vertical axis wind turbines (VAWTs) or horizontal axis wind turbines (HAWTs).

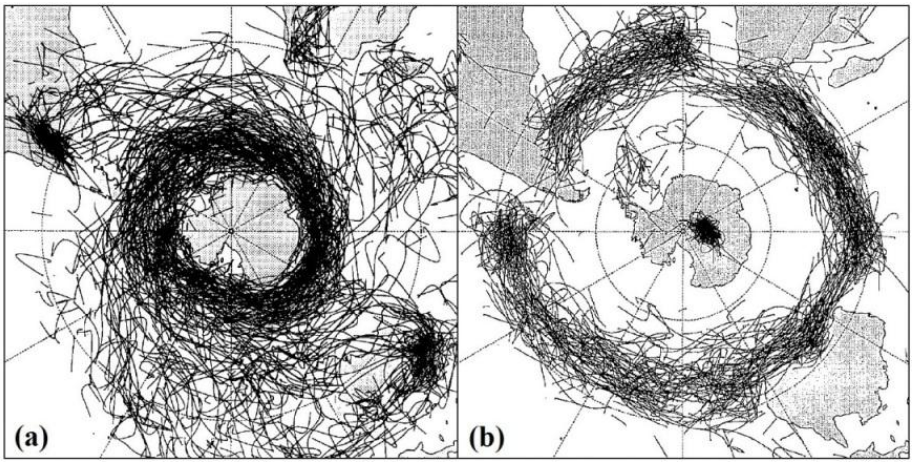

Fig. 1.5. Inferred tracks for **(a)** extra-tropical cyclones (low pressure cells) and **(b)** anticyclones (high pressure cells) for summers 1985-89. No storm fronts cross the plateau. ***Taken from Jones and Simmonds [14, 15].***

VAWTs include slow rotating Savonius rotors for pumping water, and faster Darrieus rotors ('egg beaters') for electricity generation. Darrieus rotors are not self-starting although H-rotor variants can overcome this. VAWTs do not require yaw control, are typically inefficient, and cannot be scaled up to utility size due to cyclic loading of components. HAWT blades operate under constant load and thus can be scaled up into the MW range without sacrificing reliability.

The 10 m diameter 20 kW prototype H-rotor VAWT of Fig. 1.7 (a) was installed at Neumayer in 1991 and meets 6% of station needs. It has proved reliable as it has no gearbox or moving parts other than the rotor itself. Permanent magnets are mounted in the rotor, and the travelling field generator

integrated into the frame produces variable frequency AC current. Control in high winds is achieved by eddy current braking [16].

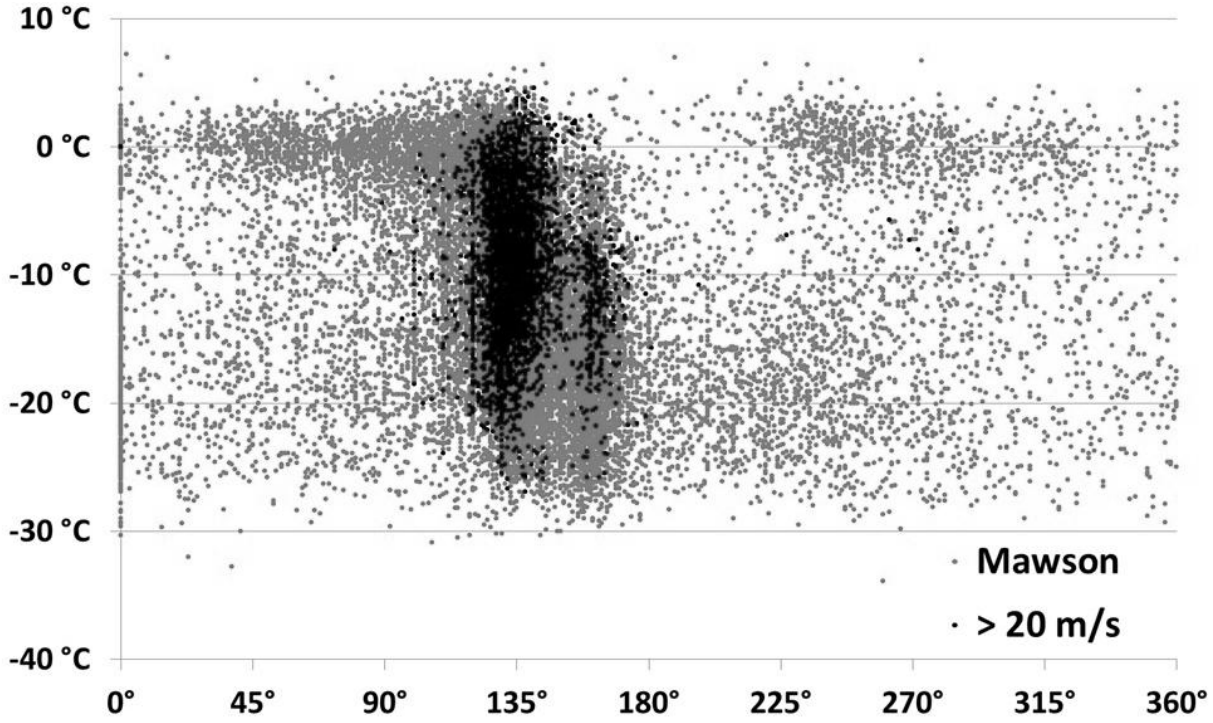

Fig. 1.6. Three-hourly wind direction and temperature for Mawson station 2000-2009. ***Data from BoM [1].***

The 30 m diameter 300 kW HAWT in Fig. 1.7 (b) has been in operation at Mawson since 2003 and also has no gearbox. Variable speed, variable pitch blades and modified control software provide sufficient turbine control to permit wind penetration that regularly exceeds 90% of station load [3]. Larger units are now routinely deployed at permanently manned stations.

A small 500 W nominal capacity Savonius variant VAWT powers an automated field station near the Italian Mario Zucchelli summer station. This ruggedized unit has been modified to solve the problem of low start-up torque and does not need any mechanical braking device. Operating wind velocity range starts at 2 m/s, extends up to 12 m/s at the nominal output of 500 W, with output slowly ramping to a maximum of 1,300 W at 70 m/s. An electronic unit controls battery charging and load switching. A dynamic system determines the optimum alternator r.p.m., thus enabling maximum power point tracking for any given wind conditions [17].

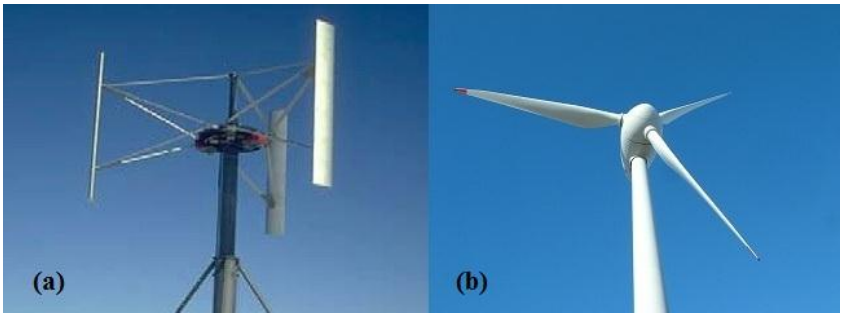

Fig. 1.7. (a) Vertical axis and **(b)** horizontal axis wind turbines.
Photos by Saad El Naggar [16] and Leslie Frost, AAD.

Other stations have numerous installed HAWT devices. 14 different HAWT models are deployed by the Japanese Antarctic program with most in the 0.1—1.2 kW range and used to power unmanned observatories [11]. Early problems included vibration, faulty slip rings, freezing grease, and poor control of battery charging, [11]. South Korea's King Sejong station have installed a 10 kW turbine and studies aim to develop anti-icing and de-icing technologies for small wind turbines under 50 kW [18].

An early wind power test program carried out at Casey station encountered initial teething problems. Operators found a dramatic shortfall in the expected power output from the 10 kW HAWT shown in Fig. 1.7 [7]. The ruggedized unit features a clever variable pitch design for speed control and stall regulation at high rotational speeds and has a very high rated survival wind speed of 90 m/s. Initial problems arose due to icing inside one of the calibrated weight bars used in the pitch control mechanism due to a cracked cap. High currents in the 3-phase induction generator during high wind episodes led to over-heating and thermal cut-out outages. Superior power output was achieved following repairs. The design was modified to correct these faults resulting in a new more robust model.

Reduced output was also noted due to the extreme gutsiness of winds. An 85% reduction factor was applied to the performance curve in Fig. 1.8 to reconcile the rated output of the turbine with power losses due to the turbulent air flow encountered at the site. Fine-scale wind speed measurements taken at 2-second intervals over several hours showed frequent instantaneous fluctuations of +/- 5 m/s, with gusts up to 80.8 m/s recorded in the past [19].

Adaptations fashioned during this trial were kept in mind when large commercial turbines were subsequently commissioned for installation at Mawson station. With only minor modifications to the off-the-shelf design, two 300 kW horizontal axis units have achieved annual wind energy penetration averaging 35% of station energy needs, along with corresponding fuel savings and emissions reduction [3, 7].

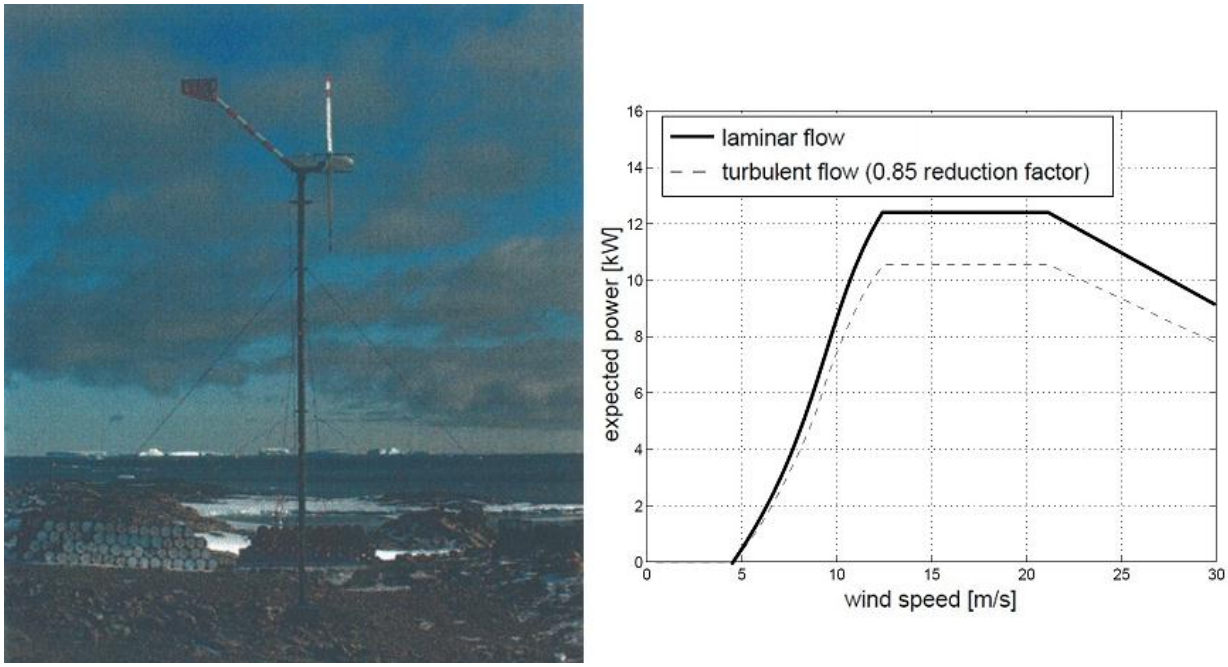

Fig. 1.8. Aerowatt UM-70X wind turbine and performance curve, Casey Station.
Photo by Christopher Brown [7].

A feasibility study into the wind power potential at South Africa's coastal SANAE IV base included energy demand analysis for the station. The performance of five commercial wind turbines was evaluated against a theoretical wind model extrapolated from near ground wind records. Analysis showed similar wind conditions to the Mawson site, with average wind speed calculated to be between 10.85 and 12.20 m/s, depending upon height above the ground. The study concluded that the favoured wind turbine would be able to produce a similar 35% of station energy needs [20].

Wind farms have since been built or are planned for various other stations around the Antarctic coastline. A wind farm shared between the US McMurdo Station and New Zealand's Scott Base was constructed on Ross Island during the 2008/09 and 2009/10 seasons and is performing in line with modelled expectations [6]. Three 330 kW maximum power rated turbines are able to produce up to 70%

of the total electrical needs of both stations at any given time. Annual fuel savings are estimated to be 11% of the total electrical requirements on Ross Island. A key achievement was the interconnection of two disparate electrical grids, one operating at 50 Hz and the other 60 Hz.

Wind energy research carried out for the high altitude French-Italian Concordia station found that the more constant but lighter winds at Dome C require more light weight turbine towers than at the coast [21]. Thin air reduces the nominal maximum power rating of a 33.4 m diameter commercial wind turbine from 335 kW down to 308 kW (at -78 °C and 630 mbar). Three base frames and guy cable stays would enable 40 m towers to access stronger winds, and so increase the capacity factor. Maximum turbine output would be double that of crucial station loads, with excess power diverted to resistor banks for snow melting and heating.

Early attempts to introduce wind energy in Antarctica included an array of small and often custom-built devices that encountered a variety of challenges. Field trials identified specific problems and ongoing refinements led to reliable designs and ultimately to the successful commissioning of large wind farms at a number of Antarctic locations today. Appropriately adapted commercial wind turbines already supplement fossil fuels at selected stations.

1.2.2 Solar energy

Despite the high latitude, incident solar radiation is quite strong at the poles due to the clean and dry polar air which absorbs much less of the Sun's energy [22]. Interior sites remain almost entirely cloud-free (as Fig. 1.5 (a) might suggest) and exceptionally high insolation is further enhanced by reflected radiation over snow which can add another 30-40%. Radiation intensity can reach 1,200 W/m^2 on inclined surfaces. Coastal sites tend to be obscured by cloud which reduces insolation by more than 50%, and as much as 80-90% on the Antarctic Peninsula.

At high polar latitudes, solar radiation is only present during the summer months, but this is more than convenient for elevated summer-only stations. Intense sunshine and clear skies make high altitude interior sites exceptionally good for solar energy applications. Mean daily insolation of ~500 W/m^2 at the poles during summer is higher than anywhere else on Earth, Fig. 1.9. Continuous

24 hour insolation means that high solar dependence is a genuine possibility over summer. A range of solar devices have been employed to provide heat and power services.

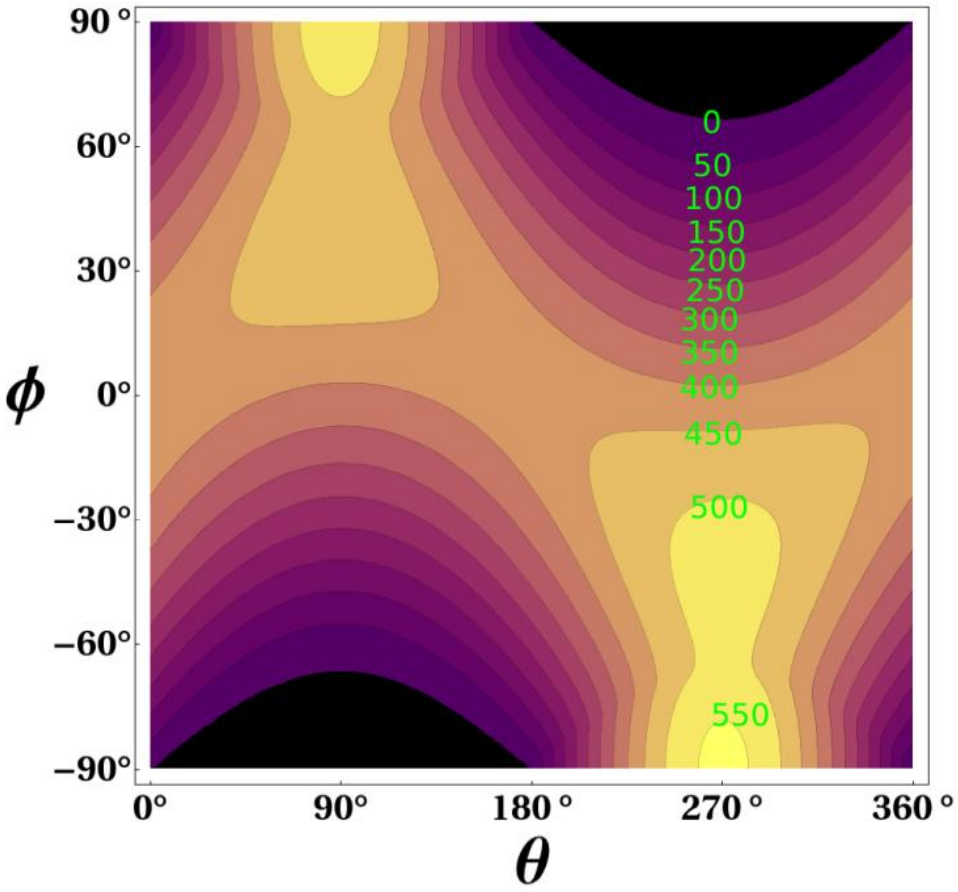

Fig. 1.9. Daily-average insolation in W/m^2 at the top of the atmosphere calculated for the year 2000. $\boldsymbol{\phi}$ is latitude, and $\boldsymbol{\theta = 0}$ and $\mathbf{180^\circ}$ at equinox, and $\mathbf{270^\circ}$ for the Austral summer [23].

Two different types of passive air-type solar collectors were designed and tested for space-heating at Syowa station. A black perforated aluminum plate comprises the solar collector in each case. In the open ventilation design the plate is mounted directly onto the exterior wall with an appropriate air-gap. Heated air surrounding the panel is drawn through an opening into the building by convection and fan. In the closed circulation design, the plate is enclosed behind an acrylic sheet and incoming cool air is drawn from inside the building. Three closed circulation acrylic panels can be seen mounted to the left of a single open vent collector in Fig. 1.10. Temperatures were recorded throughout a 24 hour period on March 27th and it was found that fan-assisted, circulation type panels on NW facing walls were best at raising room temperatures [24].

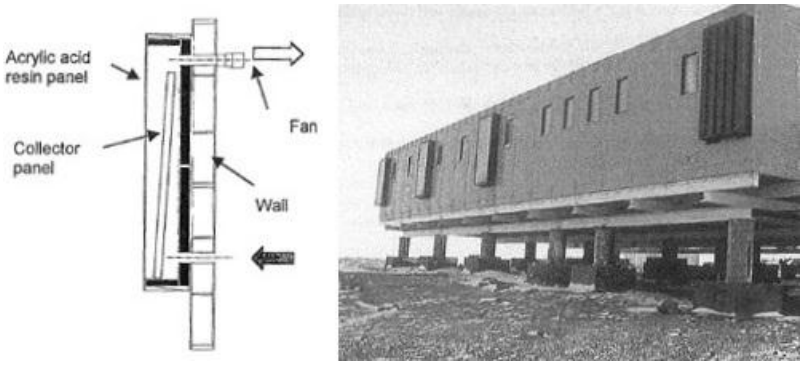

Fig. 1.10. Solar chimneys at Syowa station. ***Photo from Iwata et al [24].***

Various solar thermal devices, including commercial vacuum tube solar heaters, can be adapted to melt snow and heat water under ambient cold climate conditions. Space technologies were used in the design of a snow melting facility at Vostok station [25] that employs a lightweight solar concentrator and absorber to generate steam, see Fig. 1.11. The absorber is housed within a glazed envelope to reduce heat loss to the wind, and the heat transfer system permits high heat flux from the absorber to the snow without need for a mechanical circulation pump. Laboratory testing of an experimental design was carried out before field trials at Vostok. The system was able to produce around 6 litres of water per hour at 50% thermal efficiency. The compact mobile device was deployed by a single person and is designed to survive air temperatures of -80 °C and winds to 25 m/s.

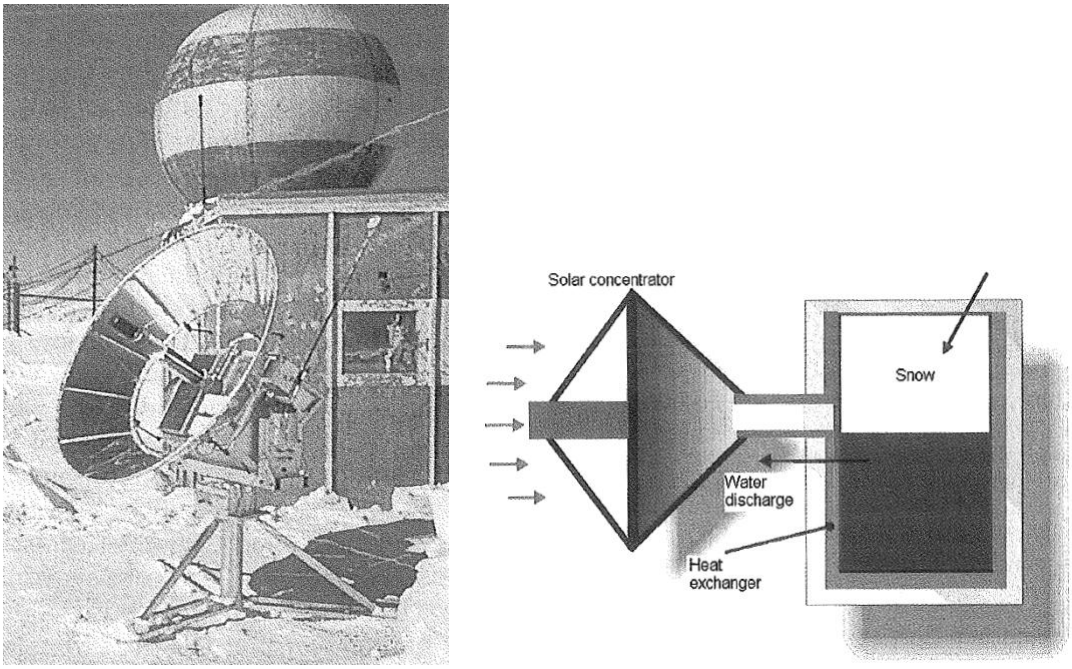

Fig. 1.11. Solar concentrator for snow melting. ***Photo and schematic by Arkadiy Sheynshteyn [25]***.

Photovoltaic (PV) arrays provide electrical rather than thermal energy output. Summer-only research stations and a variety of autonomous field stations make extensive use of PVs on the Antarctic plateau. Low-power systems for unmanned experiments use PV panels to charge low-temperature batteries. Custom cold-temperature electronics permit full-year cold operation of low-power magnetometers (LPMs) and similar devices. A medium-power system developed by the British Antarctic Survey to supply a constant 100 W for their automated geophysical observatories (AGOs) requires a 300 W PV panel, plus additional energy from two 200 W wind generators. Various methods are employed to maintain enough warmth to run common batteries and room-temperature electronics [10]. The poor storage and discharge performance of batteries at low temperatures is well known. For electrolyte at -30 °C, relative capacity of a lead acid battery is only about 30% of that at 30 °C [11]. Energy to heat the high insulation enclosure in Fig. 1.12 is supplemented by 300 kg of water which delays the temperature dropping below 0 °C for the week it takes to freeze.

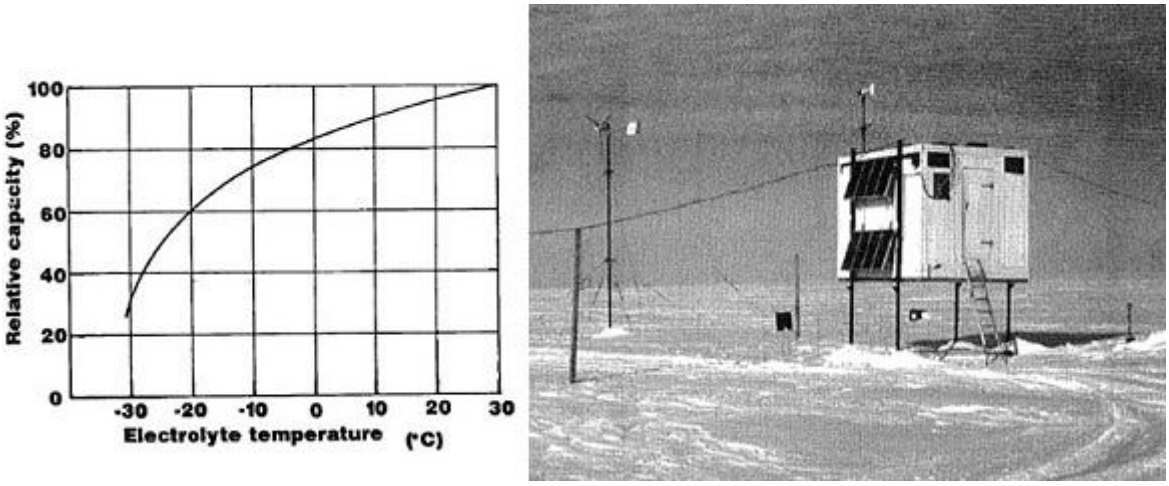

Fig. 1.12. Lead-acid battery capacity as a function of temperature. ***Chart taken from Ishizawa et al [11]*** Automated geophysical observatory (AGO) employing wind and PVs. ***Photo from Rose et al. [10]***

An analysis of energy requirements at the Swedish summer research station Wasa, built in 1989, identified capture of waste heat from existing diesel generators as a key priority to help reduce annual diesel consumption from 21 to 10 m^3 [26]. A wind generator and solar thermal collectors had previously been in operation to supplement diesel usage at the station. Since then around 2.6 kW of solar panels and associated Ni Cd battery storage have been installed [3], and various heating appliances switched to LPG operation. Passive heating, heat exchangers and other energy

conservation measures have also been introduced. A diesel generator is only needed very early or late in the summer season to provide supplementary energy. Belgium's Princess Elisabeth station makes similar use of wind turbines and numerous solar devices for its primary energy, and only maintains diesel generators for emergency backup [3].

For permanently-manned stations at high elevation, solar energy is less attractive because the hardware is out of action for six months of the year through the deep winter. Investigations into the performance of proposed PV panels for use at the South Pole [27] concluded that vertical 1-axis tracking was the preferred configuration, as vertical panels best collect reflected radiation from the snow surface. Total insolation was theoretically estimated to be 947 W/m^2, and the low solar radiation to electrical conversion efficiency of PVs meant that the average energy output modelled over six months of summer, including cloudy days, was just 58 W/m^2. Tracking panels were found to be too expensive at the time but PV prices have fallen dramatically since then. Solar-thermal devices enjoy far superior energy conversion efficiencies to photovoltaic cells which seldom exceed 20% (although thermoelectric-photovoltaic cells promise ~40%).

For stations near the coast, intermittent weak insolation typically limits penetration of solar energy to < 5% of station needs. Performance analysis of a 30 kW PV array installed at the coastal Syowa station concluded that extending the array farm to 60 kW would ultimately enable the system to meet 5% of station electrical needs [28]. A technical and economic evaluation of solar energy potential at SANAE IV base[29] found that flat-plate solar thermal collectors could be installed for use with a snow melter and would deliver solar energy with a competitive payback period of 6 years. A 40 kW photovoltaic array would only just pay back its investment cost by the end of its 25 year expected lifespan. A feasible hybrid system would save 3.5% of station fuel, and is justified on the basis of the electrical load reductions made possible during the busy summer changeover months.

A range of solar energy methods can help to make deep cuts in fossil fuel consumption over summer months, but even at the best polar renewable energy sites, diesel generators and liquid fuels are still required for emergency backup and cannot be dispensed with entirely.

1.2.3 Hybrid systems

This section describes one of the favoured hybrid system architectures devised for permanently manned Antarctic stations, and other case studies from various polar stations that map the progress of power system evolution over recent years.

In 1993 the SCALOP sub-group on Alternative Energy declared that research was needed to develop hybrid systems to integrate alternative energy sources into operating station heat and power units [30]. Broad studies of station energy needs and alternative energy options led to the identification of wind energy as the most promising option for early implementation. Subsequent detailed investigations into wind power potential by Brown identified suitable sites for deployment and integration of wind turbines [31]. Knowledge gained from these, and other trials, ultimately led to the selection of suitable commercial wind turbine models for deployment at Mawson station in 2002-03. Ten years of operation of these units, along with the design, construction and successful operation of wind farms at several other polar locations [3, 9] has proven the ability of diesel-wind hybrid systems to help reduce fossil fuel consumption.

Dual Carrier Heat and Power

A sophisticated energy management strategy underpinned the installation of plant and equipment at the Australian and French Antarctic research stations [32, 33]. In the energy services model described by Guichard [32], heat and power are delivered as distinct services, Fig. 1.13. Heating services are delivered via a thermal carrier such as steam or hot water piped to the point of use and their inherent thermal inertia provides buffer storage capacity. Non-heating services are delivered by the electrical wiring network and have no inherent capacity for energy storage.

The system comprises a three-tier energy production/carrier/service model. The diesel generator forms the heart of the energy production system and sends both electrical power to the electrical network and waste heat to the thermal carrier system. A fossil fuel boiler may also inject heat. Fossil fuel energy is supplemented by electrical power from wind turbines or photovoltaic arrays, and thermal energy from solar collectors as available. Diversion of excess power from diesel and wind

generators to discretionary thermal loads is regulated to ensure that the diesel engines run under constant load.

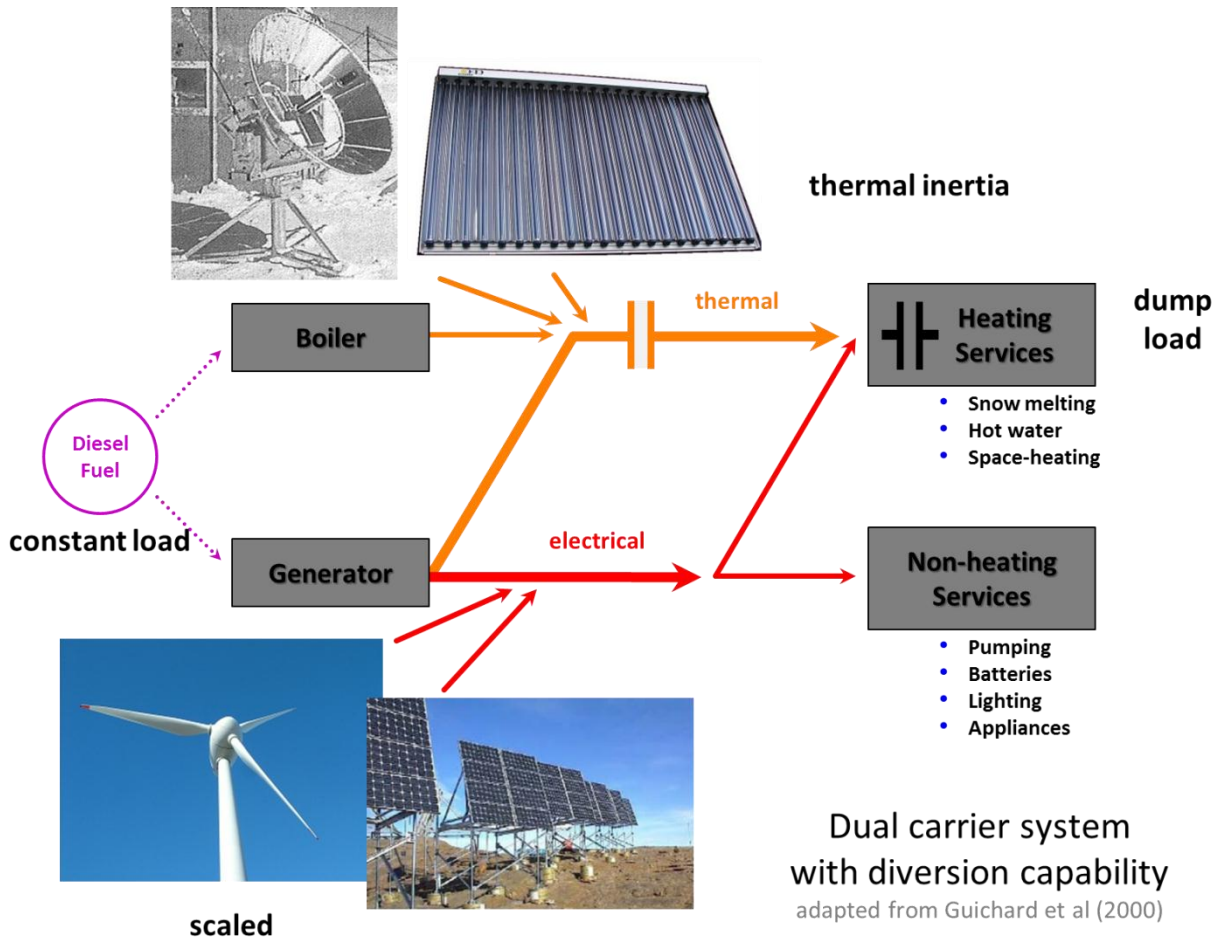

Fig. 1.13. Diesel hybrid heat and power system. Thermal storage and load diversion to integrate renewables. ***Images: Sheynshteyn (2000) [3], Wikicommons, Australian Antarctic Division (Frost), Yoshida (2000) [4].***

Direct regulation of generator output may be required in the absence of suitable diversionary loads. Running a diesel generator under part load can create engine fouling problems that may reduce plant lifespan and increase maintenance costs. Fuel cells may offer an advantage in this case as their operation is equally effective right across their load range. The need for fuel cells has been largely outmoded at most stations, however, by the development of dual carrier systems with inherent thermal inertia, and the availability of large diversionary loads.

Demand for heat and power services vary independently from one another. The thermal inertia of the hot water carrier system helps to maintain heating loads whenever demand for electrical power

takes priority. Dual carrier systems thus have a key advantage over electrical wiring alone in their inherent ability to match varying energy production with varying demand. Importantly, dual carrier systems permit space-heating loads to be delivered as direct thermal energy via hot water instead of inefficient generated electrical supply [21, 32, 33].

As previously noted, the hybrid diesel-wind system at Mawson has two 300 kW turbines and without any additional electrical storage has achieved annual wind energy penetration averaging 35% of station energy needs. In the hybrid diesel-wind system proposed for the French-Italian Concordia base, wind turbine capacity is almost double the size of crucial station loads. Excess power is dumped via resistor bank into the thermal storage buffer provided by snow melting and heating systems [21, 34].

Hybrid systems that achieve high penetration of solar energy have so far been limited to smaller summer-only sites, typically in the high interior. Most recently, the hybrid wind-solar system at Belgium's Princess Elisabeth station has achieved a remarkable 100% renewable energy input for its electrical services. The station is typically only manned during the peak summer months, so their emergency fossil fuel backup generators are seldom needed [3].

Seasonally low insolation rates, including the total absence of daylight through the polar winter, severely limits the application of solar energy devices for use at larger year round stations. High cost and low energy conversion efficiencies have limited the application of photovoltaic devices in the past [7, 27]. PV prices have fallen dramatically in recent times, but capacity factors are still low. Solar-thermal devices also miss out at some stations if their thermal output competes with thermal dump loads from fully scaled diesel-wind systems.

Chiang describes a small pioneering 5 kW hybrid wind-solar power system built for a remote telecommunications facility that is controlled via microwave link from McMurdo Station [35]. This hybrid system balances intermittent supply from four 3 kW wind turbines and three 4 kW photovoltaic panels, with backup power provided by three 1.2 kW ORMAT closed cycle vapor turbines and a 31,680 Ah 24 VDC sealed lead-acid battery bank. Energy distribution is via electrical

means alone as no thermal services are required at this remote unmanned field station. Typical energy production is 44 kWh per day in summer, and 56 kWh in winter. Ambient conditions are extreme with recorded wind gusts up to 268 kph, and minimum temperatures down to -55 °C. The specially adapted, high reliability Arctic wind turbines withstand severe storms by tilting the rotor skyward into a furled position. The ORMAT units in use at the site are more efficient than the propane-fuelled thermoelectric generators used to power other remote field installations within the US Antarctic Program.

Generator Scaling

The amount of waste heat produced by diesel generators affects how much additional heat can be injected into a dual carrier system from renewable sources before surplus heat becomes a problem [32]. Intermittent renewable energy captors and generators are thus typically scaled to match the net shortfall in heat production after all discretionary and essential loads have been accounted for. Energy conversion efficiency is very high for heat created from electrical power (especially using heat pumps) but much lower for power generated from heat.

Snow and/or ice melting requires energy equivalent to 1 litre of liquid fuel for every 65 litres of meltwater. Production of potable water comprises the main discretionary thermal energy load at most polar stations. Provision of freshwater is usually achieved by melting ice and snow and storing the liquid water below the ice surface. Schmidt and Rodriguez (1962) [36] used piped steam to melt a large cavern in the Greenland icesheet at Camp Century over 102 days in the summer of 1960. Steam was shut off on 5th October. They returned after 10 months to find that much of the meltwater had not yet refrozen. The bell shaped chamber thus created was ~15 m in diameter and held around 1,200 m^3 of water. Similar wells and surface ponds are still used to supply freshwater at polar research stations today. The inherent thermal inertia of the melting bell or pond provides a convenient thermal energy buffer for dual carrier systems.

Limits to renewable energy penetration

A natural progression from fossil-fuel-only power systems to co-generation and more recently to diesel-wind-solar hybrid power systems has taken place as power systems become more sophisticated. Power system developments have been accompanied by ongoing improvements in energy management, energy efficiency and behaviour management with the combined effect of substantially reducing the demand for imported fuels [3].

The question arises as to whether or not renewable energy can or should completely replace conventional fuels. Intermittent renewable energy systems might be constructed to completely replace fossil fuels if energy can be stored for use during quiet times.

Resource *availability* and resource *regularity* are the two key economic factors that limit the penetration of intermittent renewables at any given site. *Availability* determines how much generation capacity will be needed, and *regularity* determines how much energy storage capacity will be needed.

That is, if a renewable energy source is only *available* for 25% of the time then 4 times as much captor capacity will be needed to generate 100% of the power. If a renewable energy source appears *regularly* every day then only one day's worth of energy storage will be needed to despatch 100% of the power. If an energy source appears regularly every summer or winter then up to one year's worth of storage may be needed.

If the objective is high penetration of renewable energy, then it is obvious from this analysis that wind turbines will be preferred to solar devices at permanently manned stations because they won't need much storage. Solar devices will clearly be chosen at cloud-free summer-only sites. Hence the cost of supplementing diesel increases sharply in proportion to the use of intermittent renewables due to duplication of energy captor and generator capacity and the high cost of energy storage.

Penetration of intermittent renewables at selected permanently manned stations is so far limited by the scale of discretionary dump loads available to heat and power systems. This is despite good wind availability and regularity at coastal sites with strong katabatic winds, or interior sites with light

surface winds but tall turbine towers. Very high wind energy penetration is possible at some sites if diesel generators can be run under variable load, however, operators are reluctant to run older diesel generator sets at low load due to maintenance issues. Low load diesel units are now available that overcome this limitation, potentially enabling much higher wind penetration at the best sites [37]. It is unfortunate that economic factors do not permit large thermal power stations on the domestic grid to run under variable load.

Full time-series models help to identify optimal hybrid energy combinations with and without electrical storage. Numerous station energy audits and related studies have been undertaken at permanently manned stations including: Casey, Davis and Mawson Stations [7, 19, 31, 38-40], Dumont d'Urville [41], South Pole station [27], McMurdo and Scott Bases [9, 35, 42], Palmer [43], Dome Concordia [21, 33, 44-46], Maitri [47], Sanae IV [20, 29, 48], Syowa [5, 24, 28], Hope Bay [49], Juan Carlos I [50], Escudero [51], Vostok [22], Neumayer [16, 52, 53], Jubany/Carlini [54], Sejong [18, 55], Dome A [56], at summer-only stations including Belgium's Princess Elisabeth [57] and Sweden's Wasa station [26] among many others, and field sites and automated geophysical observatories [10, 17, 35].

Time series modelling at Australian-French Antarctic stations found that wind turbine utilization factors vary from 76.5 and 59.8% for Mawson and Dumont d'Urville stations respectively, down to a costly 26.6 and 22.8% for Casey and Davis. Analysis of wind energy data calculated capacity factors up to 70%, with an estimated 25% fuel saving possible at Mawson from the installation of a 110 kW wind turbine, Fig. 1.14 [19]. Modelling showed that penetration of renewables up to 80% of total energy needs was possible at Mawson with the introduction of just 6 hours electrical storage capacity.

Two 300 kW turbines were ultimately deployed at Mawson with no additional storage. Hydrogen energy storage systems have since been trialled at Mawson and elsewhere, but compact commercial technologies are still sought [40, 49]. Increasing renewables penetration to 90% of annual needs required four times as much storage capacity and was not economically justified. Operational constraints are also a factor.

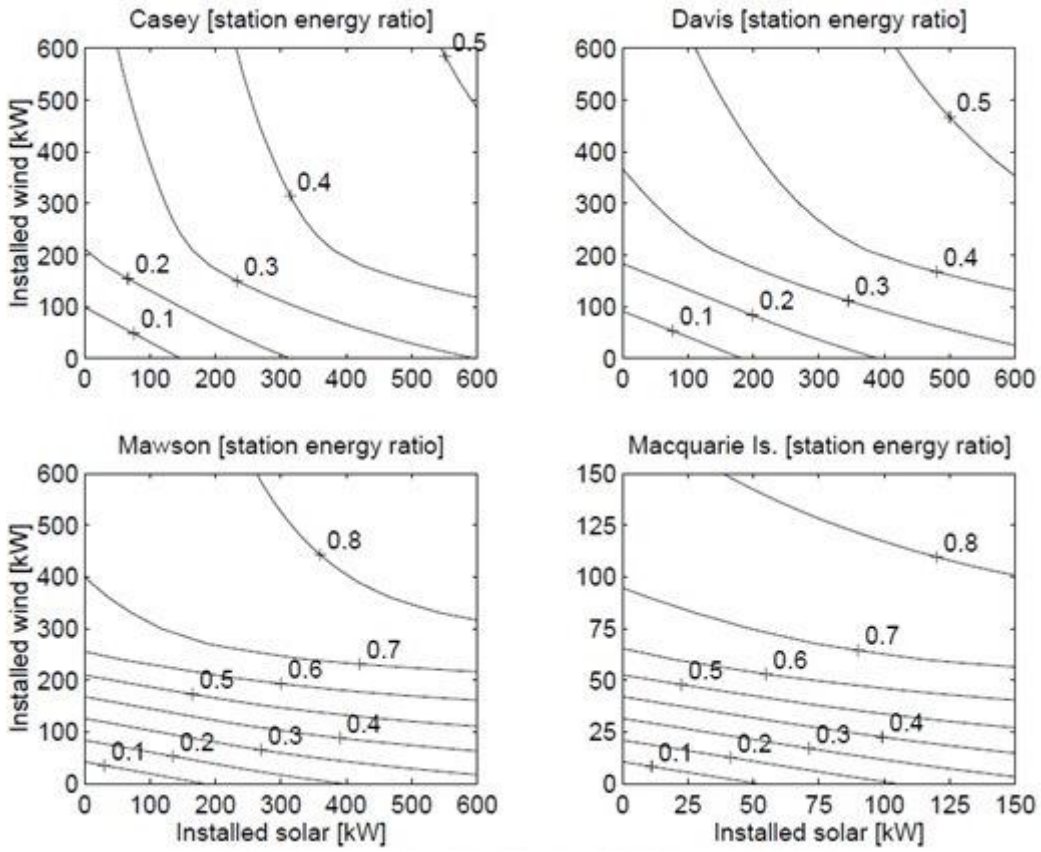

Fig. 1.14. Renewable energy penetration with diesel power regulation and no electrical storage. ***Taken from Brown, Guichard & Lyons (1996) [58]***.

Unfortunately large scale electrical energy storage of the type required to ensure continuous power supply for a polar station is either prohibitively expensive or physically unwieldy. Battery storage is difficult in such cold conditions and is expensive. Except for hydro-power in limited locations, acceptable long term energy storage systems are yet to be found that permit very high penetration of intermittent renewables. Even if they were to be found, the point is moot in the absence of a high availability renewable energy source at most sites with which to charge them.

The practical compromise that has arisen so far is to use renewable energy as a supplementary source only. Thus hybrid systems absorb surplus generation by diverting excess capacity to the most appropriate temporary load. Dependence on fossil fuels is thus reduced, but not eliminated entirely.

Wind thermal energy devices have potential to contribute to this energy mix. The availability of wind thermal energy is near constant through the polar winter, and although predominantly a winter

resource it does have some capacity to combine inherent energy storage. The following section provides some background to thermal energy in cold climate regions.

1.2.4 Thermal energy

Any number of local thermal energy sources might be used for the provision of renewable energy services. Various methods have been devised to exploit the thermal storage capacity of wind, water and ground source thermal mass in cold climate regions. Thermal energy devices can be grouped into four main classes: heat pipes; heat pumps; heat transformers; and heat engines.

Heat pipes provide enhanced heat transfer between separate hot and cold thermal masses via evaporation and condensation of a working fluid. Warm vapor flows toward the cold sink and condensate returns by capillary action to the heated end. Heat pumps also provide heating and/or cooling services but use external mechanical pump or compressor work to transfer or upgrade heat energy stored in air, ground or water sources. Heat transformers provide similar heating and/or cooling services to heat pumps, but rely on the mixing and separation of liquid solutions, rather than a mechanical compressor, to produce upgraded heat. Absorption and desorption is driven by thermal means alone with energy to drive the cycle provided by the temperature difference associated with a convenient local heat source and sink. Heat engines provide mechanical power output, rather than upgraded heat, from similar local heat sources and sinks.

The following is a brief account of how thermal technologies have evolved in cold climate regions.

Thermosyphons

In 1963 Long proposed the use of thermosyphons to keep permafrost frozen through summer [59]. Since that time closed thermosyphons have found use in cold climate civil engineering projects as an effective means of stabilizing earthwork foundations, Fig. 1.15. The thermosyphon is a vertical heat pipe with closely spaced pins or fins on the upper tube surface exposed to the air. Cold winter winds force the enclosed vapor to condense at low temperature and drain back down. Warmth is extracted

from the ground as the returning condensate boils at low pressure. In summer the vapor can't condense and circulation stops.

Fig. 1.15. Two-phase closed thermosyphons help keep permafrost frozen.
Photo: Arctic Foundations Inc.

Ground source heat pumps

Evolution of ground-source heat pump technologies has led to their widespread use for domestic and commercial space-heating in northern latitudes, Fig. 1.16. Solar absorbers collect radiant energy in summer and hot water is pumped through looped polyethylene pipes buried in the ground. The stored heat is recovered for space-heating in winter by reversing the flow of water. Ground loops buried more than 5 m below ground level are well insulated from seasonal surface temperature variations. Technological developments in recent decades have seen a significant increase in the use of GSHP's [60]. They are simple, reliable, and affordable.

In hot climates similar systems are used to store cold winter temperatures ready for summertime air-conditioning. In temperate climates, when used in conjunction with reversible heat pumps, ground source systems can also provide a mild temperature thermal mass to improve both heating and cooling efficiency across all seasons.

Fig. 1.16. Ground loops and solar collectors for a hybrid GSHP in Fairbanks, Alaska.
Images from Meyer et al (2011) [60].

Heat transformers

Heat transformers and heat engines are specifically used for renewable energy *production*.

In 1991 Schwarzer [61] described a system with thermosyphon-style vertical circular tubes for heat transfer in the mixing element of an absorption heat transformer used for space heating [61]. The upper section forms a condenser-absorber, and the lower an evaporator/desorber. The multi-stage ammonia-water absorption heat transformer is based on the principle of quasi-isothermal distillation, Fig. 1.17.

In 1994 Le Goff [62] described a multi-effect absorption cycle for combined heat and power, Fig. 1.18. A characteristic advantage of the absorption heat transformer concept is that its heat output varies in direct proportion to the coldness of the wind, so the heat supply closely matches the space-heating demand. Investigation of wind thermal devices at selected Arctic and Antarctic coastal sites demonstrates good potential for the provision of winter heating services [63].

The device works very well in winter, but not at all in summer as the temperature difference between the air and seawater disappears altogether and winds abate. Le Goff is keen to point out that wind thermal devices are potentially very robust and reliable because they have no moving parts exposed to the elements, unlike wind turbines. Absorber systems operate in a closed loop because the liquid phases are necessarily miscible.

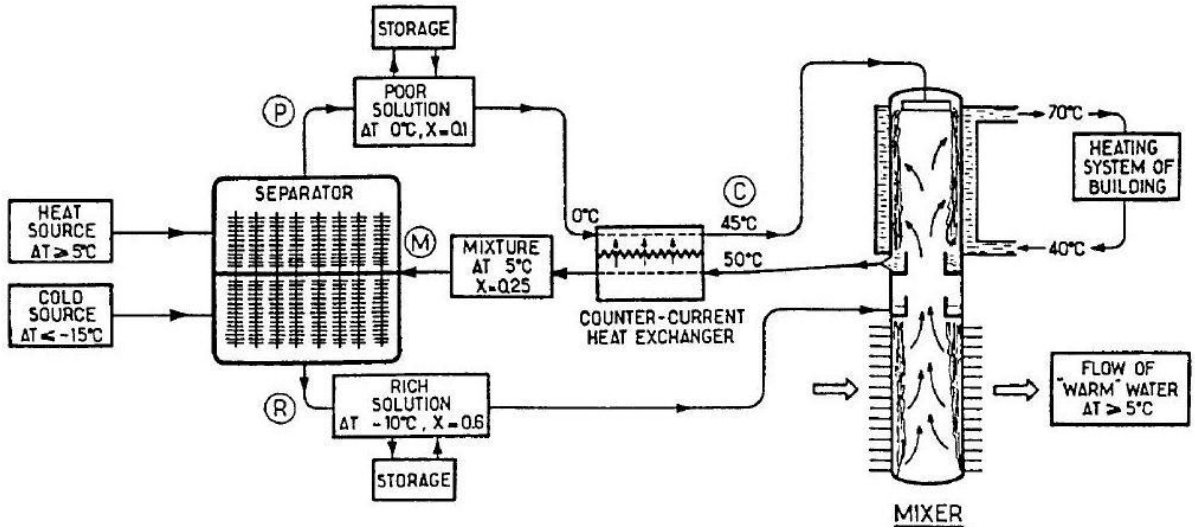

Fig. 1.17. Absorption heat transformer for space heating.
Taken from Schwarzer et al (1991) [61].

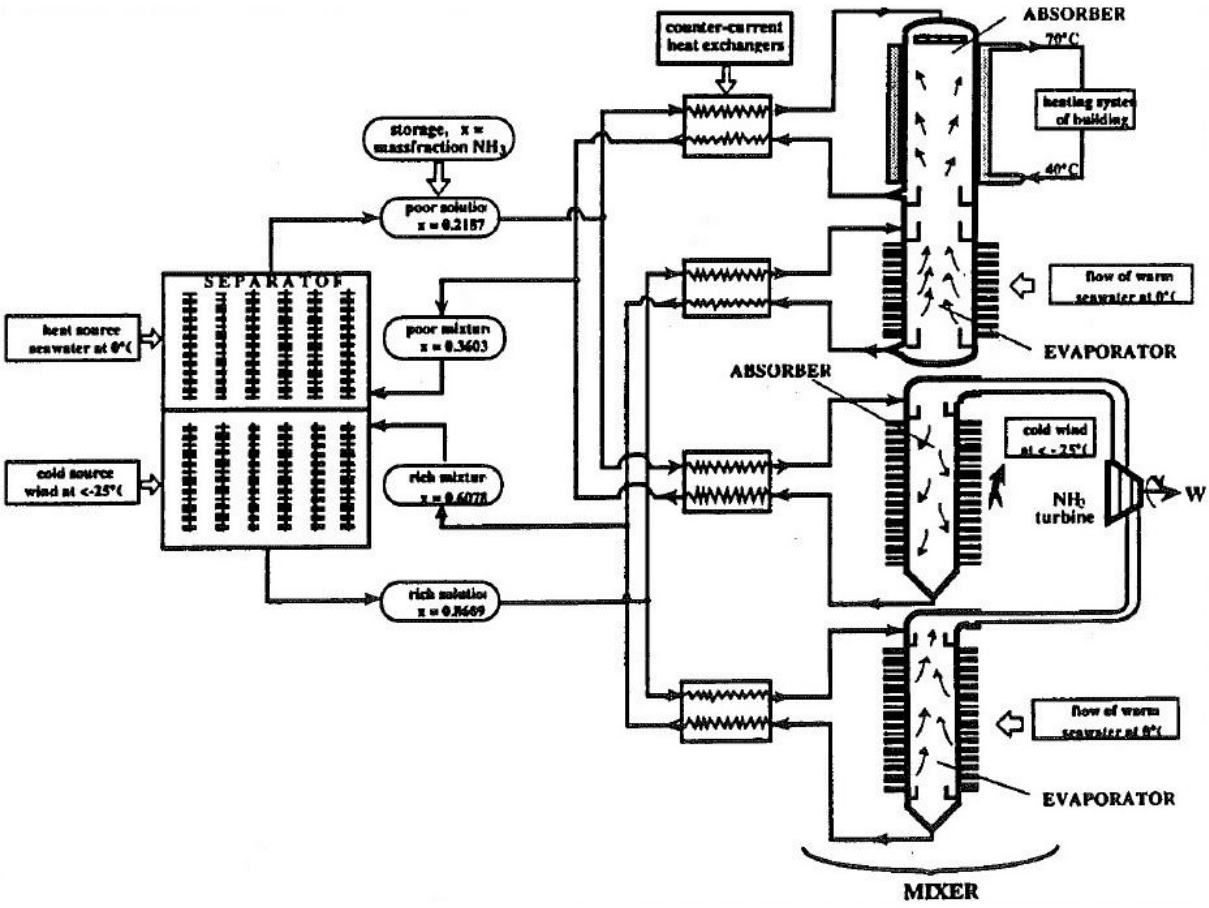

Fig. 1.18. Multi-effect ammonia-water absorption system for combined heat and power.
Taken from LeGoff et al (1994) [62].

Despite the potential for wind thermal heat transformers to supplement diesel through the winter months, they remain on the shelf. Development stalled after the 1990's following the successful installation of competing wind turbine technologies at a number of Antarctic sites. Wind kinetic energy is more regular and can potentially deliver higher capacity factors at mild coastal sites. Also around that time, new regulations came into force regarding the transport of ammonia and other hazardous chemicals. The expense, logistical complications and environmental risks all make ammonia absorption heat transformers uncompetitive for cold climate applications. Publication of wind thermal energy papers declined around this time, Fig 1.19.

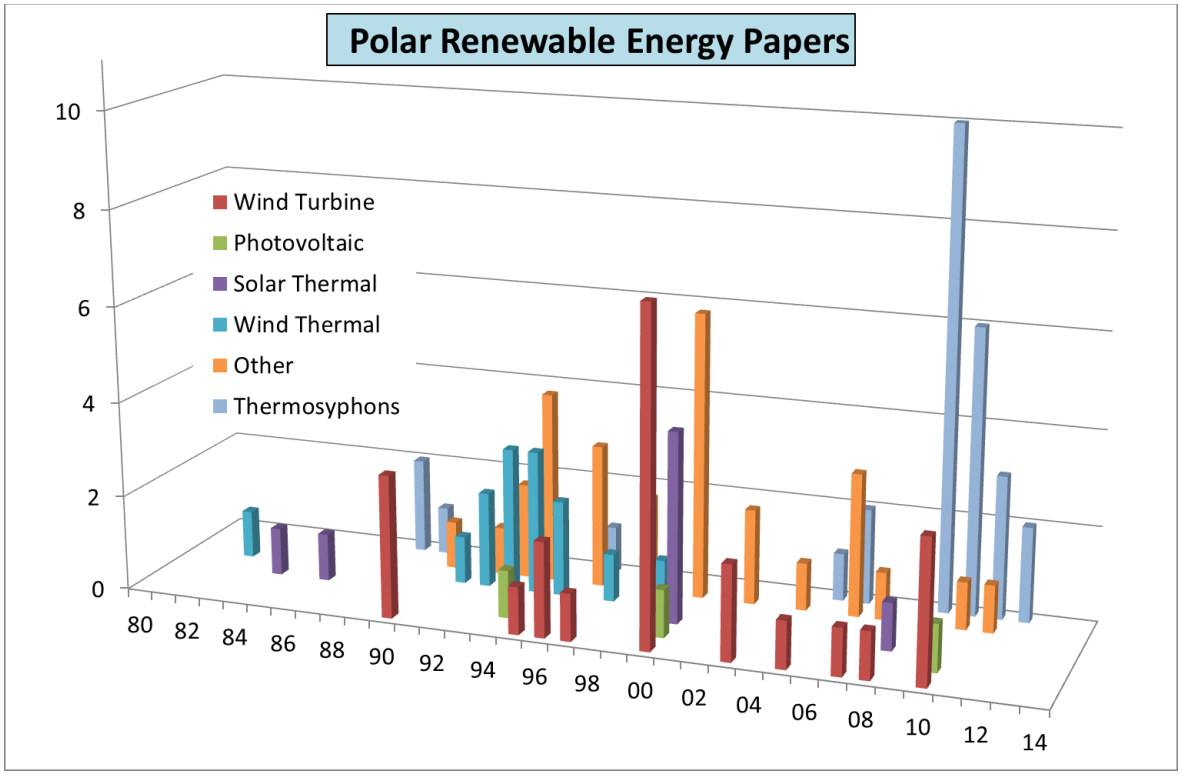

Fig. 1.19. Polar renewable energy evaluation studies 1980 – 2013

Heat engines

Latent heat from freezing seawater or meltwater provides the heat source for a wind thermal heat engine. Frigid polar air or low temperature ice slurry is the heat sink. Although the cold polar air comprises a ready-made heat sink, the ultimate heat sink is actually provided by the ice surface as it radiates heat directly out into the cold void of space through an infrared window in the dry polar atmosphere.

Heat energy released by the freezing of seawater is used to vaporise a high pressure natural working fluid that is fed to a vapor turbine or other expansion device to generate electrical power. A heat exchanger exposed to the cold polar air provides the cold sink to condense the working vapor.

The wind thermal engine is inspired by earlier ocean thermal energy conversion (OTEC) devices [64]. The closed-cycle OTEC system was conceived to exploit the temperature difference between the warm surface water of the world's tropical oceans and the cold bottom water beneath. Many of the principles of OTEC can equally be applied to wind-thermal engines in Polar Regions [62].

Jacques-Arsene d'Arsonval first proposed tapping the thermal energy of warm surface waters in the tropics in the 1880's. Lord Rayleigh suggested using high pressure refrigerants in a compact closed cycle OTEC device in the 1890's, but it wasn't until 1926 that Georges Claude built the first laboratory prototype, prior to building the first full scale plant in Cuba in 1930 [65]. Extensive research undertaken by the National Science Foundation in the United States in the early 1970's failed to produce an economically viable system [66-68]. Factors that conspired to limit the feasibility of four potential prototype OTEC system designs included: serious engineering challenges posed by tremendous ocean forces; vast pumping volumes and heat exchange surface areas due to low thermal efficiencies; fouling by marine micro-organisms; scarcity of essential raw materials (specifically titanium for fouling resistant alloys); high surfactant concentrations and hazardous working fluids; deaeration problems [69]; environmental siting constraints; and remoteness to markets. Niche markets do exist, however, for combined power and desalination plants for small tropical islands that lack freshwater resources [70].

Wind thermal systems face similar low efficiency and heat exchange challenges to OTEC, but latent heat transfer rates are much higher and different potential applications arise. Some of the principles employed in OTEC have relevance in the design of wind-thermal systems.

In their summary of polar renewable energy sources, Sheinstein & Shpilrain include a conceptual diagram of a closed cycle OTEC design adapted for Antarctic operation as a wind thermal device [22]. Following on from the 1991 paper of Schwarzer regarding absorption heat transformers, Le Goff

describes thermo-mechanical machines that use the energy of cold polar winds [64]. A later paper by LeGoff describes a thermo-mechanical machine for the production of electrical power that employs a scraped-tube boiler, ammonia vapor turbine, and finned-tube condenser, Fig. 1.20 [62].

The scraped-tube boiler derives from ice slurry generation technology developed in the refrigeration industry, but in a wind thermal engine its function is to extract heat from freezing seawater to evaporate and pressurize a working fluid. A vapor turbine or other expansion device is used to generate power. Finned-tube heat-exchangers similar to the tall thermosyphons in Fig. 1.15 are exposed to frigid polar air to condense the working vapor. Performance of the cold captor depends upon the wind velocity. Engine thermal efficiency is low but seawater pumping costs are minor, so the system might be affordable depending on the size and cost of the evaporator and condenser arrays.

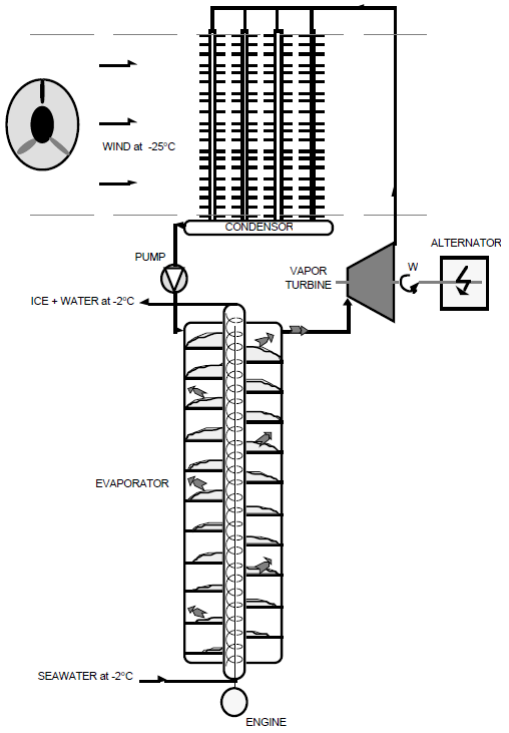

Fig. 1.20. Thermo-mechanical engine, ***as proposed by Le Goff et al (1994) [63].***

Heat transfer between the freezing seawater and evaporating working fluid is a key challenge. Direct contact of seawater and natural working fluid may be possible in the boiler of an open cycle wind thermal engine if the two fluids are immiscible and the working fluid can be properly separated from the sea-ice and brine slush prior to recycling through the condenser. Separation of ice or

clathrate from the brine fraction occurs automatically upon freezing of the liquid water component. Vapor extraction would be needed to reduce the partial pressure of the working fluid enough to remove the dissolved working fluid fraction from the brine. Heat is also needed for vapor extraction to fully dissociate the clathrate product back to vapor and pure ice. Smith describes direct contact heat exchange concepts that may be of use in wind-thermal devices [66].

LeGoff, Hasert and Guichard (1994) consider the potential for producing heat and power for polar stations from the wind-water temperature gradient, and explore the various energy components of the wind. They assert that wind thermal methods have the potential to produce at least an order of magnitude more usable heat and/or power than wind turbines for a given cross-section of air-flow. They modelled the potential for producing heat and power from the wind-water temperature gradient at selected polar sites. Results show that wind-thermal methods have the potential to produce substantial heat and/or power at favourable sites along the Arctic and Antarctic polar coastlines during winter – up to at least 300 W/m^2 of cold captor area [71]. A clear disadvantage of thermo-mechanical devices though is that demand for electrical power is greatest for most stations over summer – not during winter when wind-thermal output is peaking.

The availability of intermittent renewables varies greatly between polar stations. Costs increase sharply in proportion to intermittent renewables penetration. Are there other sources that can help? Are there any continuous sources?

1.3 Glaciothermal power generation

From this point on we adopt the term *glaciothermal* to replace the earlier term *wind-thermal* that was used in the literature. This is necessary because a potential conflict in terminology arises. Domestic power grids that integrate wind power with coal-fired thermal power are also referred to in the literature as *wind-thermal* systems. To avoid any confusion, we prefer the term glaciothermal instead to refer to systems that extract heat from freezing water or seawater for the generation of heat or electrical power. Glaciothermal relates specifically to heat production methods that use ice slurry or other quick freezing mixtures to provide high heat flux from low temperature differences.

We thus carry forward the existing concepts and analysis relating to the former wind thermal topic and continue the discussion in relation to technological developments that have taken place quite recently. Ongoing developments in ocean sciences, logistics, electronics, refrigeration, geothermal energy and other technologies have greatly improved the prospects for a practical glaciothermal engine. In answer to the above question, we suggest that glaciothermal devices do offer an alternative energy option that is worth investigating.

To recap, a glaciothermal engine uses the temperature difference between 'warm' seawater and cold polar air to generate electrical power. Heat from freezing seawater is used to boil a working fluid and the high pressure vapor drives a turbine or other vapor expander. The heat sink provided by cold air condenses the emerging exhaust vapor to start the cycle over again.

This section briefly covers some of the earlier work that describes key engine components and the status of several prospective technologies are reviewed. Previous projects to model the potential for wind thermal energy at specific Arctic and Antarctic sites are discussed, and gaps in the current research are identified.

1.3.1 Glaciothermal boiler

The function of a glaciothermal boiler is to cause seawater to freeze rapidly, and working fluid to boil vigorously. Low thermal resistance of copper boiler tubes permits maximum heat transfer with lowest possible temperature difference.

Latent heat captors

It is not as easy to capture continuous heat from freezing seawater as it is from warm water. The seawater is likely to freeze on to any cold surface that is attempting to extract heat. One strategy to avoid ice fouling is to keep the boiler tubes only 1 or 2 °C below the seawater freezing point, and to add a quantity of seed ice to the seawater before it enters the boiler. The seawater freezes onto the seed ice crystals as they grow rather than onto the pipes.

With similar processes in mind, there are several devices that might be able to effectively capture heat from freezing seawater:

Schwarzer used the evaporative half of an ammonia vapor thermosyphon as the heat captor device for their space-heating appliance [61], Fig. 1.15. Their heat source was relatively warm water at 5-10 °C, however, no mention was made of any measures to cater for latent heat exchange upon freezing of water.

Le Goff depicts a scraped-tube heat exchanger to drive the working fluid evaporator of their thermal-mechanical engine [63], Fig. 1.20. The first reference to using a scraped-tube heat exchanger as a captor for latent heat of freezing of seawater may have derived from an earlier paper by them, or by other workers in the same field (e.g., an unpublished thesis by Hasert in September 1993 [72], a paper by Le Goff, Schwarzer and Le Goff also dated September 1993 [73], or from a study by Castus of a seawater heat exchanger for use with absorption heat pumps at polar stations [74]).

Scraped-tube heat exchangers are a type of commercial ice slurry generator (ISG) used to freeze product mixes in the manufacture of ice-confection and other foodstuffs [75]. Although not devised to harvest heat from freezing seawater, they achieve similar ends as they evaporate refrigerants to make ice. There are a number of different types of ice slurry generator used in the refrigeration industry that might be considered for our purposes. Ice slurry generation and heat transfer is an established sector within the refrigeration industry and there is significant literature available about the various devices.

Numerous types of ISG are described in the literature: grinders and crunchers; mechanical scrapers; rotational or oscillatory cooled walls; fluidised beds; hydro-scrapers; vortex flow; internal flow; ice nucleating coatings; droplet sprays; direct contact with immiscible refrigerant; indirect contact with immiscible secondary refrigerant; clathrate PCM's; micro-encapsulated PCM's; lithium-bromide absorption evaporators; vacuum freezers; recuperative ice makers; high pressure shift freezers; and super-cooling water types [76-79]. Kauffeld, Kawaji and Egolf provide a useful review of ice slurry production methods [78].

Mouneer et al devised a super-cooled ISG that uses high velocity water jets rather than mechanical aids to prevent the formation of ice on the cooling surface and generates ~5% ice by volume each pass. The temperature difference between the ice slurry and evaporating refrigerant for their experimental apparatus varies up to ~20 °C, but for reliable operation they recommend refrigerant temperatures be kept warmer than -5 °C with heat flux around 12 kW [76]. Their device is potentially useful as a glaciothermal heat captor.

Meewisse devised a fluidised bed ISG with a respectable 4-5,000 W/m^2 heat transfer coefficient [80], Fig. 1.21 (c). Suspended metal beads impact the tube walls to keep the surface ice free and enhance the heat transfer coefficient.

The Danish Technological Institute in collaboration with a private refrigeration company developed an internal flow shell-and-tube ISG that employs a patented sol-gel technology to produce ice nucleation coatings (INC's) on the inside of the tubes. Nanoparticles are bonded to a pre-treated aluminium surface and arranged with alternating anti-adhesive hydrophobic and ice-nucleating hydrophilic ends presented to the carrier fluid. Ice particles form on the coating surface and are immediately released into the fluid flow thus forming ice slurry. The 10 kW refrigeration capacity units employ ammonia refrigerant. This method of ice generation may be applicable to glaciothermal boilers if the coatings are durable. MTD and heat flux data are needed.

Mechanical ISG's with moving parts that require regular maintenance or servicing may not be reliable enough for operation as glaciothermal boilers in remote locations, Fig. 1.21 (b), (c).

High heat flux is possible for ISG's that have high heat transfer coefficients and high temperature differential. Unfortunately a glaciothermal engine requires the working fluid to boil at the highest possible temperature for maximum power, so a high temperature drop across the boiler is not usually optimal. For our own basic glaciothermal boiler we have selected an ice-in-tube configuration where seeded ice slurry is pumped at moderate velocity through thin copper tubing lined with an abrasion resistant polished electroplate surface. The copper tubes form a bundle within a shell and tube style heat exchanger.

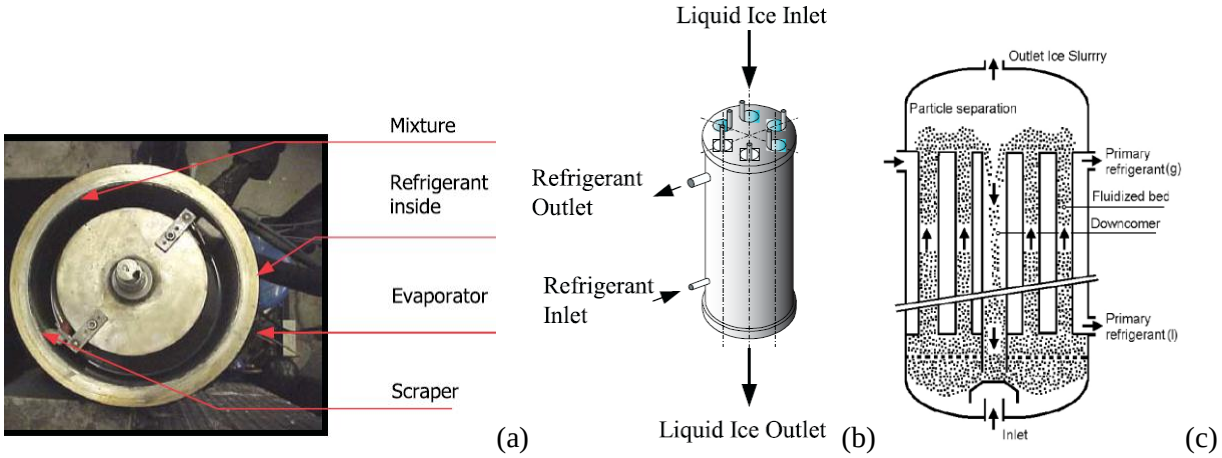

Fig. 1.21. Mechanical scraper (a) rotating slab (b) and fluidised bed (c) ice slurry generators.
Taken from Egolf & Kauffeld (a, b), and Meewisse (c) [77, 80].

Flooded evaporator

Enhanced boiling surfaces are needed to achieve high nucleate boiling heat transfer rates on the evaporator side. Commercial shell and tube flooded refrigerant evaporators already incorporate enhanced nucleate boiling surfaces and achieve exceptional heat transfer coefficients for specific refrigerants. Similar surfaces might also be used to boil high pressure natural refrigerants as working fluids in a glaciothermal boiler. Boiling surfaces need to be closely matched to each specific working fluid and to the intended vaporisation temperature. A specific enhanced surface technology has yet to be chosen.

1.3.2 Two-phase vapor expander

Vapor expander or turbine efficiency is a critical issue. As for aircraft that stall if they fly too slow, gas turbines also need high speed flow across their blades to maintain torque. Flow velocity is dependent upon the pressure difference between the boiler and condenser, which is slight if air temperature is only -20 or -30 °C. Thus familiar axial turbines are not appropriate for most sites. Positive displacement twin-screw expanders (TSE's) that exploit volume change are preferable to axial turbines when faced with low pressure ratios.

Early pioneering work by Swedish company SRM led to practical twin-screw compressors. Their rotor designs were subsequently adapted for two-phase tri-lateral flash cycle (TFC) and organic

Rankine cycle (ORC) vapour expansion [81-83]. Twin screw expanders offer significant advantages over other expanders. Their high speed means they are compact and don't need a gearbox. Nor do their rolling element bearings require an oil supply, Fig. 1.22. The mechanical simplicity of the design means they are very reliable and inexpensive, Fig. 1.23. Backup units are readily affordable.

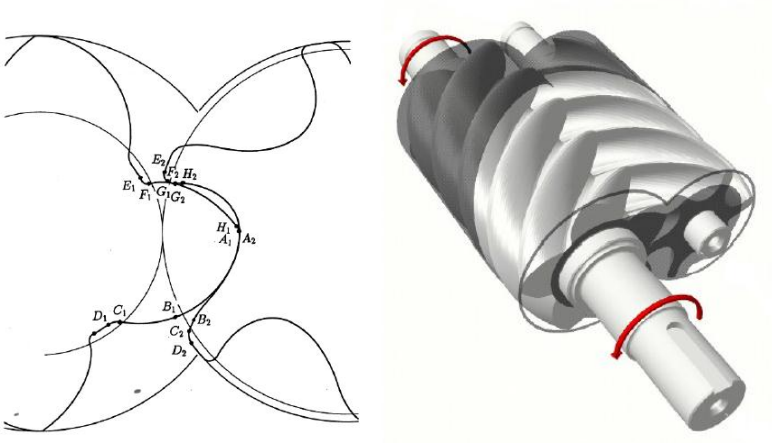

Fig. 1.22. Proprietary 'N' screw rotor profile for twin screw expander.
Taken from Smith, Stosic & Kovacevic [82].

Fig. 1.23. Dynamometer testing of twin screw expander running R-113 (20 kW, 127 mm).
Taken from Smith, Stosic & Kovacevic [81, 82].

1.3.3 Condenser

The function of the condenser is to cause the exhaust vapor to rapidly condense, and to reject this heat as expediently as possible to the passing ambient air stream. Low thermal conductivity copper tube and aluminium fins of familiar tube-fin condensers are ideally suited to this task.

Condenser tubes

Exhaust vapor returning from the expander will spontaneously condense to form a continuous film on the inside of copper tubes. Micro-fins may enhance heat transfer performance on the condensate side, but this is unwarranted because overall performance is limited by heat transfer on the air fin side. Various thermosyphon, finned-tube, tube-fin or plate-fin condensers might be chosen, but in each case the condensation process on the inside of the tube is similar. Heat transfer performance is determined by the orientation of the tube and the nature of the air flow and fins on the outside.

Cold captor fins

The performance of finned-tube heat exchangers as prototype cold captors to aid wind-thermal heat and power production has been studied. Experiments to measure the heat transfer capacity of such atmospheric heat exchangers were conducted at coastal sites in the Russian and Canadian Arctic, and at Dumont d'Urville in Antarctica [62]. A key element of this research paper is the description of an experimental 'cold wind flux-meter' designed to acquire heat transfer data for smooth-tube and finned-tube heat exchangers under real operating conditions, Fig. 1.24 (a). Field data showed heat transfer rates of ~50 W/m^2 of surface area for smooth tubes exposed to 10 m/s cold wind, and > 200 W/m^2 of basic smooth tube surface area for finned-tubes at similar wind speeds.

No data were found in the polar literature regarding the performance of other types of atmospheric heat exchange device under cold climate conditions. We propose a fan-forced tube-fin condenser of the type commonly used in domestic refrigerators for our basic glaciothermal engine, Fig. 1.24 (b). Heat exchange is better for horizontal tubes than vertical. A complete optimised condenser model is constructed from published heat transfer formulations [84].

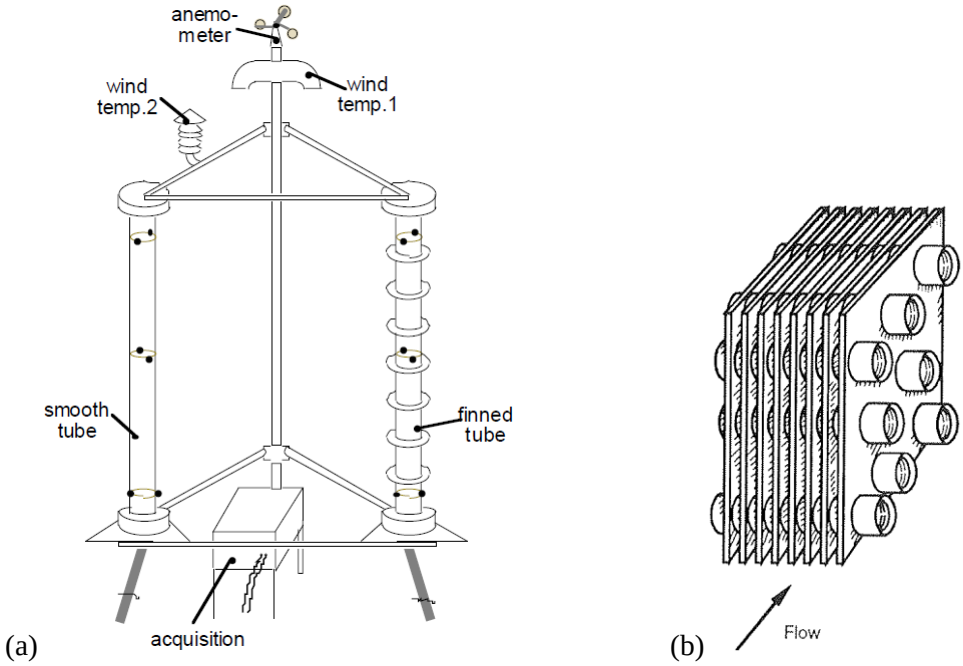

Fig. 1.24. Cold captor devices: (a) cold wind flux meter ***as drawn by Le Goff [63];*** and (b) tube-fin condenser illustration ***taken from Rohsenow et al [84].***

1.3.4 Existing device models

An extensive body of work exists in the literature regarding performance modelling of a multitude of vapour expansion and heat exchange devices. A wide range of models and modelling methods are potentially useful in designing a prototype glaciothermal engine. Industry accepted empirical correlations are used to model flow behaviour and heat transfer for forced convective flow of ice slurry within smooth tubes. These methods are readily applied to the case of freezing seawater in a glaciothermal boiler. Device specific analytical models and proprietary software are similarly available to simulate the performance of twin screw and other fluid expanders. Standard engineering texts relate the heat transfer performance of tube-fin condensers and plate-fin radiators.

Whilst there is a great deal written about modelling of specific component devices, there is little research so far into the overall performance of an integrated wind thermal or glaciothermal engine. Nor is there much literature relating ice slurry style heat transfer specifically in the context of a thermo-mechanical engine. The essential requirements for design and operation of a glaciothermal engine for critical power generation in polar conditions are very different to those for an ice slurry generator to be used in the refrigeration industry for food preservation.

We have therefore identified glaciothermal boiler design as a key research focus, along with modelling overall engine performance under varying meteorological conditions at selected Antarctic type locations. A thermal and mechanical exergy analysis for wind thermal devices has been done previously at three Antarctic sites relating to mechanical scraped-tube ice slurry heat exchangers [71]. Our brief is for a reliable low maintenance glaciothermal boiler with no moving parts.

1.4 Project objectives

Our stated aim is the evaluation of glaciothermal engines for the generation of polar renewable energy. Specifically we propose to determine the feasibility of a simple small-scale 250 kW glaciothermal engine for the provision of renewable electrical power at polar sites.

The technical challenges in conceiving the engine are to identify optimal processes to:

- Capture latent heat from freezing seawater
- Evaporate working fluid condensate
- Convert the energy of high pressure vapour into mechanical work
- Capture latent heat from condensing vapour film
- Reject latent heat of condensation to the atmosphere

Our specific project objectives as documented in this thesis are to:

- Develop a mathematical model of the heat transfer and energy conversion processes for each conceived component of the basic glaciothermal engine
- Implement this model in MATLAB and use the simulation results to prove the overall feasibility of the concept engine
- Compile curves based on the estimated overall nett thermal efficiency of the basic engine across the full range of possible cold climate ambient air temperatures (-90 to 10 °C)
- Model year round glaciothermal energy potential given meteorological data from selected type locations and use this to identify where best to implement the technology

Deliverables include:

- Conceptual and mathematical models of basic glaciothermal engine
- Working model in MATLAB
- Publications describing the same

In the event that the feasibility of a small-scale glaciothermal engine is proven, we will examine the potential for large scale glaciothermal energy production using similar heat transfer principles.

1.5 Thesis structure

Chapter 1 provides background information about the challenges of providing power in cold climate regions and some of the innovations that have been devised. Technologies with potential application for glaciothermal power devices are identified and the project objectives are defined.

Chapter 2 explores the essential physical processes at work in a glaciothermal engine. The prototype components favoured to carry out these processes are identified and the modelling method is documented in each case. Detailed background information is provided in the appendices.

Chapter 3 explains the exceptional performance of the basic glaciothermal fluid cycle and provides a detailed parametric analysis in order to optimise operation of the tube-fin condenser and glaciothermal boiler. Device dimensions and overall engine performance curves are generated. The combined results of this analysis determine the site requirements for installing a basic engine.

Chapter 4 describes the ambient environment and modelling of meteorological data. The power generation capacity of the basic engine is assessed for year round operation at selected Antarctic sites. The inability to generate power during summer is a defining characteristic.

Chapter 5 presents the key findings and conclusions of the thesis and outlines current and future work on some potential small and large scale augmentation methods. We conclude that glaciothermal engines do have significant potential for reliable cold climate energy production.

Chapter 2 – Mathematical Model of a Basic Glaciothermal Engine

This chapter explores the essential physical processes at work in a glaciothermal engine. The prototype components favoured to carry out these processes are identified and the modelling method is documented in each case. Detailed background information is provided in the appendices.

2.1 Introduction

Research into various thermodynamic cycles, heat transfer and working fluid expansion processes was undertaken to determine the feasibility of a 250 kW thermo-mechanical engine. A review of existing heat exchangers, ice slurry generators and refrigerant evaporator concepts, and a study of ice nucleation, vapour bubble nucleation and film vaporisation phenomena all lead to a specific design for an ice-in-tube glaciothermal boiler. A compact twin-screw expander was considered to be the most suitable device for two-phase vapour expansion, and a tube fin condenser was selected as the prototype cold captor.

Models are developed in MATLAB to permit the performance analysis of each engine component. Process feasibility is demonstrated across the full range of operating conditions by calculating the necessary dimensions of a prototype device capable of delivering the desired nominal output.

2.2 Engine summary

The basic glaciothermal engine prototype depicted in Fig. 2.1 comprises: an ice-in-tube boiler fed by an ice slurry loop and condensate preheater; a twin-screw expander and synchronous electrical generator; fan-forced tube fin condenser; and a positive displacement condensate pump. Heat from the freezing ice slurry vaporises low temperature working fluid which drives the expander to generate electrical power.

The tube-fin condenser extracts heat from condensing exhaust vapour and produces cold condensate that is nominally 5 K warmer than the ambient air. The condenser is modelled first in order to determine suction pressure available to the expander. Boiler pressure is fixed by nominating an arbitrary boiling temperature (typically -5 °C). Injection pump work can then be calculated. The ice

slurry mixer regulates mass fractions of seawater feed and seed ice entering the boiler. Tubes within the glaciothermal boiler transfer heat from the freezing ice slurry to the evaporating working fluid. Component scaling is in proportion to nett power output of the expander.

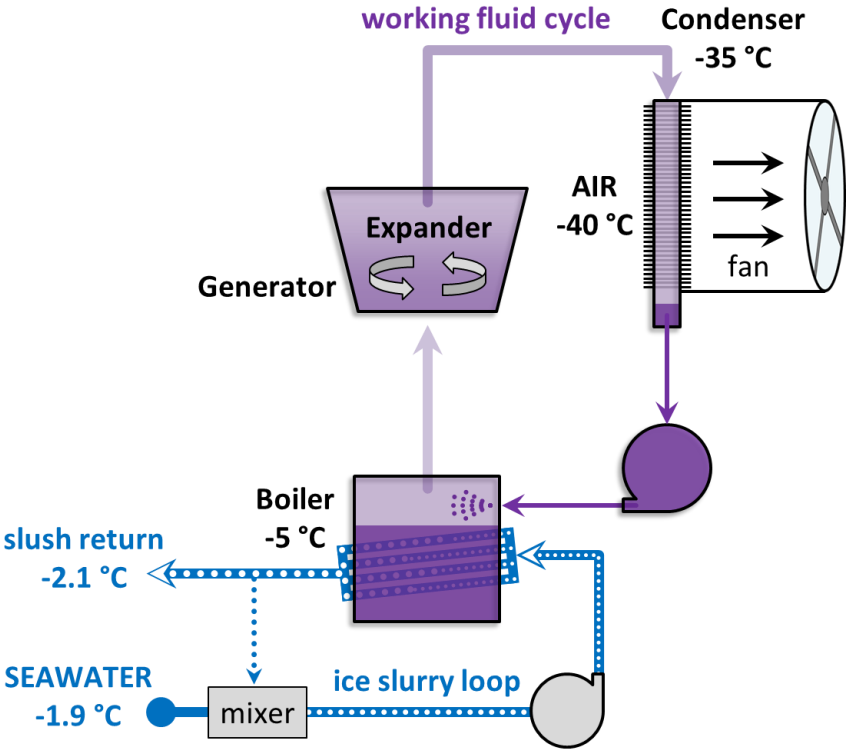

Fig. 2.1. The basic glaciothermal engine concept.

The above modelling sequence dictates the order that components are presented in this chapter:

1. Condenser
2. Injection pump
3. Ice slurry loop
4. Glaciothermal boiler (including preheater)
5. Expander

Overall working fluid, seawater and air mass flow equations are included in the final section.

2.3 Working fluid

The working fluid is considered to be a separate component of the glaciothermal engine. The function of the working fluid is to generate high pressure vapour to drive an expander. Refrigeration

applications may favour low pressure fluids, but for electricity generation purposes, high vapour pressure relates directly to power output and is crucial to the design of a practical device. Working fluid species are needed that will boil at around -5 °C and condense at temperatures down to at least -60 °C. Saturated vapour pressures for selected natural refrigerant working fluid species at nominal cold condenser and hot boiler temperatures are listed in TABLE I.

TABLE I. HIGH PRESSURE NATURAL WORKING FLUIDS

Refrigerant	**P_{COND}** (-55 °C)	**P_{BOIL}** (-5 °C)	**Q_2 point**
Xenon	9.9 bar	37.1 bar	-
Ethylene	9.0 bar	36.5 bar	-
Carbon dioxide	5.5 bar	30.5 bar	45.0 bar (9.9 °C)
Nitrous oxide	5.3 bar	27.4 bar	42.0 bar (11.8 °C)
Ethane	4.6 bar	21.1 bar	33.9 bar (14.7 °C)
Hydrogen sulfide	1.3 bar	9.0 bar	22.4 bar (29.5 °C)
Propane	*0.6 bar*	*4.1 bar*	*5.5 bar (5.7 °C)*
Ammonia	*0.3 bar*	*3.5 bar*	-
Sulfur dioxide	*0.1 bar*	*1.3 bar*	*2.4 bar (12.1 °C)*

Basic glaciothermal engine processes that specifically involve the working fluid are:

1. vapour condensation
2. condensate injection
3. condensate preheating
4. condensate evaporation
5. vapour expansion

For each of these processes we reconcile energy within the control volume according to:

$$w = (h_1 - h_2) + (V_{m,1}^2 - V_{m,2}^2)/2 + g(z_1 - z_2) + q \qquad (2.1)$$

where: w is work done by the fluid on the turbine, h is enthalpy of the fluid, V_m is the mean fluid flow velocity, g is acceleration due to gravity, z is elevation, and q is heat. Subscripts 1 and 2 denote the inlet and outlet of the control volume relevant to each process.

Major assumptions that apply to the key models presented in this chapter are:

- all fluid flow processes are steady state
- changes in fluid kinetic or potential energy are negligible unless noted otherwise
- all processes are deemed to be adiabatic with respect to the external world (except of course for condenser fin heat transfer to cold air and seawater heat transfer to ice slurry)

All engine cycle mass flow balances are calculated with respect to 1 kg of working fluid. Heat flows across the boiler and condenser tubes are quoted per m^2 of smooth tube surface area. Absolute temperatures are quoted in degrees Celsius (°C) with relative temperature differences quoted in degrees Kelvin (K). Working fluid thermophysical properties are from REFPROP, Appendix 2-A.

2.4 Tube fin condenser

Waste heat from the expander exhaust needs to be rejected into a suitable local heat sink in order to condense the working vapour ready to begin the next cycle. The cold polar winds provide enormous cooling capacity and standard tube fin heat exchangers are appropriate cold captors.

2.4.1 Tube-fins

Tube-fin heat exchanger technology is well established for air-conditioning and refrigeration applications. This type of air fin heat transfer device can act as a heat source or heat sink. For our glaciothermal engine the tube-fin heat exchanger forms the condenser and thus acts as a heat source rejecting latent heat of condensation to the cold outside air.

Fan-forced convective air flow between closely spaced continuous fins produces a low Reynolds number laminar flow regime. The convective HTC is predominantly a function of Nusselt number and hydraulic diameter. Both these parameters are related solely to the geometry of the rectangular ducts formed between adjacent fins and tubes. Heat transfer coefficients for tube-fins are very low but substantial heat transfer is achieved due to the very large surface areas involved. Surface area densities are typically in the range 800 – 1,600 m^2/m^3.

Heat transfer performance for a tube-fin condenser is thus optimised by varying the tube-fin geometry – not by increasing the air flow. Increasing laminar air flow velocity has no effect on the convective HTC and only serves to increase the fan pumping power. Optimal flow velocity is determined instead by the mass flow rate needed to maintain a realistic temperature drop for the air passing through the fins.

For the sake of our basic prototype engine we will consider a simple cross-flow condenser with a single row of copper tubes running the full length of a condenser panel. The height of a single panel is determined by the condenser cross-sectional area needed to condense 1 kg of working fluid. Device scaling equations at the end of the chapter define how many panels are needed to provide for a nett glaciothermal engine power output of 250 kW.

Fin HTC calculations

A condenser fin model was developed based on the standard approach for estimating forced convective heat transfer and extended-surface fin efficiency. The algorithm is Fig. 2.2.

A representative unit cell shape is defined for the continuous fin by bisecting the area between adjacent condenser tubes in the tube-fin array. This unit cell is subdivided into 18 radial sectors. The fin efficiency of each sector is deemed to be equivalent to that of a circular fin of the same radius. The area of each sector is calculated and the fin efficiency of the unit cell is calculated as the area-weighted fin efficiency of all the sectors.

The extended surface efficiency is calculated by taking into account the extra heat transfer associated with the smooth tube surface exposed between adjacent tube-fins:

$$\eta_{ext} = \frac{A_{bare}}{A_{ext}} + \eta_{fins} \frac{A_{fins}}{A_{ext}} \tag{2.2}$$

The air flow HTC for the tube-fin ducts is calculated from the standard HTC formula:

$$\alpha_{fins} = \lambda_{air} \frac{Nu_{duct}}{D_{h,duct}} \tag{2.3}$$

The Nusselt number is determined from a regression curve calculated using empirical Nusselt number data for smooth tubes of rectangular cross-section but varying aspect ratios, as published in Cengel [85]. The air fin HTC is constant at all points across the tube fin condenser, irrespective of position along the length of the adjacent condenser tubes.

Fig. 2.2. Algorithm for air-side tube fin condenser HTC, fin efficiency and fan pressure drop.

MATLAB code for the air-side condenser fins model is included in Appendix M: HTC_tube_fins_.

2.4.2 Horizontal in-tube condensing film

Substantial heat flux is generated as working fluid vapours condense onto condenser tube walls. Very high heat transfer coefficients are possible with drop-wise condensation for fluids that have sufficiently high surface tension. For most fluids, however, including the natural refrigerant working fluids ethane and CO_2 that are proposed for our basic glaciothermal engines, heat transfer via film-wise condensation is the predominant mechanism.

For film condensation of exhaust vapour onto internal horizontal condenser tube walls, both the heat transfer coefficient and two-phase flow velocity change as the vapour quality decreases downstream, Fig. 2.3. High speed annular flow conditions exist at the condenser inlet. As the liquid fraction increases the decelerating flow stratifies then transitions to slug and plug flow before becoming 100% liquid. The HTC and pressure gradient both vary continuously along the length of the condenser tube.

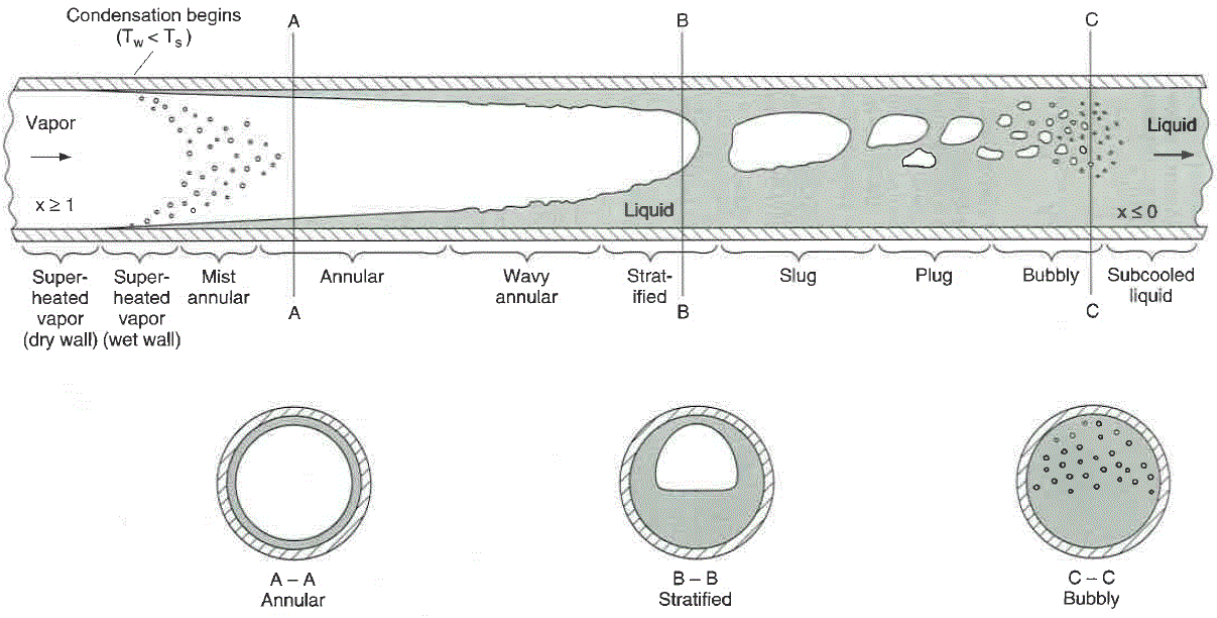

Fig. 2.3. Flow regimes for film condensation in long tubes. ***Taken from Rohsenow et al [84].***

The following horizontal in-tube condensing film software model has been developed in MATLAB and validated against literature data.

Condensing film HTC calculations

Full design models for horizontal tube condensers normally comprise 3 tube sections:

- vapour desuperheater section
- condensing film section
- sub-cooled condensate section

For the basic glaciothermal engine cycle there is no superheat due to either the boiler or the expander, so the first section is ignored. For our feasibility model we report the exact tube length needed to achieve 100% condensation, so no sub-cooled section need be considered either. Thus, our model only comprises the condensing film section. Wet exhaust fluid emerging from the expander is deemed to have passed through a phase separator so we can assume 100% vapour quality for gas drawn into the suction port of the condenser.

The horizontal in-tube condensing film model is constructed as per Figs 2.4 and 2.5. This model divides the condenser tube into variable length segments based on fixed vapour quality increments. HTC calculations are performed for each node based in part on an empirical model proposed by Cavallini [86] that calculates condensing film HTC and pressure loss for ΔT dependent and independent annular flow regimes associated with various working fluids. The algorithm is summarised in Fig. 2.6.

The flow regime at each node is characterised using the Lockhart-Martinelli parameter X_{tt}, and a dimensionless gas velocity parameter J_G, as per the method described by Breber [87]:

$$X_{tt} = \left(\frac{1-x}{x}\right)^{0.9} \left(\frac{\rho_g}{\rho_l}\right)^{0.5} \left(\frac{\mu_l}{\mu_g}\right)^{0.1} \tag{2.4}$$

$$J_G = \frac{xG}{\left(g\rho_g(\rho_l-\rho_g)D\right)^{0.5}} \tag{2.5}$$

where x is vapour quality, G is working fluid mass flux, ρ is density, D is the internal diameter of the condenser tube, and μ is dynamic viscosity of the liquid l or vapour g.

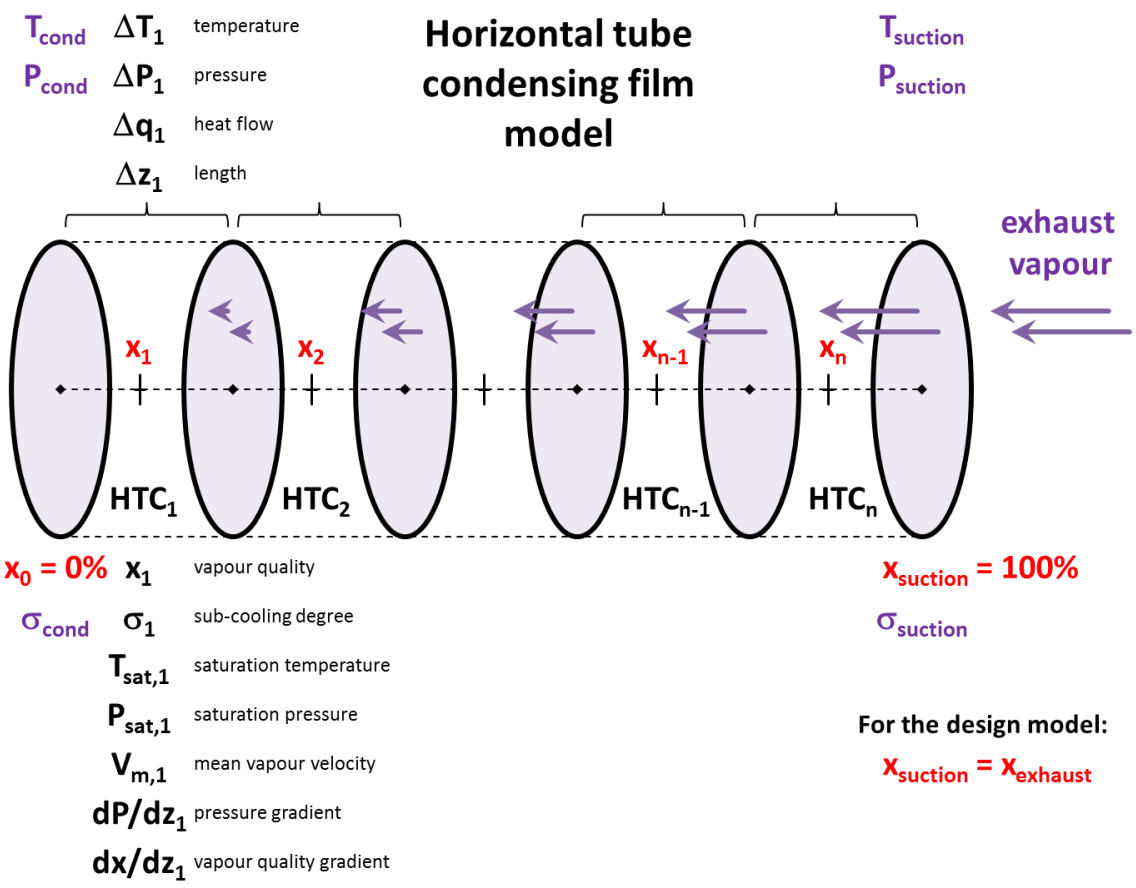

Fig. 2.4. Condensing film model for smooth condenser tube based on fixed vapour quality increments.

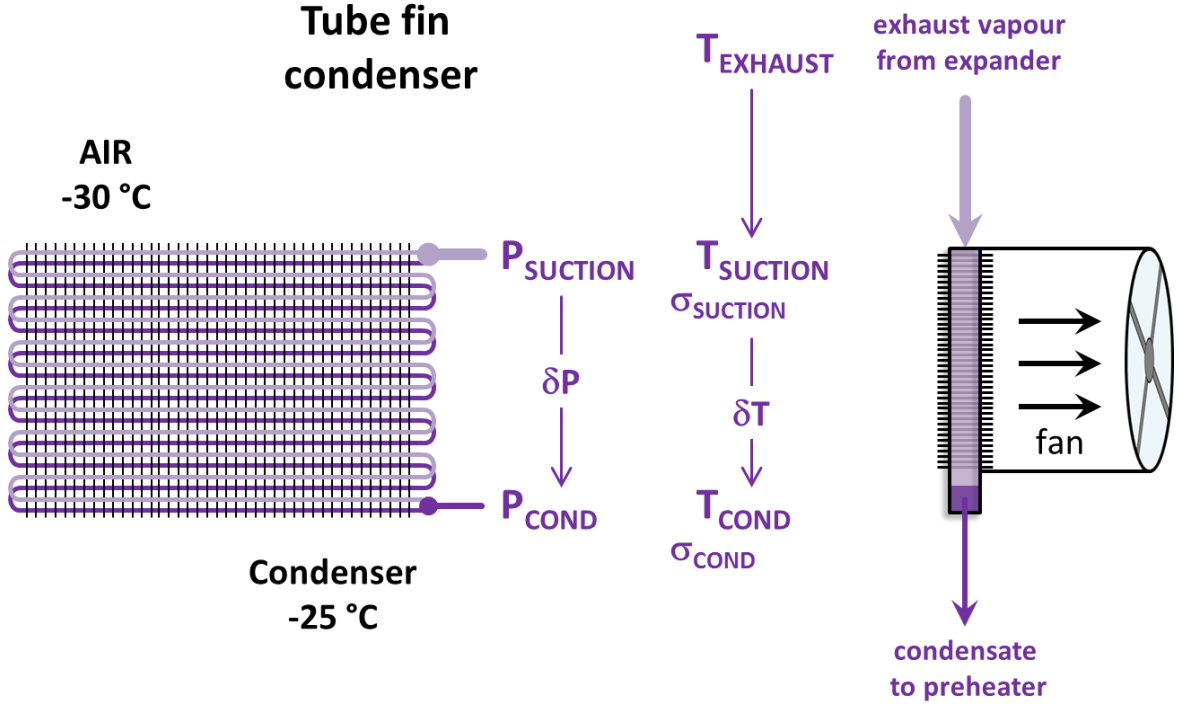

Fig. 2.5. Schematic of a fan-forced tube fin condenser, including temperature glide terminology.

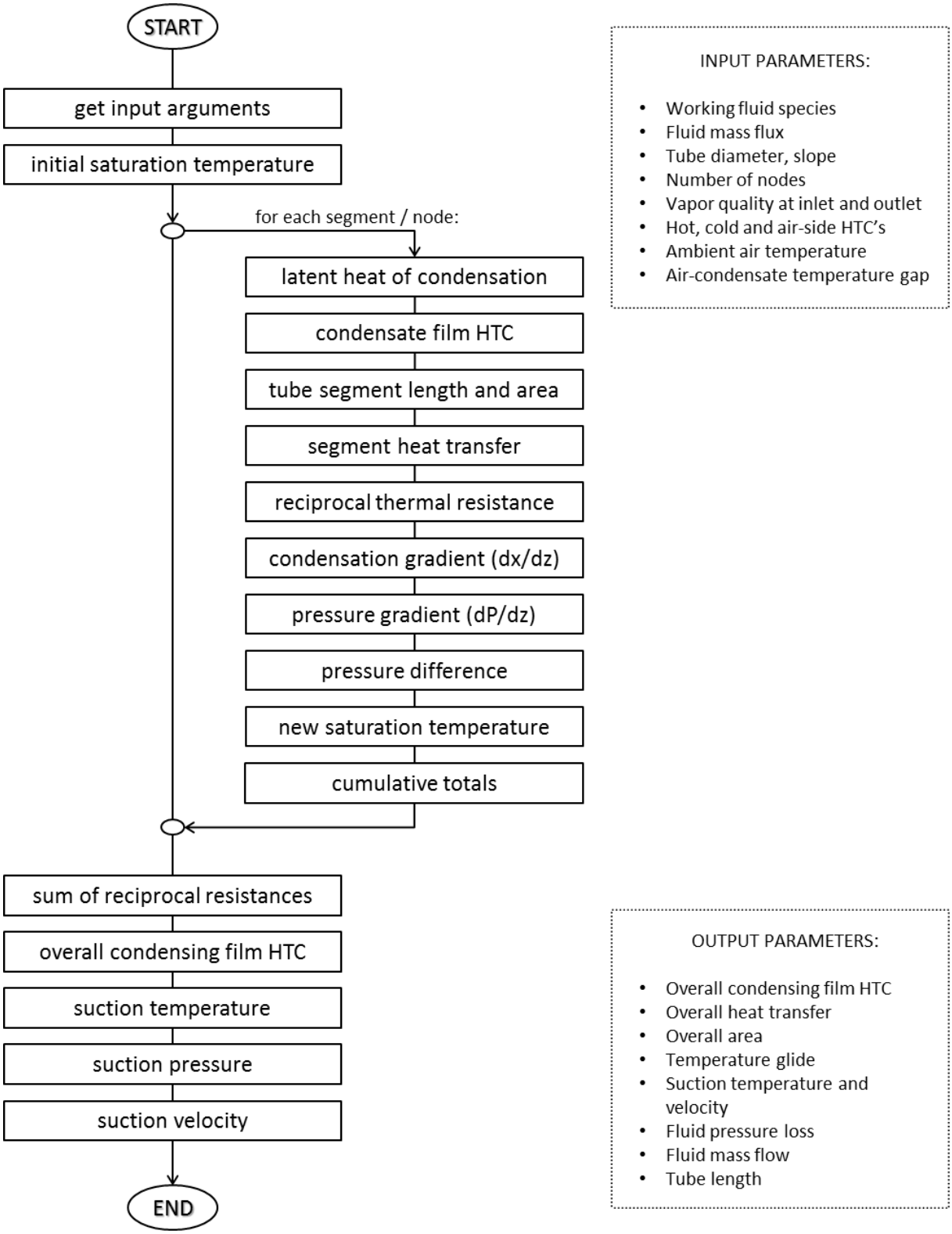

Fig. 2.6. Algorithm summary for horizontal tube condensing film heat and mass flows.

The transitional dimensionless gas velocity J_G^T proposed by Cavallini determines whether or not the heat transfer coefficient (HTC) of a given flow regime is dependent or independent of the temperature difference across the condensing film:

$$J_G^T = \left(\left(\frac{7.5}{4.3 X_{tt}^{1.111} + 1} \right)^{-3} + {C_T}^{-3} \right)^{-1/3} \tag{2.6}$$

where $C_T = 1.6$ for hydrocarbons and 2.6 for other working fluids.

HTC for ΔTindependent annular flows is calculated at each node as a function of the liquid-only HTC, with the condenser tube wall temperature calculated from ambient air and condensate saturation temperatures using the thermal resistance model shown in Fig. 2.7. For ΔTdependent flows the HTC calculation needs an extra term to account for stratified flow effects. An iterative loop is also needed to reconcile hot and cold side heat flow estimates. The temperature difference across the condensing film increases with each iteration until the calculated heat flow across the condensing film matches the estimated heat flow across the continuous fins exposed to the ambient air.

Combined thermal resistance for each node R_i is calculated from heat flow $\dot{q}_i$:

$$R_i = \frac{T_{sat,i} - T_{air}}{\dot{q}_i} \tag{2.7}$$

The combined HTC for each node is then:

$$\alpha_i = \frac{1}{R_i \, A_{wall}} \tag{2.8}$$

The length of each tube segment is calculated from the energy balance between the enthalpy loss of the condensing fluid mass flow versus estimated heat transfer across the tube segment:

$$\Delta z_i = \frac{\left(G \, D \, \Delta x_i \, (h_{tf,i} + \Delta KE) \right)}{\left(4 \, \alpha_i \left(T_{sat,i} - T_{air} \right) \right)} \tag{2.9}$$

where h_{tf} is the latent heat of condensation, and $\triangle KE = (V_{m,2}^2 - V_{m,1}^2)/2$

Surface area of each tube segment:

$$\triangle A_i = \triangle z_i \, \pi \, D \tag{2.10}$$

Heat flow for each tube segment:

$$\triangle q_i = \alpha_i \, \triangle A_i \, (T_{sat,i} - T_{air}) \tag{2.11}$$

Reciprocal thermal resistance for the node:

$$UA_i = \alpha_i \, \triangle A_i \tag{2.12}$$

Total condensing film thermal resistance along the full length of tube:

$$R_{film} = \frac{1}{\sum_{i=1}^{n} UA_i} \tag{2.13}$$

Condensing film HTC over the full length of tube:

$$\alpha_{film} = \frac{1}{R_{film} \, A_{tube}} \tag{2.14}$$

Total area of the full length of condenser tube:

$$A_{tube} = \sum_{i=1}^{n} A_i \tag{2.15}$$

Overall thermal resistance along the full length of tube:

$$R_{tube} = R_{hot} + R_{film} + R_{cold} + R_{fins} \tag{2.16}$$

Overall tube fin condenser HTC:

$$U_{tube} = \frac{1}{R_{tube} \, A_{tube}} \tag{2.17}$$

Tube fin condenser MTD:

$$MTD_{cond} = \dot{q}_{tube}\, R_{tube} \tag{2.18}$$

Temperature glide

An integrated thermal resistance model permits overall heat flows to be determined at each node by summing together the individual thermal resistances of all layers, Fig. 2.7. This part of the model implements the method described by Rohsenow [84] p.17.30 (17.9).

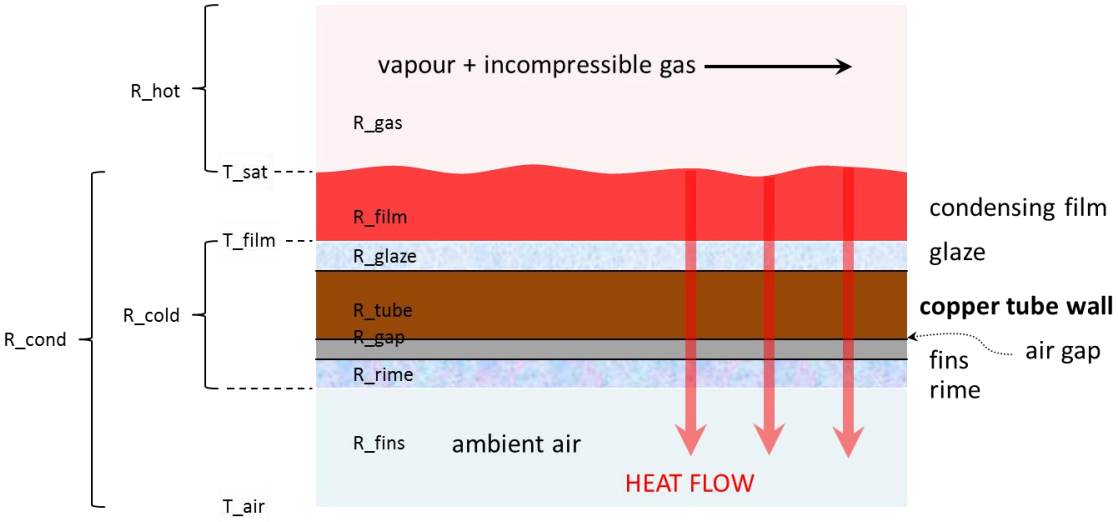

Fig. 2.7. Thermal resistance layers for cross-flow horizontal tube condensing film node.

We assume a fixed nominal temperature difference of 5K between the ambient air and the condensate outlet. The method permits the tube wall temperature to float as we work upstream from the condenser outlet along the full length of the condenser tube to the condenser inlet (suction).

Thus:

$$T_{wall,i} = \frac{\left(T_{sat,i} + \left(\frac{R_{film,i} + R_{hot,i}}{R_{fins,i} + R_{cold,i}}\right) T_{air}\right)}{\left(1 + \left(\frac{R_{film,i} + R_{hot,i}}{R_{fins,i} + R_{cold,i}}\right)\right)} \tag{2.19}$$

where

$$R_{fins,i} = \frac{1}{\eta_{ext}\, \alpha_{fins}\, A_{ext,i}} \tag{2.20}$$

$$R_{glaze,i} = \frac{t_{glaze}}{k_{glaze}\, A_{wall,i}} \tag{2.21}$$

$$R_{wall,i} = \frac{t_{tube}}{k_{tube}\, A_{wall,i}} \tag{2.22}$$

$$R_{gap,i} = \frac{t_{gap}}{k_{gap}\, A_{base,i}} \tag{2.23}$$

$$R_{rime,i} = \frac{t_{rime}}{\eta_{ext}\, k_{rime}\, A_{ext,i}} \tag{2.24}$$

$$R_{cold,i} = R_{glaze,i} + R_{tube,i} + R_{gap,i} + R_{rime,i} \tag{2.25}$$

$$R_{gas,i} = \frac{1}{\alpha_{gas,i}\, A_{wall,i}} \tag{2.26}$$

$$R_{hot,i} = R_{gas,i} \tag{2.27}$$

$$R_{film,i} = \frac{1}{\alpha_{film,i}\, A_{wall,i}} \tag{2.28}$$

Saturation temperature $T_{sat,i}$ is a function of pressure and increases as we work upstream from the 100% cold liquid condensate end toward the 100% warm vapour suction end. The temperature of the cold condensate outlet is deemed to be 5 K warmer than the ambient air temperature.

MATLAB code relating to the above model is included in Appendix M: air_sink_.

Pressure gradient

The pressure gradient model calculates the pressure gradient as a function of the condensation gradient at each node. The condensation gradient is simply the change in vapour quality per incremental length of tube:

$$\left(\frac{\mathrm{dx}}{\mathrm{dz}}\right)_i = \frac{\triangle x_i}{\triangle z_i} \tag{2.29}$$

Friction, gravity and fluid acceleration forces all affect the flow of vapour and condensate phases in a condenser tube. Our condensing film model calculates the pressure drop by resolving the two-phase friction coefficients as per Rohsenow [84]:

$$\left(\frac{dP}{dz}\right)_i = \frac{dP}{dz_f} + \frac{dP}{dz_g} + \frac{dP}{dz_a} \tag{2.30}$$

In estimating the frictional pressure gradient, vapour void fractions are calculated using the Rouhani model as cited by Cavallini [88]. Two-phase Reynolds numbers, laminar and turbulent flow friction factors are also calculated according to Cavallini in estimating the frictional pressure gradient for adiabatic two-phase flow. The Freidel correlation as cited in Rohsenow [84] is used as the most appropriate two-phase flow frictional multiplier correlation.

In estimating the effect of mass transfer across the liquid-vapour interface on interfacial shear stress the Mickley correction factor is used to scale the frictional pressure gradient for condensing flow as proposed by Sardesai [89] and cited by Cavallini [88].

Having thus determined the pressure gradient, the pressure change can now be calculated for each segment of condenser tube:

$$\Delta P_i = \left(\frac{dP}{dz}\right)_{\mathrm{i}} \Delta z_i \tag{2.31}$$

The pressure of the next node is increased by this amount as we move upstream. The saturation temperature at the next node is simply a function of the new working fluid saturation pressure:

$$T_{sat} = f(P_{sat}) \tag{2.32}$$

MATLAB code for the pressure gradient model includes detailed annotation and is found in Appendix M: dPdz_horz_tube_cond_film_.

Validation of software model

The horizontal tube condensing film model is based on the method described by Cavallini [86]. Output from our routine developed in MATLAB is plotted and found to precisely reproduce the equivalent chart published in the same paper, Fig. 2.8.

Model output was also compared with experimental data of Kim [90] for CO_2 condensation at temperatures down to -25 °C, Fig. 2.9. The paper by Kim describes a laboratory apparatus to provide precise experimental measurements of heat transfer from refrigerant condensing within a condenser

tube test section. Lengths of smooth and microfin copper tubes were soldered within an enclosing brass jacket. Cooling was provided by chilled hydrofluoroether (HFE) circulating within an array of copper tubes soldered onto the external surface of the brass jacket. The test refrigerants, including CO_2, were delivered to the tube test section by a variable speed gear pump. A calorimeter provided precise heating in order to control the exact vapour quality entering the test section. Temperature, pressure and flow measurements were taken at critical points around the refrigerant loop. An array of 12 thermocouples embedded within the brass jacket provided accurate wall temperature measurements which were used to calculate an averaged local heat transfer coefficient according to:

$$\dot{Q}_{CO_2} = h \cdot A_{surf}(T_{CO_2} - T_{wall}) \tag{2.33}$$

Precise heat capacity data and equations provided by the HFE manufacturers permitted accurate estimates to be made of the heat flowing into the coolant. Heat transfer from the environment was estimated using a calibrated UA value for the test section.

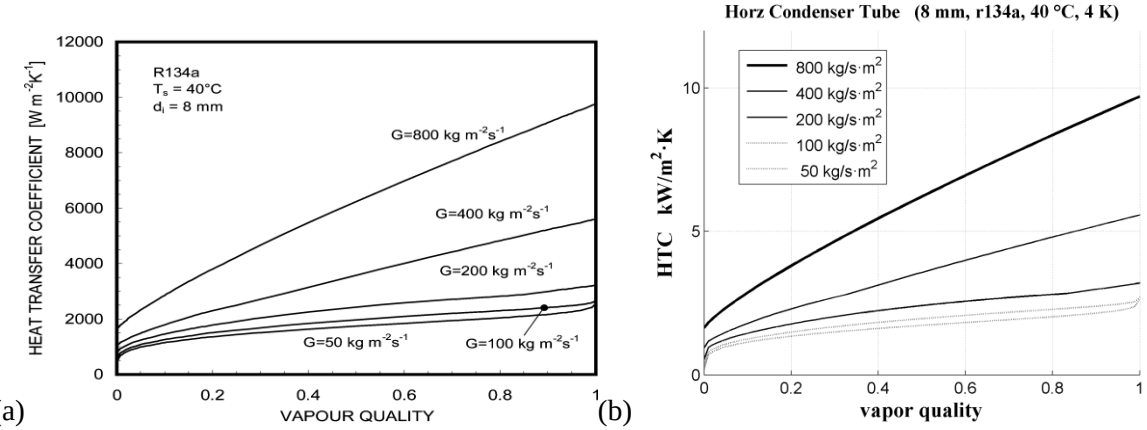

Fig. 2.8. R134a condensing film HTC from (a) ***Cavallini [86]*** and (b) our model as described in section2.4.2.

Smooth tube condensing film HTC estimates for CO_2 obtained from these experiments were found to be around 10% lower than estimates made using the Cavallini method across the full range of vapour qualities for mass flux of 200 kg/s·m^2, and up to 40 % lower for high quality vapour at mass flux of 800 kg/s·m^2. A low mass flux of ~100 kg/s·m^2 is appropriate for the basic glaciothermal engine condenser because this uses less copper tubing than would be required at higher mass fluxes.

In this low mass flux range there is good agreement between HTC values obtained using the experimental method of Kim and the empirical correlations of Cavallini.

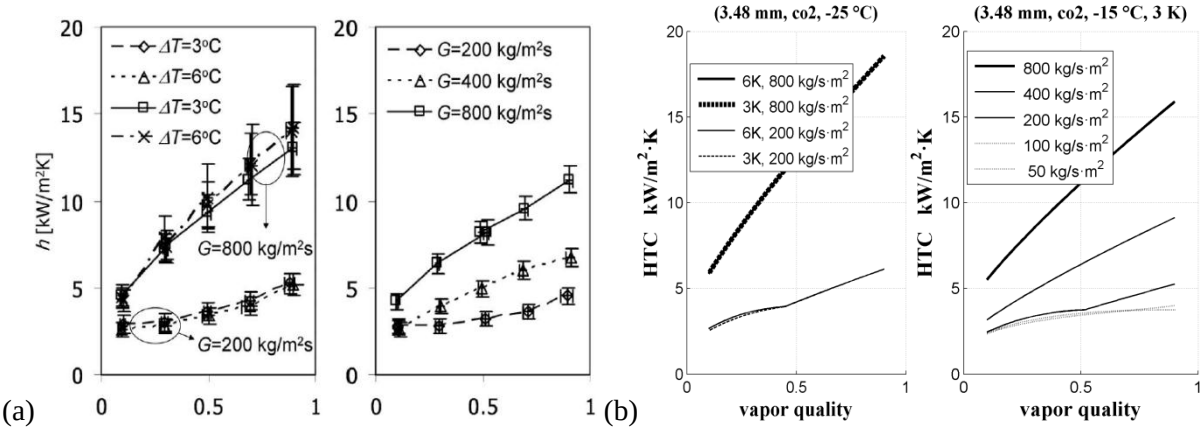

Fig. 2.9. CO_2 condensing film HTC from (a) ***Kim et al [90]*** and (b) our model with same parameters.

2.4.3 Condenser panel scaling

A single condenser panel is scaled to condense 1 kg of working fluid. The number of tubes is:

$$n_{tubes} = \dot{m}_{panel} \,/\, \dot{m}_{tube} \tag{2.34}$$

$$H_{panel} = n_{tubes}\, pitch \tag{2.35}$$

The width of the panel is equal to the cut length, which is simply the cumulative total of all the condenser tube segments. Air mass flows are calculated equivalent to the cross-sectional area of the tube fin condenser panel exposed to the air flow. Thus:

$$v_{air} = V_{m,fan}\, A_{panel} \tag{2.36}$$

$$\dot{m}_{air} = v_{air}\, \rho_{air} \tag{2.37}$$

MATLAB code for the tube fin and horizontal in-tube condensing film model based on the above literature methods [84, 86, 88] is in Appendices M: air_sink_ and M: HTC_horz_tube_cond_film_.

2.4.4 Condenser fan work

Condenser fan work relates directly to pressure drop across the tube fins. This is a function of the friction factor and varies in direct proportion to the square of the mean air flow velocity for a given tube fin geometry and hydraulic diameter:

$$\Delta P_{fi} = f_{duct} \frac{L_{duct}}{D_{h,duct}} \frac{\rho_{air} \cdot V_{m,fan}^2}{2} \tag{2.38}$$

The height and width of rectangular air flow ducts are determined by the fin spacing and tube spacing (pitch) respectively. Friction factors for fully developed flow within a smooth tube are a function of the Reynolds Number for both laminar and turbulent flow conditions:

$$f_{lam} = \frac{64.00}{Re} \qquad Re < 2300 \tag{2.39}$$

$$f_{turb} = 0.184\, Re^{-0.2} \qquad Re > 4000 \tag{2.40}$$

Laminar flow regimes are normal for a tube fin condenser. Under laminar flow conditions the heat transfer coefficient is independent of flow velocity so there is generally no heat transfer advantage gained by increasing the fan speed. The condenser fan is deemed to operate at a nominal mechanical efficiency of 70%.

Fan power per square metre of condenser panel is then given by:

$$w_{fin} = \frac{\dot{m}_{air}\, V_{m,fan}^2}{2} + \frac{v_{air}\ \Delta P_{fin}}{\eta_{fan}} \tag{2.41}$$

MATLAB code to calculate fan power requirements is included in Appendix M: air_sink_ .

An overview of the integrated tube-fin condenser software model as discussed above is provided in Fig. 2.10.

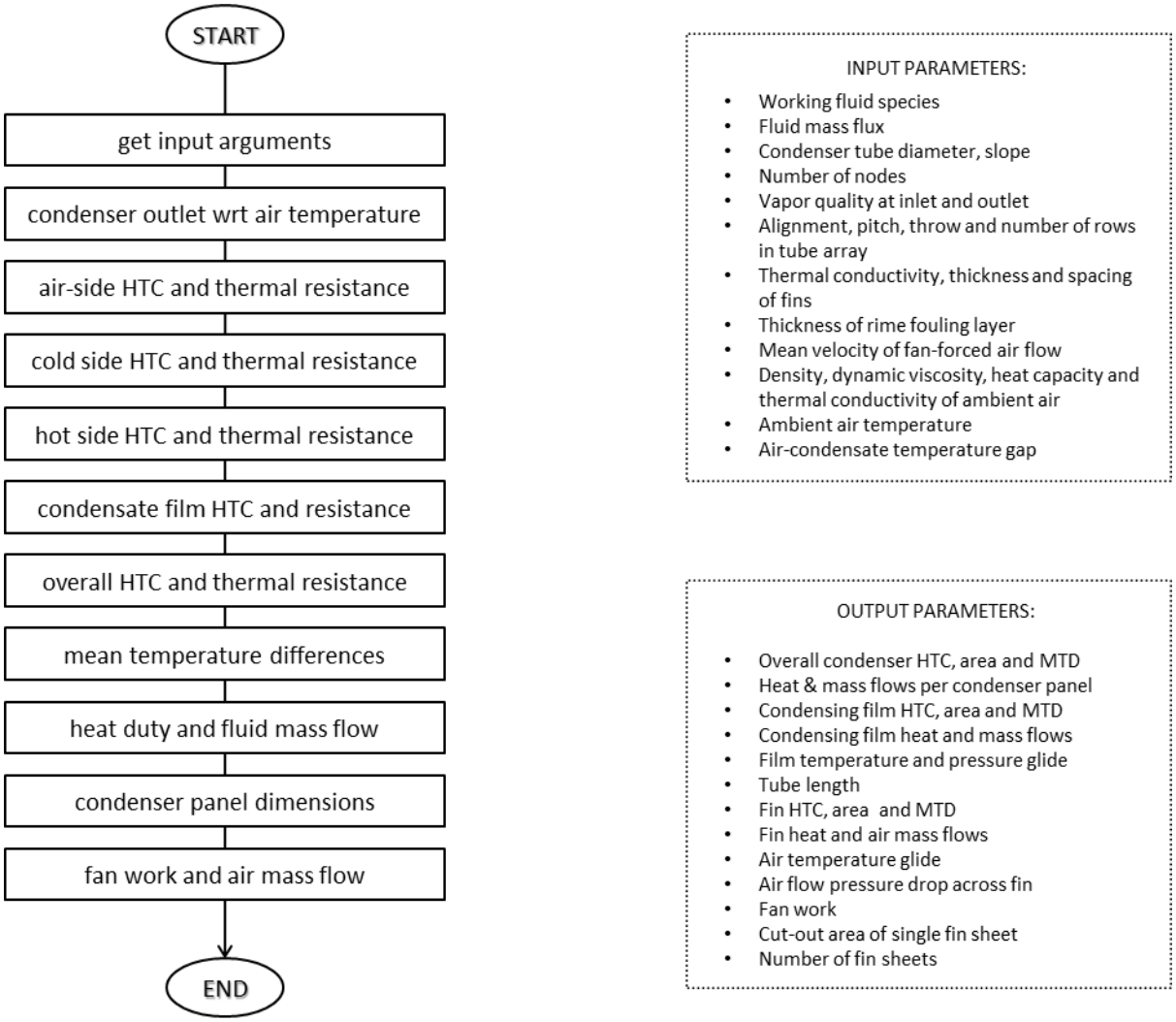

Fig. 2.10. Algorithm summary for integrated tube-fin condenser heat and mass flows.

2.5 Condensate injection pump

The function of the condensate pump is to inject cold condensate liquid returning from the condenser into the condensate preheater. The pressure of the returning condensate varies widely and is dependent upon the outside ambient air temperature. The preheater operates at the same fixed high pressure as the flooded evaporator section of the ice-in-tube glaciothermal boiler.

The condensate pump is deemed to operate under adiabatic conditions with injection of the condensate into the preheater at a nominal isentropic efficiency of 70%.

General requirements for liquid refrigerant pumps are discussed in Appendix 2-B.

2.6 Ice slurry loop

The function of the ice slurry loop is to provide a constant flow of consistent quality seeded ice slurry to the boiler. Full heat transfer cannot commence in an ice-in-tube glaciothermal boiler until the ice slurry loop has been primed with an appropriate fraction of seed ice. At start-up, fine ice crystals may be supplied from an external source and added to the seawater feed. Once underway, the ice slurry that burns within the boiler tubes will produce an increasing volume of ice as individual crystals grow and new seed crystals are created by crunching the mixture in an ice blender.

The ice slurry loop consists of an ice-in-tube heating element, classifier, mixer, pump, flow meters and electrical conductivity probes, Fig. 2.11.

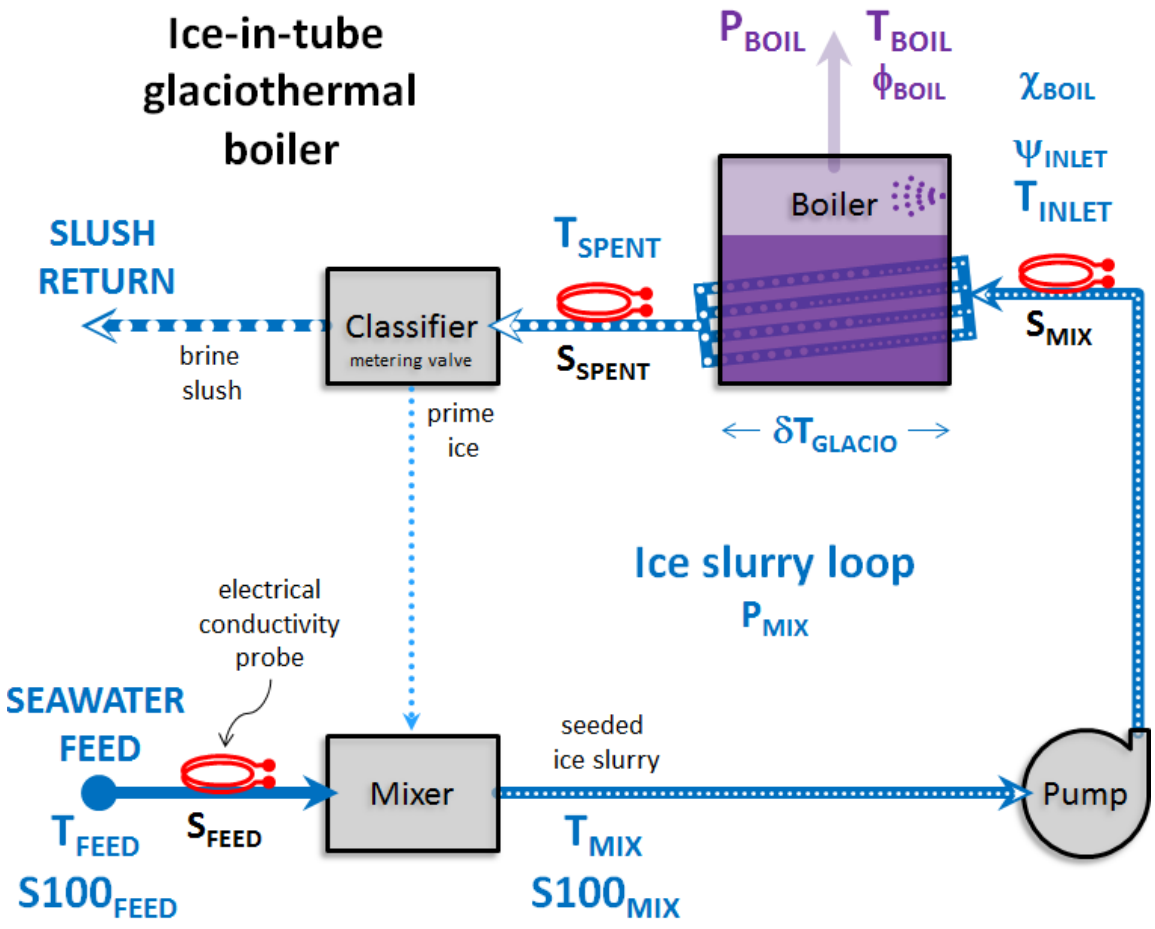

Fig. 2.11. Schematic of ice slurry loop for an ice-in-tube glaciothermal boiler.

An efficient and reliable method is sought to extract heat from the flow of freezing seawater. Literature suggests that pumping seawater directly into cold boiler tubes poses a number of

operational problems and would not produce high heat flux, nor achieve optimal boiling temperatures [76, 80, 91]. Seeded ice slurry is used instead to achieve high heat flux without undue supercooling of the mixture. Methods developed to model heat transfer processes in the refrigeration industry are used to design a novel ice-slurry loop for a glaciothermal boiler. Ice mass fraction is regulated within an open loop to provide a fixed volume of seed ice for the ice-slurry mixture sent to the boiler. This ensures optimal heat transfer due to prompt ice crystal growth, prevents supercooling of the feed water, and helps to reduce the possibility of ice forming on the inside of boiler tube walls. High velocity flow further helps to mitigate ice fouling and also delivers high heat transfer coefficients.

If the seawater is much warmer than freezing, more prime ice will be required to cool the mixture and so the mixture will have a lower characteristic salinity, Appendix 2-D. If the seawater is too warm, more prime ice will be required than is available from the spent ice slurry. The *critical threshold* temperature of the seawater feed will have been reached for the given flow rate, Fig. 2.12. In this case, subsequent looping of the ice slurry mixture will consume all the spent ice, until no ice remains to exit the mixer. In the absence of any seed ice with which to sustain high heat flux within the ice-in-tube boiler, the boiler is either shut-down or continues to operate but under reduced capacity. In mono-phase mode warm seawater is fed directly to the boiler inlet at high flow velocity and/or the boiler temperature is increased to prevent the tubes from freezing over.

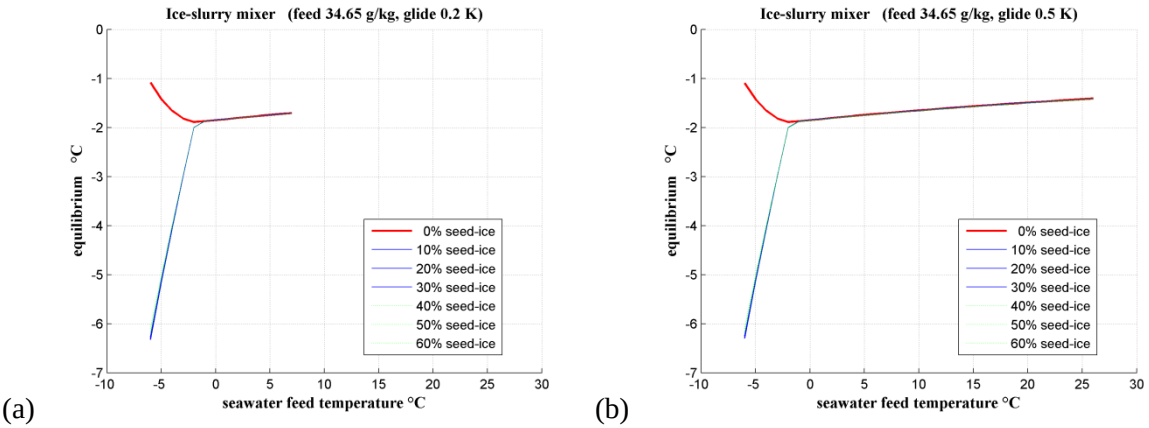

(a) (b)

Fig. 2.12. Ice slurry mixer equilibrium temperature as a function of seawater feed temperature. The critical threshold temperature is ~7 °C for a temperature glide of (a) 0.2 K, and ~26 °C for (b) 0.5 K.

Background information regarding seawater properties, characteristic salinity and the continuous properties model is provided in Appendices 2-C, 2-D and 2-E respectively.

2.6.1 Ice-slurry pump

The volume flow rate of the ice slurry pump determines the velocity of ice slurry flow within the glaciothermal boiler tubes. This in turn regulates heat flux within the boiler.

The literature recommends use of positive displacement screw pumps (Moineau pumps) for transporting ice slurry at ice concentrations above 35%, or multi-stage centrifugal pumps for lower ice concentrations [78]. If seed ice fractions can be reliably regulated between 10—30% then a centrifugal pump appears best suited for our basic ice slurry loop.

Pump rotors and housing of Grundfos CR5-11 centrifugal pumps have been specially modified to optimise ice slurry pumping efficiency, Fig. 2.13. This particular ice slurry pump is selected for the feasibility model and a best fit curve for pump efficiency is calculated based on the plotted data:

$$\eta_{pump,is} = -9.167C_m^3 + 2.75C_m^2 - 0.6333C_m + 0.63 \qquad 0 < C_m < 0.3 \qquad (2.42)$$

where C_m is the ice mass fraction.

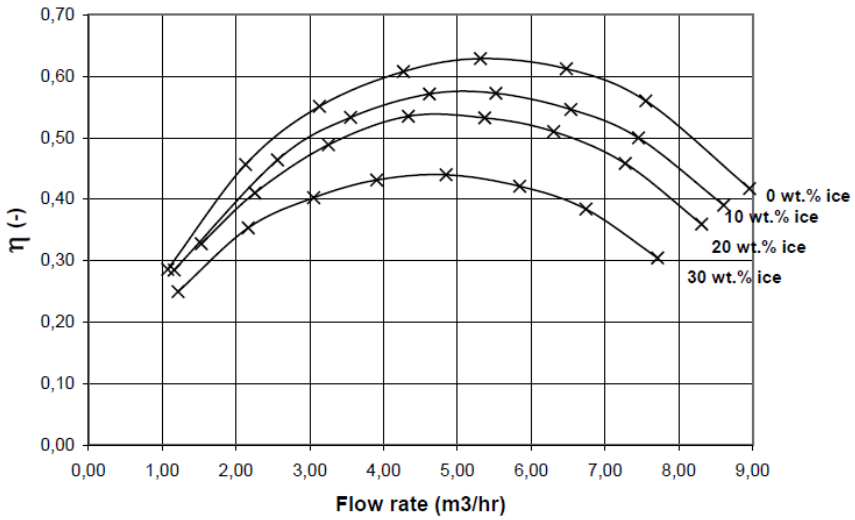

Fig. 2.13. Pumping efficiency for a 5 m^3/hour rated, 11-stage centrifugal pump, ***taken from Kauffeld et al [78].***

Pump work calculations

Ice slurry pump work relates to pressure drop along the tube. For a given tube diameter this is a function of the friction factor and varies in direct proportion to the square of the mean flow velocity. We adopt a friction factor $f = 0.184\, Re_{is}^{-0.2}$ for smooth tubes and apply the standard equation to calculate pressure drop over a given length of tube:

$$\Delta P_{tube} = f \frac{L}{D} \rho \frac{V_m^2}{2} \tag{2.43}$$

The pumping power is then:

$$\dot{W}_{is,pump} = \frac{\dot{m}_{is}\, \Delta P_{tube}}{\rho_{is}} \tag{2.44}$$

2.6.2 Ice-slurry mixer

The function of the ice slurry mixer is to combine the incoming prime ice and seawater feed in the appropriate ratio to achieve the desired seed ice fraction in the resulting equilibrium ice slurry mixture sent to the boiler, Fig. 2.11.

A portion of the *spent ice* fraction emerging from an ice-in-tube or ice-injection boiler is recycled within the ice slurry loop to provide *seed ice* for the next boiler pass. The portion of spent ice directed from the classifier back to the mixer for this purpose is called the *prime ice* fraction. The surplus spent ice that is piped back to the sea for disposal is referred to as *slush ice*.

Spent ice emerging from the boiler is colder than the ambient seawater feed, and the fraction of prime ice sent to the mixer can be regulated in order to deliver the desired fraction of seed ice to the boiler at the maximum possible freezing point temperature. Ice slurry flow rate and mixture composition must be regulated to supply consistent quality ice slurry. A metering valve on the ice slurry classifier delivers an appropriate volume fraction of prime ice to the mixer to maintain the correct seed ice mass fraction to the boiler. Measurements need to be taken in real time to determine the status of the ice slurry loop.

Background information regarding ice slurry loop control and classifier circuit layout are included in Appendices 2-F and 2-G respectively.

Ice-slurry mixer mass flow calculations

An effective way to model the metering of prime ice to the mixer is to nominate a fixed temperature drop for the ice slurry passing through the boiler tubes, Fig. 2.14. The enthalpy at the inlet is deemed to be equivalent to that of ice slurry in thermal equilibrium at its incipient freezing point, having brine phase salinity equal to the seawater feed, plus the arbitrarily nominated seed ice fraction at the same temperature. Ice slurry of equivalent enthalpy is produced in a working ice slurry loop by mixing appropriate proportions of cold spent ice with the warmer seawater feed. The mass fraction of spent ice required to prime the mixer is calculated from the ratio of enthalpy differences:

$$C_{m,prime} = \frac{h_{is,inlet} - h_{feed}}{h_{ice,spent} - h_{feed}} \tag{2.45}$$

The spent ice being colder will cool the incoming seawater feed until an equilibrium temperature is reached equivalent to the salinity liquidus of the new brine phase. The high latent heat of fusion of crystallising ice, compared to sensible heat capacity of the liquid phase, means that the actual ice fraction in the resulting mixture should be close to the arbitrary seed ice fraction that was nominated in setting the enthalpy target – especially if the ambient seawater is at or near to its incipient freezing point. The ice mass fraction entering the boiler is thus deemed to be equal to the nominated seed ice mass fraction. Overall mass flows within the boiler are calculated from the heat energy balances.

Energy required to preheat and vaporise 1 kg of pressed cold condensate is calculated from enthalpy data derived from the thermophysical properties database [92] as a function of temperature and pressure, or temperature and vapour quality in the case of saturated fluid:

$$\dot{q}_{boil} = (h_{tp} + \Delta h_{pre}) \tag{2.46}$$

where h_{tp} is the latent heat of vaporisation and Δh_{pre} is the change in specific enthalpy needed to preheat the pressed condensate, thus:

$$h_{tp} = h_{boil,v} - h_{boil,l} \tag{2.47}$$

$$\Delta h_{pre} = h_{boil,l} - h_{press} \tag{2.48}$$

$$q_{boil} = h_{boil,v} - h_{press} \tag{2.49}$$

Ice slurry enthalpy is calculated as:

$$h_{is} = C_m \, h_{ice} + (1 - C_m) \, h_{brine} \tag{2.50}$$

Heat produced from 1 kg of ice slurry on a single pass through the boiler tubes must be:

$$q_{is} = h_{is,inlet} - h_{is,spent} \tag{2.51}$$

Mass flow of ice slurry per kg of working fluid is:

$$m_{is/wf} = \frac{q_{boil}}{q_{is}} \tag{2.52}$$

Required ice slurry loop mass flow rate is calculated knowing the working fluid mass flow rate:

$$\dot{m}_{is} = \dot{m}_{wf} \cdot m_{is/wf} \tag{2.53}$$

Seawater mass flow rate then derives from the ice slurry mass flow rate and ice mass fraction:

$$\dot{m}_{sea} = \dot{m}_{is} \, (1 - C_{m,seed}) \tag{2.54}$$

The above mass flow calculations as implemented in MATLAB can be found in Appendices M: slurry_mix_ and M: GT_engine_.

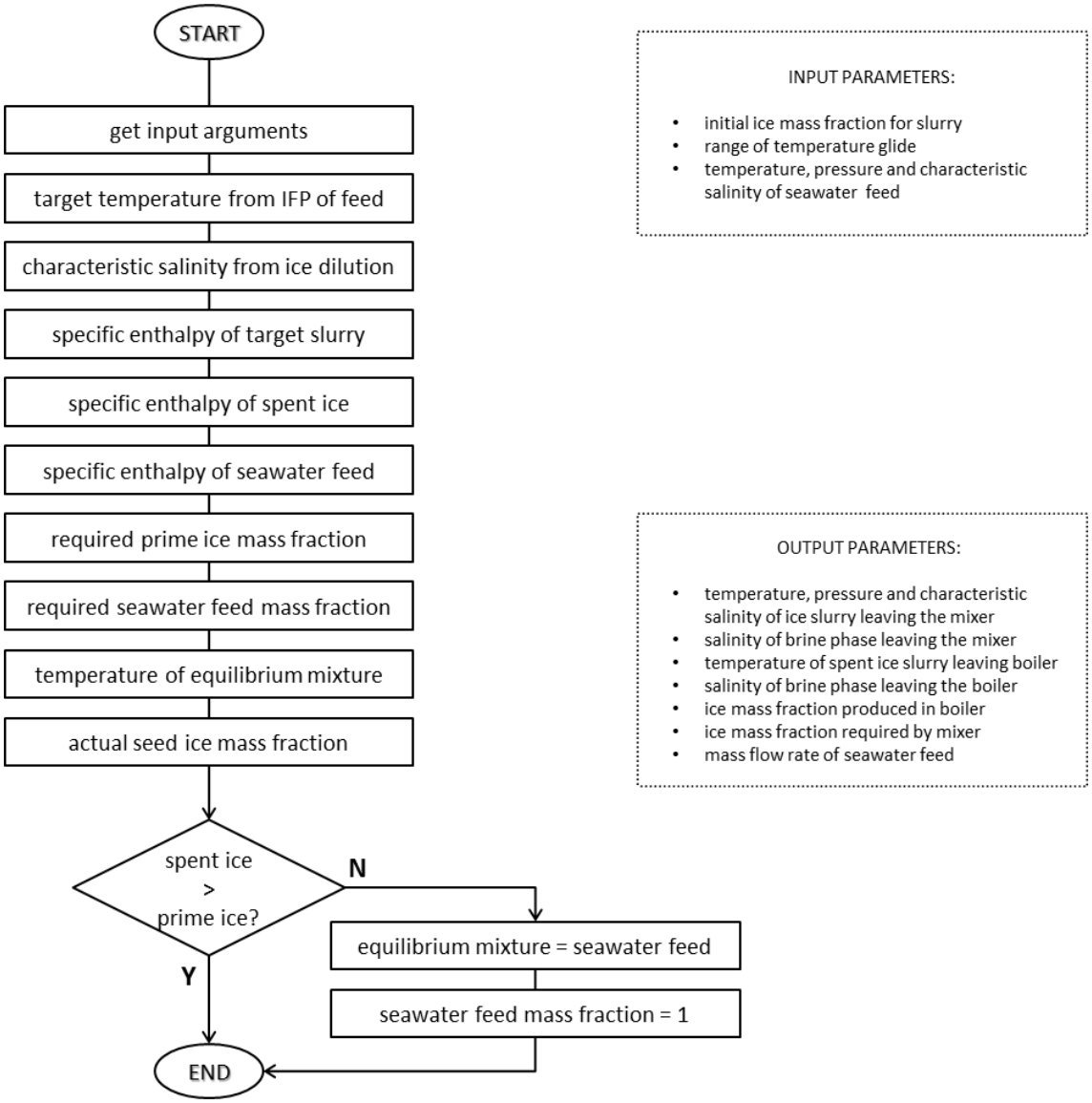

Fig. 2.14. Algorithm summary for ice slurry mixer heat and mass flows.

2.7 Ice-in-tube boiler

2.7.1 Condensate preheater

The function of the condensate preheater is to raise the temperature of the cold condensate liquid returning from the condenser to match the temperature of the flooded evaporator.

It is not possible to use ice slurry to directly heat the cold condensate because the temperature difference between the two would cause copper tubes of an ice-in-tube boiler to quickly freeze over. Nor is it possible to discharge the cold condensate directly into the flooded evaporator as this would eliminate the superheat necessary for vapour bubble formation and immediately kill the nucleate

boiling heat transfer. A simple solution, however, is to either sparge the incoming cold condensate with warm vapour from the boiler, or to spray the cold condensate into the warm vapour stream.

Sparging or spraying

A portion of the high pressure heated vapour emerging from the glaciothermal boiler can be redirected to heat an incoming flow of cold condensate from the condenser. Heat is transferred as the incoming stream of warm vapour condenses on contact with the cold liquid until it is warm enough to safely discharge into the flooded evaporator without suppressing the nucleate boiling.

Directly mixing warm vapour and cold liquid involves some loss of entropy from the fluid cycle and is not an ideal thermodynamic solution for preheating the condensate. It is, however, a convenient and reliable way to return the condensate to the boiler. No modelling is required, other than to account for the lesser enthalpy of the cold condensate when calculating the heat duty of the boiler, thus:

$$q_{boil} = h_{boil,v} - h_{press} \tag{2.55}$$

2.7.2 Glaciothermal heater

The glaciothermal boiler performs two functions. The first is to provide efficient convective heat transfer from circulating seeded ice slurry on one side, and the second is to enable rapid nucleate boiling of the working fluid on the other. The ice slurry side comprises the ice-in-tube glaciothermal heater, and the working fluid side is a shell-and-tube flooded evaporator. This section describes the working principles of the glaciothermal heating element.

The strategy behind the proposed internal flow glaciothermal heater is to optimise the ice slurry temperature, flow rate, ice mass fraction and ice particle size to maximise heat generation and heat transfer. We seek to *maximise* ice crystal growth within the ice slurry and to *minimise* formation of new (small) crystals both within the ice slurry and on the heater tube walls.

Ice fouling of copper tube surfaces is rare for ice slurry with less than 2 K supercooling [78, 91], whereas ice invariably forms on stainless steel cooling surfaces of mechanical scraper ISG's that

typically operate with 15—20 K of supercooling [76]. Somewhere in between these two extremes is a sensitive transition zone. Smooth surfaces and special coatings [93] help to suppress nucleation and to reduce ice adhesion. High ice slurry flow velocity helps to clear weakly adhering ice by hydro-scraping. Slick surfaces and strong jets may thus broaden the transition zone [76, 77].

Ice nucleation and ice crystal growth are discussed in more detail in Appendices 2-H and 2-I. Appendix 2-J discusses issues and strategies regarding operation of the glaciothermal heater.

Ice-slurry HTC calculations

A segmented model is constructed to simulate ice slurry flow within a smooth tube glaciothermal heater, Figs 2.15 and 2.16. Standard methods for calculating convective heat transfer are employed in the ice slurry literature with particular attention paid to the characteristic physical properties of ice slurries. In the absence of empirical data for turbulent flow of high ice-fraction *freezing* seawater ice slurry we restrict our calculations to modest ice volume fractions $(C_v \leq 0.3)$. This section provides a summary of our algorithms including relevant heat and mass flow equations. Changes in ice slurry kinetic and potential energy along the tube are negligible compared to heat flow and are ignored.

We begin by calculating the ice slurry mean flow velocity by comparing the ice slurry density at each node with that of the inlet. Ice slurry density and mean ice slurry flow velocity are:

$$\rho_{is,i} = \frac{1}{\frac{c_m}{\rho_{ice}} + \frac{(1-c_m)}{\rho_{brine}}} \tag{2.56}$$

$$V_{m,i} = V_{m,inlet} \frac{\rho_{is,inlet}}{\rho_{is,i}} \tag{2.57}$$

The *Nusselt number* is required to calculate ice slurry HTC. In turn, *Reynolds* and *Prandtl* number estimates require the *effective thermal conductivity* λ_{is} of ice slurry. This is derived from seawater and ice thermal conductivities using Jeffrey's model [94, 95]. *Apparent heat capacity* is estimated as the enthalpy gradient with $\mathrm{d}T = 0.01\ ^\circ C$.

Effective dynamic viscosity of Newtonian suspensions is a function of ice volume fraction [78]:

$$\mu_{is} = \mu_{sea} \cdot (1 + 4.5 C_v) \tag{2.58}$$

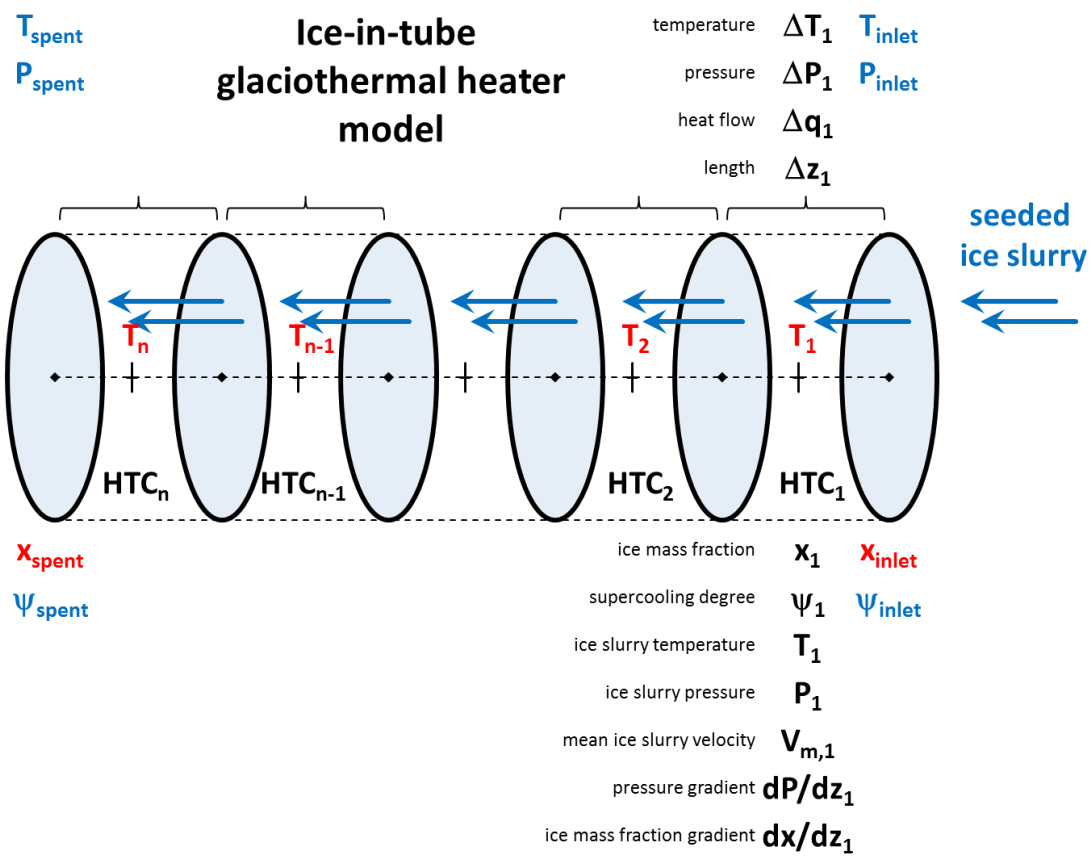

Fig. 2.15. Freezing ice slurry model for an ice-in-tube glaciothermal heater.

Tube diameters vary between 5—40 mm, and we assume fully developed flow for the full length of the tubing ($V_{m,is} \gg 1.5\ m/s$). $Nu_{is,lam} = 3.66$ for laminar flow in smooth tubes. For turbulent flow the Nusselt number is calculated using the Chilton-Colburn equation [78] but modified as per Dittus-Boulter to signify cooling:

$$Nu_{is,turb} = 0.125\ f\ Re_{is}\ Pr_{is}^{0.3} \tag{2.59}$$

Corrugating the inner surface of the copper tube may improve the ice slurry HTC somewhat but also adds to the pumping power demands according to the change in hydraulic diameter:

$$D_h = 4\frac{A_c}{p} \tag{2.60}$$

Ice slurry HTC at each node is then:

$$\alpha_{is} = \lambda_{is} * \frac{Nu_{is}}{D_{h,is}} \tag{2.61}$$

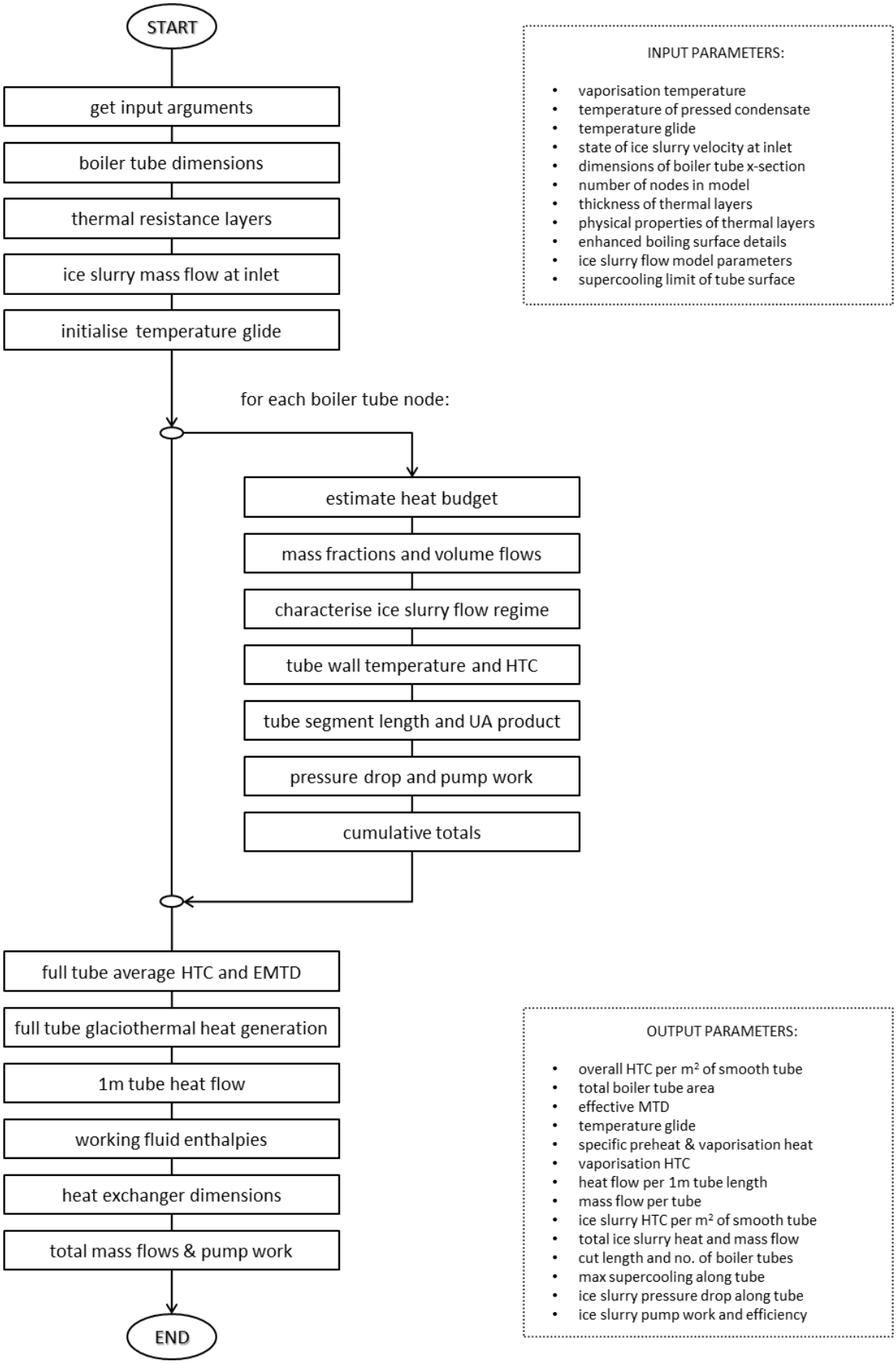

Fig. 2.16. Summary of algorithm for ice-in-tube glaciothermal boiler heat and mass flows.

Overall boiler HTC for each node is calculated by summing the thermal resistances of all the layers as was done for the condenser, Fig. 2.17. Evaporator HTC is deemed to be constant along the full length of the boiler tube. Only the ice slurry HTC changes between nodes.

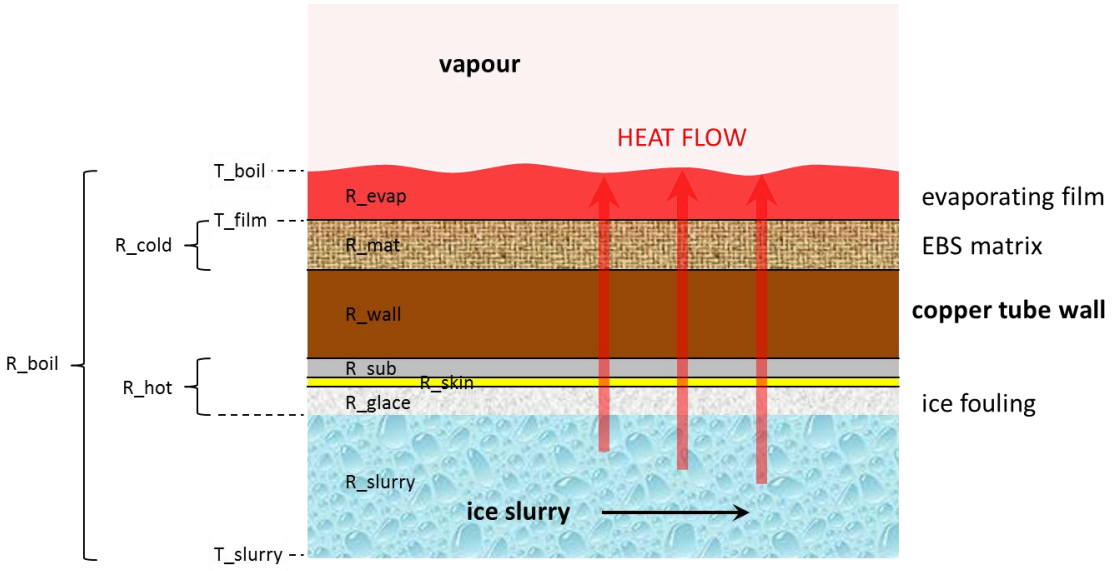

Fig. 2.17. Thermal resistance layers for ice-in-tube glaciothermal boiler node.

The length of each tube segment is readily calculated knowing the required surface area of the segment which in turn derives from the familiar heat transfer energy balance equation:

$$A_i = \frac{\triangle h_i}{\alpha_{is}\,\psi_i} \tag{2.62}$$

Total area of the full length of boiler tube:

$$A_{tube} = \sum_{i=1}^{n} A_i \tag{2.63}$$

Cut length of single boiler tube:

$$L_{tube} = \frac{A_{tube}}{2\pi} \tag{2.64}$$

Mean temperature difference across the ice slurry for the full length of boiler tube:

$$MTD_{is} = \frac{\sum_{i=1}^{n} \triangle h_i}{\sum_{i=1}^{n} UA_i} \tag{2.65}$$

Overall thermal resistance along the full length of boiler tube is calculated as the reciprocal sum of thermal resistances for each node:

$$R_{is} = \frac{1}{\sum_{i=1}^{n} UA_i} \tag{2.66}$$

Overall ice slurry heat transfer coefficient for the full length of boiler tube:

$$U_{is} = \frac{1}{R_{is}\, \mathrm{A_{tube}}} \tag{2.67}$$

Total heat flow across the boiler tube wall is then calculated from Newton's Law of Cooling:

$$\dot{q}_{is} = U_{is}\, A_{tube}\, MTD_{is} \tag{2.68}$$

2.7.3 Boiler tube bundle scaling

A single shell-and-tube bundle is scaled to boil 1 kg of working fluid.

The length of the bundle is equal to the cut length, which is simply the cumulative total of all the estimated boiler tube segment lengths. The number of tubes required in the bundle is determined from the ratio of specific boiler heat duty to single tube heat transfer:

$$n = \frac{\dot{q}_{boil}}{\dot{q}_{tube}} \tag{2.69}$$

$$L_{total} = n\, L_{tube} \tag{2.70}$$

Complete MATLAB code relating to these calculations is included in Appendix M: slurry_burn_

2.7.4 Flooded evaporator

Working fluid vaporisation requires effective vapour bubble nucleation. Commercial shell and tube flooded refrigerant evaporators incorporate enhanced nucleate boiling surfaces (EBS's) and achieve exceptional heat transfer coefficients for specific refrigerants. Similar surfaces might also be used to boil high pressure natural working fluids in a glaciothermal boiler. EBS's must be closely matched to each specific working fluid and intended vaporisation temperature. However, as of 1999, *"A complete understanding of the mechanism of boiling on enhanced surfaces does not exist." [96].*

Principles of nucleate pool boiling and potential nano-scale EBS's are described in Appendix 2-K.

Evaporator HTC calculations

The degree of condensate superheating for an EBS is designated ϕ_{boil} and can be determined from the HTC at any point along the boiler tube if the heat flux can be calculated on the ice slurry side:

$$\phi_{boil} \cdot HTC_{boil} = \psi_{\text{is}} \cdot HTC_{is} \tag{2.71}$$

$$\phi_{boil} = \psi_{\text{is}} \cdot \frac{HTC_{is}}{HTC_{boil}} \tag{2.72}$$

This relationship is critical if we wish to maximise heat flux across glaciothermal boiler tubes. Our modelling suggests that ice slurry HTC's at least as high as 30 kW/m^2K are possible for high flow velocities within small diameter tubes, Fig. 3.5. If the ice tube surface of our proposed glaciothermal heater can tolerate more than a degree or two of supercooling (ψ_{is}) then the overall heat flux might be substantial. The evaporator side would need to match this flux. For actual enhanced boiling surfaces the HTC varies greatly with heat flux and the pore diameters must be closely matched with the corresponding degree of condensate superheating. As Fig. 2K-1 indicates, nano-scale pores are required if ϕ_{boil} is more than a degree or two. In the absence of a commercial EBS of this specification it is likely that the maximum heat flux across our glaciothermal boiler tubes will be more modest.

We nominate an optimistic 10 kW/m^2 for the evaporator HTC at 1 K superheating.

2.8 Two-phase expander

An essential feature of a glaciothermal engine is that, although the boiler pressure remains constant, the condenser pressure varies in direct response to the ambient air temperature. The challenge for the selected expander is to maintain optimal power output as the pressure ratios change. Axial turbines rely on aerodynamic effects and will stall unless high vapour velocities can be maintained. Variable low pressures do not permit such turbines to maintain effective torque. Axial turbines also require gas or dry vapour for trouble-free operation. Depending on expander efficiency, non-superheat ORC's and glaciothermal cycles may undergo wet vapour expansion with >10% wet fraction. Positive displacement expanders overcome this problem but isentropic efficiencies vary.

Piston expanders are mechanically complex, bulky and inefficient when used with low pressure ratio glaciothermal expansions.

By comparison, fixed volume ratio two-phase twin screw expanders are mechanically simple, compact and high revving. Isentropic efficiencies are quoted between 65 and 90% depending on the geometry of the rotor profile for volume expansion ratios similar to the glaciothermal working fluid range. The literature suggests consistently high isentropic efficiencies for screw expanders running under steady state conditions at constant 1,500 or 3,000 rpm [81, 97] although results vary somewhat.

Accordingly, a two-phase twin screw expander is the preferred expander for the basic glaciothermal engine cycle. For the purposes of our feasibility study, the relative volume ratio of the expander is allowed to vary according to the density ratio of the working fluid between inlet and outlet, Fig. 2.18.

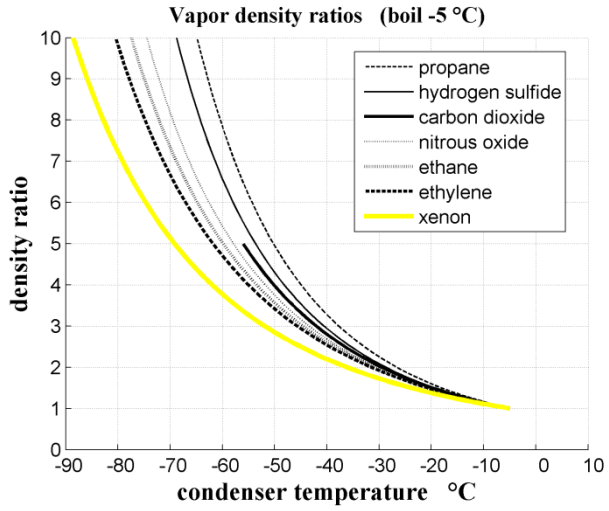

Fig. 2.18. Vapour density ratios of various working fluids for a boiling temperature of -5 °C [92].

Discussion regarding controlled volume vapour expanders and electrical generators is to be found in Appendix 2-L. Conclusions about the basic glaciothermal engine are included in Appendix 2-M.

Energy conversion calculations

The overall nett power output of our twin-screw expander determines the scaling of all other device components. We need to determine the mass flow rate of working fluid required to maintain nett power output of 250 kW. This is calculated knowing the expander and generator efficiencies.

Our glaciothermal engine feasibility study does not attempt to model the dynamic performance of the twin screw expander or electrical generator. Instead, we nominate a flat isentropic efficiency, η_{isen}, of 70% as a conservative approximation for a twin screw expander performing a wet expansion of ethane comfortably below the critical point and with no superheating. A flat 80% mechanical to electrical conversion efficiency, η_{elec}, is deemed for the generator.

The power output produced by 1 kg/s of working fluid passing through the expander is:

$$\dot{w}_{turb} = \eta_{isen}\, \dot{q}_{in} \tag{2.73}$$

Parasitic loads must be taken into consideration. Condensate injection and condenser fan operating loads are calculated with respect to 1 kg/s of working fluid as documented in the relevant sections of this chapter. Ice slurry pumping load is initially calculated with respect to 1 kg/s of ice slurry, and subsequently converted per 1 kg/s of working fluid.

Total parasitic loads are reconciled as:

$$\dot{w}_{loads} = \dot{w}_{press} + \dot{w}_{is\_pump} + \dot{w}_{fan} \tag{2.74}$$

Nett work rate is thus:

$$\dot{w}_{nett} = \dot{w}_{turb} - \dot{w}_{loads} \tag{2.75}$$

Nett thermal efficiency is:

$$\eta_{nett} = \frac{\dot{w}_{nett}}{\dot{q}_{in}} \tag{2.76}$$

Overall thermal efficiency is then:

$$\eta_{th} = \eta_{nett} \cdot \eta_{elec} \tag{2.77}$$

2.9 Component scaling

Mass flow rate of working fluid needed to maintain 250 kW:

$$\dot{m}_{wf} = \frac{\dot{w}_{duty}}{\dot{w}_{nett}} \tag{2.78}$$

where $\dot{w}_{duty} = 250{,}000\ W$.

Total number of boiler tube bundles or condenser panels is thus:

$$n = \dot{m}_{wf} \tag{2.79}$$

Engine performance results are presented in Chapter 3.

Chapter 3 – Performance Evaluation of the Basic Glaciothermal Engine

This chapter explains the exceptional performance of the basic glaciothermal fluid cycle and provides a detailed parametric analysis in order to optimise operation of the tube-fin condenser and glaciothermal boiler. Device dimensions and overall engine performance curves are generated. The combined results of this analysis determine the site requirements for installing a basic engine.

3.1 Introduction

Numerous parameters affect the performance of the basic glaciothermal engine described in Chapter 2. Ambient environmental conditions, configuration of engine components and operational settings all affect power output and efficiency.

Potential performance of the concept engine is analysed by reviewing the thermodynamic cycle and modelling the different input parameters for each engine component in turn. Performance curves are constructed for engines running both ethane and CO_2 and plotted across the full operating temperature domain. This facilitates subsequent analysis of year-round performance under ambient polar conditions. Critical operating points and engine management under extreme cold are discussed.

3.2 The working fluid cycle

3.2.1 Thermodynamic efficiency of glaciothermal cycles

The basic glaciothermal working fluid cycle achieves very high thermal efficiency relative to the Carnot limit. Absolute thermal efficiency is modest due to the meager temperature dipole between cold air and freezing water, but the amount of heat generated upon freezing of water is substantial (~335 kJ/kg). Thus the power output per litre of seawater feed is considerable – and the water is free.

We employ a variant Rankine cycle that has no superheat stage, and refer to it as a *basic glaciothermal cycle*, Fig. 3.1. This is equivalent to an *Organic Rankine Cycle* with no superheat. Operators familiar with the relative thermal efficiencies of geothermal ORC's might be surprised at the optimistic efficiencies plotted for the basic glaciothermal engine cycle in Fig. 3.2.

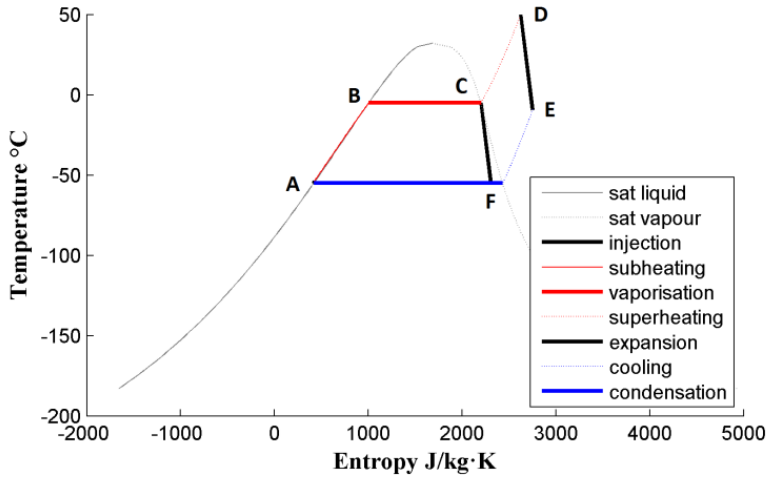

Fig. 3.1. T-S diagram of basic glaciothermal cycle (A-B-C-F-A) compared to an ORC Rankine cycle (A-B-C-D-E-F-A) with 50 °C superheat. Both run ethane: $\eta_{isentropic}$ = 70%; T_{BOIL} -5 °C and T_{COND} -55 °C.

Remarkable overall glaciothermal power efficiencies are due to the following fortuitous circumstances:

1. Boiler MTD's are very modest (~5 °C) due to latent heat transfer on both sides
2. Condenser MTD's are also very modest (~5 °C) due to over-sized condensers (affordable because of the premium value of reliable cold climate RAPS's)
3. Wet expansion of ethane or CO_2 in two phase saturated region involves no superheat
4. High speed twin screw expanders (TSE's) require no gearbox or converter electronics
5. Fixed volume ratios of dual phase TSE's closely match ethane-CO_2 density ratios
6. Extreme conditions (100 °C colder than normal) reduce denominator of Carnot equation

All these factors combine to produce thermal efficiencies *relative to Carnot* that are better than typical geothermal ORC cycles and much better than superheated steam cycles operating across similar heat source-sink temperature differences. Industry experience holds that standard superheat Rankine Cycles cannot achieve thermal efficiencies higher than 30—40% of Carnot. It is clear from Fig. 3.3 (a) that this is also true for low temperature working fluid cycles. Relative efficiency drops substantially with increasing superheat. Power cycles operating entirely within the two phase saturation dome, however, achieve fluid efficiencies around 90% of Carnot without superheating, Fig. 3.3 (b). Power cycles are also possible that employ quasi-isothermal reheat or heat recuperation,

but for small scale devices the minor efficiency gains do not justify the added complexity.

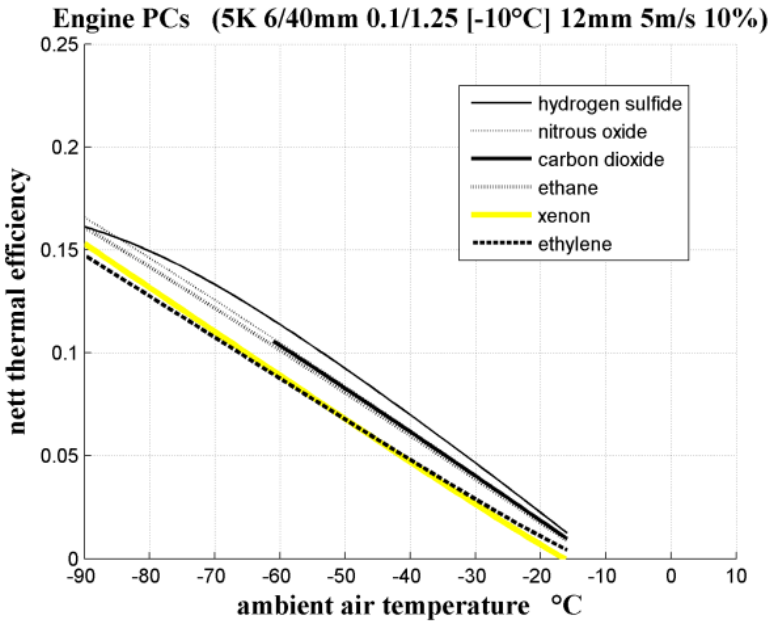

Fig. 3.2. Performance curves for nominal basic glaciothermal engine as a function of ambient air temperature for various working fluids (at 70% isentropic efficiency and 80% mechanical to electrical conversion efficiency).

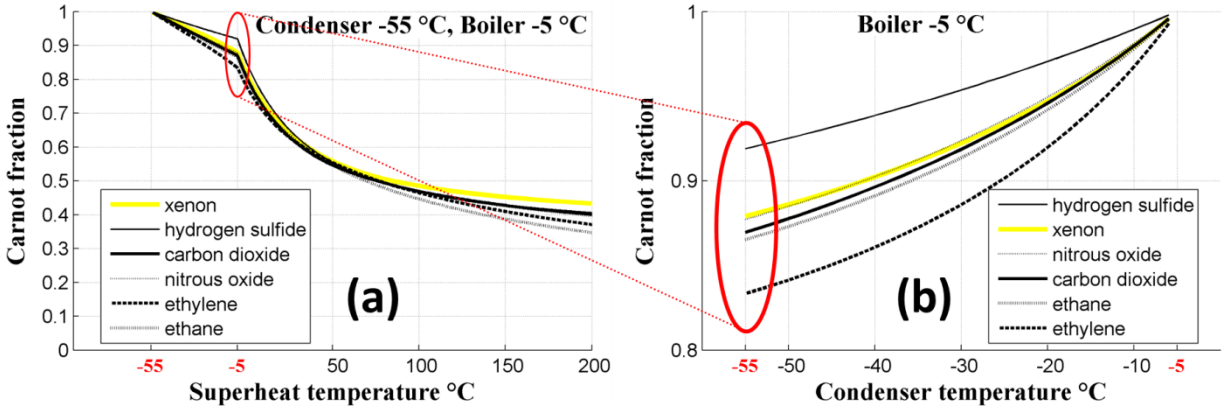

Fig. 3.3. Theoretical performance of natural refrigerant working fluids. Ideal isentropic efficiencies for (a) Rankine cycles of varying superheat, and (b) basic glaciothermal cycles (both $\eta\_expander$=100%).

3.2.2 Selection of working fluid species

Various physical properties of working fluids affect their ability to absorb and release heat and to generate motive power. Latent heat of vaporisation, heat capacity, density, thermal conductivity, viscosity, surface tension, and saturation pressure range all affect the performance of engine components in different ways. Characteristic properties may be beneficial in some parts of the engine cycle and detrimental in others. High fluid density aids compression, but hinders power output for

example. With all the permutations of inter-relating properties and processes it is necessary to plot the total engine performance in order to choose between competing fluids.

In the main region of interest for glaciothermal power generation between -40 and -60 °C the contrast between high and low performing fluids in terms of comparative nett engine thermal efficiency is around 40%, Fig. 3.2. Clearly hydrogen sulphide is very efficient, but may not be appropriate for other reasons, including corrosiveness. Carbon dioxide and ethane share very similar mid-range performance characteristics. A nett engine thermal efficiency of around 10% at an ambient air temperature of -60 °C is exceptional. Operational properties such as thermal stability, non-toxicity, and safe handling lead us to choose either ethane, CO_2 or a mixture of both as our preferred working fluid. Xenon permits very compact condensers but overall engine thermal efficiency is low.

3.3 Parametric analysis

This section explores the parametric relationships that affect the performance of individual heat transfer components. MATLAB device models calculate temperature glide along the full length of boiler and condenser tubes. This provides detailed quantitative estimates of heat and mass flows and permits an in depth analysis of the effects of competing input parameters.

3.3.1 Tube-fin condenser configuration

The tube-fin condenser comprises a condensing film heat source within the condenser tube and a forced convective air flow heat sink through external fins. Key variables affecting condensing film HTC include: condenser tube diameter and spacing, working fluid mass flux, and nominated condensate outlet temperature gap relative to ambient air. Tube thickness and thermal conductivity are also important, but for this study we only consider copper tubes of proportional thickness.

Variables affecting the air fin HTC include fin spacing and thickness, and condenser tube diameter and spacing. Typical air flow velocities fall within the laminar flow regime so heat transfer is purely by conduction and fan speed has no effect on the HTC within the normal fan working range.

Condenser tube diameter and spacing

The effect of condenser tube diameter and tube spacing on the heat transfer performance of our tube-fin condenser is depicted in Fig. 3.4. For each given set of input parameters our model calculates the required condenser tube lengths and number of tubes required to achieve the required heat sink capacity. These dimensions are used to estimate the total tonnes of copper needed by the tubes and fins per MW of engine nett power output. Small 3 mm diameter tubing permits the construction of very compact condensers across a range of tube spacings, Fig. 3.4 (a). Larger 12 mm tubing results in bulkier condensers for the same nett engine output, Fig. 3.4 (b). In each case, tube spacing of around 20 mm is optimal for the given 2.0 mm fin spacing.

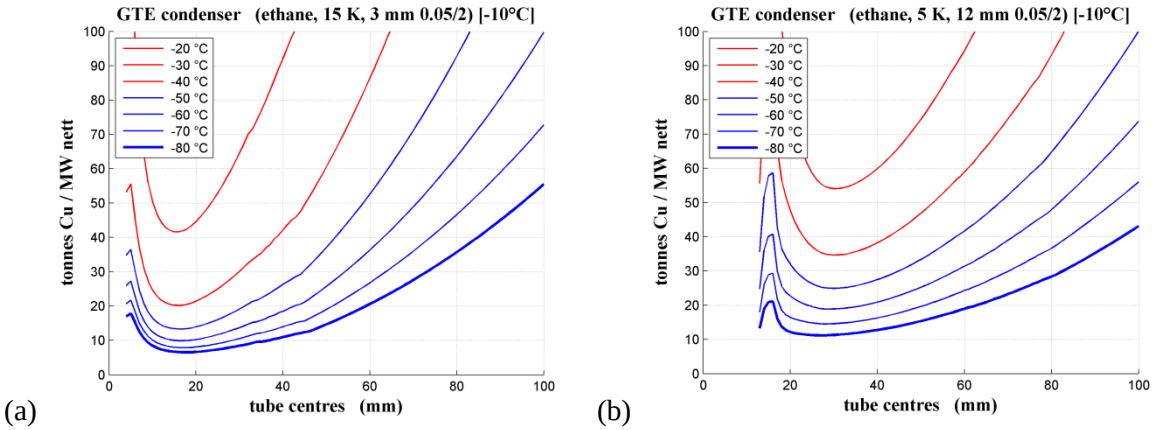

(a) (b)

Fig. 3.4. Tonnes of copper per MW nett power for (a) 3 and (b) 12 mm condenser tubes versus tube spacing.

A large number of similar plots were constructed to find the most practical tube-fin condenser geometry. 12 mm tubes need much thicker walls to deal with the high pressure working fluid vapor. Although needing less Cu, 3 mm tubes become quite fragile and very many need to be constructed.

Condensing film mass flux

Condensing film HTC for selected working fluids are plotted as functions of vapour quality along the full length of the condenser tube for mass fluxes of 100 and 500 kg/s·m^2, Fig. 3.5 (a) and (b) respectively. Very high HTC's result for most working fluids at high mass flux and CO_2 outperforms ethane across most of the vapour quality range. It must be noted, however, that ammonia, hydrogen

sulphide, ethylene and xenon are not explicitly included in the Cavallini model empirical correlations and so their validity cannot be guaranteed. Refer to section 2.4.2 for validation of software model.

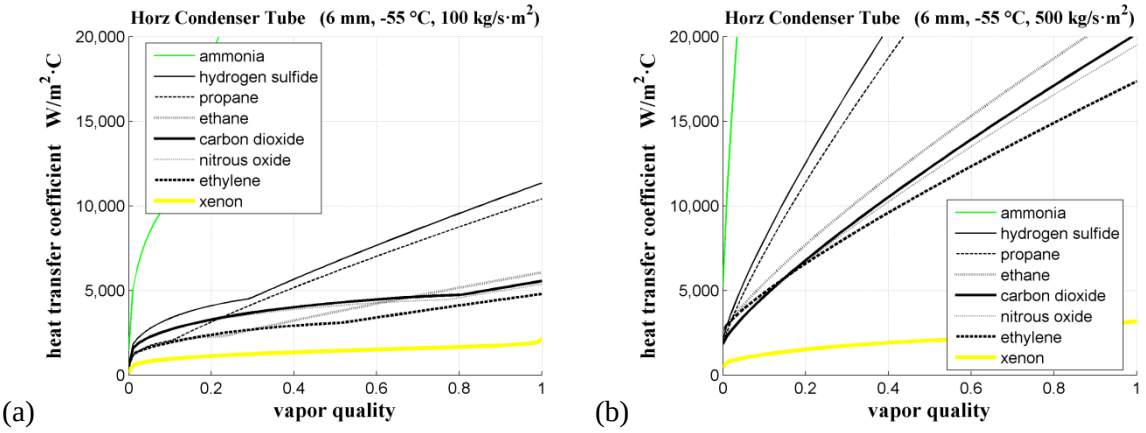

Fig. 3.5. Overall horizontal condenser tube HTC's as a function of vapour quality for natural working fluids of (a) 100 and (b) 500 kg/s·m^2 mass flu, as estimated using the Cavallini model [86]. Note that ammonia, hydrogen sulphide, ethylene and xenon are not explicitly included in the Cavallini model empirical correlations.

Condenser outlet temperature gap

The temperature difference χ_{cond} between ambient air and liquid condensate leaving the condenser outlet is arbitrarily set at 5 K. Although not plotted, analyses of numerous tube fin condenser temperature glides has shown that condensate film saturation temperatures rapidly converge within a narrow equilibrium temperature range regardless of the initial temperature gap that was nominated. 5 K works out to be near to the natural equilibrium temperature that exists for tube fin condensers of similar geometry.

Fan speed

Increasing the laminar air flow velocity has no effect on the convective HTC of the condenser, Fig. 3.6 (a), and only serves to increase the fan pumping power and thus reduce the overall nett thermal efficiency of the engine, Fig. 3.6 (b). Optimal flow velocity is determined by the mass flow rate needed to maintain a realistic temperature drop for the air passing through the fins. Barometric pressure has a direct effect on the mass flow rate, and fan speeds at high altitude sites will be greater than those nearer to sea level. We nominate 1.5 m/s as the typical air stream flow rate unless otherwise noted.

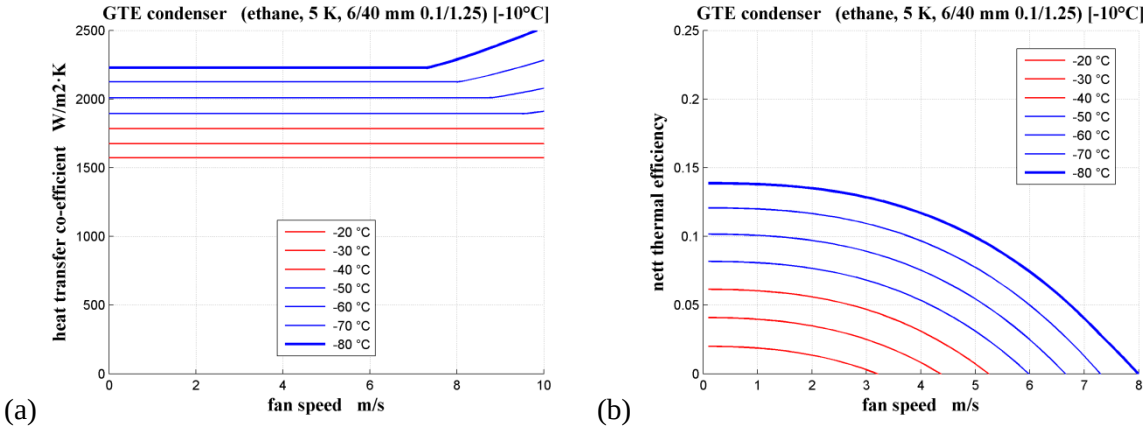

Fig. 3.6. Condenser HTC (a) and nett thermal efficiency of engine (b) as a function of condenser fan speed.

Condenser tube and fin spacings

Fan-forced air flow between closely spaced fins produces a low Reynolds number laminar flow regime. The convective HTC is predominantly a function of Nusselt number and hydraulic diameter. Both these parameters are related solely to the geometry of the rectangular ducts formed between adjacent fins and tubes. Heat transfer performance of the tube is thus optimised by varying the radiator geometry rather than the air flow.

In Fig. 3.7 (a), there is a marked change in the air fin HTC as a function of fin spacing. It is no surprise that highest HTC's occur with more numerous closely spaced fins. Although not shown, the pressure drop across the air fins rises asymptotically as fin spacing approaches zero. The ratio of HTC per unit of pressure drop provides a useful measure of heat transfer efficiency with respect to fan work, Fig. 3.7 (b). A local maximum at 5 mm suggests the optimal fin spacing for 6 mm tubes with respect to minimum fan work.

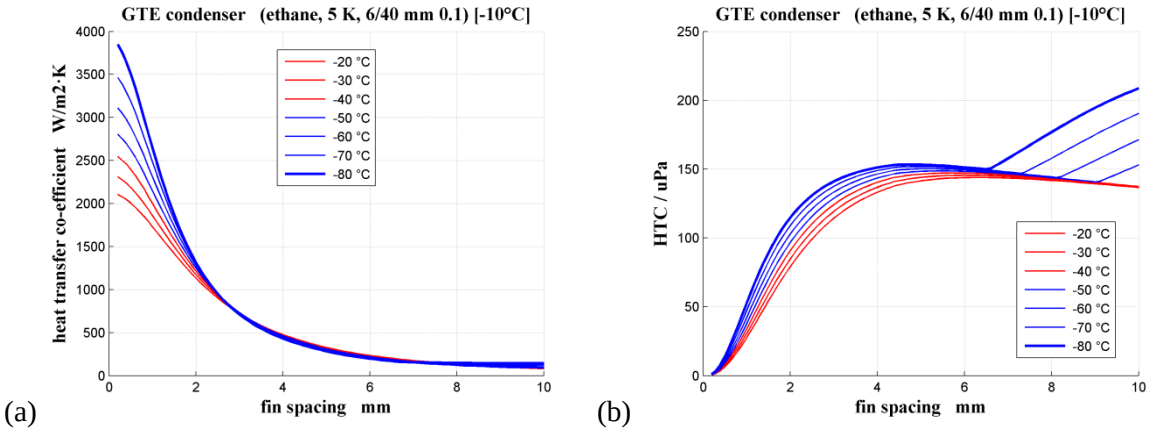

Fig. 3.7. Tube fin HTC (a) and HTC per μPa of fin pressure drop (b) as functions of fin spacing.

Condenser tube cut length

The required cut length of condenser tubes is near constant for low mass flux operation, Fig. 3.8. Condensation of CO_2 is achieved with shorter tubes than for ethane across most of the working range.

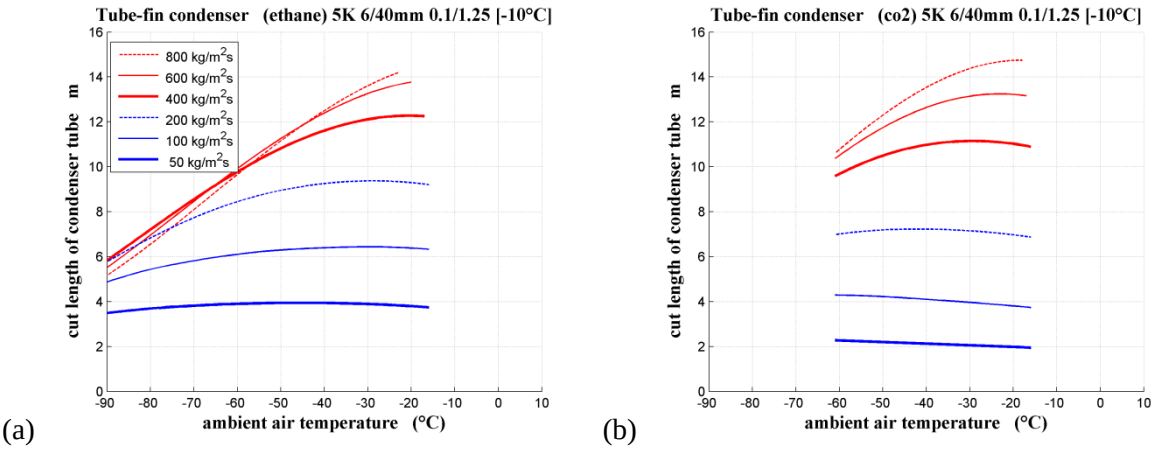

Fig. 3.8. Cut length of horizontal tubes for (a) ethane and (b) CO_2 condensers. Heat transfer is near constant across the full glaciothermal temperature domain for low mass flow tubes.

Temperature glide along condenser tube

In Fig. 3.9 we plot the temperature glide of 100 kg/s·m^2 condensing fluid by travelling upstream from the liquid condensate outlet (on the left margin) to the exhaust vapour inlet (suction) on the right hand side, shown as red dots along the top of the four charts below. The condensing fluid flow is right to left. Air is single pass cross-flow. The solid red line represents the overall condensing film MTD (heat source). The blue line along the bottom of each chart is the temperature of the ambient air (heat sink). The dotted red line in between is the condensation temperature. The dotted blue line is the condenser tube wall. All charts use the same scale axes to aid quick comparison.

It is evident from this series of charts that low (100 kg/s·m^2) condensing film mass flux (a, c) requires shorter cut lengths of condenser tube than does high (500 kg/s·m^2) mass flux (b, d).

Ethane (a, b) requires longer tubes than does CO_2 (c, d) for low mass flux, but shorter tubes than CO_2 for high mass flux. For given working fluid mass flux CO_2 yields the coldest inlet saturation temperature, and thus the lowest condenser suction pressure, although for low fluid mass flux the difference is negligible.

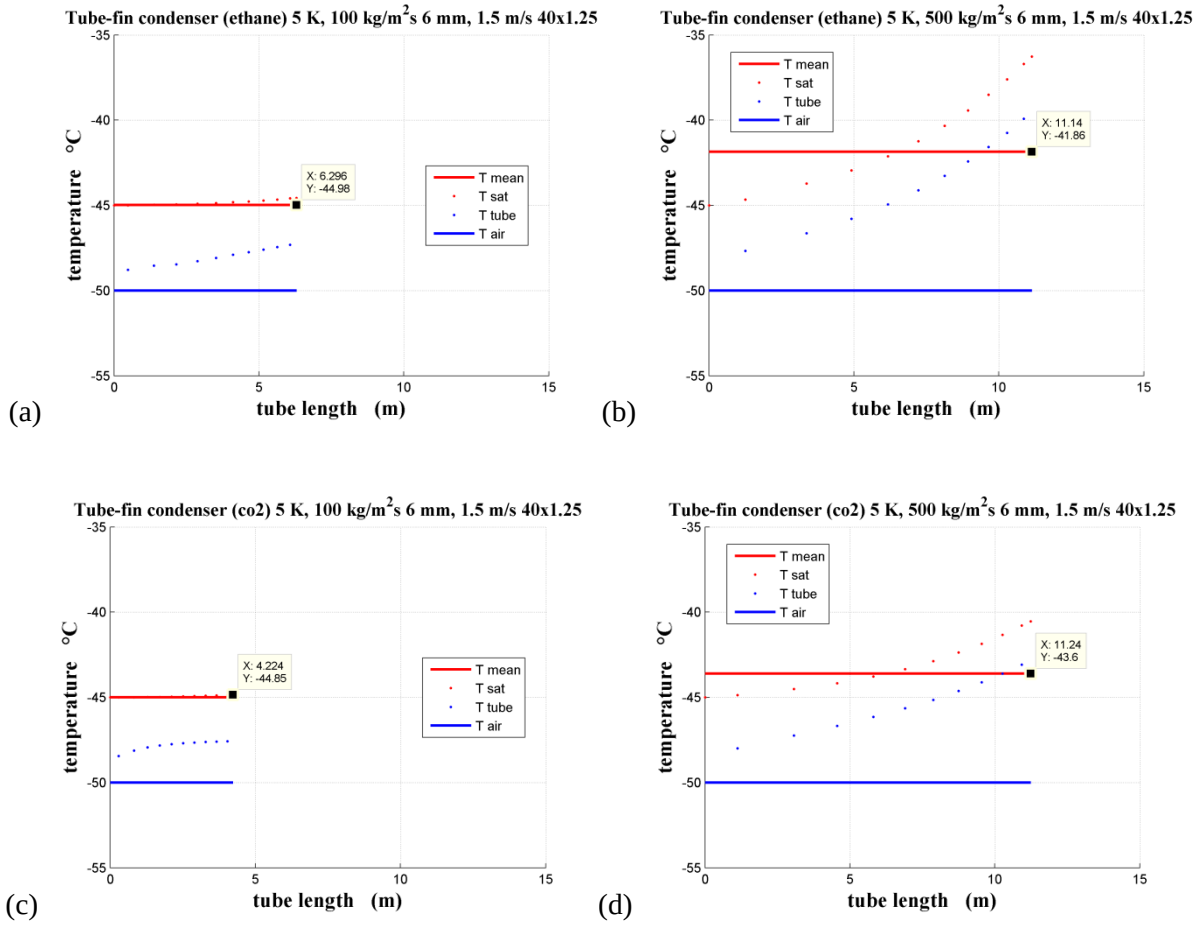

Fig. 3.9. Tube-fin condenser temperature glides at 100 and 500 kg/m^{2}s for ethane (a, b), and CO_2 (c, d).

Nominal configuration

The nominal standard tube-fin condenser configuration is set to:

- 6 mm diameter condenser tube
- 100 kg/s·m^2 condensing fluid mass flux
- 40 mm tube spacing
- 0.1 mm thick fins
- 5 mm fin spacing for optimal fan work (200 fpm)
- 2 mm fin spacing for minimum tonnes of copper (500 fpm)
- 1.5 m/s fan speed

3.3.2 Glaciothermal boiler configuration and operation

The principle measure of performance for a glaciothermal boiler tube is the overall Heat Transfer Coefficient (HTC). In this section we analyse the effect of various parameters on the ice slurry HTC. An analysis of the evaporative side of the boiler tube awaits successful identification of a specific nano-scale enhanced nucleate boiling surface.

Key variables affecting ice slurry HTC include: flow velocity, boiler tube diameter, and seed ice mass fraction. Brine salinity also has a marked effect.

Convective HTC's increase directly with ice slurry flow velocity and apparent heat capacity. Overall heat flux is also proportional to the Mean Temperature Difference (MTD) between the ice-slurry and the boiling working fluid. The need to maintain a high boiler temperature, and to avoid ice fouling on boiler tubes, dictates that a low MTD is desirable. For normal operation we set a modest MTD by default in defining a nominal boiler temperature of -5 °C. The boiling point temperature of the working fluid and the ice slurry flow velocity should be regulated such that the temperature of the copper tube wall never drops below the nominated maximum degree of supercooling ψ_{loop} which is typically ~ 2 K. Temperatures decrease downstream within the boiler tubes as the ice slurry freezes. The heat transfer coefficient varies with flow velocity and brine salinity as ice mass fraction increases, so the degree of supercooling must also vary along the full length of the boiler tube.

A more detailed analysis is now performed for each of the key parameters in turn.

Ice slurry flow velocity

Overall boiler HTC is plotted as a function of ice slurry flow velocity for boiler tubes of selected diameter, Fig. 3.10. Laminar flow conditions prevail at low velocities and the HTC increases sharply as the ice slurry transitions to turbulent flow. Turbulent flow conditions are not established in small diameter tubes until ice slurry flow velocity reaches around 3 m/s. At higher velocities small tubes produce the greatest HTC's. HTC increases with increasing ice slurry flow velocity for all tube sizes, but tapers off at higher velocities.

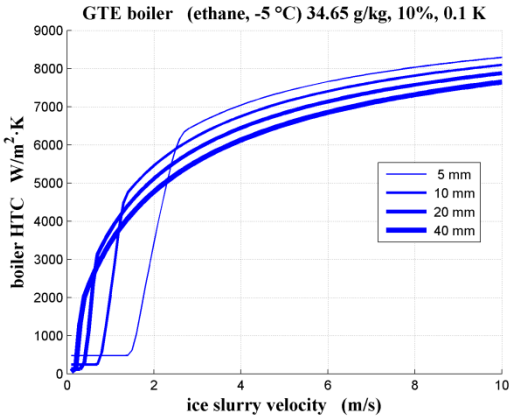

Fig. 3.10. Glaciothermal boiler heat transfer coefficients as a function of ice slurry velocity.

Boiler tube diameter

In Fig. 3.11, ice slurry HTC is plotted as a function of boiler tube diameter for various degrees of supercooling at fixed flow velocities of (a) 1.5 m/s and (b) 5 m/s. HTC's approaching 10 kW/m^2·K are evident for ice slurry under low supercooling at 1.5 m/s within boiler tubes smaller than 10 mm diameter. For faster flows at 5.0 m/s, HTC's greater than 30 kW/m^2·K occur under low supercooling but peak heat transfer requires tube diameters much less than 5 mm.

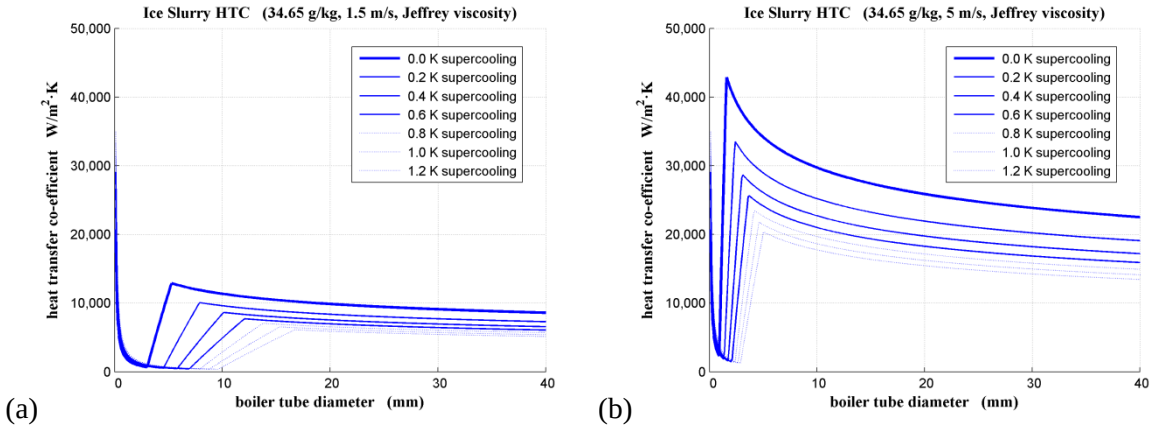

Fig. 3.11. Ice slurry HTC as a function of boiler tube diameter for various degrees of ice slurry supercooling at (a) 1.5 m/s and (a) 5.0 m/s ice slurry flow velocity.

Seed ice mass fraction

Overall boiler HTC is plotted as a function of ice seed fraction for selected nominal boiler tube diameters in Fig. 3.12. Heat transfer is observed to decrease with increasing seed ice mass fraction for all selected boiler tube diameters. For longer 0.5 K temperature glides the overall boiler HTC is seen to decrease rapidly for small 5 mm diameter boiler tubes due to rapid increase in brine salinity.

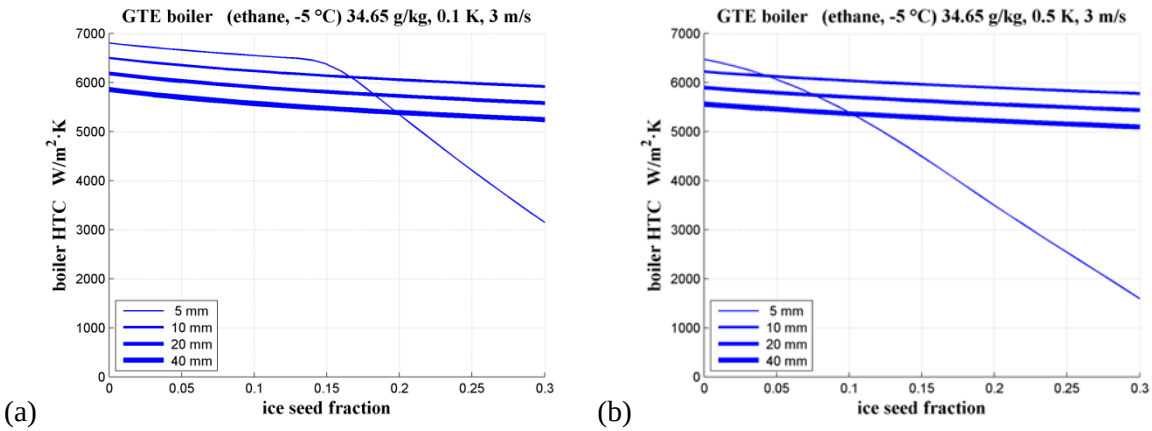

Fig. 3.12. Glaciothermal boiler heat transfer coefficients as a function of seed ice mass fraction.

Feed water salinity

Feed water salinity directly determines ice slurry salinity and has a marked effect on the heat transfer performance of a glaciothermal boiler. As ice crystal growth progresses over time the salinity of the remaining brine phase increases. This has the effect of reducing the apparent heat capacity of the ice slurry. In Fig. 3.13 the heat capacity and HTC of ice slurry are plotted as a function of ice slurry temperature for slurries of selected characteristic salinity. Apparent heat capacity falls dramatically for higher salinity brines (a), which is directly reflected in the ice slurry HTC (b).

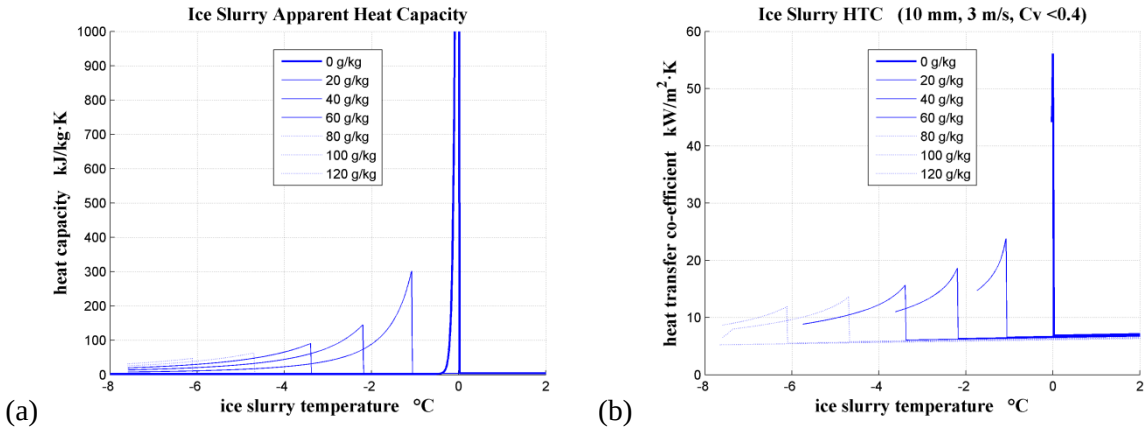

Fig. 3.13. Apparent heat capacity (a) significantly influences the ice slurry forced convective HTC (b).

Feed water temperature

Feed water temperature has little bearing on the operation of our basic glaciothermal engine, Fig. 3.14. The high heat flux achieved in a glaciothermal boiler is due to latent heat of freezing which means that the circulating ice slurry needs to be kept at the incipient freezing point. Warm feed water is introduced into the ice slurry mixture at a slower rate to avoid melting the seed ice fraction. A very

small improvement in boiler HTC is evident with increasing feed temperature. The marginal decrease in ice slurry salinity increases apparent heat capacity of the ice slurry and very slightly improves HTC.

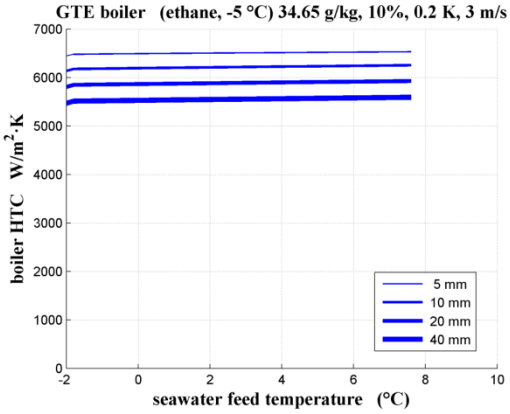

Fig. 3.14. Glaciothermal boiler tube heat transfer coefficients as a function of feed temperature.

Boiler tube cut length

The length of glaciothermal boiler tube needed to achieve a short 0.1 K temperature glide with 10% seed ice mass fraction is plotted as a function of ice slurry flow velocity for tubes of various selected diameters in Fig. 3.15. Required tube length varies widely with changing HTC as low speed ice slurry flow transitions from laminar to turbulent flow. For flow velocities higher than 3 m/s the required cut length of boiler tubing increases consistently for tubes of all sizes, with large diameter tubes needing longer lengths than small diameter tubes.

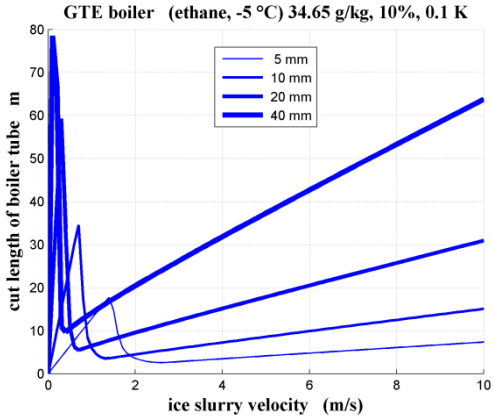

Fig. 3.15. Cut length of glaciothermal boiler tubes as a function of ice slurry flow velocity.

Ice slurry HTC increases with increasing ice slurry flow velocity, but increasing flow velocity also reduces the ice slurry residence time within a given fixed length of tube. Tube lengths need to be greater to allow sufficient time for the ice slurry to cool and achieve the target temperature.

Temperature glide along boiler tube

In this section we lower the boiler temperature to -10 °C in order to more clearly demonstrate control over ice slurry supercooling. In Fig. 3.16 we plot the temperature glide of ice slurry of 10% seed ice mass fraction flowing downstream from the boiler inlet, shown as red dots along the top of the four charts below. The solid red line represents the overall ice slurry MTD (heat source). The blue line along the bottom of each chart is the temperature of the evaporating working fluid (heat sink). The dotted line in between is the falling temperature of the boiler tube wall. All charts use the same scale axes to aid quick comparison. The evaporator HTC is deemed to be a constant 10 $kW/m^2 \cdot K$.

It is evident from this series of charts that short 0.1 K temperature glides (a, c) and high 5 m/s flow velocities (c, d) reduce the degree of ice slurry supercooling at the boiler tube walls. Low flow velocities (a, b) reduce the ice slurry HTC, thus increasing the ice slurry MTD needed to match the evaporator heat transfer. Long temperature glides (b, d) produce colder ice slurry with increased ice mass fraction and increased brine salinity. The more concentrated brine produces a lower apparent heat capacity that acts to further reduce the ice slurry HTC and increase the ice slurry MTD (b). Thus it is entirely possible to maintain low degrees of supercooling within the boiler tubes by regulating the flow velocity and length of boiler tube (c).

Fig. 3.17 depicts the same set of boiler operating conditions, except that the seed ice mass fraction has been increased to 30%. The temperature glides remain much the same in each case, except for (b) where the combination of low 1.5 m/s velocity and 0.5 K extended temperature glide combined with high initial seed ice fraction produces a very low ice slurry HTC and correspondingly large MTD.

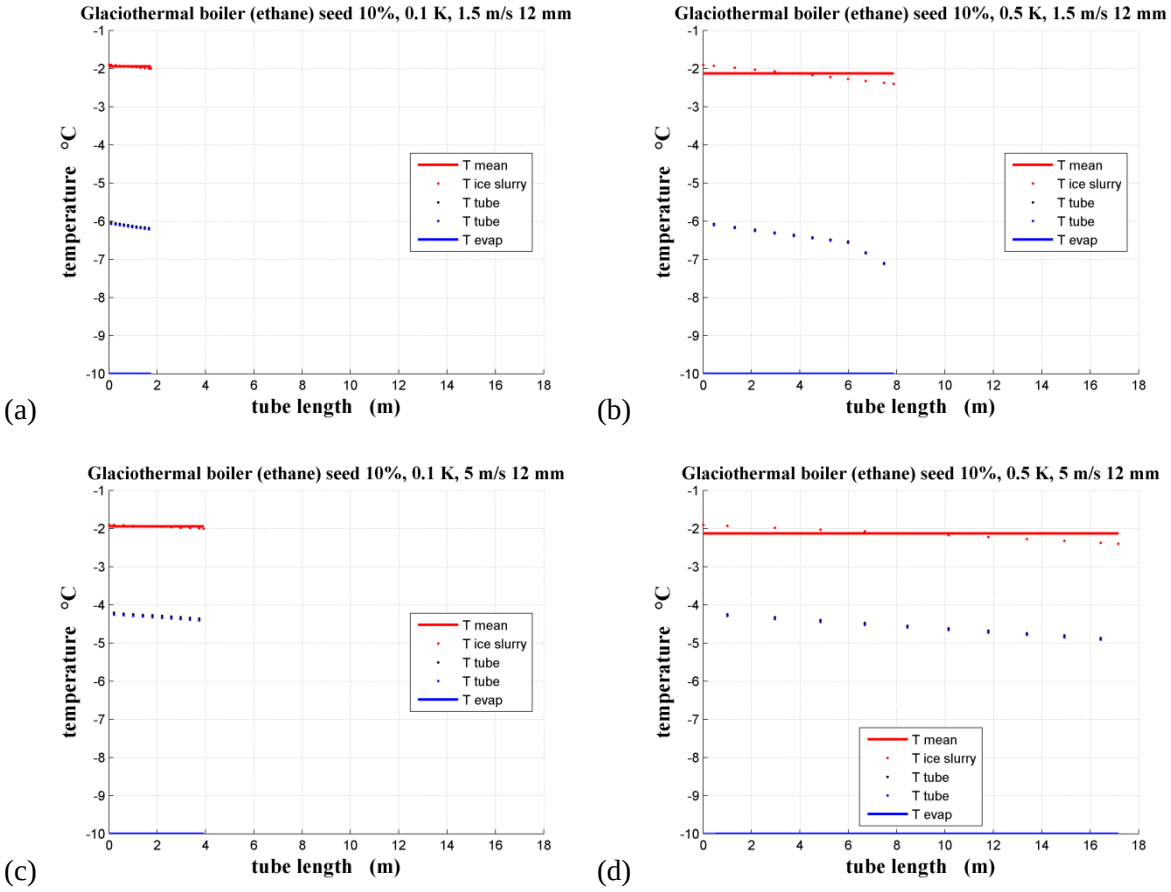

Fig. 3.16. 10% seed ice fraction. Glaciothermal boiler temperature glides of 0.1 and 0.5 K at 1.5 and 5 m/s.

Nominal configuration

Although there is a peak HTC per pump work point for low velocity ice slurry flow in very thin tubes we are obliged to maintain a much higher flow velocity to avoid ice plugging and ice-fouling problems. Based on the preceding analysis we nominate our standard ice-in-tube boiler settings to be:

- 10 mm diameter tubing
- 10% mass fraction of seed ice
- 5 m/s ice slurry flow velocity

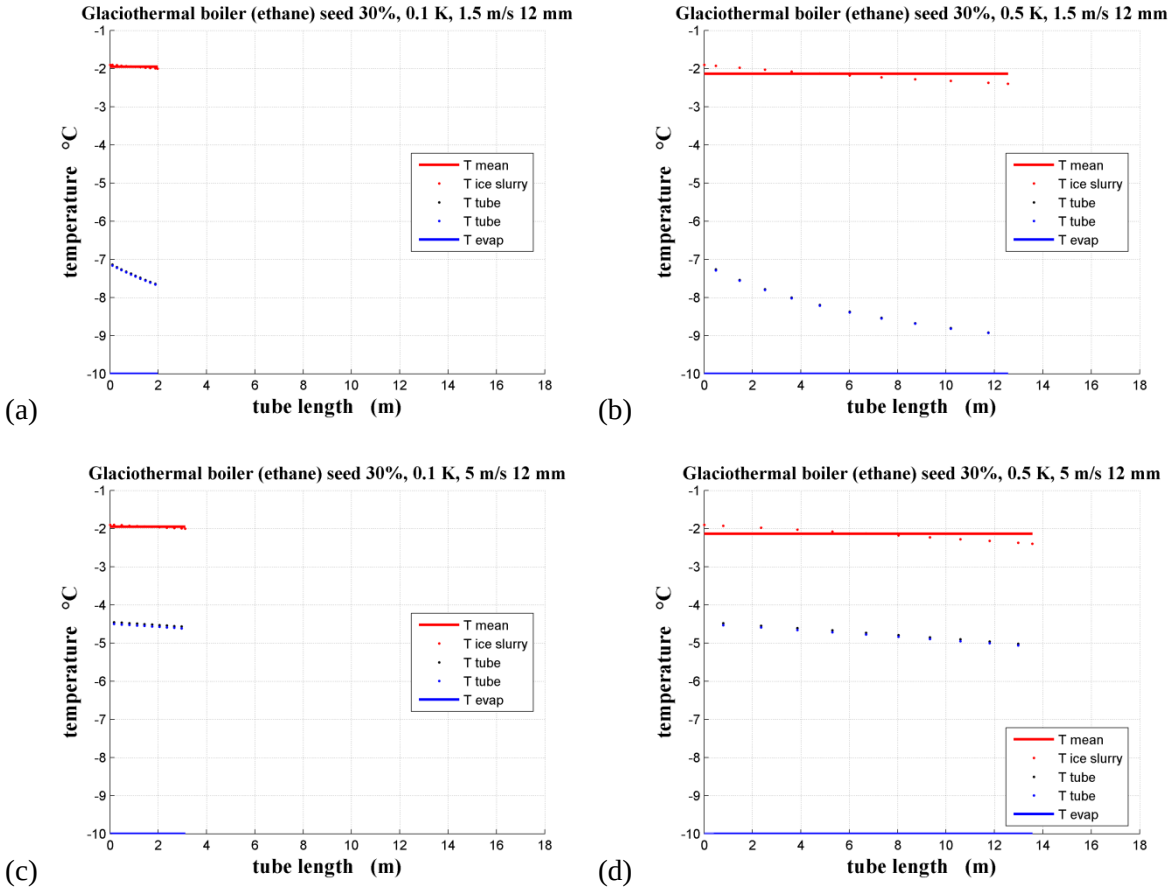

Fig. 3.17. 30% seed ice fraction. Short 0.1 K temperature glides (a, c) and high 5 m/s flow velocities (c, d) reduce the degree of ice slurry supercooling at boiler tube walls.

3.3.3 Turbine and generator

Fixed volume-ratio twin-screw expanders between 25 and 3,000 kW capacity are commercially available that achieve 60—90% adiabatic efficiency at a constant 1,500 or 3,000 rpm. A power output model has not been developed for any specific twin-screw expander. We have deemed a flat 70% isentropic efficiency for ORC-style working fluid expansion for the sake of simplifying the comparative heat transfer analysis.

3.3.4 Engine parasitic losses

Ice slurry pump

Ice slurry HTC varies markedly with flow velocity and with glaciothermal boiler tube diameter, Fig. 3.18 (a). Low HTC is typical of laminar flow at low speeds with a steep transition to high HTC values for turbulent flow. Small tube diameters and high ice slurry flow velocity combine to produce the greatest heat transfer. Although not shown, ice slurry pump work also increases according to the

ice slurry flow regime. The ratio of HTC per unit of ice slurry pump work suggests that peak ice slurry pumping efficiencies occur at quite low ice slurry velocities, typically $< 2\ m/s$, Fig. 3.18 (b). Ice fouling constraints, however, may dictate that higher velocities are required with a consequent increase in the relative parasitic losses from the ice slurry pump.

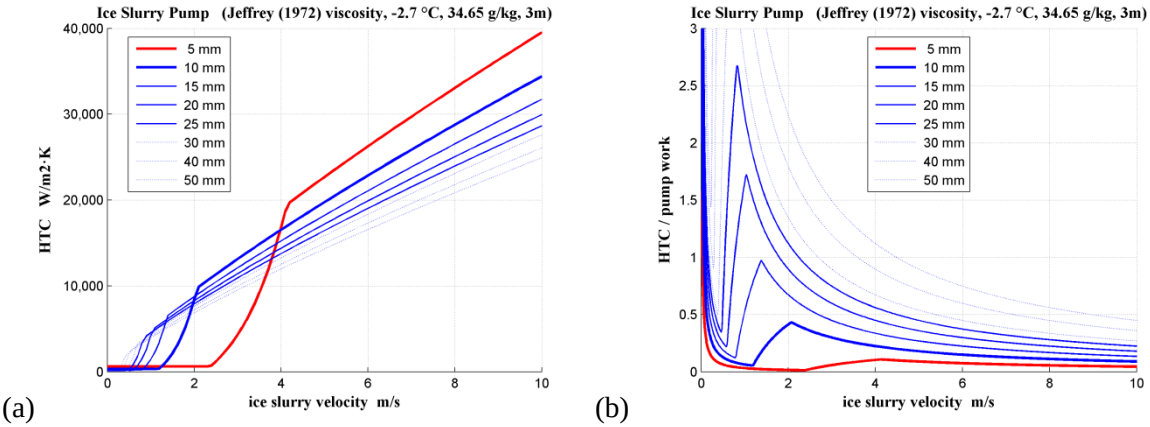

(a) (b)

Fig. 3.18. Ice slurry HTC (a) and HTC per pump work (b) as a function of ice slurry velocity.

Relative parasitic losses due to the ice slurry pump are plotted as a function of glaciothermal engine efficiency for selected ice slurry flow velocities in Fig. 3.19. For our previously stated nominal ice slurry flow velocity of $5\ m/s$ the pump losses remain well below 5% of nett engine power output across the full glaciothermal operating range. For nett engine efficiencies above ~4% pump losses fall progressively below 1%. Ice slurry pumping losses only become prohibitive for engine nett thermal efficiencies below about 2% if very high ice slurry flow velocities of 10 m/s are needed for hydro-scraping. Data relates to basic 250 kW glaciothermal engine with stated nominal boiler and condenser.

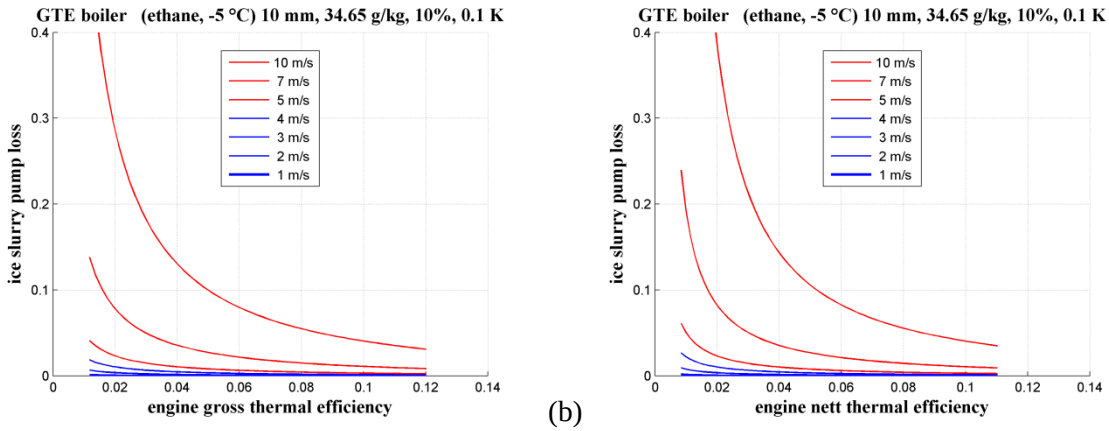

(a) (b)

Fig. 3.19. Ice slurry pump parasitic losses as a proportion of (a) gross and (b) nett engine efficiencies for selected fan speeds between 1 and 10 m/s.

Condensate injection pump

The key factor affecting condensate injection losses is the delta-P to condensate density ratio, where delta-P is the working pressure difference between the condenser and boiler, Fig. 3.20. Ethane requires somewhat greater injection pump work than CO_2 across the glaciothermal temperature range.

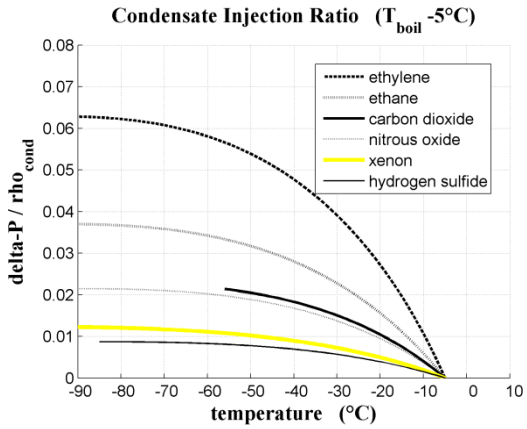

Fig. 3.20. Condensate injection ratios demonstrate the relative pumping effort needed for various fluids.

Condenser fan

Relative parasitic losses due to the condenser fan are plotted as a function of glaciothermal engine efficiency for selected air flow velocities in Fig. 3.21. For our previously stated nominal fan speed of 1.5 m/s the fan losses remain well below 5% of nett engine power output across the full glaciothermal operating range. For nett engine efficiencies above ~4% fan losses fall progressively below 1%. These data also relate to the basic 250 kW glaciothermal engine running with the stated nominal boiler and condenser configurations.

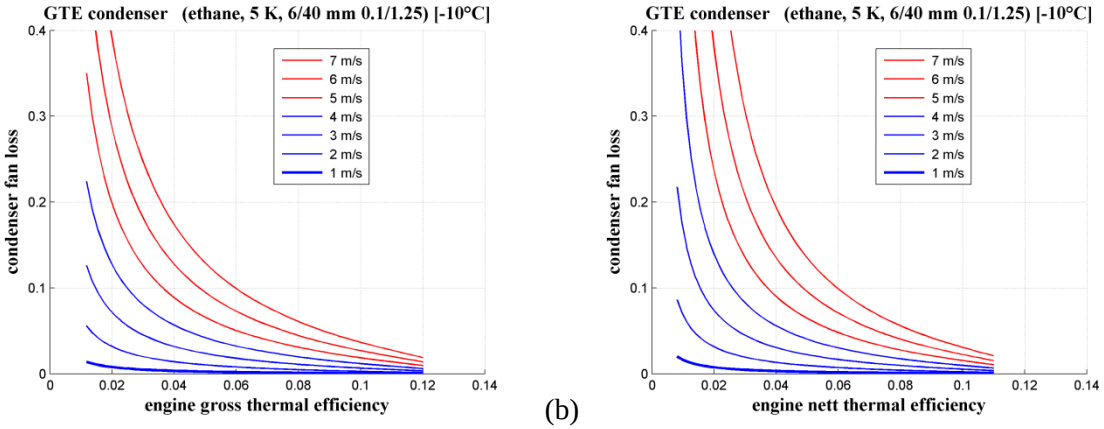

(a) (b)

Fig. 3.21. Condenser fan parasitic losses as a proportion of (a) gross and (b) nett engine efficiencies for selected fan speeds between 1 and 7 m/s.

3.4 Performance curves and device dimensions

Overall glaciothermal engine performance has been calculated across the full range of ambient air temperatures for a basic engine running the nominated standard boiler and condenser configurations, Fig. 3.22. The results show relatively high thermal efficiency given the modest temperature difference between cold air and water. This is possible because the temperature drop across both the boiler and condenser heat exchangers is so small. Latent heat transfer in each case permits very close approach temperatures without the pinch points that occur with some other types of heat exchanger.

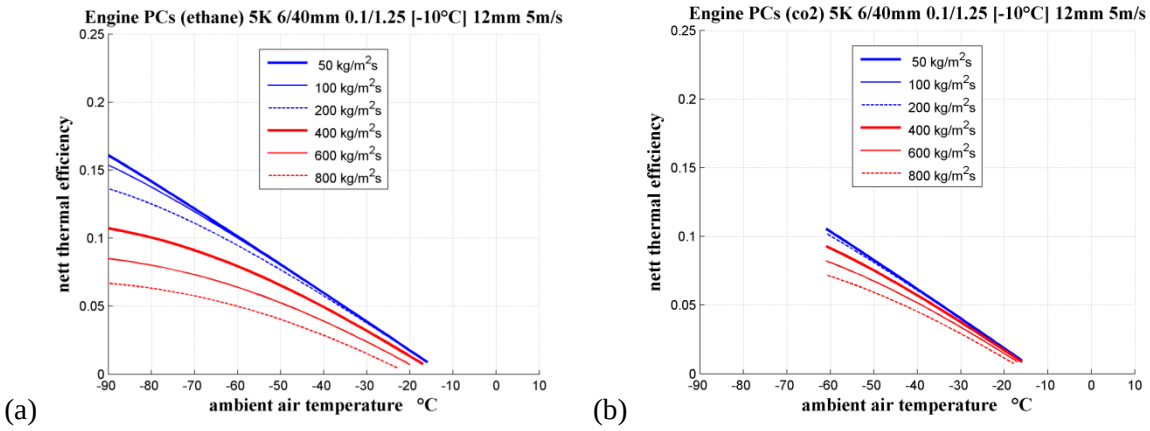

Fig. 3.22. Basic glaciothermal engine performance curves as a function of ambient air temperature and working fluid mass flux at the condenser running ethane (a) and CO_2 (b) at 70% isentropic efficiency and 80% mechanical to electrical conversion efficiency).

A conspicuous feature of the performance curve in Fig. 3.22 (b) is the truncated operating range corresponding to the freezing point of CO_2. The triple point temperature and pressure of CO_2 are -56.558 °C and 5.1796 bar respectively. Operation of the CO_2 condenser below about -60 °C requires that the working fluid mass flow rate be carefully regulated relative to the condenser heat flux to manage the precipitation of solid CO_2 (dry ice).

3.5 Critical operating points

3.5.1 Maximum nett thermal efficiency

Ethane remains liquid all the way down to -90 °C, so the condenser in Fig. 3.22 (a) is able to operate across the full range of extreme ambient winter temperatures. The maximum nett thermal

efficiency of the glaciothermal engine does not peak, but rather continues to increase with increasing cold. Maximum efficiency corresponds to the coldest day in winter.

For the CO_2 condenser, however, the maximum efficiency peak occurs for ambient air temperatures around -60 °C. In Fig. 3.22 the nominal temperature difference χ_{cond} between the ambient air and the chilled condensate leaving the condenser is arbitrarily set to 5 K. Higher values are possible to allow operation at air temperatures below -61 °C but the higher the MTD for a given mass flow rate, the colder the condensate.

The mass flux within each tube would need to be continually increased to keep up and the pressure drop across the condenser would rise as a result. The overall nett thermal efficiency would fall away as the condenser suction pressure drops and progressively stalls the engine. This approach is problematic; not least because the geometry and scaling of the condenser is fixed.

A better way to manage a CO_2 condenser at air temperatures below -61 °C is to throttle back the air flow instead. Reducing the fan speed reduces the mass flow rate of air and will cause the exhaust temperature of the air flow to rise. Engine performance is still limited by the same CO_2 condensate discharge temperature but condenser function is maintained and fan work is reduced.

3.5.2 Maximum power output

For a glaciothermal engine of fixed size, maximum power output is a function of the pressure difference across the expander and the working fluid volumetric flow rate. Pressure difference is a direct function of the highly variable ambient air cold sink temperature. There is little freedom to vary the boiler temperature because the heat source temperature is fixed by the ice slurry freezing point, and, although the working fluid boiling temperature can be regulated within a short range, ice fouling constraints limit the degree of supercooling on the ice slurry side to only a couple of degrees. Pressure difference also varies between working fluid species with CO_2 producing higher pressures than ethane.

For a given pressure difference, fluid volume flow is predominantly a function of the rotational speed of the turbine. The normal mode of operation for high speed twin screw turbines is to run at a

constant 1,500 or 3,000 rpm to permit synchronisation with an AC bus. Inlet geometry and volume ratios of individual turbine models are optimised accordingly. Power output of an operational glaciothermal engine is generally constant for a given condenser temperature. The rate of supply of working fluid to a constant speed rotor can be regulated, however, to vary the torque and thus control the power output of the generator.

Results of laboratory testing of twin screw turbines demonstrate a typically flat power curve as a function of rotation speed [81], with the power output varying largely as a function of condenser temperature. For geothermal power generation the air sink temperature varies over a small range relative to the hot water / ambient air thermal dipole, and the ambient air temperature never gets close to the hot water temperature. For glaciothermal power, however, the thermal dipole can close over completely as air temperatures approach or exceed the feed water temperature. The turbine pressure ratios for a glaciothermal engine thus vary across a wide range.

Power output drops in response to under- or over- expansion of working fluid passing through a twin screw expander. Maximum power output occurs when outlet to inlet vapor density ratio approaches the fixed volume ratio of the expander. Ground source thermal storage may be required to moderate the extreme ambient temperature range experienced at interior icesheet sites. Hot swapping between turbines with different volume ratios may also be a practical way to maintain power output between the seasons.

The main objective of this thesis is to conduct a feasibility analysis rather than present a design model, so a specific twin screw expander power model has not been developed thus far.

3.5.3 Zero power output

The zero power point notionally occurs when the temperature difference between the cold ambient air and freezing ice slurry retreats below the combined boiler and condenser MTD's. For the engine performance curves of Fig. 3.22, minimum power output commences as the air temperature first drops below -15 °C to -23 °C depending on the nominal boiler temperature and working fluid mass flux. Such sharp cut-off temperatures are an artefact of the modelling algorithm. In reality the

curves will taper towards zero as the actual MTD's fall back to nothing. For practical purposes though it is reasonable to deem the zero point as the sum of the nominal MTDs.

3.6 Conclusions

Regarding operation of the ice-in-tube boiler, it is apparent from this analysis that short boiler tubes and high ice slurry flow velocities can be used to reduce the degree of supercooling experienced at the boiler tube walls and hence decrease the risk of ice fouling. 10% seed ice mass fraction appears to be appropriate. Higher seed ice fractions must be avoided if long boiler tubes are allowed to operate at low flow velocity.

Evaporator HTC appears to be the main factor that limits the overall HTC of a glaciothermal boiler. New nano-scale enhanced boiling surfaces are sought that can match the ice slurry HTC on the opposite side of the boiler tube. Evaporator MTD's remain large in the absence of high performance nano surfaces. This invariably reduces the boiler temperature and is undesirable for a compact glaciothermal boiler.

For the condenser there are no operational settings to optimise. Performance is determined only by the fixed tube-fin geometry and sizing of the installed condenser panel. Fin HTC is very low compared to the condensing film HTC and is the limiting factor controlling overall condenser HTC. External laminar film condensation on horizontal smooth tubes should be investigated in conjunction with secondary refrigerant atmospheric droplet sprays. This type of condenser may prove more affordable if less convenient than the all-copper tube fin condenser that we have modelled.

The key environmental and geographic factors that impact the performance of a glaciothermal engine and determine placement relate to the heat source and heat sink. They are for the heat source:

- Feed water salinity (seawater, meltwater or a diluted mixture of both)
- Distance to feed water source
- Elevation relative to sea level

And for the heat sink:

- Ambient air temperature
- Barometric pressure

The physical bulk of the condenser typically dictates where a glaciothermal engine should be sited. Large volumetric air flows need to be accommodated. Local feed water can be pumped in. Sites with the best potential for glaciothermal power therefore occur where cold air and secure feed water sources are located nearby to one another.

Ideal sites are those subject to very cold year round air temperatures, especially below -40 °C, with access to low salinity feed water sources at similar elevation. Depending on ice slurry flow performance with pure water, freshwater may be preferable to seawater. Except for one or two notable geothermal springs, warm ambient water temperatures are rare in the polar environment and of little importance to our analysis. Local meltwater and warm surface water temperatures in summer invariably correspond to warm air temperatures which prevent the use of non-augmented glaciothermal power at that time of year anyway.

In practice, glaciothermal power at shoreline coastal sites is only possible during the depths of winter and thus derives largely from seawater at the incipient freezing point of sea-ice.

Chapter 4 – Potential Year-Round Power Output of the Basic Glaciothermal Engine

This chapter describes the ambient environment and modelling of meteorological data. The power generation capacity of the basic engine is assessed for year round operation at selected Antarctic sites. The inability to generate power during summer is a defining characteristic.

4.1 Introduction

Based on the performance criteria identified in Chapter 3 it is now possible to search for prospective glaciothermal energy provinces. Prospective sites occur where frigid air masses meet liquid water. High elevated regions deep within the continental interior are remote from the warming effects of the ocean and thus sustain the coldest temperatures. A frigid ground level air layer is cooled due to infrared radiation escaping from the surface. Oceans of cold dense air pool atop the flat lying icesheet ridges and high altitude plains, Fig. 4.1. These begin to move slowly then gather pace before converging and spilling down to the coast as powerful katabatic streams, Fig. 1.2 [13]. Substantial heat sink capacity exists at high altitude sites adjacent to these transitional katabatic air masses.

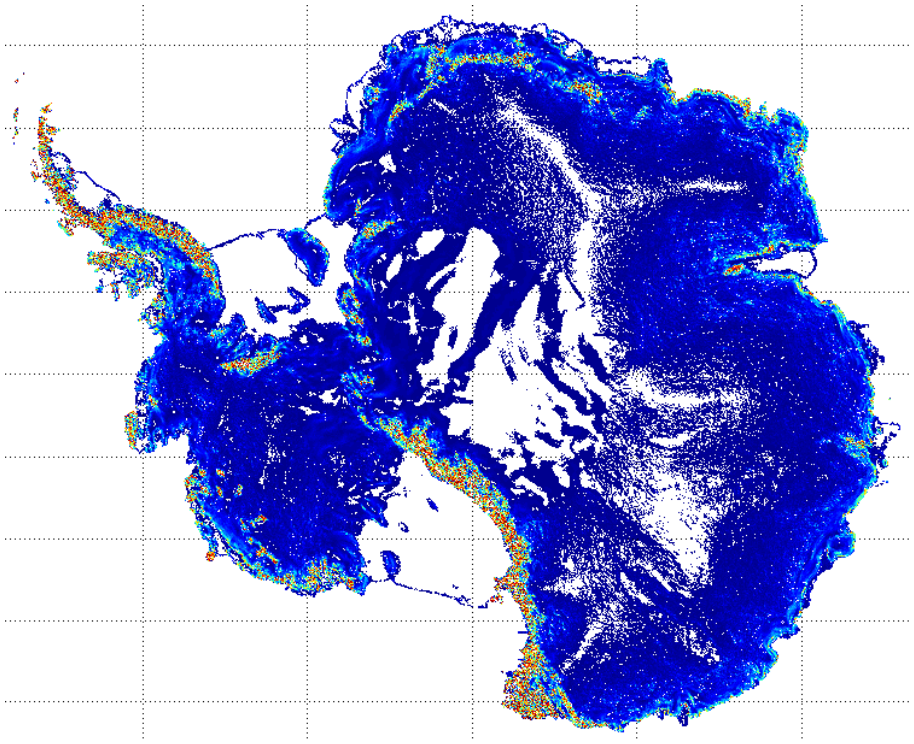

Fig. 4.1. Surface gradient map of Antarctica. Ice surfaces sloping at less than 0.2 m/km appear as white. **Constructed using *Radarsat Antarctic Mapping Project Digital Elevation Model (RAMPDEM)* data [98].**

Very cold air masses also form at lower level in sheltered areas on or above the ice shelves (and appear as white or lightest grey between the warmer katabatic streams in Fig. 1.2). Coastal sites are markedly warmer due to their low elevation and proximity to liquid surface water. Glaciothermal energy might be extracted by pumping seawater a short distance inland or by utilising local meltwater as a potential heat source. The large ice-shelves extending hundreds of kilometres inland offer access to unlimited seawater immediately below, Fig. 4.1.

Whereas the temperature and strength of cold surface winds vary markedly from place to place and season to season, seawater temperatures not surprisingly remain quite uniform year round. Only minor temperature and salinity changes occur due to alternate sea-ice freezing and surface warming. Seawater density drives overturning of surface waters. Cold water is denser than warm water however salinity plays the dominant role. The maximum density of freshwater occurs at around 4 °C, Fig. 4.2 (a), however, for seawater with salinity around 35 g/kg maximum density is not achieved until the incipient freezing point of -1.9 °C is reached, Fig. 4.2 (b).

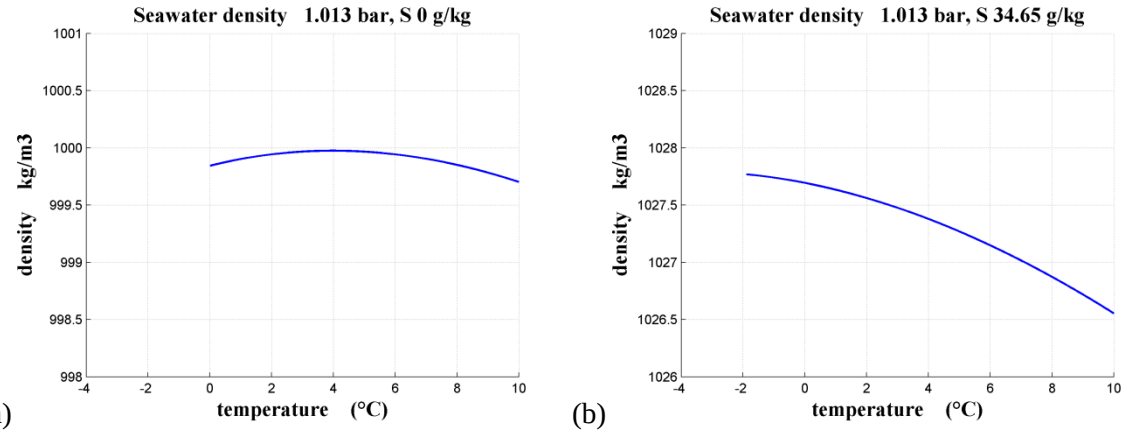

(a) (b)

Fig. 4.2. Density curves for (a) freshwater and (b) ice-shelf water (ISW). Derived from TEOS-10 data [99].

Stratification of the seawater column occurs during the polar winter as cold dense brines are expelled from freezing sea-ice and sink to the bottom. Surface waters flow toward the coast from the vicinity of the Antarctic divergence and replenish the brines running downslope to feed the Antarctic bottom water circulation, Fig. 4.3 [100]. Seawater close in to the Antarctic shoreline is generally characterised as ice shelf water (ISW) and has uniform temperature and salinity, Fig. 4.4. This polar

seawater remains at freezing point year round, except for shallow surface waters that may warm as high as 3 or 4 °C for brief periods in summer after the sea-ice has thawed.

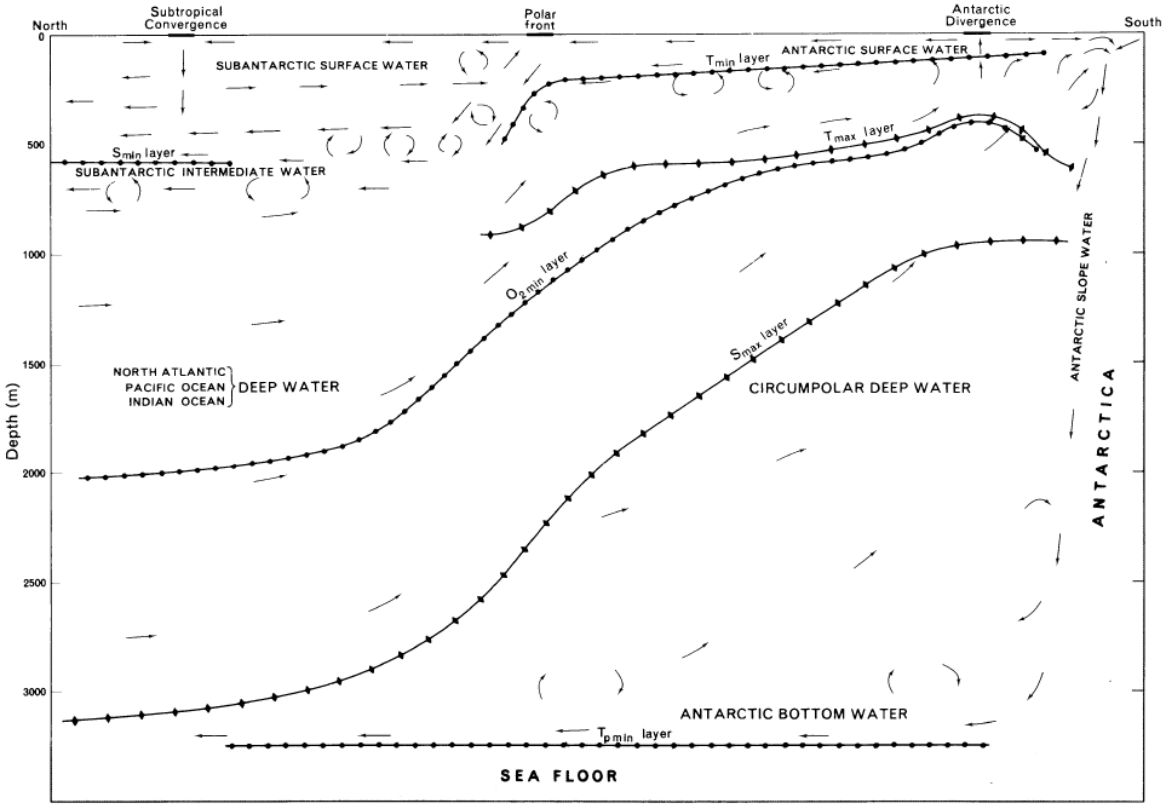

Fig. 4.3. Southern Ocean circulation. Surface seawater flows to the coast from the Antarctic divergence. **Drawing taken from Foldvik and Gammelsrød (1988) [100]**.

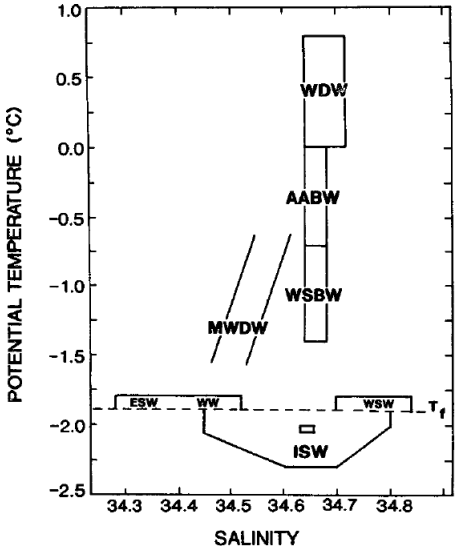

Fig. 4.4. Ice shelf water (ISW) of uniform salinity around 34.65 g/kg. **Drawing taken from Toggweiler and Samuels (1995) [101]**.

Wind conditions are incidental to the operation of a basic glaciothermal engine because tube-fin condensers rely on fan-forced air circulation. Wind speed and direction are only of interest if finned tube condensers are used instead. Soft snow surfaces and snow drifts may hinder operation.

Secure hard surfaces are required to mount engine components and provide reasonable access for operation and maintenance. On the icesheet, hard blue ice surfaces are ideal. Wind glazed surfaces may also meet the requirements for meltwater storage and/or ground-source thermal storage, Fig. 4.5.

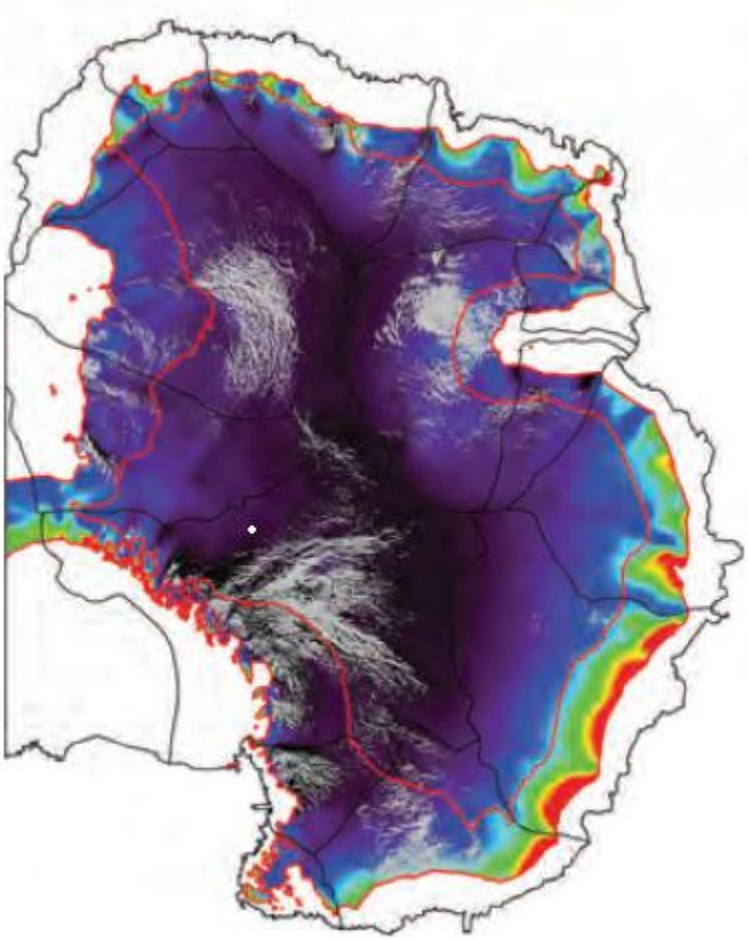

Fig. 4.5. Wind glaze areas (grey) on East Antarctic plateau. ***Taken from Scambos et al (2012) [102].***

4.2 Modelling of ambient conditions for glaciothermal engine

Existing published datasets are used to model meteorological and seawater conditions. Simple statistical models were constructed to represent seawater temperature and salinity data. Statistical reduction of the closely inter-related bimodal temperature and wind speed distributions was not attempted. Processed data from nominated type locations was considered representative instead.

4.2.1 Ambient air temperature data processing

Meteorological data including ambient air temperature, wind speed and humidity is available from an extensive network of Automated Weather Stations (AWS) around Antarctica and Greenland. 10 and 30 minute datasets [1, 103] were used to construct temperature profiles for selected sites, Fig. 4.6, before constructing 5 year composite air temperature calendars, Fig. 4.7, as described below:

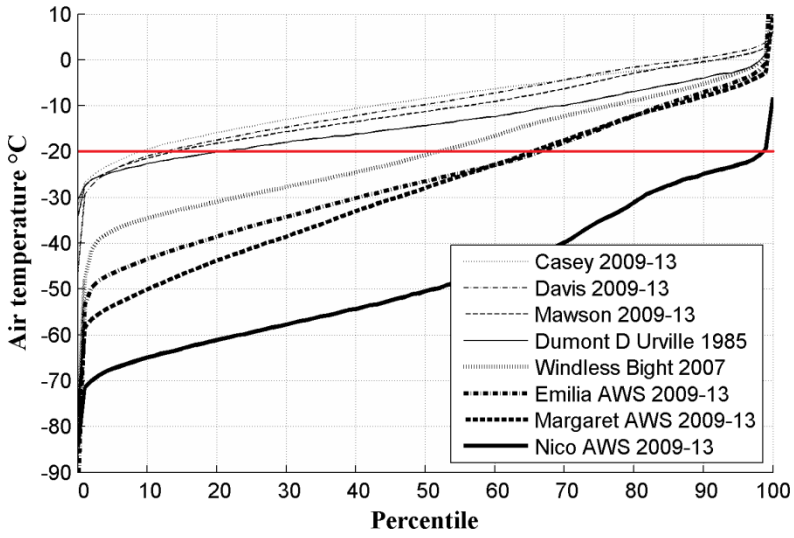

Fig. 4.6. Year round air temperature percentiles for selected Antarctic stations. **Constructed from *Australian Bureau of Meteorology* and *Antarctic AWS Network* meteorology datasets [1, 103]**.

Method

1. Import and collate meteorological data from BoM and UW-M web sites.
2. Determine relative offset between local time zone and UTC code in the data.
3. Filter out any incomplete or suspect data points.
4. Plot air temperature histograms and percentile curves, Fig. 4.6.
5. Process data into 10 minute daily series (3 hourly data carries forward).
6. Plot full year 10 minute ambient air temperature calendars, Fig. 4.7.

Daily temperature variations are only apparent in the temperature calendars during the summer months at coastal sites. Frigid interior sites reflect mainly seasonal variations.

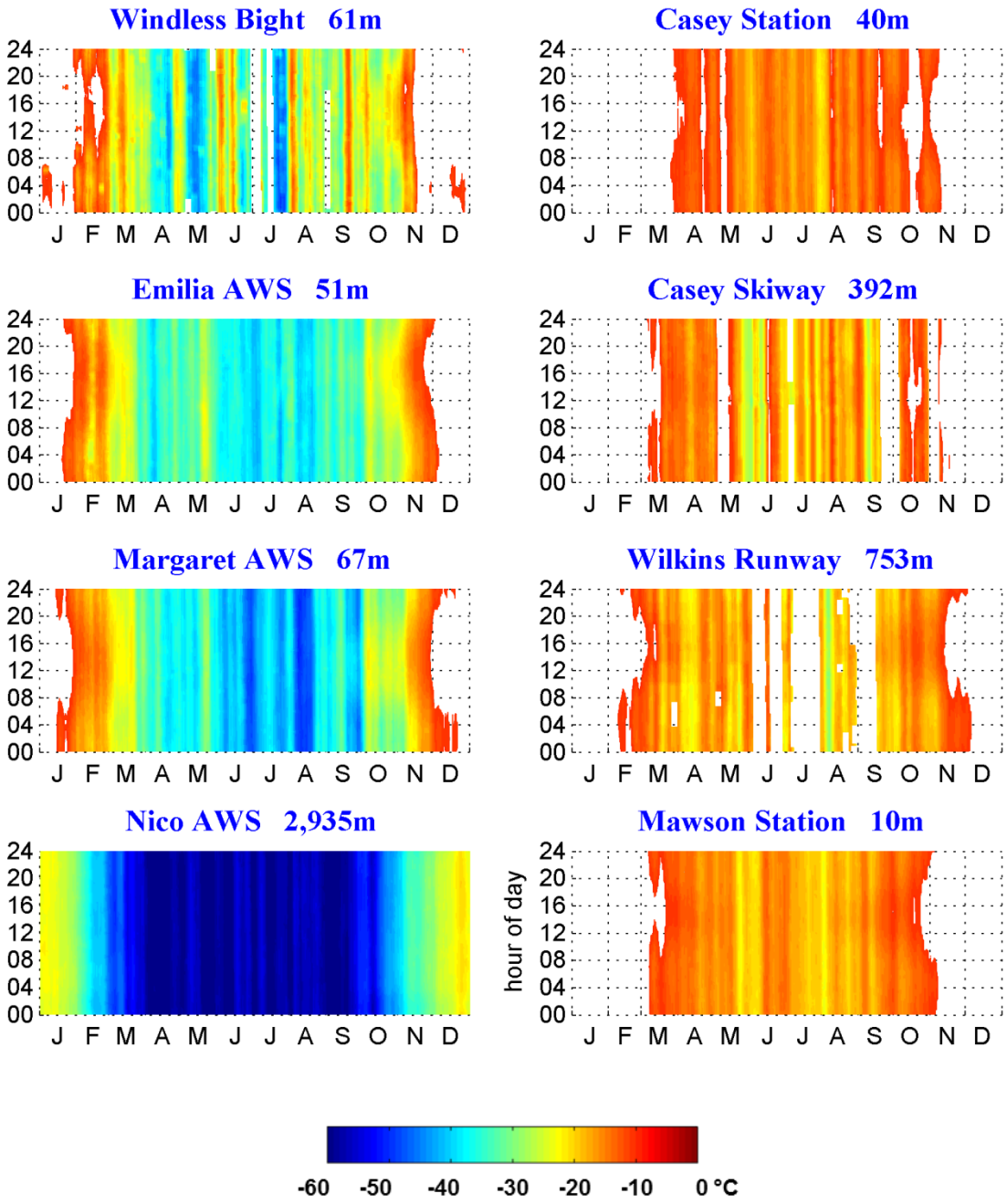

Fig. 4.7. Five year mean ambient air temperature calendars for selected Antarctic sites. Warm summer temperatures truncated above -10 °C appear as white. Missing data during cold winter months also appear white. **Constructed from *Australian BoM* and *Antarctic AWS Network* meteorological datasets [1, 103].**

4.2.2 Ambient seawater temperature modelling

Empirical correlations for year round seawater temperature and salinity were obtained using polynomial regression from measurements made in the vicinity of coastal Antarctic stations by the Australian Antarctic research vessel *MRV Aurora Australis*. Tracks of selected voyages between 2009 and 2014 are shown in Fig. 4.8, with locations of various research stations shown relative to Hobart.

Method

1. Collate voyage track seawater data from AAD – CAASM web data, Fig. 4.8.
2. Filter data by proximity to each Antarctic port, Fig. 4.9, 4.10.
3. Plot seawater temperature and salinity across the full calendar year, Fig. 4.11.
4. Process raw 1 minute data into a single mean daily data point
5. Filter seawater data set to remove any data points at or below the freezing point
6. Find best fit curves for warm summer seawater salinity and temperature, Fig. 4.12, 4.13.
7. Use IFP intercept dates to define the start and end of the sea-ice season
8. Write MATLAB routine to provide T_{sea} and S_{sea} values across the year for input to simulator

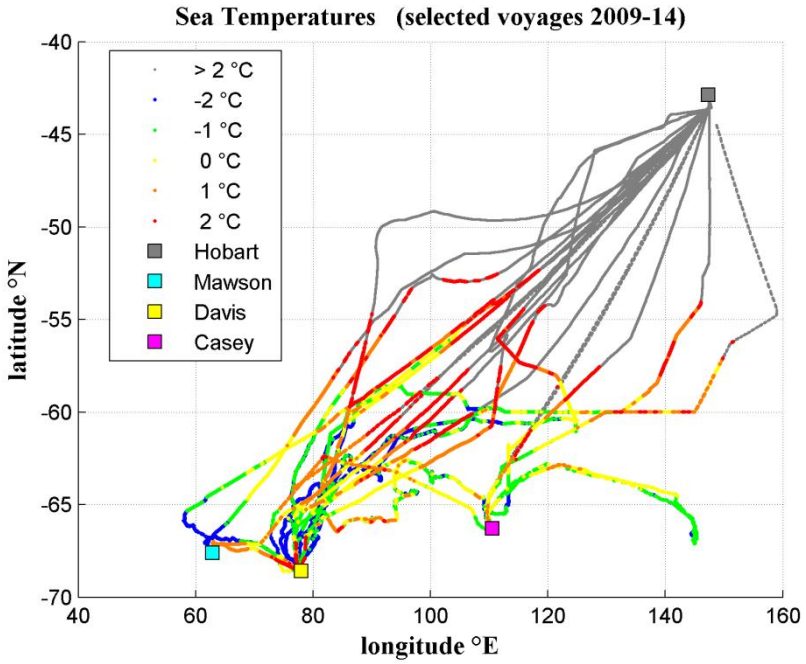

Fig. 4.8. Seawater surface temperature. **Constructed from Aurora Australis *Season Voyage Track and Underway Data* datasets 2009-14 [104]**.

Seawater temperatures are automatically recorded every minute from port and starboard sensors on board the *MRV Aurora Australis* ice-breaker. Data logged with the vessel in port in Hobart is clearly distinguishable from colder open water and sea-ice passages in the Southern Ocean, Fig. 4.9.

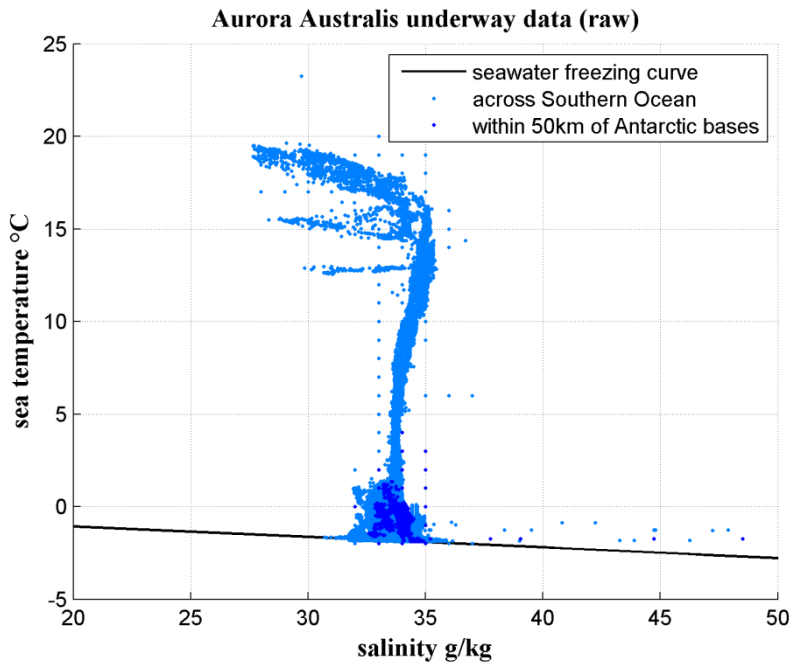

Fig. 4.9. Seawater surface temperature and salinity. **Constructed from Aurora Australis *Season Voyage Track and Underway Data* datasets 2009-14[104]**.

Older thermometers record temperature to the nearest degree Celsius, but more recent sensors provide much greater precision. The higher resolution data clearly identify the coastal Ice Shelf Water (ISW) within a 50 km radius of the station ports, Fig. 4.10. Lower salinity supercooled water is also evident below the seawater freezing curve.

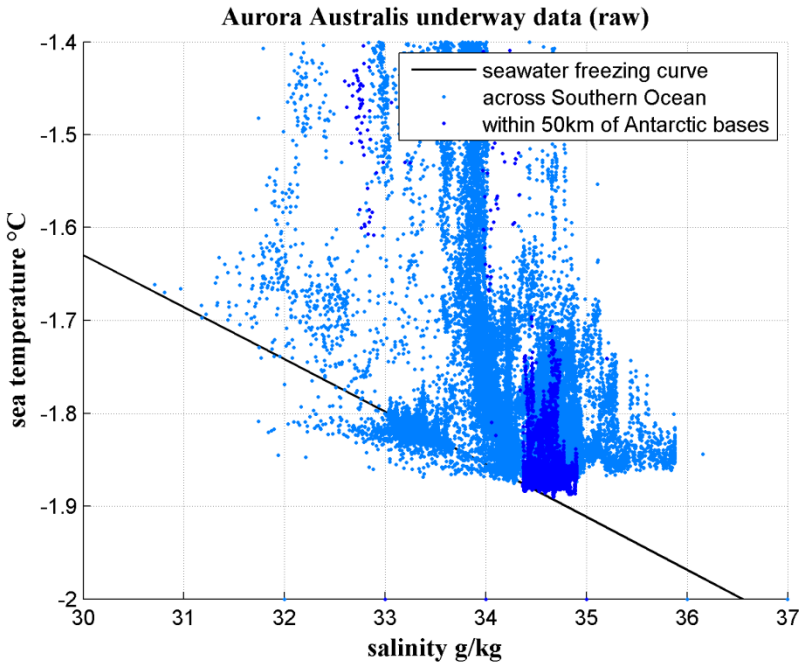

Fig. 4.10. Seawater temperature and salinity. Ice shelf water (ISW) 34.65 g/kg shown in dark blue. **Constructed from Aurora Australis *Season Voyage Track and Underway Data* datasets 2009-14 [104]**.

The 1 minute seawater temperature and salinity data are grouped into daily aggregates and plotted against the calendar day of the year, Fig. 4.11 and 4.12, respectively. Voyages are only made between October and March due to the extensive sea-ice and fast ice that surrounds the continent during winter. The seawater temperature is assumed to be at freezing point right throughout the winter months. Early voyages pick their way through the sea-ice and record seawater temperatures at the incipient freezing point. Only over summer do the coastal surface water temperatures rise above zero.

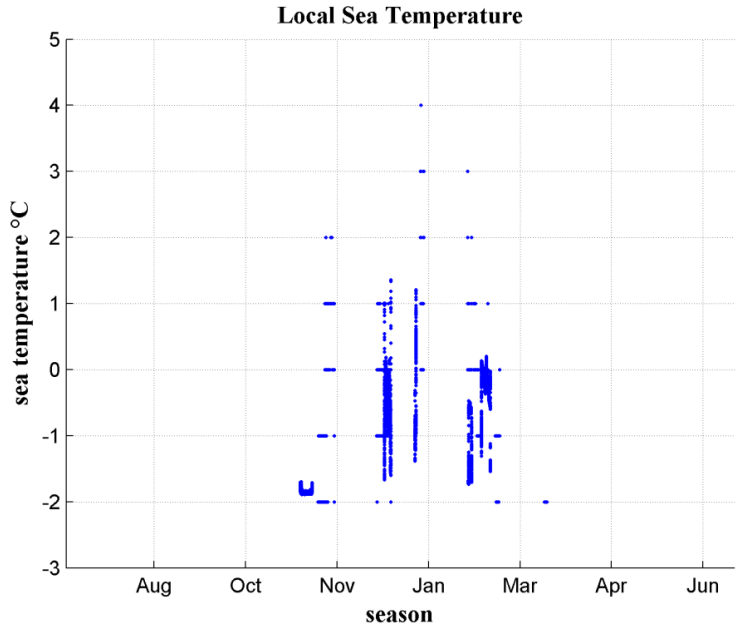

Fig. 4.11. Daily aggregates of 1 minute seawater temperature data within 50 km of Antarctic ports.

A simple model was constructed based on the aggregated data that estimates warm coastal seawater temperature and salinity on a given calendar day in summer. The MATLAB polyfit tool (cftool) was used to find polynomial coefficients of best fit curves for seawater salinity, Fig. 4.12:

$$S = 35.47 - 0.024d + 0.00007102d^2 \tag{4.1}$$

and seawater temperature, Fig. 4.13:

$$T = -4.508 + 0.08786d - 0.0004245d^2 \tag{4.2}$$

where d is the day of the year.

For the rest of the year, salinity values are deemed to be at the nominal salinity value for ISW of 34.65 g/kg, Fig. 4.12. Resulting salinity estimates are input to the temperature modelling algorithm.

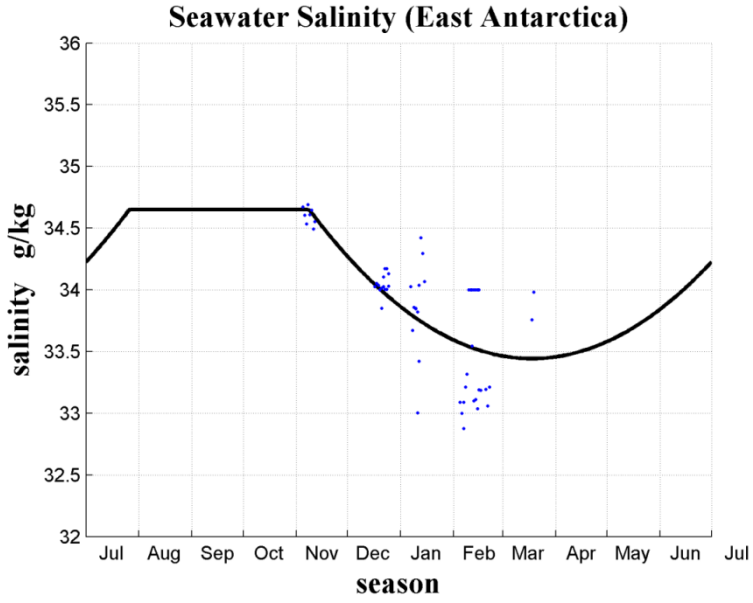

Fig. 4.12. Year round seawater salinity estimate using polynomial regression truncated by sea-ice.

Temperature estimates are truncated at the incipient freezing point for seawater of equivalent salinity, Fig. 4.13. The above models are deemed to apply to exposed surface waters along the full length of the East Antarctic coast. Seawater beneath the Ross Ice Shelf is not exposed to solar radiation so the temperature is assumed to remain close to the freezing point year round.

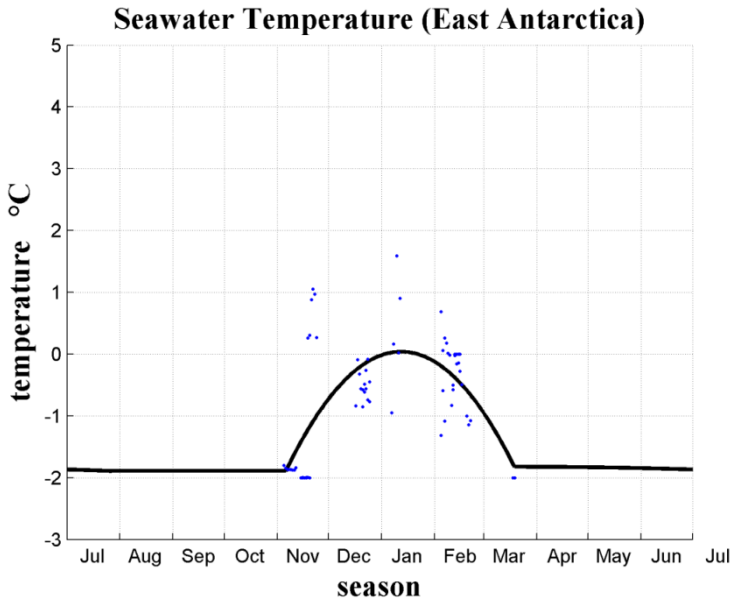

Fig. 4.13. Year round seawater temperature estimate using polynomial regression truncated by sea-ice.

4.3 Year round glaciothermal engine performance

4.3.1 Potential glaciothermal power locations

Based on the siting requirements identified in Chapter 3, we have selected three geographical regions to represent potential glaciothermal power applications in Antarctica, Fig. 4.14. Casey, Davis and Mawson stations are all typical of mild coastal sites. Windless Bight, Emilia and Margaret AWS's are situated on or near to the Ross Ice Shelf. Clean Air and Nico AWS's are indicative of elevated interior sites near to the South Pole. Sites representative of Ross Ice Shelf and the East Antarctic coastline are assumed to be directly over or adjacent to liquid seawater. Frigid interior sites are at high elevation and require seawater to be pumped in. Ambient air temperatures contrast significantly between these regions. The year round meteorological conditions for each are discussed in turn.

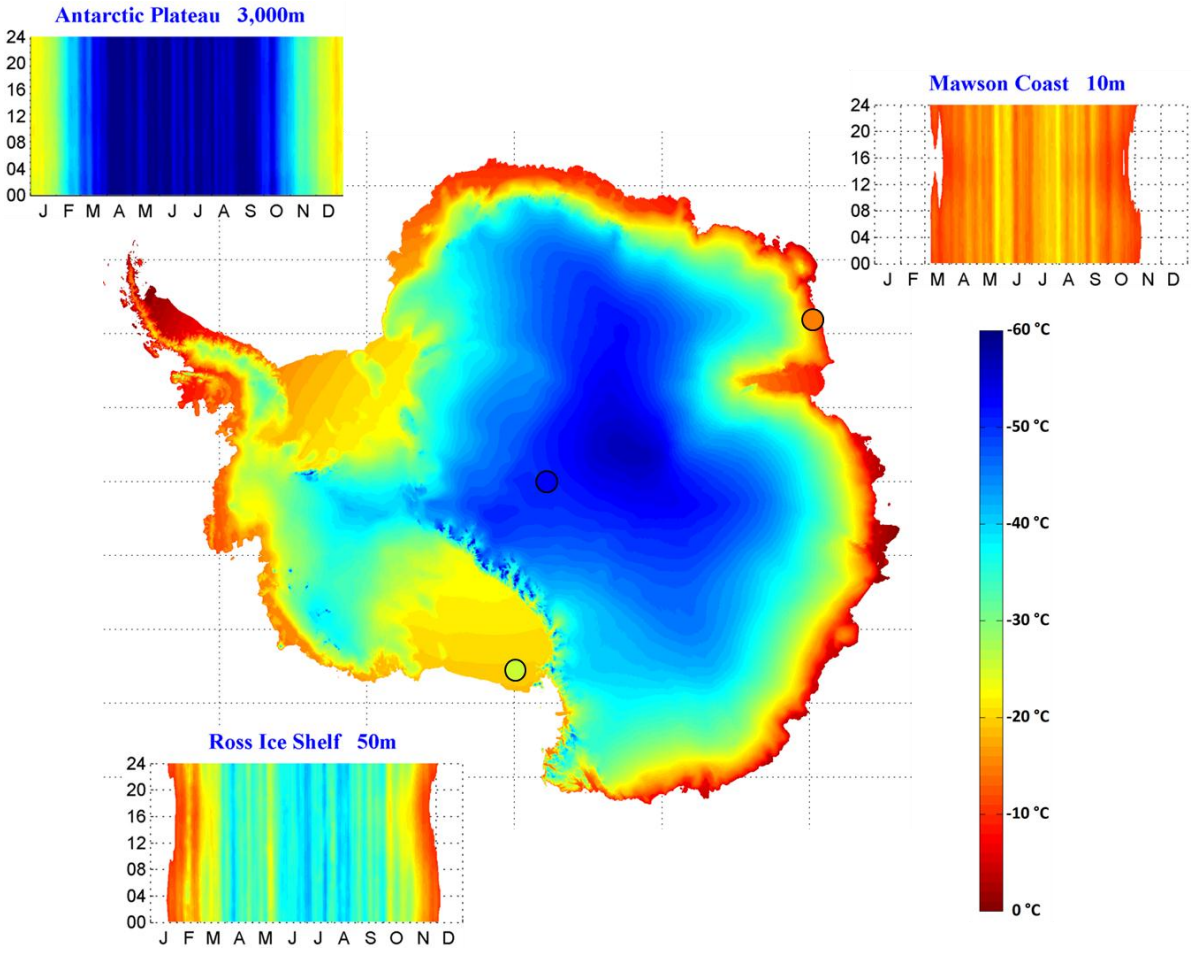

Fig. 4.14. Mild coastal, cold ice-shelf and frigid interior regions chosen for glaciothermal case studies plotted against mean annual ice surface temperature map of Antarctica. **IST map constructed by crude regression analysis of *THERMAP* 10m ice temperature data overlaid on *RAMPDEM* grid [98, 105]. Ambient air temperature calendars constructed from *Australian BoM* and *Antarctic AWS Network* datasets [1, 103].**

Interior sites

Air temperature data has been collated from Automated Weather Stations (AWS's) at two elevated interior sites in Antarctica: Clean Air AWS located at the Amundsen-Scott South Pole station, and Nico AWS about 110 km away at latitude 89° S, longitude 90° E. Air temperature measurements taken at 3m AGL reveal a bimodal seasonal temperature distribution for these high elevation interior sites, Fig. 4.15. Cold winter temperatures dominate, but the warm spike in summer is conspicuous.

Relative humidity averages ~50%. Wind speed is typically low and averages 4 to 5 m/s over the full year. Barometric pressure is very low due to the high elevation (~3,000 m) and varies between 650 and 710 hPa at the two sites. We nominate 670 hPa as the mean pressure for our glaciothermal engine performance modelling.

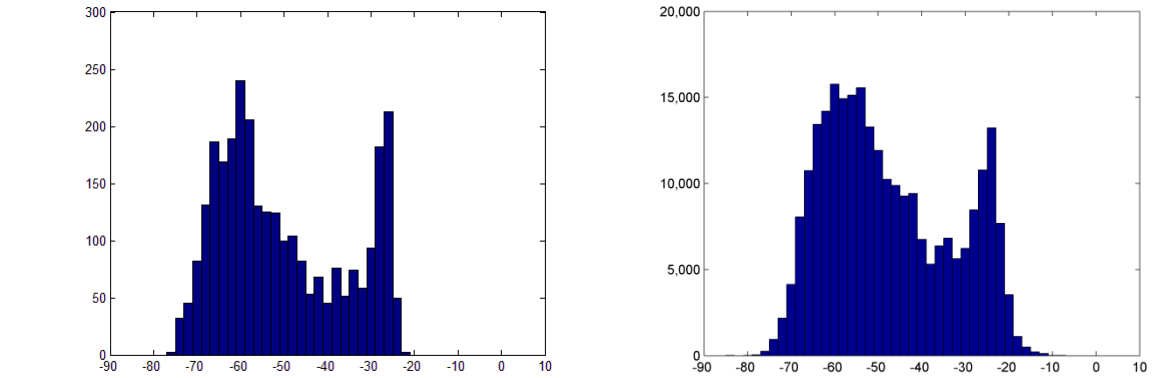

(a) (b)

Fig. 4.15. Histograms of year round ambient air temperature data for (a) Clean Air AWS (South Pole) and (b) Nico AWS. **Constructed from *Antarctic AWS Network* meteorological datasets [103]**.

Ice-shelf sites

Numerous AWS's are installed across the Ross Ice Shelf. Amelia and Margaret AWS's have been selected as suitable examples of exposed katabatic wind sites and radiatively cooled calm air sites respectively, Fig. 4.16. Both sites share the same latitude and elevation but Amelia AWS is situated nearer to the western flank of the ice shelf directly underneath the major katabatic stream.

Relative humidity ranges between 20 and 100% with a median average of ~70%. Median wind speed is ~3 to 4 m/s with maxima up to ~20 m/s for Amelia AWS. Median wind is ~2 m/s with maxima up to ~10 m/s at Margaret. We adopt a mean barometric pressure of 985 hPa.

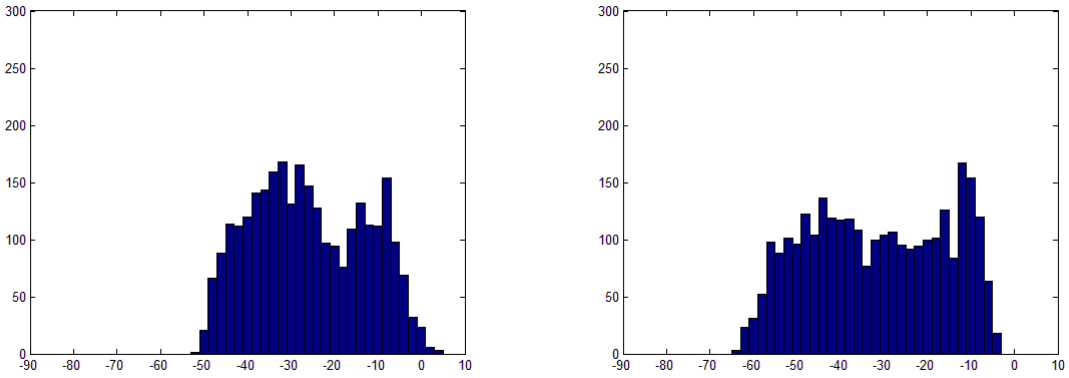

Fig. 4.16. Histograms of year round ambient air temperature data for (a) Amelia and (b) Margaret AWS. **Constructed from *Antarctic AWS Network* meteorological datasets [103].**

Coastal oases

In Antarctic parlance an *oasis* is a small island of bare rock outcropping amidst the ocean of ice. Many of the manned stations around the Antarctic coastline are located on these rocky outcrops. Mild conditions prevail for much of the year due to the low elevation and proximity to the warming effects of the ocean. Dry winds blow predominantly down off the icesheet for most of the year. Ambient temperature histograms for Dumont d'Urville and Mawson stations show a less prominent peak in summer and milder winters, Fig. 4.17.

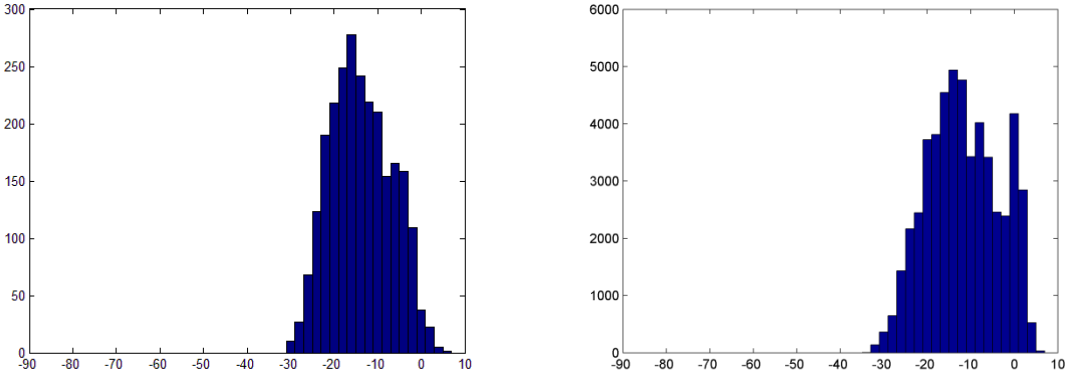

Fig. 4.17. Ambient air temperature data for Dumont d'Urville and Mawson stations. **Constructed from *Australian BoM* and *Antarctic AWS Network* meteorological datasets [1, 103].**

All the above sites are readily grouped on the basis of their temperature record. Five years of air temperature data is plotted for Nico AWS, Fig. 4.18, with 5-year combined averages for each of the three type locations displayed in Fig. 4.19.

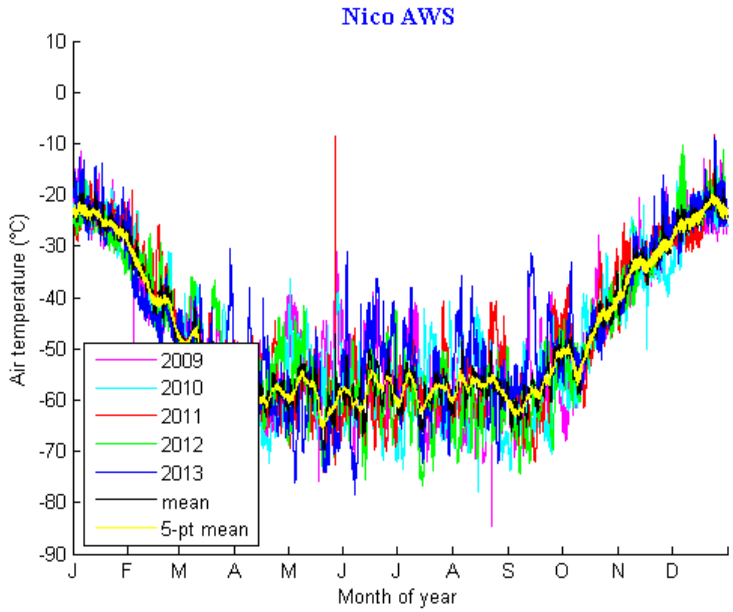

Fig. 4.18. Year round ambient air temperature data for high elevation interior site.
Constructed from *Antarctic AWS Network* meteorological datasets [103].

The potential for glaciothermal power generation varies markedly between sites depending on proximity to the ocean, ground conditions, elevation and seasonal climate. If the cut-off temperature for economic operation of our engine is -20 °C then the prospects for each site become apparent. The following section explores the potential year round performance of the basic engine in more detail.

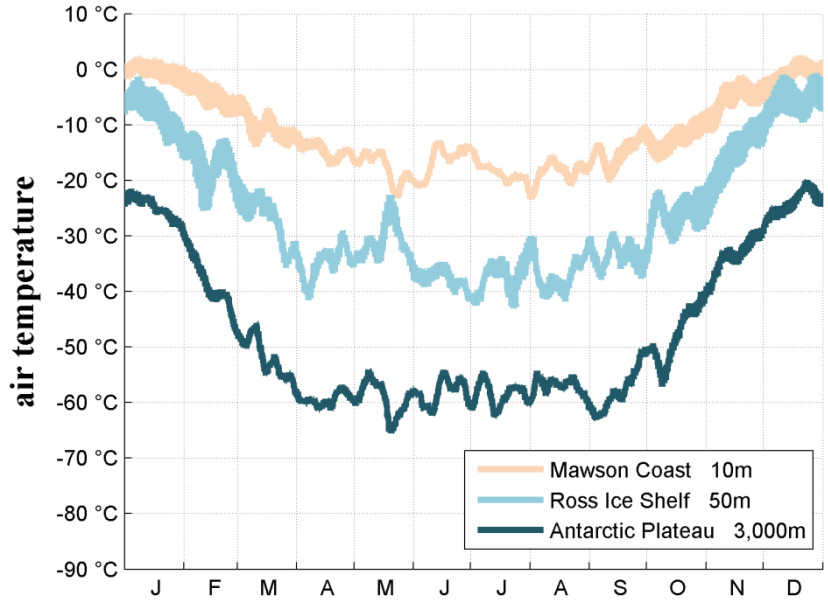

Fig. 4.19. 5-year 5-pt moving average air temperatures for selected Antarctic sites.
Constructed from *Australian BoM* and *Antarctic AWS Network* meteorological datasets [1, 103].

4.3.2 Year round performance at potential locations

Based on the performance curves compiled in Chapter 3 (Fig. 3.22) and the temperature data just described, the nett thermal efficiency of the basic glaciothermal engine cycle can now be calculated across the full year at each of the three type locations.

Nett thermal efficiency of basic engine

There is a marked difference in performance between the three sites as evident in Fig. 4.20. Nett thermal efficiency varies between 2 and 11% for operation of the basic engine under the conditions that prevail high on the East Antarctic plateau. On the Ross Ice Shelf direct operation is only feasible during winter between April and September with efficiencies ranging between 4 and 6%. At low level coastal sites operation is not possible except for brief periods in winter. Even then operation is marginal with efficiencies no more than 2%.

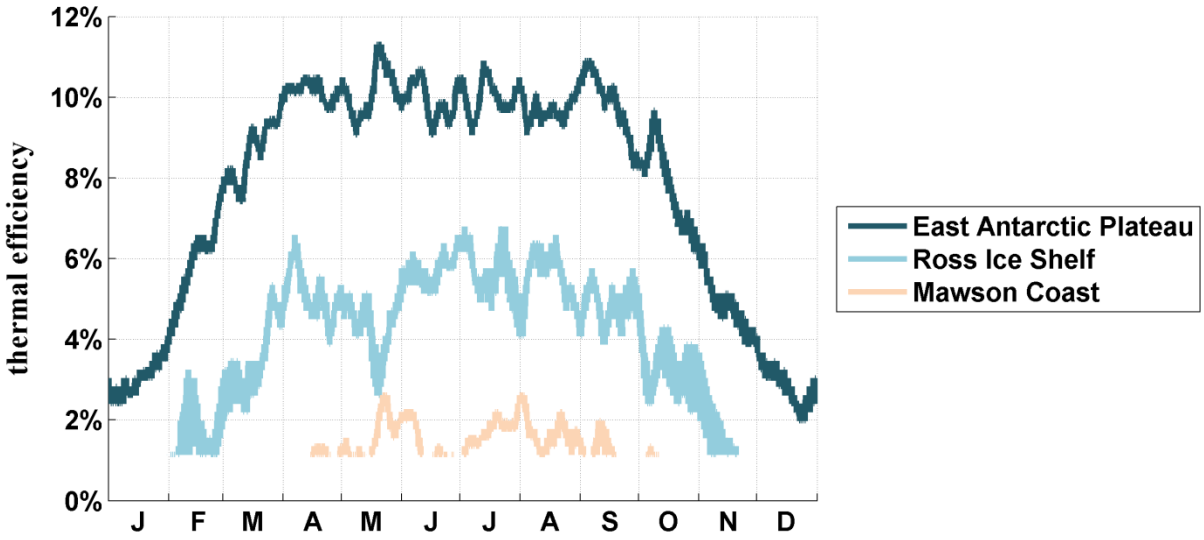

Fig. 4.20. Year round nett efficiency of basic glaciothermal engine based on 5-year 5-pt mean temperatures.

These glaciothermal energy profiles have been calculated assuming that the ice slurry loop is only subject to a temperature glide of 0.1 K. That is, the ice slurry will only cool by 0.1 °C before it exits the boiler. Approximately 5% mass fraction of ice will form during this time. 95% of the seawater feed will remain as brine and be returned to the sea. This is quite acceptable for coastal and ice shelf sites situated immediately at the water's edge but for interior sites, however, it makes little sense to pump seawater any great distance inland and only extract such a small amount of heat.

Overall performance with seawater pumping

For interior sites it is desirable to freeze a much greater proportion of the seawater. For a temperature glide of 1 K around 33% of the seawater will freeze to ice. For a glide of 5 K about 68% will freeze. Performance of the glaciothermal boiler needs to be recalculated for these settings.

Hydraulic and pumping losses also need to be considered. For water flowing through a partially filled tunnel or pipe we allow 2 m of fall per 1 km distance for hydraulic loss, in line with the Manning velocity formulae, Fig. 4.21. Power can potentially be recovered from the returning ice slush using a Pelton wheel at 90% conversion efficiency, and helps to offset a nominal inbound pumping loss of 85%. These figures are both optimistic and we also assume that the Pelton wheel and seawater pump might be attached to the same shaft thus avoiding electrical conversion losses.

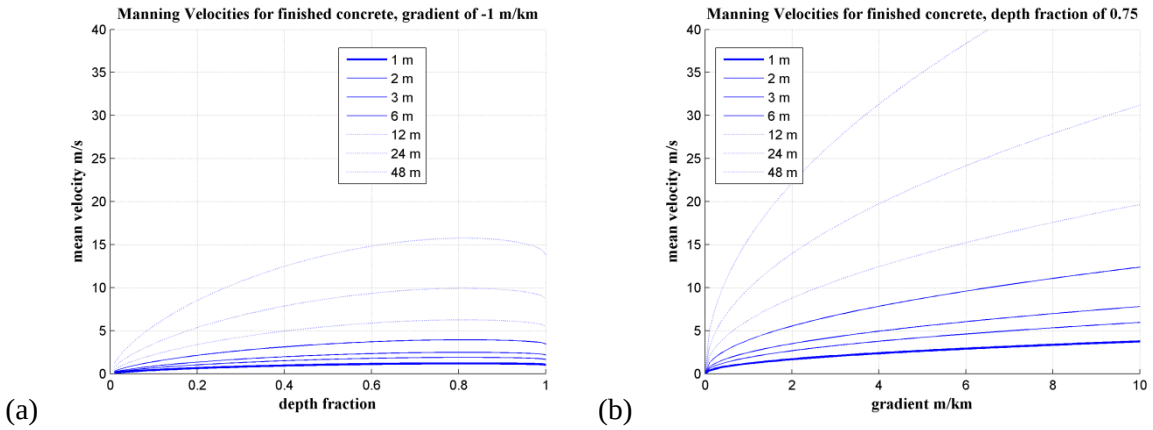

(a) (b)

Fig. 4.21. Manning velocities for finished concrete tunnels as a function of (a) depth fraction and (b) gradient.

Ice slurry temperature glide, hydraulic and pump losses are all included in recalculating the overall glaciothermal power system performance curves shown in Fig. 4.22. These new performance curves are now applied to the year round temperature data to produce revised estimates of the actual glaciothermal cycle efficiency, Fig. 4.23. There is a substantial difference in the overall thermal efficiency of the new configuration. The 5 K ice slurry temperature glide is vastly more efficient than the 1 K temperature glide. This is largely due to the greater relative proportion of freezing seawater (68% compared to 33%) that is contributing latent heat to the glaciothermal engine. The efficiency of the best seawater pumping configuration is still substantially less than the original stand-alone engine.

This is mainly due to the considerable energy conversion losses associated with the Pelton wheel and seawater supply pump.

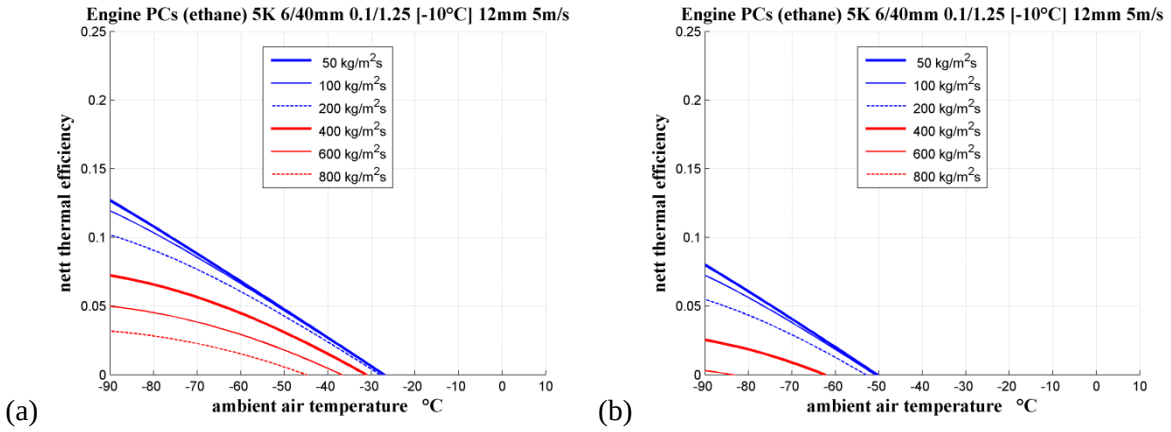

Fig. 4.22. Performance of basic glaciothermal engine at 3,000 m interior Antarctic site assuming nett 100 km round-trip seawater pumping losses and with ice slurry temperature glides of (a) 5 K; and (b) 1 K.

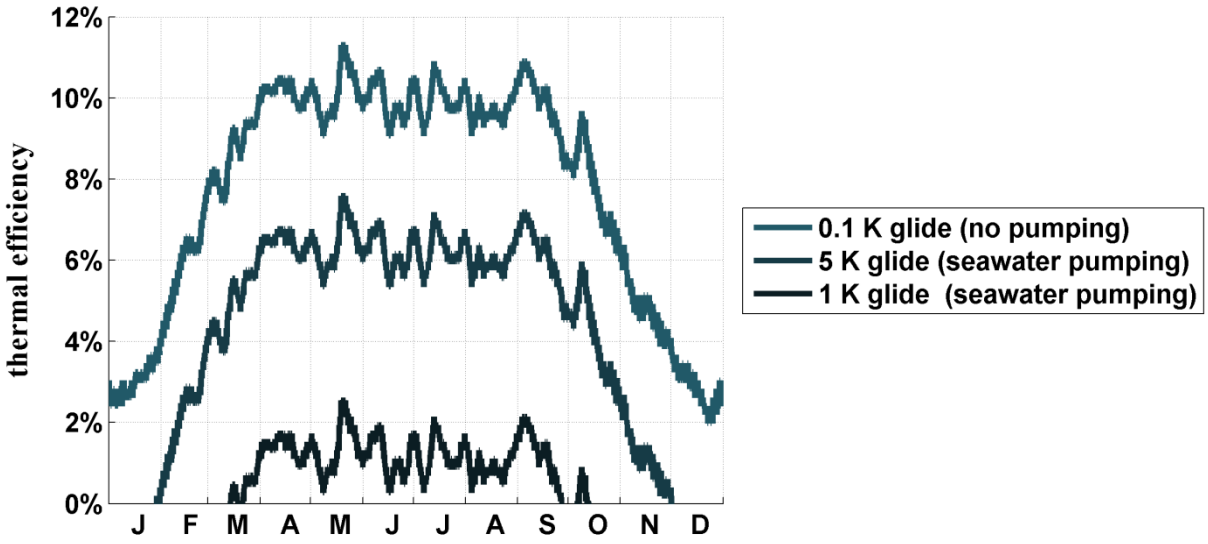

Fig. 4.23. Nett efficiency of glaciothermal system on East Antarctic Plateau with and without seawater pumping losses.

A more accurate comparison can now be made between the three type locations regarding the potential for glaciothermal power generation. With freezing and pumping effects taken into account there is little difference in overall efficiency between systems built on the ice shelf compared to those constructed at high elevation on the icecap, Fig. 4.24. Clearly the extraordinary engineering challenges and costs associated with pumping seawater inland by conventional means cannot be justified on the basis of thermal efficiency given the possibility of generating the same amount of

power much more simply at the nearby ice shelf sites. Other approaches are possible, however, and other factors do come into play for very large scale systems.

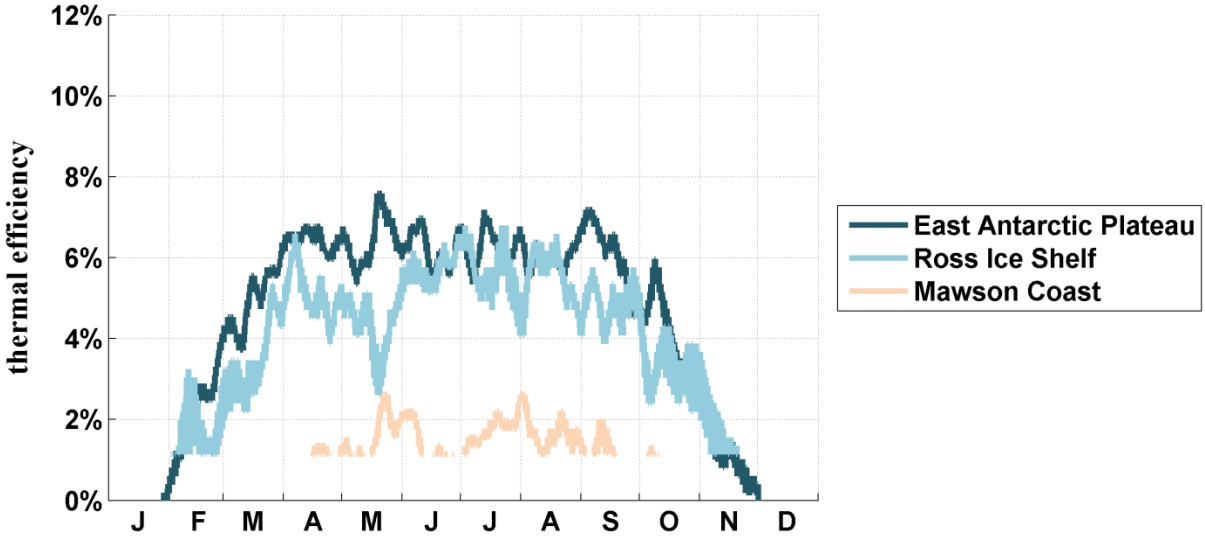

Fig. 4.24. Comparative efficiency of glaciothermal power systems with pumping losses factored in.

A similar comparison of maximum efficiencies for the *basic* glaciothermal engine is carried out at three sites on the Windmill Coast in East Antarctica, Fig. 4.7 and 4.25. Casey Station is modelled with seawater feed at minimum temperature glide; Casey Skiway includes pumping of seawater over 7 km to an elevation of 392 m with a 5 K temperature glide; and Wilkins Runway site is modelled with a 5 g/kg meltwater brine and minimum temperature glide. Casey Station and Skiway are not feasible, but the Wilkins Runway is a potential candidate for year round power but with oversize components.

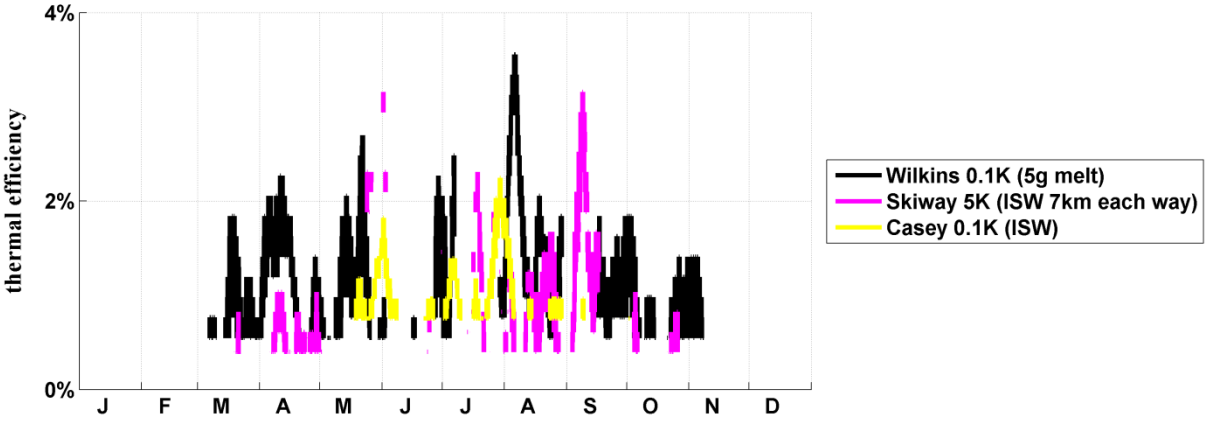

Fig. 4.25. Nett thermal efficiency of glaciothermal power systems on the Windmill Coast. Coarseness of the plotted curves is due to 1 °C discretisation of input temperature data. Gaps are missing meteorological data.

4.4 Conclusions

Coastal shoreline sites are not cold enough at any time of the year to produce glaciothermal power, however, nearby icesheet sites have potential to provide continuous power through winter with over-size components. Conditions on the East Antarctic Plateau and on the Ross Ice Shelf both permit glaciothermal power production through the six months or so of winter. Summer temperatures are too mild to permit significant nett power generation from freezing seawater.

The inability to produce electrical output for at least six months of the year is a major limitation of the basic glaciothermal engine. Suitable augmentation methods must be employed if year round power output is to be achieved by glaciothermal means.

Fortunately there are a number of options available that do make year round supply of glaciothermal power possible. Storage of manufactured meltwater within the icesheet, and ground source cold storage also in the icesheet are both surprisingly simple to implement. Interior and coastal icesheet sites can all potentially use local meltwater from solar absorbers or concentrators to provide year round glaciothermal power.

These and other potential augmentation methods are discussed in Chapter 5, with more detailed analysis included in Appendices 5-A, 5-B and 5-C.

Chapter 5 – Conclusions and Future Work

This chapter presents the key findings and conclusions of the thesis and outlines current and future work on some potential small and large scale augmentation methods. We conclude that glaciothermal engines do have significant potential for reliable cold climate energy production

5.1 Major findings of this thesis and conclusions

A number of outcomes have resulted from our research on cold climate energy systems, and glaciothermal engines in particular.

We have been able to develop the concept of the thermo-mechanical wind thermal device as envisaged by Le Goff and others [62, 71] into a viable prototype device that has the potential to provide reliable continuous power at very cold polar locations. By researching the underlying physical processes we were able to identify and devise solutions to the key heat transfer and heat conversion challenges.

These solutions were modelled in MATLAB and the major finding that emerged from simulations was that remarkably high nett thermal efficiencies of at least 10% can be achieved with a basic glaciothermal engine for ambient air temperatures around -60 °C. Efficiency drops to ~5% at -40 °C.

Meteorological investigations showed that around 5 million square kilometres of East Antarctica has mean annual temperatures colder than -40 °C. In this region power generation from a basic glaciothermal engine is possible for approximately 8 months of the year. Engine efficiency of ~10% at interior sites drops to ~6% nett if seawater needs to be pumped in from the coast. Conditions on Ross Ice Shelf can sustain ~5% efficiency for 6 months of winter. Seawater immediately below need only be raised up 50—70 m and so such sites are ideally suited to glaciothermal energy production.

Meteorological studies also demonstrate astonishing mean daily insolation of ~500 W/m^2 on the high plateau during the Austral summer. Solar concentrators and absorbers can capture exceptional radiant energy, suggesting that stored meltwater has excellent potential to deliver year round

glaciothermal power at interior sites. There is every reason to believe that the heat transfer processes employed in the small engine can be directly extrapolated to power very large generators.

The major research findings of this project can be summarised as follows:

- Ice slurry flow regulation is possible by measuring electrical conductivity of the brine
- Twin screw expanders and synchronous generators running at constant 3,000 rpm will provide very high energy conversion efficiency, especially when fixed volume ratios coincide with the density ratio of the working fluid
- Tube fin condenser parts need to be all copper to avoid differential thermal expansion
- The preferred *objective function* when comparing boiler and condenser dimensions in order to select a nominal configuration is *tonnes of copper per MW of nett power*.
- The glaciothermal engine must be sited at the elevated condenser location. Feed water can be pumped in and electrical power transmitted out to the point of use.
- Mean annual temperature is the over-riding factor that defines the best heat sink.

The feasibility analysis conducted in this thesis demonstrates that the basic glaciothermal engine can potentially contribute to the provision of sustainable energy in very cold climate conditions.

5.2 Potential augmentation methods and future work

The intermittency of power generation with the basic glaciothermal engine can potentially be overcome by icesheet thermal storage devices. Such inherent energy storage capability is a unique feature of glaciothermal energy compared to other intermittent renewables.

Meltwater production and ground source cold storage have potential as essential elements of year round glaciothermal power systems, Fig. 5.1. The nature and operation of the proposed thermal storage devices are outlined in Appendix 5-A. A summary of the potential performance of augmented glaciothermal power systems at each of three nominated type locations around Antarctica is provided in Appendix 5-B. Year round glaciothermal power can potentially eliminate the need to import any fossil fuels to the East Antarctic plateau.

Thermal augmentation methods also include direct mixing of feed water with natural working fluids to create clathrate ices that freeze at elevated temperatures. This potentially produces higher boiler pressures and more efficient glaciothermal cycles. Direct contact heat transfer is a key element in the development of large scale working fluid expanders capable of generating many thousands of megawatts in a single device. Key aspects of potential direct contact glaciothermal boilers, vaporjet expanders and hydro turbine systems are described and illustrated in Appendix 5-C.

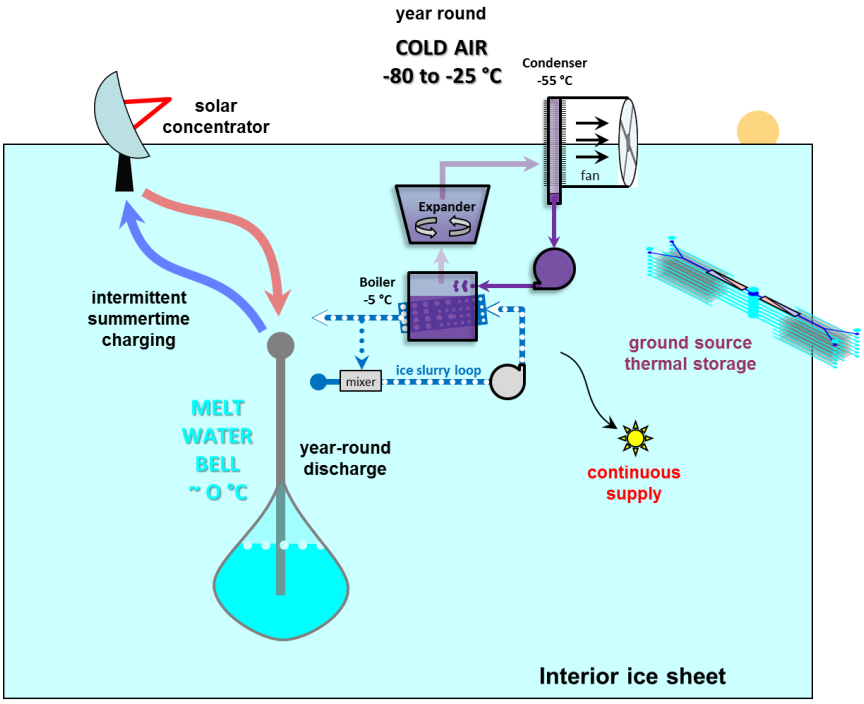

Fig. 5.1. A meltwater bell provides latent heat for year round glaciothermal power generation.

Some numerical modelling has been carried out for the ground source thermal storage and meltwater bell augmentation devices but they are yet to be fully analysed. Accordingly, these systems do not form part of the research findings of this thesis but are included to highlight the ultimate potential of glaciothermal power. We cannot guarantee that some unanticipated factor will prevent them from performing as anticipated. More research is needed.

Further discussion regarding minor findings and miscellaneous future work is provided in Appendices 5-D and 5-E respectively.

References

[1] Australian Bureau of Meteorology. (2014). *Weather station data - half hourly observations (1990-2013 ed.)*. Available: http://www.bom.gov.au/climate/data/stations/

[2] J. Jacka and A. B. Giles, "Mean monthly surface air temperature data," ed. Hobart, Tasmania: Antarctic CRC, 2003.

[3] T. Tin, B. K. Sovacool, D. Blake, P. Magill, S. El Naggar, S. Lidstrom*, et al.*, "Energy efficiency and renewable energy under extreme conditions: Case studies from Antarctica," *Renewable Energy,* vol. 35, pp. 1715-1723, Aug 2010.

[4] P. Magill, A. Guichard, and C. Paterson, "Using large commercial wind turbines in Antarctica (Wind Power for Australian Antarctic Stations)," presented at the Ninth SCALOP Symposium, Tokyo, Japan, 2000.

[5] K. Ishizawa, S. Kimura, and T. Takanaga, "Wind power utilization at Syowa Station," presented at the Ninth SCALOP Symposium, Tokyo, Japan, 2000.

[6] I. Miller, "Ross Island wind energy project: Sustainability through collaboration," presented at the COMNAP Symposium 2010, Buenos Aires, Argentina, 2010.

[7] C. Brown, A. Guichard, and D. Lyons, "Wind energy in polar regions: Casey Station Antarctica," presented at the 12th Annual Conference of the Canadian Wind Energy Association, Kananaskis, Alberta, Canada, 1996.

[8] T. Laakso, H. Holttinen, G. Ronsten, L. Tallhaug, R. Horbaty, I. Baring-Gould*, et al.*, "State-of-the-art of wind energy in cold climates," *IEA annex XIX,* 2003.

[9] I. Baring-Gould, R. Robichaud, and K. McLain, "Analysis of the Use of Wind Energy to Supplement the Power Needs at McMurdo Station and Amundsen-Scott South Pole Station Antarctica," National Renewable Energy Laboratory NREL/TP-500-37504, 2005.

[10] M. C. Rose, R. Kressman, N. Cobbett, J. Fox, D. Maxfield, and L. Kitson, "Low and medium power environmental energy systems for the Antarctic Plateau," presented at the Tenth Symposium on Antarctic Logistics and Operations, Shanghai, China, 2002.

[11] K. Ishizawa, S. Kimura, and T. Takanaga, "A new designed wind generator for Antarctica," presented at the Fourth Symposium on Antarctic Logistics and Operations, Sao Paulo, Brazil, 1990.

[12] P. LeGoff, "Exploitation d'une nouvelle forme de l'energie solaire : la froideur du vent," *Entropie,* pp. 107-108, 1982.

[13] T. R. Parish and J. J. Cassano, "Diagnosis of the katabatic wind influence on the wintertime Antarctic surface wind field from numerical simulations," *Monthly Weather Review,* vol. 131, pp. 1128-1139, 2002.

[14] D. A. Jones and I. Simmonds, "A climatology of Southern Hemisphere extratropical cyclones," *Climate Dynamics,* vol. 9, pp. 131-145, Dec 1993.

[15] D. A. Jones and I. Simmonds, "A climatology of Southern Hemisphere anticyclones," *Climate Dynamics,* vol. 10, pp. 333-348, Sep 1994.

[16] S. El Naggar, H. Gernandt, and J. Janneck, "Operational experience with wind power technology at Neumayer station," presented at the Ninth SCALOP Symposium, Tokyo, Japan, 2000.

[17] U. Bonafe, F. Evangelisti, V. Vitale, F. Calzolari, V. Nanni, G. Trivellone*, et al.*, "Wind-generator system applied to scientific instrumentaiton in remote Antarctic sites," in *Eleventh SCALOP Symposium*, Bremen, 2004, pp. 44-48.

[18] S.-W. Kim and N.-H. Kyong, "Demonstration of 10kw Wind Turbine System at the King Sejong Station," *Journal of the Korean Solar Energy Society,* vol. 26, pp. 25-30, 2006.

[19] A. Guichard, P. Magill, P. Godon, D. Lyons, and C. Brown, "Potential for significant wind power generation at Antarctic stations," presented at the Seventh Symposium on Antarctic Logistics and Operations, Cambridge, UK, 1996.

[20] H. W. Teetz, T. M. Harms, and T. W. von Backström, "Assessment of the wind power potential at SANAE IV base, Antarctica: a technical and economic feasibility study," *Renewable Energy,* vol. 28, pp. 2037-2061, 2003.
[21] C. Boccaletti, P. Di Felice, and E. Santini, "Designing wind plants for extreme ambient conditions," in *Electrical Machines (ICEM), 2010 XIX International Conference on*, 2010, pp. 1-6.
[22] A. S. Sheinstein and E. E. Shpilrain, "Potential for renewable energy sources in the Antarctic," presented at the Fourth Symposium on Antarctic Logistics and Operations, Sao Paulo, Brazil, 1990.
[23] Incredio. (2009). *Theoretical insolation at top of atmosphere*. Available: https://commons.wikimedia.org/wiki/File:InsolationTopOfAtmosphere.png
[24] M. Iwata, T. Tanoue, K. Kawai, K. Ishizawa, and N. Endo, "Utilization of air-type solar collector at Syowa Station," presented at the Ninth SCALOP Symposium, Tokyo, Japan, 2000.
[25] A. S. Sheynshteyn, "A new type of solar snow melting facility based on space technologies," presented at the Ninth SCALOP Symposium, Tokyo, Japan, 2000.
[26] C. Thormark, B. Fredlund, and T. Olsrud, "WASA - Analysis of energy requirements for the Swedish research station in Antarctica," presented at the Seventh Symposium on Antarctic Logistics and Operations, Cambridge, United Kingdom, 1996.
[27] S. M. Peeran, "Performance of PV panels for solar energy conversion at the South Pole," presented at the Sixth Symposium on Antarctic Logistics and Operations Rome, Italy, 1994.
[28] J. Yoshida, K. Ishizawa, and T. Izutsu, "Project of 60kW photovoltaic system at Syowa Station and assessment of the effects," presented at the Ninth SCALOP Symposium, Tokyo, Japan, 2000.
[29] J. R. Olivier, T. M. Harms, and D. J. Esterhuyse, "Technical and economic evaluation of the utilization of solar energy at South Africa's SANAE IV base in Antarctica," *Renewable Energy,* vol. 33, pp. 1073-1084, 2008.
[30] A. Guichard, "Status report on the potential for the application of alternative energy systems at Antarctic stations," Latitude Technologies, May 1994.
[31] C. Brown, "Renewable energy systems for the Australian Antarctic stations," Master of Science, Institute of Antarctic and Southern Ocean Studies, University of Tasmania, 1998.
[32] A. Guichard, P. Magill, C. Paterson, and G. Williams, "Energy services: Back to basics and up to hybrids," presented at the Ninth SCALOP Symposium, Tokyo, Japan, 2000.
[33] P. Godon and A. Pierre, "Power system for the continuous and efficient operation of the new CONCORDIA Station," Institut Polaire2000.
[34] P. Godon and N. Cucinotta, "Power system for the continuous and efficient operation of the new CONCORDIA Station," presented at the Ninth SCALOP Symposium, Tokyo, Japan, 2000.
[35] E. Chiang, "Antarctic alternative energy summary," presented at the Sixth Symposium on Antarctic Logistics and Operations, Rome, Italy, 1994.
[36] R. P. Schmitt and R. Rodriguez, "Glacier water supply and sewerage disposal systems," presented at the Symposium on Antarctic Logistics, Boulder, Colorado, 1962.
[37] J. Hamilton, M. Negnevitsky, and X. Wang, "Low Load Diesel Perceptions and Practices within Remote Area Power Systems," presented at the IEEE International Symposium on Smart Electric Distribution Systems and Technologies (EDST) CIGRE SC C6 Colloquium, Vienna, 2015.
[38] A. Guichard and J. Steel, "Alternative energy systems for Antarctic stations: Investing for the future," presented at the Growth and Environment: Challenging Extreme Frontiers, Second International Design for Extreme Environments Assembly 'IDEEA 1993', Montreal, Canada 1993.
[39] C. Paterson, J. Bonnice, and P. Magill, "The use of building monitoring and control systems to reduce energy consumption in Antarctic stations," presented at the Ninth SCALOP Symposium, Tokyo, Japan, 2000.

[40] D. Pointing, "A strategy for hydrogen energy use in Antarctica," PhD, IASOS, University of Tasmania, Hobart, Australia, 2008.
[41] P. Alain, P. Godon, and A. Guichard, "Dumont d'Urville energy management system," presented at the Ninth SCALOP Symposium, Tokyo, Japan, 2000.
[42] N. P. Milani, "Performance optimization of a hybrid wind turbine-diesel microgrid power system," 2007.
[43] D. Mazzeo and W. Cornell, "Harvesting energy in Antarctica," in *Twelfth SCALOP Symposium*, 2006.
[44] M. Falchetta, A. Lori, R. Maso, A. Nunzi, D. Prischich, F. Caricchi*, et al.*, "A new wind turbine for remote installations in inner Antarctica," presented at the Ninth SCALOP Symposium, Tokyo, Japan, 2000.
[45] C. Boccaletti, P. Di Felice, and E. Santini, "Designing photovoltaic plants for extreme ambient conditions," in *Power Electronics Electrical Drives Automation and Motion (SPEEDAM), 2010 International Symposium on*, 2010, pp. 641-646.
[46] D. Prischich, A. Benedetti, G. Cara, M. Falchetta, and R. Maso, "Wind speed data acquisition at Dome-C using low power consumption equipment," presented at the Ninth SCALOP Symposium, Tokyo, Japan, 2000.
[47] M. P. Ramesh, "Wind energy utilization at Maitri, The Indian Antarctic scientific station," presented at the Ninth SCALOP Symposium, Tokyo, Japan, 2000.
[48] J. Stander, "Selecting a small wind turbine for the South African Antarctic research base SANAE IV," presented at the Winter Wind Conference, Norrkoping, Sweden, 2008.
[49] J. L. Aprea, "Two years experience in hydrogen production and use in Hope bay, Antarctica," *International Journal of Hydrogen Energy,* vol. 37, pp. 14773-14780, 2012.
[50] J. Castellvi, E. Meana, and A. Castejon, "Alternative energy at the SAB (BAE) "Juan Carlos I"," in *Sixth SCALOP Symposium*, Rome, 1994, pp. 115-122.
[51] D. Domenech, "Automated fuel and water system at Escudero station," in *Twelfth SCALOP Symposium*, 2006.
[52] D. Stolten, "Overview on hydrogen and fuel cells as energy technologies," presented at the Eleventh SCALOP Symposium, Bremen, Germany, 2004.
[53] L. Adamek, G. Filip, and S. von Hoyningen-Huene, "Fuel cell technology for sensitive environmental areas," in *Eleventh SCALOP Symposium*, Bremen, 2004.
[54] C. M. Marschoff, "Transition from non-renewable to renewable energy sources: Fuel cells in Antarctica as an economically attractive niche," *International Journal of Hydrogen Energy,* vol. 23, pp. 303-306, 1998.
[55] S. Kim, N. Kyong, S. Kim, Y. Ju, and B. Lee, "Wind-Diesel Hybrid Operation at the King Sejong Station," in *SCARCOMNAP Conference*, 2006.
[56] J. Lawrence, M. Ashley, S. Hengst, D. Luong-Van, J. Storey, H. Yang*, et al.*, "The PLATO Dome A site-testing observatory: Power generation and control systems," *Review of Scientific Instruments,* vol. 80, p. 064501, 2009.
[57] F. Pattyn, "Construction and operation of the new Belgian research station, Dronning Maud Land, Antarctica. Final comprehensive environmental evalation (CEE).", ed: Belgian Federal Public Planning Service Science Policy; Mar 2007.
[58] C. Brown, A. Guichard, and D. Lyons, "Analysis of the potential for wind and solar energy systems in Antarctica," presented at the Wind Energy Conversion 1996, Exeter, UK, 1996.
[59] E. Long, "The long thermopile," in *Permafrost: Proceedings, International Conference, Purdue University*, 1963.
[60] J. Meyer, D. Pride, J. O'Toole, C. Craven, and V. Spencer, "Ground-source heat pumps for cold climates," Alaska Center for Energy and Power, Alaska, USA, May 31st 2011.
[61] B. Schwarzer, S. De Oliveira, and P. Le Goff, "An absorption heat transformer for spaceheating driven by the thermal energy of the wind," presented at the IECEC Proceedings, 1991.

[62] H. LeGoff, U. Hasert, and A. Guichard, "Producing energy for polar stations from the wind-water temperature gradient," presented at the Sixth Symposium on Antarctic Logistics and Operations, Rome, Italy 1994.
[63] H. LeGoff, K. Stefan, B. Lefauconnier, Chubenok, and V. Maiorov, "Alternative energy systems for polar stations," ed, 1994.
[64] H. LeGoff, B. Schwarzer, S. j. De Oliveira, and P. Le Goff, "Thermodynamical machines using the energy of cold polar winds," presented at the COLD 92 conference, Buenos-Aires, Argentina 1992.
[65] E. J. Beck, "Ocean thermal gradient power plant," USA Patent US3967449, 1975.
[66] C. Smith Jr., "Production of energy by direct contact of water immiscible working fluid with hot or warm water to vaporize working fluid," USA Patent 4,009,082, 1975.
[67] L. G. Lewis and N. F. Sather, "OTEC performance tests of the Union Carbide flooded-bundle evaporator," Argonne National Lab., IL (USA)1978.
[68] W. H. Avery, "Open cycle OTEC plant," USA Patent US 4,430,861, 14 Feb 1984, 1982.
[69] C. Zener and J. Fetkovich, "Foam solar sea power plant," *Science,* vol. 189, pp. 294-295, 1975.
[70] D. Tanner, "Ocean thermal energy conversion: Current overview and future outlook," *Renewable Energy,* vol. 6, pp. 367-373, 1995.
[71] H. LeGoff, U. F. Hasert, and P. LeGoff, "A “new” source of renewable energy: the coldness of the wind," *International Journal of Thermal Sciences,* vol. 38, pp. 916-924, 1999.
[72] U.-F. Hasert, "Thermische energie von kaltem polarwind," Diplomarbeit, Universitat Stuttgart / Laboratoire des Sciences du Genie Chimique-CNRS, 1993.
[73] H. LeGoff, B. Schwarzer, and P. Le Goff, "Utilisation des énergies renouvelables en milieu polaire," presented at the Congres de genie des procedes, Grenoble, France 1993.
[74] E. Castus, Y. Schleis, and O. Cheneson, "Etude d'un Echangeur de Chaleur a Eau de Mer autour de Zero Degree Celsius, pour Application aux pompes a Chaleur a Absorption pour les Bases Polaires," Universite de Nancy, Nancy, France, 1994.
[75] G. Bylund and T. Pak, *Dairy processing handbook*: Tetra Pak Processing Systems AB Lund, 2003.
[76] T. A. Mouneer, M. S. El-Morsi, M. A. Nosier, and N. A. Mahmoud, "Heat transfer performance of a newly developed ice slurry generator: A comparative study," *Ain Shams Engineering Journal,* vol. 1, pp. 147-157, 12// 2010.
[77] P. W. Egolf and M. Kauffeld, "From physical properties of ice slurries to industrial ice slurry applications," *International Journal of Refrigeration,* vol. 28, pp. 4-12, 2005.
[78] M. Kauffeld, M. Kawaji, and P. W. Egolf, *Handbook on Ice Slurries: Fundamentals and Engineering*: Institut international du froid= International institute of refrigeration, 2005.
[79] M. Kauffeld, "Behaviour of ice slurry in thermal storage systems," ASHRAE2002.
[80] J. W. Meewisse, "Fluidized bed ice slurry generator for enhanced secondary cooling systems," Doctoral Thesis, Technische Universiteit Delft, 2004.
[81] I. K. Smith, N. Stosic, and A. Kovacevic, "Screw expanders increase output and decrease the cost of geothermal binary power plant systems," *Geothermal Resource Council Transactions,* vol. 29, 2005.
[82] I. K. Smith, N. Stosic, and A. Kovacevic, "Power recovery from low cost two-phase expanders," *Transactions-Geothermal Resources Council,* pp. 601-606, 2001.
[83] I. Smith, N. Stosic, C. Aidis, and A. Kovacevic, "Twin screw two-phase expanders in large chiller units," in *IMECHE CONFERENCE TRANSACTIONS*, 1999, pp. 105-116.
[84] W. M. Rohsenow, J. P. Hartnett, and Y. I. Cho, *Handbook of heat transfer* vol. 3: McGraw-Hill New York, 1998.
[85] Y. A. Cengel, "Heat Transfer A Practical Approach. 1998," *ISBN: 0-07-115223-7. WCB McGraw-Hill,* 1998.

[86] A. Cavallini, D. D. Col, L. Doretti, M. Matkovic, L. Rossetto, C. Zilio*, et al.*, "Condensation in horizontal smooth tubes: a new heat transfer model for heat exchanger design," *Heat Transfer Engineering,* vol. 27, pp. 31-38, 2006.
[87] G. Breber, J. Palen, and J. Taborek, "Prediction of horizontal tubeside condensation of pure components using flow regime criteria," *Journal of Heat Transfer,* vol. 102, pp. 471-476, 1980.
[88] A. Cavallini, D. Del Col, L. Doretti, G. Longo, and L. Rossetto, "Heat transfer and pressure drop during condensation of refrigerants inside horizontal enhanced tubes," *International Journal of Refrigeration,* vol. 23, pp. 4-25, 2000.
[89] R. Sardesai, R. Owen, and D. Pulling, *Pressure drop for condensation of a pure vapour in downflow in a vertical tube*: UKAEA Atomic Energy Research Establishment, 1982.
[90] Y. J. Kim, J. Jang, P. S. Hrnjak, and M. S. Kim, "Condensation heat transfer of carbon dioxide inside horizontal smooth and microfin tubes at low temperatures," *Journal of Heat Transfer,* vol. 131, p. 021501, 2009.
[91] J.-P. Bédécarrats, T. David, and J. Castaing-Lasvignottes, "Ice slurry production using supercooling phenomenon," *International Journal of refrigeration,* vol. 33, pp. 196-204, 2010.
[92] E. Lemmon, M. McLinden, and D. Friend, "Thermophysical Properties of Fluid Systems in NIST Chemistry WebBook, NIST Standard Reference Database Number 69, Eds. Linstrom, PJ and Mallard, WG, National Institute of Standards and Technology, Gaithersburg MD, 20899," ed, 2011.
[93] R. Menini and M. Farzaneh, "Advanced icephobic coatings," *Journal of adhesion science and technology,* vol. 25, pp. 971-992, 2011.
[94] D. J. Jeffrey, "Conduction through a random suspension of spheres," *Proceedings of the Royal Society of London. A. Mathematical and Physical Sciences,* vol. 335, pp. 355-367, 1973.
[95] M. H. Sharqawy, J. H. Lienhard, and S. M. Zubair, "Thermophysical properties of seawater: A review of existing correlations and data," *Desalination and Water Treatment,* vol. 16, pp. 354-380, 2010.
[96] M. W. Browne and P. K. Bansal, "Heat transfer characteristics of boiling phenomenon in flooded refrigerant evaporators," *Applied Thermal Engineering,* vol. 19, pp. 595-624, 6// 1999.
[97] H. Tang, H. Wu, X. Wang, and Z. Xing, "Performance study of a twin-screw expander used in a geothermal organic Rankine cycle power generator," *Energy,* vol. 90, pp. 631-642, 2015.
[98] H. Liu, K. Jezek, B. Li, and Z. Zhao. (2001). *RADARSAT Antarctic Mapping Project Digital Elevation Model*. Available: http://nsidc.org/data/nsidc-0082
[99] T. McDougall, R. Feistel, F. Millero, D. Jackett, D. Wright, B. King*, et al.*, "The International Thermodynamic Equation Of Seawater 2010 (TEOS-10): Calculation and Use of Thermodynamic Properties," *Global Ship-based Repeat Hydrography Manual, IOCCP Report,* 2009.
[100] A. Foldvik and T. Gammelsrød, "Notes on Southern Ocean hydrography, sea-ice and bottom water formation," *Palaeogeography, Palaeoclimatology, Palaeoecology,* vol. 67, pp. 3-17, 1988.
[101] J. Toggweiler and B. Samuels, "Effect of sea ice on the salinity of Antarctic bottom waters," *Journal of Physical Oceanography,* vol. 25, pp. 1980-1997, 1995.
[102] T. Scambos, M. Frezzotti, T. Haran, J. Bohlander, J. Lenaerts, M. Van den Broeke*, et al.*, "Extent of low-accumulation'wind glaze'areas on the East Antarctic plateau: implications for continental ice mass balance," *Journal of Glaciology,* vol. 58, pp. 633-647, 2012.
[103] (2014). *Antarctic AWS Network - 10 minute observations (1990-2013 ed.)*. Available: http://amrc.ssec.wisc.edu/aws/index.php?region=All%20Stations&mode=international
[104] J. Reeve. (2013). *2012-13 Season Voyage Track and Underway Data*. Available: http://data.aad.gov.au/aadc/metadata/metadata_redirect.cfm?md=/AMD/AU/201213_10_second_underway

[105] J. Bohlander and T. A. Scambos. Antarctic ten meter temperature data [Online]. Available: https://nsidc.org/data/docs/agdc/thermap/documentation.html
[106] E. W. Lemmon, M. L. Huber, and M. O. McLinden, "NIST Standard Reference Database 23," *Reference Fluid Thermodynamic and Transport Properties (REFPROP),* 2012.
[107] T. B. Jekel and D. T. Reindl, "Liquid refrigerant pumping in industrial refrigeration systems," American Society of Heating, Refrigerating and Air-Conditioning Engineers, Inc, Atlanta, GA, Technical feature, 2011.
[108] A. Melinder and M. Ignatowicz, "Properties of seawater with ice slurry use in focus," presented at the 11th IIR Gustav Lorentzen Conference on Natural Refrigerants, Hangzhou, China, 2014.
[109] D. Jamieson and J. Tudhope, "Physical properties of sea water solutions: thermal conductivity," *Desalination,* vol. 8, pp. 393-401, 1970.
[110] J. K. Landauer and H. Plumb, *Measurements on anisotropy of thermal conductivity of ice*: Snow, Ice and Permafrost Research Establishment, Corps of Engineers, US Army, 1956.
[111] J. Cooper, "Release on the IAPWS Formulation 2008 for the Thermodynamic Properties of Seawater," *The International Association for the Properties of Water and Steam, September,* pp. 1-19, 2008.
[112] J. Hallett, "The temperature dependence of the viscosity of supercooled water," *Proceedings of the Physical Society,* vol. 82, p. 1046, 1963.
[113] B. M. Fabuss, A. Korosi, and D. F. Othmer, "Viscosities of aqueous solutions of several electrolytes present in sea water," *Journal of Chemical and Engineering Data,* vol. 14, pp. 192-197, 1969.
[114] J. Isdale, C. Spence, and J. Tudhope, "Physical properties of sea water solutions: viscosity," *Desalination,* vol. 10, pp. 319-328, 1972.
[115] F. J. Millero, "Seawater as a multicomponent electrolyte solution," DTIC Document, 1974.
[116] P. W. Egolf and H. Manz, "Theory and modeling of phase change materials with and without mushy regions," *International Journal of Heat and Mass Transfer,* vol. 37, pp. 2917-2924, 1994.
[117] H. Wiegandt, A. Madani, and P. Harriott, "Ice crystallization developments for the butane direct-contact process," *Desalination,* vol. 67, pp. 107-126, 1987.
[118] T. Hansen, M. Radošević, and M. Kauffeld, "Behaviour of ice slurry in thermal storage systems," *ASHRAE Research Project,* vol. 1166, 2002.
[119] V. P. Walden, S. G. Warren, and E. Tuttle, "Atmospheric ice crystals over the Antarctic Plateau in winter," *Journal of Applied Meteorology,* vol. 42, pp. 1391-1405, 2003.
[120] J. J. Doorschot, M. Lehning, and A. Vrouwe, "Field measurements of snow-drift threshold and mass fluxes, and related model simulations," *Boundary-Layer Meteorology,* vol. 113, pp. 347-368, 2004.
[121] J. Nyvlt, *Kinetics of industrial crystallization*: Elsevier; Elsevier Science Pub. Co., Inc.[distributor], 1984.
[122] A. Myerson, *Handbook of industrial crystallization*: Butterworth-Heinemann, 2002.
[123] P. W. Egolf, A. Kitanovski, D. Ata-Caesar, E. Stamatiou, M. Kawaji, J.-P. Bedecarrats*, et al.*, "Thermodynamics and heat transfer of ice slurries," *International Journal of Refrigeration,* vol. 28, pp. 51-59, 2005.
[124] M. J. Wang, S. Sugiura, and V. Goldstein, "Latest development of ice slurry applications," presented at the 8th Conference on PCMS and Slurries for Refrigeration and Air Conditioning, Karlsruhe, Germany, 2009.
[125] P. Pronk, C. I. FERREIRA, and G. Witkamp, "Melting of ice slurry in a tube-in-tube heat transfer coil," *Natural working fluids,* vol. 6th, 2004.
[126] R. N. Wenzel, "Resistance of solid surfaces to wetting by water," *Industrial & Engineering Chemistry,* vol. 28, pp. 988-994, 1936.

[127] A. Saito and S. Okawa, "Fundamental research on initiation of freezing of supercooled water on heat transfer surface," *Heat Transfer,* pp. 121-126, 1994.
[128] S. Okawa, A. Saito, and H. Suto, "The experimental study on freezing of supercooled water using metallic surface," *International journal of refrigeration,* vol. 25, pp. 514-520, 2002.
[129] R. Parkinson, "Properties and applications of electroless nickel," *Nickel Development Institute,* vol. 37, 1997.
[130] S. Jones, G. Evans, and K. Galvin, "The cycle of bubble production from a gas cavity in a supersaturated solution," *Advances in Colloid and Interface Science,* vol. 80, pp. 51-84, 1999.
[131] S. F. Jones, G. M. Evans, and K. P. Galvin, "Bubble nucleation from gas cavities — a review," *Advances in Colloid and Interface Science,* vol. 80, pp. 27-50, 2/28/ 1999.
[132] T. J. Jarvis, M. D. Donohue, and J. L. Katz, "Bubble nucleation mechanisms of liquid droplets superheated in other liquids," *Journal of Colloid and Interface Science,* vol. 50, pp. 359-368, 2// 1975.
[133] N. Bulanov and B. Gasanov, "Characteristic features of the boiling of emulsions having a low-boiling dispersed phase," *Journal of Engineering Physics and Thermophysics,* vol. 79, pp. 1130-1133, 2006.
[134] N. Bulanov, B. Gasanov, and E. Turchaninova, "Results of experimental investigation of heat transfer with emulsions with low-boiling disperse phase," *High temperature,* vol. 44, pp. 267-282, 2006.
[135] A. Das, P. Das, and P. Saha, "Performance of different structured surfaces in nucleate pool boiling," *Applied Thermal Engineering,* vol. 29, pp. 3643-3653, 2009.
[136] R. L. Webb and N.-H. Kim, *Principles of enhanced heat transfer*: New York, Wiley, 1994.
[137] R. M. Milton, "Heat exchange system with porous boiling layer," ed: Google Patents, 1971.
[138] J. Arshad and J. Thome, "Enhanced boiling surfaces: heat transfer mechanism and mixture boiling," in *Proceedings of ASME-JSME Thermal Engineering Joint Conference*, 1983, pp. 191-197.
[139] W. Nakayama, T. Daikoku, H. Kuwahara, and T. Nakajima, "Dynamic Model of Enhanced Boiling Heat Transfer on Porous Surfaces—Part I: Experimental Investigation," *Journal of Heat Transfer,* vol. 102, pp. 445-450, 1980.
[140] W. Nakayama, T. Daikoku, H. Kuwahara, and T. Nakajima, "Dynamic model of enhanced boiling heat transfer on porous Surfaces—Part II: Analytical modeling," *Journal of Heat Transfer,* vol. 102, pp. 451-456, 1980.
[141] W. Nakayama, T. Daikoku, and T. Nakajima, "Effects of pore diameters and system pressure on saturated pool nucleate boiling heat transfer from porous surfaces," *Journal of Heat Transfer,* vol. 104, pp. 286-291, 1982.
[142] P. Griffith and J. D. Wallis, "The role of surface conditions in nucleate boiling," Cambridge, Mass.: Massachusetts Institute of Technology, Division of Industrial Cooperation, 1958.
[143] S. Khorsand, K. Raeissi, and F. Ashrafizadeh, "Corrosion resistance and long-term durability of super-hydrophobic nickel film prepared by electrodeposition process," *Applied Surface Science,* vol. 305, pp. 498-505, 6/30/ 2014.
[144] I. K. Smith, N. Stosic, and C. A. Aldis, "Lysholm machines as two-phase expanders," presented at the International Compressor Engineering Conference, Purdue University, School of Mechanical Engineering, 1994.
[145] N. Stosic, I. K. Smith, and A. Kovacevic, "A twin screw combined compressor and expander for CO2 refrigeration systems," 2002.
[146] B. R. Koci, "Hot water drilling in Antarctic firn, and freezing rates in water-filled boreholes," DTIC Document, 1984.
[147] K. Makinson, "The BAS hot water drill: development and current design," *Cold regions science and technology,* vol. 22, pp. 121-132, 1993.
[148] I. Collaboration, "First year performance of the IceCube neutrino telescope," *arXiv preprint astro-ph/0604450,* 2006.

[149] M. Craven, I. Allison, R. Brand, A. Elcheikh, J. Hunter, M. Hemer*, et al.*, "Initial borehole results from the Amery Ice Shelf hot-water drilling project," *Annals of Glaciology,* vol. 39, pp. 531-539, 2004.
[150] T. Jacka, "The time and strain required for development of minimum strain rates in ice," *Cold Regions Science and Technology,* vol. 8, pp. 261-268, 1984.
[151] M. D. Eisaman, K. Parajuly, A. Tuganov, C. Eldershaw, N. Chang, and K. A. Littau, "CO_2 extraction from seawater using bipolar membrane electrodialysis," *Energy & Environmental Science,* vol. 5, pp. 7346-7352, 2012.
[152] K. S. Lackner and F. S. Zeman, "Systems and methods for extraction of carbon dioxide from air," 2010.
[153] K. S. Lackner, H.-J. Ziock, and P. Grimes, "Carbon dioxide extraction from air: Is it an option?," presented at the 24th International Conference on Coal Utilization & Fuel Systems, Clearwater, Florida, 1999.
[154] F. S. Zeman, "An investigation into the feasibility of capturing carbon dioxide directly from the atmosphere," presented at the Second Annual Conference on Carbon Sequestration, paper, 2003.
[155] M. Ha-Duong, M. J. Grubb, and J.-C. Hourcade, "Influence of socioeconomic inertia and uncertainty on optimal CO2-emission abatement," *Nature,* vol. 390, pp. 270-273, 20-Nov-1997.
[156] M. Ha-Duong, D. W. Keith, and J. K. Stolaroff, "Climate strategy with CO2 capture from the air," *Climatic Change,* vol. 74, pp. 17-45, 2005.
[157] O. Yamamuro and H. Suga, "Thermodynamic studies of clathrate hydrates," *Journal of Thermal Analysis and Calorimetry,* vol. 35, pp. 2025-2064, 1989.
[158] K. Hand. (2002) Air clathrate hydrate formation in Antarctic sub-glacial lakes. *GES?* 26.
[159] A. Yokozeki, "Solid–liquid–vapor phases of water and water–carbon dioxide mixtures using a simple analytical equation of state," *Fluid phase equilibria,* vol. 222–223, pp. 55-66, 2004.
[160] S. L. Miller, "Clathrate hydrates of air in Antarctic ice," *Science,* vol. 165, pp. 489-490, 1969.
[161] S. D. Larson, "Phase studies of the two component carbon dioxide-water system involving the carbon dioxide hydrate," University of Illinois, Urbana, 1955.
[162] S. Adisasmito, R. J. Frank, and E. D. Sloan, "Hydrates of carbon dioxide and methane mixtures," *Journal of Chemical & Engineering Data,* vol. 36, pp. 68-71, 1991/01/01 1991.
[163] M. Wendland, H. Hasse, and G. Maurer, "Experimental pressure-temperature data on three- and four-phase equilibria of fluid, hydrate, and ice phases in the system carbon dioxide-water," *Journal of Chemical & Engineering Data,* vol. 44, pp. 901-906, 1999.
[164] G. K. Anderson, "Enthalpy of dissociation and hydration of carbon dioxide hydrate from the Clapeyron equation," *J Chem. Thermodynamics,* vol. 35, pp. 1171-1183, 2003.
[165] G. K. Anderson, "Solubility of carbon dioxide in water under incipient clathrate formation conditions," *J. Chem. Eng. Data,* vol. 47, pp. 219-222, 2002.
[166] E. J. Beck, "Ocean thermal gradient hydraulic power plant," USA Patent US 6,202,417 B1, 1999.
[167] T. Honjou and H. Sano, "Huge CO_2 storage in Antarctic ice sheet," *Energy Conversion Management,* vol. 36, pp. 501-504, 1995.

Appendices

2-A	**Working fluid thermophysical properties**	**132**
2-B	**Liquid refrigerant pump**	**133**
2-C	**Seawater thermophysical properties**	**134**
2-D	**Characteristic salinity**	**135**
2-E	**Continuous properties model**	**136**
2-F	**Ice slurry loop control**	**137**
2-G	**Ice slurry classifier**	**141**
2-H	**Ice crystal nucleation**	**143**
2-I	**Ice crystal growth**	**146**
2-J	**Glaciothermal heater**	**148**
2-K	**Vapour bubble nucleation**	**154**
2-L	**Twin screw expander**	**158**
2-M	**Glaciothermal engine summary**	**160**
5-A	**Potential augmentation methods**	**162**
5-B	**Year round augmented power**	**168**
5-C	**Potential large scale augmentation methods**	**171**
5-D	**Miscellaneous findings**	**175**
5-E	**Future work**	**176**

2-A Working fluid thermophysical properties

Various utilities were developed for real time retrieval and conversion of thermophysical data. The NIST Standard Reference Database 23 [106], version 9.1, REFPROP DLL was installed, along with the **refpropm.m** utility for real time retrieval of air, water and working fluid thermophysical property data in MATLAB.

Output of selected working fluid thermophysical data is presented in Fig. 2A-1 to 2A-2 below:

Latent heat of vaporisation

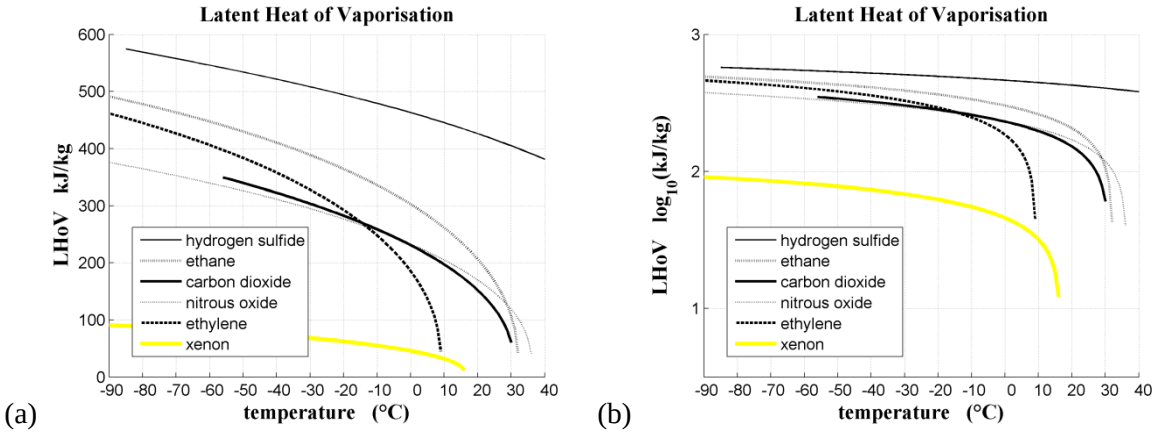

Fig. 2A-1. Latent heat of vaporisation of natural working fluids across extended temperature domain.

Fluid density

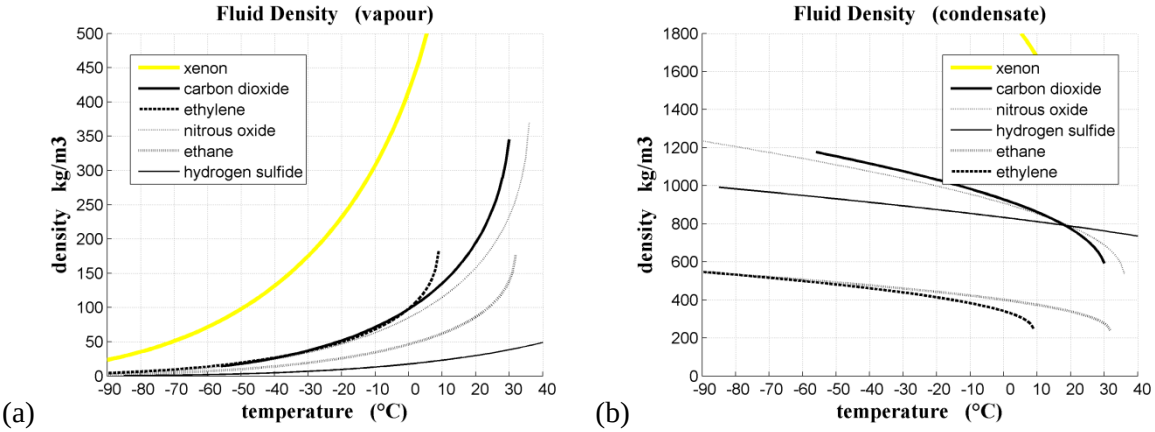

Fig. 2A-2. Working fluid densities for (a) vapour and (b) condensate.

2-B Liquid refrigerant pump

A commercial self-priming liquid refrigerant pump is required that is appropriately certified to operate with the selected high pressure working fluids – nominally ethane and/or carbon dioxide. Nominal evaporator temperature is -5 °C and pressures may vary up to 50 bar depending on the fluid. Condenser temperature is variable down to -80 °C. Appropriate refrigerant pressurisation, purging and recovery systems would need to be provided, along with lubrication oil recovery and inlet strainer. An efficient pump with good quality seals, minimum line restrictions, and steady flow is ideal [107].

A separate sub-cooler may not be required to suppress cavitation on the suction side if the returning condensate is sufficiently colder than the equivalent boiler saturation temperature.

2-C Seawater thermophysical properties

Various utilities were developed in MATLAB for real time retrieval and conversion of seawater thermophysical data. The GSW Oceanographic Toolbox was downloaded [http://www.teos-10.org/] and provides continuous seawater and ice property data down to -7.7 °C according to the Thermodynamic Equation Of Seawater – 2010 standard, as published by the Intergovernmental Oceanographic Commission [99]. Seawater brines at various diluted concentrations are the only aqueous solutions used in glaciothermal ice slurry mixtures. The TEOS-10 continuous enthalpy data for ice and brine phases agree well with earlier published ice slurry datasets of Melinder & Ignatowicz [108].

As described by Sharqawy et al [95], thermal conductivity data for seawater brine is derived from an empirical correlation by Jamieson & Tudhope (1970) [109], and of ice from Landaeur & Plumb (1956) [110]. The best fit curve for pure water viscosity data of IAPWS 2008 [111] has a maximum deviation of ±0.05% and although only guaranteed between 0 and 180 °C, the same correlation function still returns useful viscosity values at temperatures below 0 °C. The function closely reproduced the viscosity data of White-Twining (1914) [112] (as quoted on page F-37 of the CRC Handbook of Chemistry and Physics 69th Edition) and accurate to < 1% for zero salinity seawater at temperatures between 0 and -9.3 °C (i.e. supercooled freshwater). The pure water viscosity data of IAPWS 2008 is also used to normalise seawater viscosity datasets of Fabuss [113], Isdale et al [114], and Millero [115]. The resulting best fit curve for seawater dynamic viscosity has a maximum deviation of ±1.5% from the measured data.

2-D Characteristic salinity

Seawater ice-slurry mixtures are modelled here as a two phase alloy of ice and brine. For an alloy mixture the different molecular species form separate phases upon solidification. In this case, water separates from salt as ice freezes out of the seawater brine. MATLAB routines have been written to calculate the physical properties of each phase in turn, and of the combined ice-slurry mixture.

Mixing and separation of different mass flows within the ice-slurry loop means that a method is needed to characterise different mixtures. A simple way to distinguish seawater brine ice-slurries is to refer to their specific salt content. Any change in the specific salt content comprises a new mixture. For convenience we define the characteristic salinity $S100$ of an ice brine mixture as the salinity in g/kg that would be measured if the mixture was to melt entirely. The state of any mixture is then uniquely defined as a function of temperature, pressure and $S100$ alone, Fig. 2D-1.

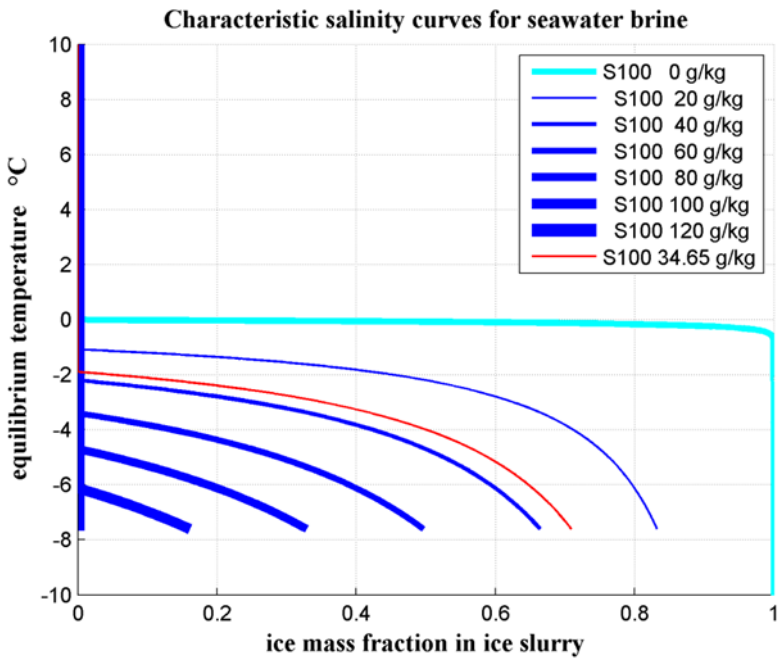

Fig. 2D-1. Characteristic salinity curves for seawater brine at 1 atm pressure. GSW seawater data limit at -7.7 °C.

2-E Continuous properties model

The ice mass fraction at any temperature is readily calculated by noting the brine phase salinity on the seawater salinity liquidus curve, Fig. 2E-1. At any given temperature and specific salt content, the equilibrium salinity dictates the mass of the brine fraction, and thus by difference the ice mass fraction.

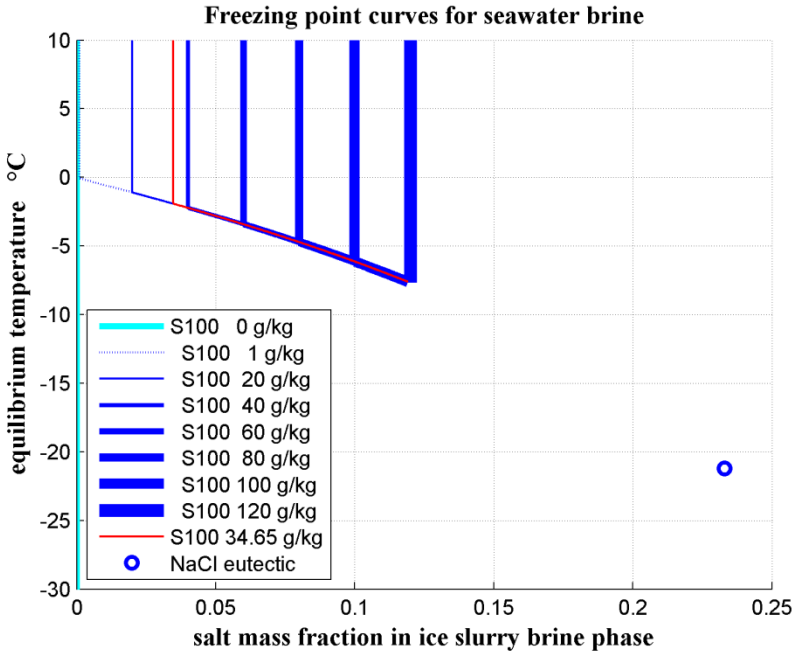

Fig. 2E-1. Salinity liquidus curve for seawater brine at 1 atm pressure. GSW data limit at 120 g/kg salinity.

A problem arises for freshwater, however, because at the freezing point of 0.01 °C the ice fraction is not uniquely defined. We adapt a method proposed by Egolf & Manz [116] to eliminate this discontinuity, and define the ice mass fraction above and below the freezing point according to:

$$C_m = \frac{\tau_2}{\tau}\, e^{(T_{fp}-T)/\tau_2} \qquad T > T_{fp} \qquad \text{(2E.1)}$$

$$C_m = \frac{\tau_2}{\tau} + \frac{\tau_1}{\tau}\,(1 - e^{(T-T_{fp})/\tau_1}) \qquad T \le T_{fp} \qquad \text{(2E.2)}$$

where $\tau = \tau_1 + \tau_2$ (2E.3)

$\tau_1 = 0.05\ ^\circ C$ and $\tau_2 = 0\ ^\circ C$ (2E.4, 2E5)

This formulation generates a continuous exponential curve about the freshwater FP, thus permitting ice slurry properties including ice mass fraction, density and enthalpy to be determined as a continuous function of temperature.

2-F Ice slurry loop control

Regulating seawater and ice flows to the mixer

Regulation of seawater feed and prime ice mass flows in the working engine can be achieved by measuring the mass fraction of either the ice or brine phase at key points within the ice slurry loop. Accurate measurements are required of the seawater feed and prime ice flows entering the mixer, and of ice slurry entering and leaving the ice-in-tube boiler. The relative proportions of ice and brine phases are determined by the seawater brine liquidus curve as a function of temperature. Thus either ice slurry temperature or brine salinity measurements might provide potentially useful proxies.

Flow control by temperature measurements

Unfortunately, control of ice mass fraction by temperature regulation becomes impractical for slurries of low secondary fluid concentration (brine salinity) because the measurement error increases too much as initial freezing point temperatures approach 0 °C [78]. There isn't enough operating range for the traditional control method, Fig. 2F-1. Ice mass fractions rise too high too quickly and may begin to plug equipment. Experience with some falling film ice slurry generators has shown that mechanical damage can result from early formation of flake ice, for example.

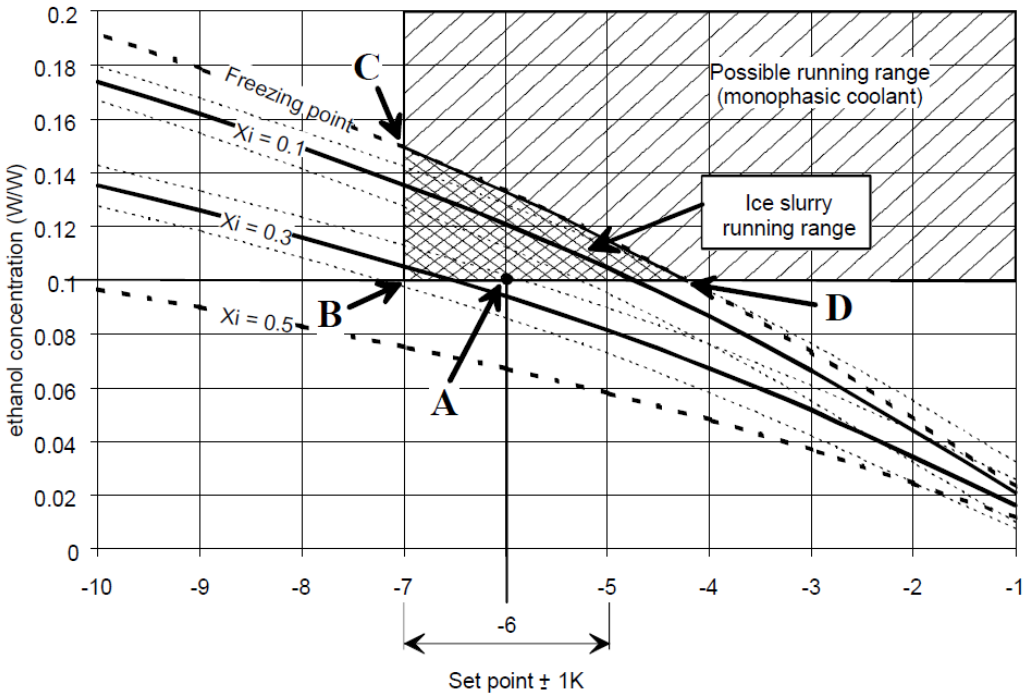

Fig. 2F-1. Operating range for ice slurry loop showing wide set point. ***Copied from Kauffeld et al (2005) [78].***

"It is not recommended to operate in the ice slurry domain at temperatures higher than -3 to -4 °C." Handbook on Ice Slurries, page 285. [78]. Unfortunately for our purposes, ice slurry brines produced from seawater typically freeze in the range -1.9 to -3 °C (and even higher for dilute meltwater slurries). Using temperature measurements to control ice fraction and ice slurry pumping rates may not be appropriate for open loop systems.

Regulation of the ice mass fraction can be better achieved by varying the relative ice slurry to refrigerant flow rate and/or heat flux. In so doing, the ice slurry temperature *results* from the heat and mass flow balance – not the other way around. Weigandt et al [117] adjusted the flow of R114 refrigerant to control ice slurry temperature and ice crystallisation from acetone solutions in their butane freezing process direct contact ISG. *"Concentration of ice slurry leaving the continuous freezer depends on the composition of the overall feed and the slurry temperature."* For a 6.5 wt. % acetone solution and a 0.12 ice mass fraction the equilibrium crystalliser temperature was effectively regulated at -2.43 °C by controlling the refrigerant mass flow. Operating experience with a working prototype would soon demonstrate the appropriate refrigerant and ice slurry flow rates for controlling ice mass fractions within our proposed glaciothermal ice slurry loop.

Flow control by conductivity measurements

Ice slurry brines become more concentrated in salt as the ice mass fraction grows. Electrical conductivity measurements might thus permit real time regulation of the ice slurry mass fraction. Although the conductivity method faces similar measurement sensitivity issues for low salinity brines, Fig. 2F-2, it has the advantage that salinity is a direct measure of actual freezing. The temperature method is *suggestive* of freezing state but is blind to supercooling effects. Hansen (2002) notes two patent applications relating to measurement of electrical conductivity in ice slurry carrier fluids [118]. A patent application by Integral (Germany) relates to measurement of the electrical conductivity in the carrier fluid with respect to additive concentration. A patent application by Chicago Bridge and Iron Company (USA) relates to the same method, but specifically in relation to salt ions as the additive.

Electrical conductivity measurements

Use of electrical conductivity to measure the *practical salinity* of seawater is an established technique in oceanography. Conductivity probes are available off the shelf and can be accurately calibrated. Ice mass fractions within the ice slurry loop can be accurately determined if precise salinity estimates are available for both the seawater feed and mixed ice slurry, Fig. 2F-2(b). The release of more or less prime ice from the classifier may be automated by control of a metering valve to maintain the desired seed ice fraction, Fig. 2.9.

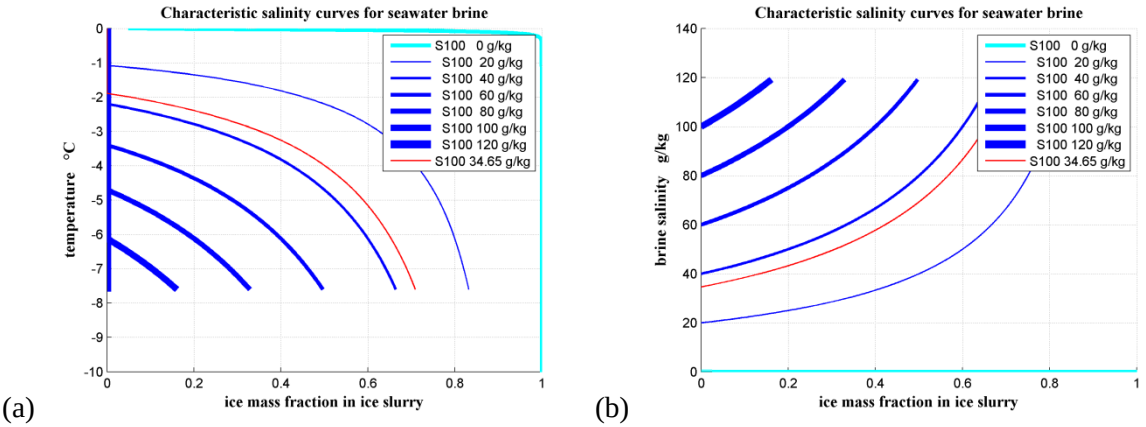

(a) (b)

Fig. 2F-2. Ice slurry freezing curves for (a) temperature and (b) brine salinity as a function of ice mass fraction.

Ice separation

Ice slurry phases will separate if a minimum flow velocity is not maintained at all times so pumping rates need to be closely monitored. Separation of ice particles from the brine carrier fluid can cause blockage of pipes.

Flow velocities greater than ~1 m/s are usually turbulent enough to suppress separation [118]. Separation is mitigated by:

- Low ice fraction
- Large pipe diameter
- High ice/brine density ratio
- Less viscous additives
- Large mean crystal size (especially older slurries)
- Velocities $> 2\ \mu_{min}$

Piping should be dimensioned to avoid velocities lower than twice μ_{min} [118]:

$$\mu_{min} = 1.4 \sqrt{g\ D\ \left(1 - \frac{\rho_{ice}}{\rho_{cf}}\right)} \qquad \text{(2F.1)}$$

where g is acceleration due to gravity, and D is tube diameter.

Ice is also prone to cluster inside the housing of centrifugal pumps if ice concentrations become too high or flow rates too slow. If trials require ice concentrations above 35% an alternative screw pump would become necessary. Pumps are also available with titanium components to resist corrosion by seawater, and motors can include frequency control for continuously variable operation.

On/off actuators are preferred over proportional actuators to avoid ice plugging problems in ice slurry secondary loops. Control of heat exchange units cannot be based on three way valves or throttling devices.

2-G Ice-slurry classifier

The glaciothermal burn produces progressively larger ice grains with each successive loop. At some point the largest grains need to be separated out for crushing and recycling, or to be disposed of within the slush return.

The function of the classifier is to sort the spent ice grains emerging from the glaciothermal boiler tube heat exchanger according to their size, and to direct a measured fraction of appropriately sized prime ice to the ice slurry mixer, Fig. 2.9. Energy and mass balance equations regarding the splitting of spent ice slurry into prime ice and brine slush streams are incorporated within the ice slurry mixer analysis as previously described.

An ice blender is used to crush larger grains down to size. The effect of grain size distribution on the heat transfer process is not specifically modelled. We assume that seeded ice slurry entering the boiler is suitable for glaciothermal heat exchange.

The following processing circuit is proposed to manage ice crystal size distribution, but may prove unnecessary if heat transfer performance is not sensitive to grain size distribution:

Over-size particle separator

The overflow of a reverse settling tank may be used to discharge a lesser fraction of the ice floats. Coarse ice grains predominate in the overflow and the much larger volume flow of fine ice slurry reports to the underflow exit.

Ice-brine separator

The underflow stream is permitted to separate by floatation. The ice fraction is recycled via the prime ice feed and the brine fraction is directed to the slush return line for disposal. Weirs may be adjusted to permit extra-fine particles to exit with the brine fraction.

Splitter

The coarse ice fraction discharged from the over-size separator is fed into a splitter. The forward stream from the splitter is directed to the ice blender for recycling and the opposite stream is sent to the slush return line for disposal.

Ice blender

The forward stream of over-size ice grains is fed through a high speed blender to reduce the mean ice crystal size. Discharge from the blender is looped back to the ice-brine separator (or isothermal coarsening tank) to remove any fines that may have been produced. The speed of the impeller is adjusted to ensure optimal particle size distribution.

Start-up

An external supply of seed ice may be needed at start-up to chill the warm seawater feed down to freezing point. The ice slurry loop must operate with the prescribed seed ice fraction to achieve optimal heat transfer and to avoid supercooling / ice fouling problems within the heat exchanger [91].

Drift snow may be used as seed ice. On the Antarctic plateau the super-fine dry powder snow consists predominantly of elongated particles of mean diameter $11 - 25\ \mu m$ [119]. Drift snow that extends down to the coast may have coarser particles. A study of drift snow in the milder conditions of the Swiss Alps published mean grain sizes in the range $313 - 676\ \mu m$ [120].

Storing seed ice for any length of time is not recommended because small particles invariably freeze together to form a solid mass. Suitable clean snow may be fed through the ice blender to provide fine seed ice. A bypass valve will permit the ice-brine separator to double as an ice slurry mixing vessel during start-up.

2-H Ice crystal nucleation

Two principle mechanisms are identified for the formation of ice crystal nuclei. Homogeneous nucleation refers to ice crystals that are formed spontaneously within the body of a supercooled aqueous solution. Heterogeneous nucleation requires a foreign material to initiate the nucleation. By way of example, in a scraped tube ISG, small dendritic ice grains (A) form by homogeneous nucleation in the body of the ice slurry, and larger slightly flattened grains (B) form by heterogeneous nucleation on the tube wall and are scraped off, Fig. 2H-1.

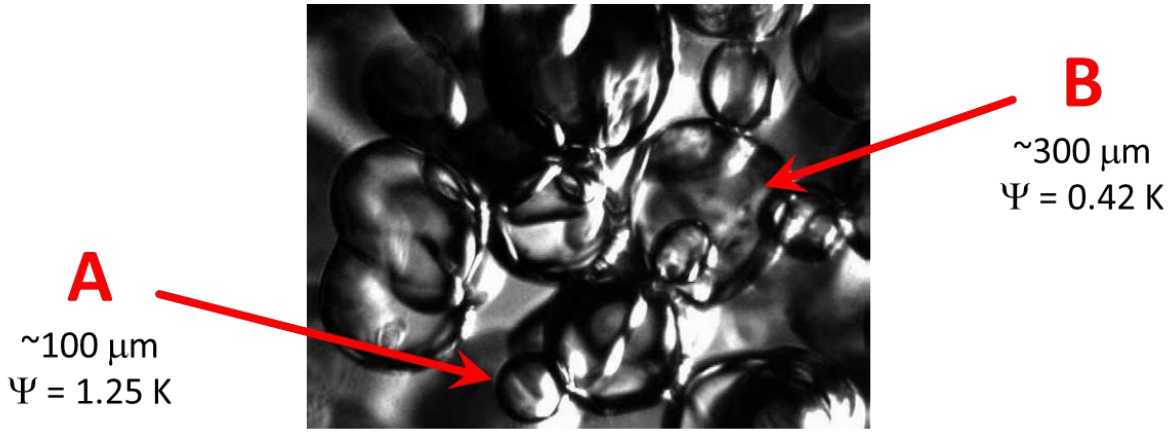

Fig. 2H-1. Supercooling degree for scraped tube ice nuclei. Ice slurry photomicrograph 1,062 x 762 µm, ***taken from Egolf and Kauffeld (2005) [77].***

Both homogeneous and heterogeneous nucleation processes attempt to minimise the Gibbs free energy associated with competing volume free energy and surface free energy components. Under isothermal equilibrium conditions small grains tend to dissolve over time in order to minimise GFE. In Fig. 2H-2, the Gibbs free energy is plotted as a function of nuclei radius according to:

$$\Delta G = -\frac{4}{3}\pi r^3\left(\Delta G_V\right) + 4\pi r^2\gamma_{iw} \qquad (2H.1)$$

where

$$\Delta G_V = \frac{h_f\,\psi}{\mathrm{T_m}} \qquad (2H.2)$$

γ_{iw} is ice-water surface tension, h_f latent heat of freezing, ψ degree of supercooling, and T_m is the melting temperature.

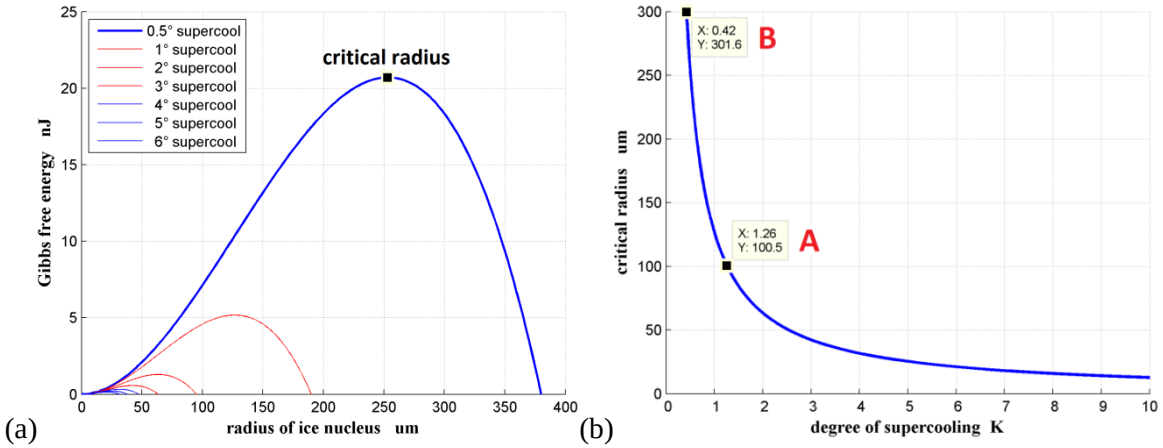

Fig. 2H-2. Radius (a) and critical radius (b) of homogeneous ice nuclei in seawater brine (ice slurry surface tension 0.077 N/m at 38.33 g/kg salinity and -2.1 °C)

For heterogeneous nucleation against a smooth flat surface the change in Gibbs free energy is proportional to the homogeneous nucleation free energy multiplied by a scaling factor f:

$$f = \frac{1}{4}(2 + \cos\theta) \cdot (1 - \cos\theta)^2 \qquad (2H.3)$$

where θ is the contact angle, as plotted in Fig. 2I-3.

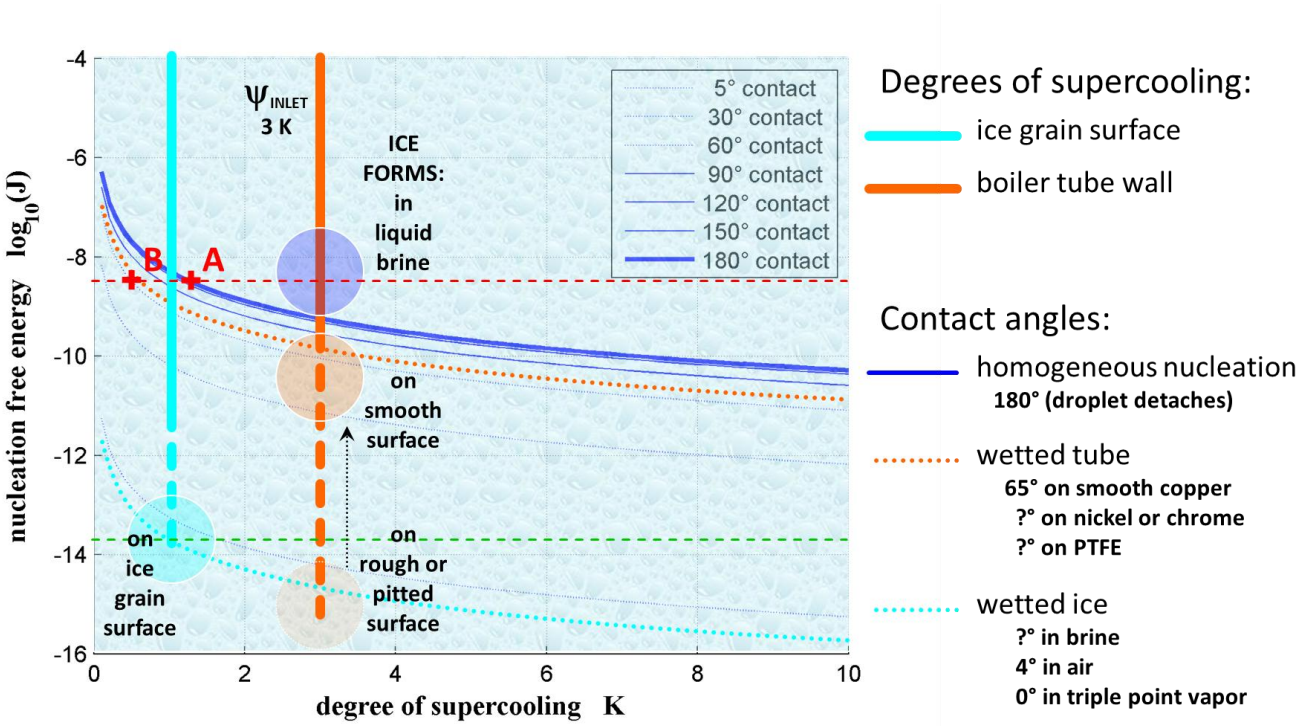

Fig. 2H-3. Free energy of heterogeneous ice nucleation. Ice grain surfaces of low nucleation free energy freeze before wetted smooth tube walls of high NFE, and well before spontaneous crystal formation due to homogeneous nucleation of ice in the liquid brine.

Ice nucleation is a stochastic process [91] and maintaining a low degree of supercooling helps to prevent nucleation on the interior boiler tube walls. The temperature of the working fluid as it vaporises on the flooded evaporator side of the tube determines the degree of supercooling at the tube surface on the ice slurry side.

2-I Ice crystal growth

After an ice nucleus exceeds the critical radius, growth proceeds as additional water molecules are incorporated at the crystal surface. The transport of water molecules through an aqueous solution toward the crystallizing interface is described by a diffusion layer model that considers molecular diffusion through the boundary layer; and incorporation of molecules into the surface layer [78, 121, 122]. The diffusion layer model estimates the rate of growth of an individual ice crystal according to:

$$\frac{dm_c}{dt} = \frac{A \cdot \triangle C}{\frac{\delta}{\mathrm{D}} + \frac{1}{k_i}} \qquad (2I.1)$$

Where m_c is the ice crystal mass, t is time, A is the ice crystal surface area, $\triangle C$ is boundary layer concentration change, δ boundary layer thickness, D boundary layer diffusion coefficient and k_i is the molecular incorporation mass transfer coefficient. The ice crystal growth rate equation is presented here only to demonstrate the effect of different parameters on crystal growth. The equation has not been incorporated into our ice slurry heat transfer model.

It is apparent from this relationship that crystal growth increases in proportion to crystal area and boundary layer concentration change; and in *inverse* proportion to the boundary layer thickness.

We propose to seed our ice slurry mixture with an optimal 10—30 % volume fraction of ice grains to provide a large surface area for crystal growth and latent heat transfer. This keeps the ice slurry mixture near to the freezing point temperature and helps to maintain a steep temperature gradient across the turbulent ice slurry boundary layer, especially for high flow velocities. Experiments with melting ice slurry show that heat transfer is primarily due to latent heat whenever ice slurries contain more than 5—10% ice volume fraction. Increasing the flow velocity and the ice mass fraction up to 30% will help to increase heat transfer [123-125]. Experiments have shown that heat transfer for *melting ice slurries* deteriorates if seed ice volumes drop below 5% and superheating becomes a problem [125]. It is assumed that an analogous relationship holds for *freezing ice slurries* with respect to supercooling.

The proposed seed ice mass fraction of 10 % is quite low relative to the brine fraction and so should help to maintain the high apparent heat capacity necessary for superior heat transfer. Glaciothermal heat derives from the liquid brine fraction that freezes – not from the existing ice fraction. Maximum ice crystal growth rates occur for medium size grains > 0.5 mm. Fine grains < 0.1 mm in the bulk of the ice slurry freeze at a slightly lower temperature and contribute less to the overall heat flow.

2-J Glaciothermal heater

Ice quality

An account of ice crystallisation by Weigandt, Madani and Harriot (1987) [117] notes that ice crystal melting rates increase with grain size up to at least 1mm. They explore ways to increase average crystal size in a laboratory scale direct contact BFP ice slurry crystalliser. Their approach is to either decrease the frequency of secondary nucleation or to destroy or remove small crystals. At very low degrees of supercooling (< 0.01 °C) crystals are observed to grow to moderate size with little secondary nucleation but this is not possible in a practical device.

Their solution instead is to restrict secondary nucleation by limiting ice slurry crystal growth to a short time period then passing the slurry through a holding zone for a short isothermal relaxation period of at least 5 minutes (possibly with some melting to selectively remove the smallest particles) before recommencing growth. This isothermal coarsening method was quite successful for their direct-contact process that operates with a bulk supercooling of 0.02 to 0.05 °C (although locally up to 1 °C in the boundary layer surrounding evaporating refrigerant droplets). They also observe that the dendritic ice crystals formed from secondary nucleation are readily broken up by vigorous liquid shear.

This approach translates well to our glaciothermal process which typically exposes ice slurry to freezing periods of only a few seconds and also relies on high velocity flow to maximise HTC. The ice slurry classifier settling tank doubles as the isothermal holding tank. Spent ice slurry takes only a second or two to reach an isothermal state after leaving the ice-in-tube boiler. A holding tank large enough to permit a residence time of at least 10 minutes would be quite feasible.

Also, ice crystals formed in concentrated brines are typically smaller than those formed at lower salinity. This is a desirable feature of pumpable slurries, but for our purposes pumpability is not the major consideration. Heat transfer rate is most important for glaciothermal power generation and there may be some advantage in using meltwater or diluted seawater over pure seawater feed.

Supercooling degree

Maintaining a low degree of supercooling helps prevent ice fouling of smooth boiler tube surfaces yet still allows existing ice slurry grains to grow. By carefully regulating the ice slurry temperature above the homogeneous ice nucleation point it is anticipated that few new ice nucleii will form in the body of the ice slurry [91]. Any accompanying heterogeneous nucleation on the very smooth boiler tube surfaces might be readily dislodged by the fast flowing slurry.

The ice slurry temperature is held constant by the freezing point of the seawater brine. Departures from the desired low degree of supercooling within the ice slurry can only occur due to changes in the ice slurry flow velocity or to temperature variations on the evaporator side, Fig.'s 3.10 and 3.11. Vaporisation of working fluid at low temperature consumes heat from the freezing ice slurry mixture in contact with the thin copper boiler tubes. Fine control of the evaporation temperature is possible if the boiler pressure can be closely regulated. The pressure of working vapour will vary depending upon the rate of vapour consumption by the expander in response to varying loads. Falling pressures will supress the boiling temperature but also increase the MTD across the heat exchanger thus increasing heat flux and helping to maintain power output of the expander. A high pressure storage vessel between the boiler and expander might also help to smooth out transient pressure variations.

In any event, the inevitable temperature fluctuations will produce irregular degrees of supercooling within the ice slurry flow and restrict evaporator operation to a specific temperature and pressure range. Surplus boiler capacity and ice slurry flows with very high heat transfer coefficients are desirable. High velocity ice slurry flow through thin tubes will maximise the HTC, thus reducing the MTD across the ice slurry and also the degree of ice slurry supercooling.

Ice fouling and adhesion

It is difficult to generate high heat flux in a glaciothermal boiler without freezing the tubes. Pits and other defects in the tube surface provide potential sites for ice nucleation, and surface roughness increases ice adhesion. The critical radius of homogeneous ice nucleation is a function of the degree

of supercooling, Fig. 2D-2 (b). Tiny cavities in the appropriate size range reduce the Gibbs free energy needed to achieve nucleation. Rough surfaces thus increase the likelihood of ice fouling.

The force with which ice adheres to the tube surface also impacts on the ice fouling problem. The strength of adhesive forces acting on a droplet in contact with a solid surface are quantified by the surface adhesion equation of Wenzel [126]:

$$rA = \gamma_2 \cos\theta \tag{2J-1}$$

Where r is the surface roughness factor, A is adhesive force, γ_2 is the liquid surface tension, and θ is the contact angle. The roughness factor is the ratio of rough to smooth surface areas:

$$r = \frac{actual\ surface\ area}{geometric\ surface\ area} \tag{2J-2}$$

Contact angle measurements are traditionally used to determine the surface energy of different materials. Materials of low surface energy are preferred when selecting a surface resistant to ice fouling, Fig. 2D-3. It is clear from Wenzel's equation that surface texture is also important.

Surface roughness increases both the likelihood of ice fouling and the strength of the adhesion. It is highly desirable to provide an ice tube surface that is completely smooth and free of defects.

Ice tube surfaces

Copper tubes provide minimal thermal resistance and are in widespread use for similar heat transfer processes in the refrigeration industry. The nature of the tube surface determines the degree of supercooling that a tube can withstand before the onset of freezing. Ice slurry literature states that ice fouling of porous copper surfaces is not a problem if there is less than 2 K of supercooling [91].

Studies have also shown that polished and/or oxidised copper surfaces may withstand supercooling up to ~8 or 9 K without significant ice fouling [127, 128]. Simple copper tubes might be a good choice except that naked copper is too soft, is prone to abrasion at flow velocities greater than 1.5 m/s; and is prohibited for use in direct contact with seawater in an open loop system due to toxicity and high susceptibility to corrosion. Cupronickel has traditionally been used for heat

exchangers exposed to seawater due to its neutral electronegativity, however, its surface texture and relatively low thermal conductivity may constrain its use in glaciothermal boilers.

Modern surface finishes are available that can overcome these problems and it is proposed that copper tubes be coated on the inside with an appropriate safe, smooth and durable finish. High purity nickel has an amorphous grain structure and can be polished to a very high lustre to reduce ice nucleation but is relatively soft. Chrome plating over polished nickel may provide a more durable and corrosion resistant smooth surface. Electroless nickel (EN) finishes are a less hazardous alternative to traditional chrome plating for providing tough wear resistant surfaces [129]. Composite EN coatings are also available that consist of a nickel-phosphorous matrix deposited from a chemical bath that contains stabilised particulate matter. Particles of industrial diamond and PTFE confer hardness and low friction properties respectively, however, the textured surface this creates is likely to promote ice nucleation and fouling. Industry expertise is sought regarding an appropriate ice repellent finish. Resistance to seawater corrosion might also be achieved with high phosphorous EN coatings.

Even the best quality tubes deteriorate over time and defects may arise. Should a tube start to freeze over, heat transfer will slowly diminish. Once ice has formed at a nucleation site on the tube surface it will continue to grow at an increasing rate. The tube surface is the coldest part of the ice slurry system and ice formation here will eliminate local supercooling within the ice slurry boundary layer and thus retard the normal growth of ice grains in the slurry. A backup strategy is needed to clear any build-up of ice that might occur from time to time on boiler tube surfaces.

Ice removal

Various methods are employed by the different ice slurry generators to manage ice fouling. Removal of ice build-up in fluidised bed ISG's is achieved by mechanical abrasion with circulating steel balls suspended in a vertical ice slurry column [80]. This approach is not only effective in clearing ice, but also improves heat transfer by disrupting the supercooled boundary layer. High velocity jets have also been used successfully to keep tube surfaces free of ice build-up in an experimental supercooling ISG [76].

For our proposed ice-in-tube heater, it is hoped that the combination of a suitable hard smooth tube surface to reduce adhesion; low degree of supercooling to minimise heterogeneous nucleation; and high velocity ice slurry flow to dislodge adhering crystals will be enough to mitigate ice fouling during normal operation. Laboratory or pilot scale experiments are needed to verify this.

A defrosting procedure is improvised in the event that tube surfaces do freeze over. Multiple glaciothermal boiler units are arranged in parallel and their high pressure vapour streams are linked to the expander cluster via a common inlet manifold. This permits individual boilers to be taken offline if the need arises. Defrosting of tube surfaces is easily achieved by purging with warm water. The ice slurry feed to the glaciothermal heater inlet is turned off and ambient seawater is diverted directly through the boiler tubes. A resistive heating element at the inlet to each boiler ensures that the incoming seawater feed is warm enough to fully defrost any frozen tube surfaces. Temporary over-pressure in the evaporator may be moderated by the manifold thus enabling units to stay online as defrosting proceeds. Normal operation of the unit resumes upon restoration of ice slurry flow from the mixer.

Direct contact heat exchange

An ultimate solution to the problem of ice fouling the tube surface is to do away with boiler-tubes altogether. Direct contact of ice slurry with the working fluid permits vigorous heat transfer without the need for any physical interface [117]. Separating the working fluid from the spent ice slush afterwards does, however, present an additional obstacle for a direct contact open loop system.

Vacuum pumping and additional heat are needed to dissociate any clathrate that has formed and the energy requirement increases with increasing condenser temperature. A direct contact glaciothermal boiler may not be feasible for a small-scale engine; however, vapour separation can be achieved by thermal means alone if the ambient temperature is low enough. Condenser pressure alone can extract entrained ethane vapour from clathrate if the outside temperature is colder than about -50 °C; and CO_2 vapour from its clathrate if colder than around -34 °C. This is entirely possible

for devices on the Antarctic plateau where mean winter temperatures are typically much colder than -50 °C.

For our basic 250 kW glaciothermal engine we model the ice-in-tube style heat exchanger.

2-K Vapour bubble nucleation

The general principles of nucleate pool boiling are well understood, but much essential detail is lacking when it comes to modelling complex surface geometries [96]. For nucleate boiling, heat transfer varies in direct proportion to the number of nucleation sites on a heating surface. Vapour bubble nucleation theory explains how the free energy of nucleation varies with the diameter of a nascent bubble, and what the critical radius is for bubble formation at any given degree of supercooling, Fig. 2K-1 (a) [78, 130-134]. The free energy required for a bubble to spontaneously form due to homogeneous nucleation in a liquid is much higher than that required for a bubble to form and grow within a small subsurface pore space given the same degree of supercooling.

The size and shape of re-entrant cavities formed on an enhanced heating surface has a profound effect on the boiler performance for each different fluid. It is very convenient for our purposes that, at a boiler temperature of -5 °C, the three natural refrigerant working fluids, ethane, CO_2, and N_2O all share much the same critical bubble nucleation radii *at 1 K of supercooling*, Fig. 2L-1 (b). A common optimal enhanced surface will thus have pore diameters around ~122 nm (or less depending on the degree of superheating for a given boiler configuration and operating mass flow rates).

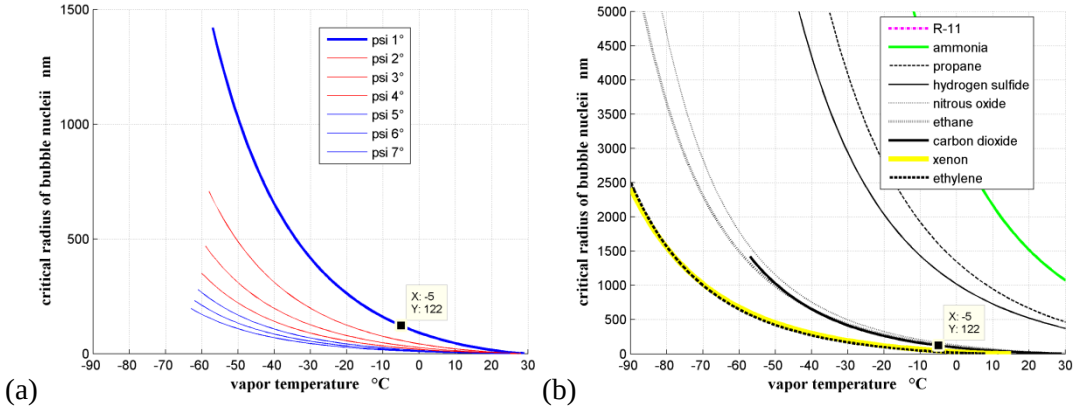

(a) (b)

Fig. 2K-1. Critical radius for homogeneous nucleation of vapour bubble nucleii for (a) CO_2 at various degrees of supercooling and (b) various working fluids at 1 K supercooling.

Enhanced boiling surfaces

Porous and structured surfaces are the two main types of high performance boiling surface geometries discussed in the thermal engineering literature. Other surface treatments that also enhance nucleate boiling heat transfer include chemical etching, electroplating and hydrophobic coatings [84, 135, 136]. Research is ongoing in these areas.

The main principles that govern enhanced surface boiling include:

- re-entrant cavities provide active nucleation sites;
- surface pores supply condensate liquid to subsurface capillaries;
- liquid in contact with EBS surface material needs to be freely wetting [137];
- liquid is heated as it passes through the capillaries;
- thin film evaporation at the liquid-vapour interface within the capillaries is the main heat transfer mechanism [96, 138-141];
- ΔT across the thin film increases as the critical radius increases [137].

Early studies were conducted to understand how to promote incipient boiling with the least degree of superheat. Griffith & Wallace [142] verified that the mouth diameter of re-entrant cavities determines the degree of superheat needed to initiate boiling, and that cavity shape determines boiling stability. Additives may also enhance boiling (e.g. ethanol in the case of steam).

Effective pore diameters of selected manufactured surfaces vary between 0.005 and 0.25 mm, Fig. 2K-2. A mean pore diameter of 0.1 mm is quoted for the Thermoexcel-E enhanced surface, with a channel gap of 0.25 mm quoted for Gewa-T. The porous surface of Union Carbide's High Flux product (presumably similar to that used to boil ammonia in their ocean thermal energy conversion pilot plant [67]) consists of grains of mean diameter around 0.05 mm, or 50 μm. Pore spaces around the inter-granular cavities are thus in the vicinity of, say, ~5 μm. This compares quite well with the 1.5 μm critical radius calculated for ammonia bubbles forming ~ 20 °C in OTEC plant, Fig. 2K-1 (b).

As already demonstrated, required pore diameters for our enhanced surface need to be somewhere around ~125 nm or smaller depending on the degree of supercooling in the evaporator. This is more

than an order of magnitude smaller than the High Flux surface. A much finer porous surface is needed, or an equivalent fine textured surface prepared by chemical etching or electroplating. Further research is needed to identify a suitable process. Estimation of critical heat flux for such porous or etched surfaces by numerical analysis is exceedingly difficult due to the irregular geometry.

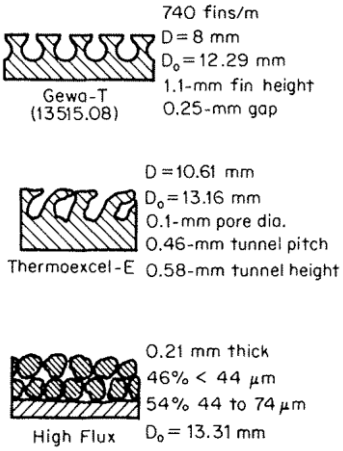

Fig. 2K-2. Indicative dimensions of some structured and porous enhanced boiling surfaces.
Taken from Rohsenow, Hartnett and Cho (1998) [84].

Nano-scale enhanced boiling surfaces

In the absence of a specific commercial product, we might speculate about a process to create nano-scale conical pits on the exterior evaporative surface of our glaciothermal boiler tube. Heat transfer coefficients of nucleate boiling surfaces increase in direct proportion to the number or density of nucleating sites on the surface. Nano-scale conical pits would have the potential to act as nucleating sites on ethane or CO_2 flooded evaporator tube surfaces.

The author does not claim any metallurgical expertise and so cannot guarantee the validity or soundness of the following process. It would, however, appear a straightforward matter to create a partial mould of the nickel micro cone surface texture shown in Fig. 2K-3, by stamping or rolling against a softer metal. Nickel has a high melting point around 1,450 °C and so might readily withstand heating of a few hundred degrees in a neutral atmosphere. A suitable low melting point metal alloy might thus be softened by heating before being lightly stamped with a similar micro cone textured surface. There is no need to produce a perfect mould, merely to produce a comparatively sparse distribution of shallow conical pits with surface diameters of the order of 125 nm or less.

The nickel micro cone surface described by Khorsand et al [143] was intended as a hydrophobic surface coating. Our process would re-purpose the inverted form of the micro cone texture to instead provide vapour bubble nucleation capability. Similar nucleate boiling surfaces have been investigated in the past and require that the surfaces be kept exceptionally clean. This should not be a limiting problem for high positive-pressure closed-loop working fluid cycles. Clogging with minute particles quickly destroys the nucleating ability of the microscopic pits.

Many other textured surface technologies may also have application, including carbon nano-tube treatments. A review of currently available commercial shell-and-tube flooded refrigerant evaporators is needed to identify the best candidate for a glaciothermal boiler. Ideally a device might be found that currently operates with either ethane, CO_2 or N_2O. Units operating with other fluids, but at higher temperatures or superheating degree (where critical radii are lowest) might also possibly fall within the range of optimal pore sizes and appropriate surface energies.

(a) 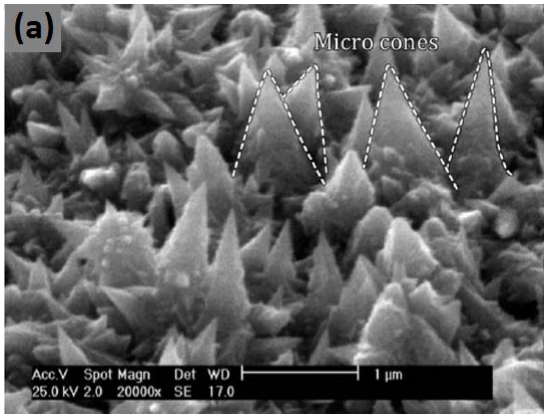

(b) 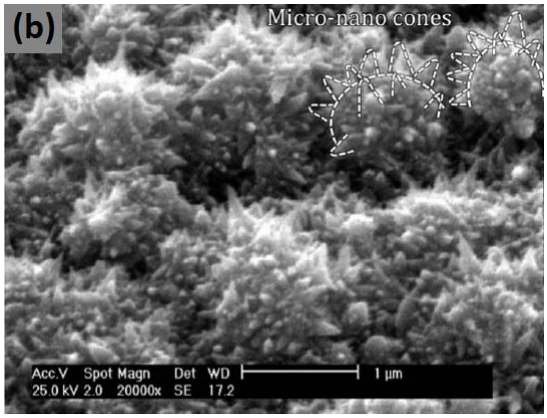

Fig. 2K-3. SEM images of (a) micro and (b) micro-nano cones formed by electro deposition of nickel films on bare copper substrate. ***Taken from Khorsand, Raeissi and Ashrafizadeh (2000) [143].***

2-L Twin screw expander

The twin screw device is commonly used in air compressors and has more recently been adapted for use with organic Rankine cycles in geothermal power generation [81, 144]. Units are readily converted from compressors to expanders by making minor adjustments to the inlet port geometry. Compact twin-screw expanders rated between 300 kW and 3,000 kW claim 70—80% mechanical efficiency for the Trilateral Flash Cycle [81], however, this liquid flash cycle is not as thermodynamically efficient as the standard ORC vapour expansion.

Modelling of dynamic two-phase fluid flows for a twin screw expander has not been undertaken, however, a detailed thermodynamic model including full mathematical analysis is well described in the literature [97]. Indicator and volumetric efficiencies above 80% have been demonstrated experimentally for a 200 kW twin screw ORC expander using R123 and running 3:1 volume ratio.

Overall thermal efficiencies up to 7.5% are quoted for this installation which is fed by 100 °C hot water with mean annual ambient air temperatures around 15 °C. R123 evaporator and condenser temperatures of 78.4 and 37.0 °C respectively provide a Carnot efficiency of 11.8% with respect to the fluid cycle. This equates to an isentropic efficiency of 63.7% for this particular twin screw expander configuration which is very satisfactory for such a small output device. As previously mentioned, twin screw expanders run at high speed without the need for a gearbox or separate bearing lubrication so overall efficiency remains high.

Controlled volume vapour expansion

The glaciothermal boiler produces high pressure ethane (23 bar) or CO_2 (30 bar) vapour streams at -5 °C. Such pressures are considered high for most twin screw expanders and consideration needs to be given to long term reliability under such conditions [145].

The key defining feature of twin screw expanders for our purposes is their inherent reliability. Individual expanders are constructed with fixed volume ratios, however, their compactness and affordability means that multiple units can be installed; thus making it possible to swap from one device to another as ambient temperature changes affect the operating condenser pressure. For some

interior icesheet sites, however, winter temperatures can be relatively constant. A single volume ratio corresponding to the median ambient operating temperatures might be sufficient if efficiency losses due to under- or over-expansion are acceptable. As an example, for sites with average ambient air temperatures around -60 °C a single expander volume ratio of 4—5 X might prove sufficient for ethane or CO_2 condensing around -50 to -55 °C. Condenser mass flows might be regulated to maintain constant condenser pressure across a modest ambient temperature range.

For the above reasons, compact twin-screw expanders are the preferred dual phase expander [97] for small to medium scale (ORC-style) glaciothermal engines.

Electrical generator

Choice of generator is limited for a glaciothermal engine. Under normal circumstances it might be desirable to control power output from this type of expander using a variable speed generator by regulating the working fluid mass flow. This is not an option for units deployed in cold climate regions, however, because variable speed generators (and also doubly-fed induction generators) require room temperature electronic control circuitry which is unsuited to the frigid conditions.

Synchronous generation is preferable because a 2- or 4-pole squirrel cage generator requires much less critical electronics to maintain power output. Any suitable PID might suffice. Geothermal power is typically produced using synchronous generators, but ambient temperatures have less relative impact on the overall efficiency than is the case for glaciothermal systems.

2-M Glaciothermal engine summary

The heating element is critical to the performance of our prototype glaciothermal engine. Ice crystals growing within seawater ice slurry supply the heat that drives the engine. Large ice crystals are preferred as they grow more rapidly than small ones. Convective heat transfer within the ice slurry flow delivers this heat to the boiler tube walls. Various surface coatings may provide the low adhesion surface texture, hardness and corrosion resistance needed for high heat flux under high degrees of supercooling but without ice fouling. Superior heat transfer is due to high apparent heat capacity of ice slurry and is aided by high velocity turbulent flow. Apparent heat capacity is highest for fresh water and reduces with increasing salinity, thus favouring melt water over pure seawater.

The ice slurry loop also needs to supply new ice crystal seeds upon disposal of the larger spent grains. Seed crystals can be produced by various methods. Homogeneous nucleation within ice slurry occurs at high degrees of supercooling and produces small dendritic crystals. Secondary nucleation within the slurry occurs at low supercooling and produces similar dendritic ice. Heterogeneous nucleation directly on cold tube surfaces creates somewhat larger ice particles but these need to be physically removed. All these forms of ice crystal formation are undesirable within the ice slurry loop.

Although the heat sink provided by the evaporator is a convenient way to form new ice crystals the crystals are invariably too small and reduce the efficiency of the heat transfer process. The heating element produces highest heat transfer with uniform large crystals. It would be a mistake to try to optimise the ice slurry loop to achieve seed ice nucleation within the boiler tubes. The glaciothermal heating element needs to be optimised instead for maximum heat generation and heat transfer.

The more effective way to manage seed ice production is to crunch the large spent ice crystals in an ice blender and selectively remove the smaller grains prior to recirculation. This provides a more acceptable grain size distribution. At start-up, seed ice is provided from an external source and run through the blender as needed.

For the shell-and-tube flooded evaporator side of our boiler, optimum heat flux from nucleate boiling is provided by an appropriately matched enhanced boiling surface. A high evaporator HTC

permits lower combined MTD across the boiler which is desirable, but care is needed to ensure that the MTD on the ice slurry side doesn't rise too high as a result and cause supercooling and ice fouling problems. For our chosen working fluids, optimum nucleate boiling performance requires an EBS with nano-scale surface pores. Further research is needed to determine if any such superior surfaces are commercially available. A potential method is outlined to manufacture nano-scale EBS surfaces. Existing evaporative surfaces still provide adequate performance.

Regarding the tube-fin condenser, however, standard off-the-shelf components are all that is required. An all-copper (tube and fin) condenser can be fabricated to specific dimensions to guarantee optimal performance across the extreme temperature range at the coldest polar sites. The thermal expansion differential prevents the use of aluminium fins with copper tubes in Antarctica.

Similarly for the twin screw ORC-style expander, standard off-the-shelf devices are available that will perform very satisfactorily for glaciothermal power generation with our chosen cold temperature working fluids ethane and/or carbon dioxide. In the event that standard units are not exactly to our required specification, it should be possible to build custom units using existing manufacturing methods.

The above analysis demonstrates that a practical thermo-mechanical engine can be built that is capable of generating power from freezing seawater solutions at the ambient temperatures existing in cold climate regions.

Detailed results from the numerical models are discussed in Chapter 3.

5-A Potential augmentation methods

Local and manufactured meltwater

Meltwater may be locally abundant during summer at some cold climate sites, but generating glaciothermal power from pure meltwater is problematic. Salt ions need to be present in ice slurry to prevent neighbouring ice crystals from sticking to each other. In the absence of salt ions, ice crystals tend to agglomerate into a frozen mass and become very difficult to pump. Local meltwater supplies comprise an open system. Addition of salt is problematic and there may be little opportunity to mix meltwater with seawater to create diluted solutions. Local meltwater supplies are likely to be limited in volume, intermittent and seasonally unreliable.

Storage of manufactured meltwater in surface ponds or bells within the ice sheet has much better potential. Extremely high daily insolation makes it possible for dual tracking solar concentrators to generate copious quantities of steam during the three peak months of summer, Fig. 5.1. Steam lances directed into the ice sheet have long been used at interior icesheet sites to melt glacial ice to form meltwater bells for potable water supplies [36]. A large fraction of the meltwater produced will remain liquid throughout the year due to the insulating properties of the bulk ice mass.

Meltwater bells are closed systems so it becomes possible to add modest amounts of salt directly to the ice slurry circuit. Glaciothermal boilers also perform better using diluted seawater mixtures. The lower salinity ice slurry mixture has greater apparent heat capacity than undiluted seawater and thus provides improved heat transfer performance within the glaciothermal heater.

For the purposes of modelling glaciothermal feed water, we can assume that water supplied from a meltwater pond or bell will be at the incipient freezing point. We are free to add salt directly to the mixture and to nominate the initial feedwater salinity. Brine salinity will increase as the spent slush returning from the ice slurry loop becomes progressively more concentrated in salt. We make the reasonable assumption that the total mass of salt in the system will remain constant. The characteristic salinity of the feed water is readily calculated over time.

A 60 m diameter pure meltwater globe stores enough latent heat to sustain >80 kW glaciothermal power for an entire year (assuming 10% nett engine efficiency, ~90% storage efficiency), Fig. 5A-1. Dual tracking solar concentrators of ~7,000 m^2 need 3 summer months to recharge at nett 500 W/m^2. Alternatively, solar absorbers might be used to supply meltwater for a large volume meltwater pond.

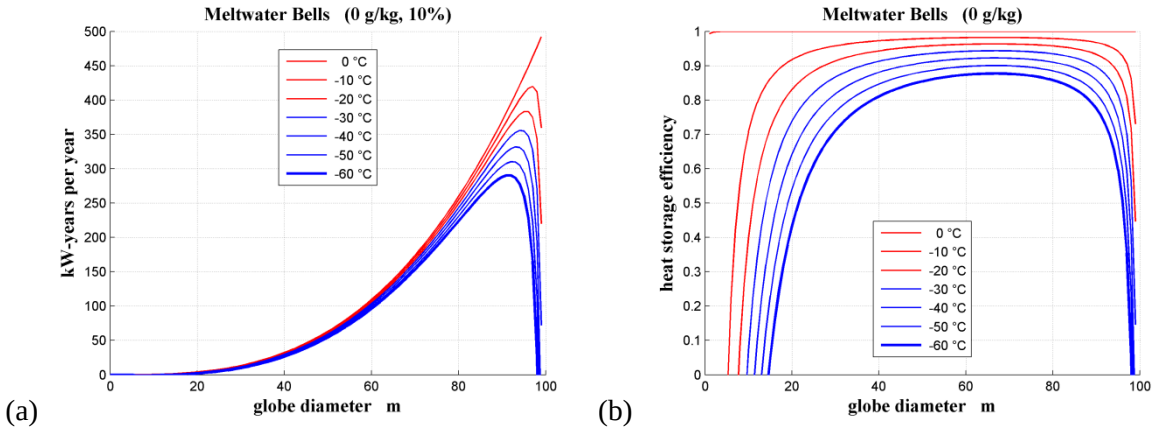

Fig. 5A-1. Glaciothermal power output (a) and thermal storage efficiency (b) of pure meltwater globes at thermal equilibrium as a function of globe (spherical bell) diameter.

Ground source cold storage

It is possible to store cold winter air temperatures by sensible heat transfer to the large thermal mass of the ice sheet. During the coldest weather, fans force frigid ambient air through long open holes (or vents) drilled into the ice and thus lower the ground temperature. This charges the thermal cold store, Fig. 5A-2 (a). Cold ice temperatures can be maintained for extended periods due to the insulating properties inherent in such a large thermal mass. During warm weather conditions, the cold is discharged by reversing the flow of air and directing the chilled air exhaust through the condenser of the glaciothermal engine, Fig. 5A-2 (b). Heat rejected by the condenser only raises the air temperature a few degrees, so the emerging air stream is still cooler than the ambient air and can be recirculated through the ice vents multiple times. The system discharges under closed circulation independently of the outside temperature.

Lack of cold winter temperatures will limit the feasibility of the system at a given site, but warm summer conditions are not a problem if a large enough mass of ice can be sufficiently chilled to

supplement the cold air heat sink. With a 10 K charge, the cold storage device depicted has sufficient thermal mass to support an 80 kW glaciothermal engine of 10% thermal efficiency for 1 month.

The practicality of constructing such a large thermal store depends entirely on the local meteorology and ground conditions. Several kilometres of ice drilling are needed to provide thermal contact with a sufficiently large thermal mass. Drilling rates of 100 m per hour are typical of modern vertical hot water drills [146-149]. Similar speeds might be possible for horizontal drilling if a purpose built rig can be devised to quickly melt away the 25 m long by 25 cm diameter cross-cut vents, Fig. 5A-2 (c). Drilling time for the 36 km (1,770 m^3) of vents depicted in this illustration could be less than 500 hours. Associated tunnels can be extended by coring rather than by melting the entire ice volume. Only a small fraction of the total excavated ice volume of ~21,800 m^3 (including tunnels) need be melted. The extreme mean daily solar insolation of ~500 W/m^2 that prevails high on the icesheet would permit 2,000 m^2 of dual tracking solar concentrators to provide enough steam to melt 10,000 m^3 of cold (-50 °C) ice within a single 3 month Austral summer season.

Ground source thermal storage can potentially provide more consistent cold sink temperatures for reliable continuous power generation and may permit year-round operation at many sites. Stable ice or firn ground conditions are needed for affordable construction of such a large thermal store. Icesheet sites thus offer much greater prospects for year round glaciothermal power generation.

Ice strength is temperature and time dependent and shear-strain rates decrease markedly with decreasing temperature, Fig. 5A-3. [150]. Further research is required to determine the serviceable life of ice and firn tunnels excavated at shallow depth.

In determining the feasibility of glaciothermal engine operation augmented by ice sheet thermal storage we need to model the heat transfer process. Pending finalisation of a precise external transient conduction model for long cylinders we can apply some simplifying assumptions regarding the performance of our ice sheet thermal storage system. Preliminary analysis suggests that for a 10 K air-ice temperature difference, vents within the ice thermal mass achieve ~20 W/m heat transfer when configured for counter-current flow. For mild sites where engine thermal efficiency is low we may

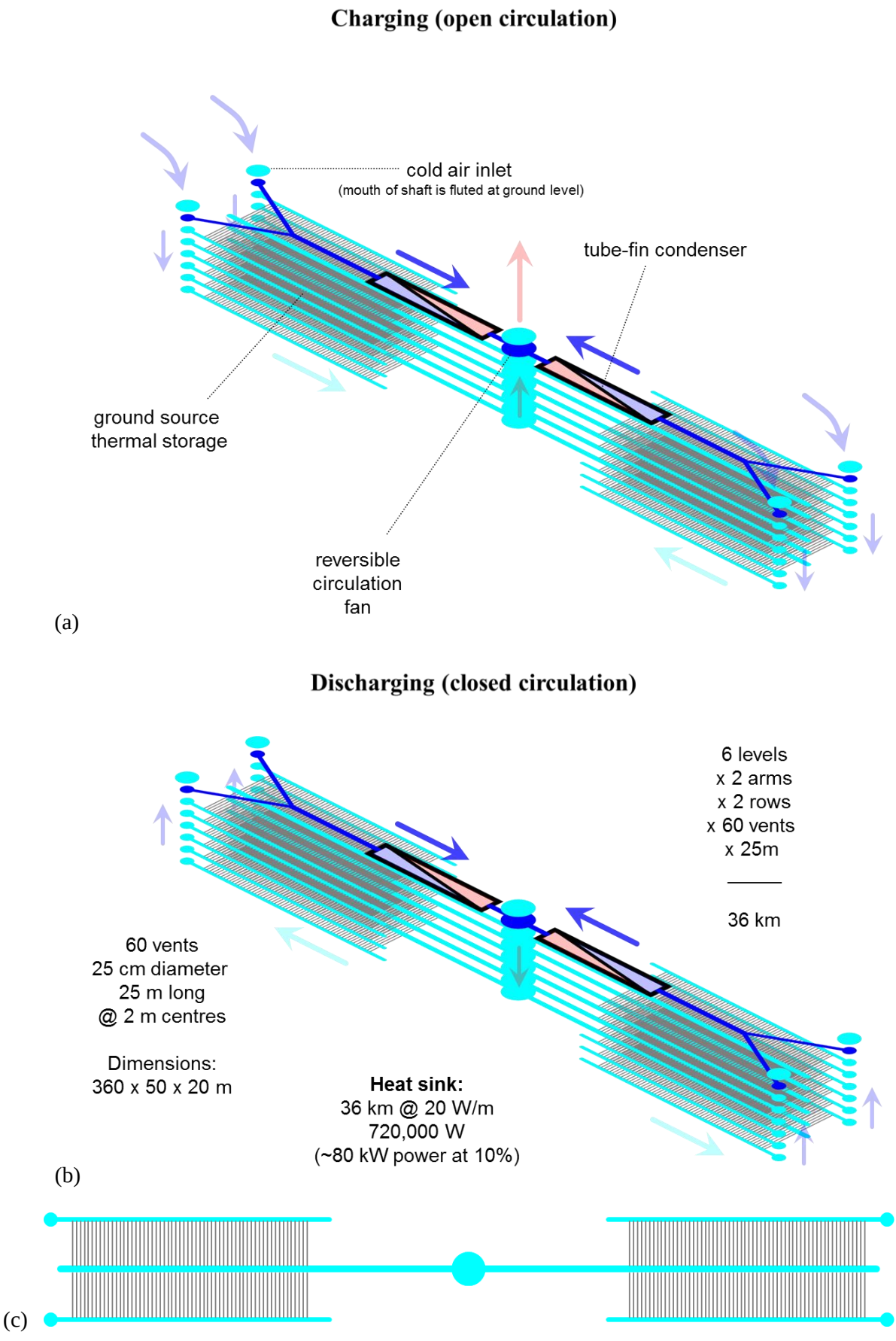

Fig. 5A-2. Proposed ground source thermal storage scaled for 80 kW glaciothermal engine $\eta_{th} = 10\%$

prefer to optimise for lowest heat sink temperature rather than device compactness. Thus, we can double the total length of vents within our prototype GSHX and adopt a more modest 10 W/m at 5 K temperature difference.

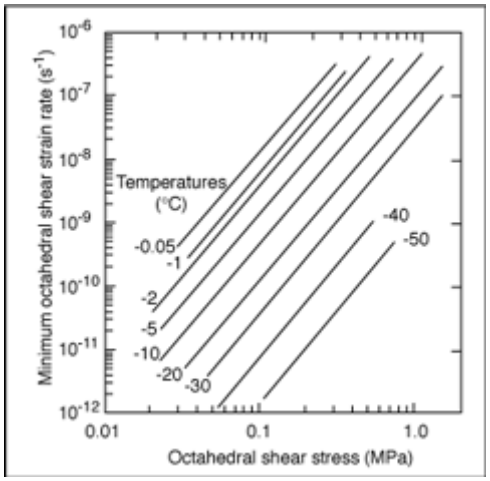

Fig. 5A-3. Shear strain rates for low temperature ice, ***taken from Jacka [150].***

In discharge mode, air circulation is regulated in a closed loop to maintain a constant fixed temperature difference between the glaciothermal engine condenser and the thermal mass of the ice as it warms. By contrast, in charging mode, air circulation is open to the ambient atmosphere and the temperature difference is quite variable. In practice, however, the ice chest temperature cools down with the season and charging only takes place when the outside air is more than 5 K colder than the ice vent walls anyway. Colder relative temperatures only improve the heat transfer performance, so a fixed 5 K difference is conservative.

Required fan work is estimated by cross-referencing the glaciothermal engine efficiency to the GSHX thermal performance according to the mass flow rate of air required at the condenser. Depending on ambient temperature conditions the augmented glaciothermal power plant operates in one of four modes, as depicted in Fig. 5A-4. If the air is more than 5 K colder than the ice chest the open circulation fan is switched on to charge. The condenser for the engine runs simultaneously, but with a separate ambient air stream. If the air temperature is warmer than the ice chest but still below the designated charging temperature, then the ice chest circulation fan is switched off and the condenser continues to run directly on ambient air. When the air temperature rises above the rated

temperature of the engine the closed circulation fan ensures that cold is discharged from the thermal store. Eventually the ice becomes too warm to support the duty cycle of the condenser and the glaciothermal engine must either shut down or swap to another heat sink.

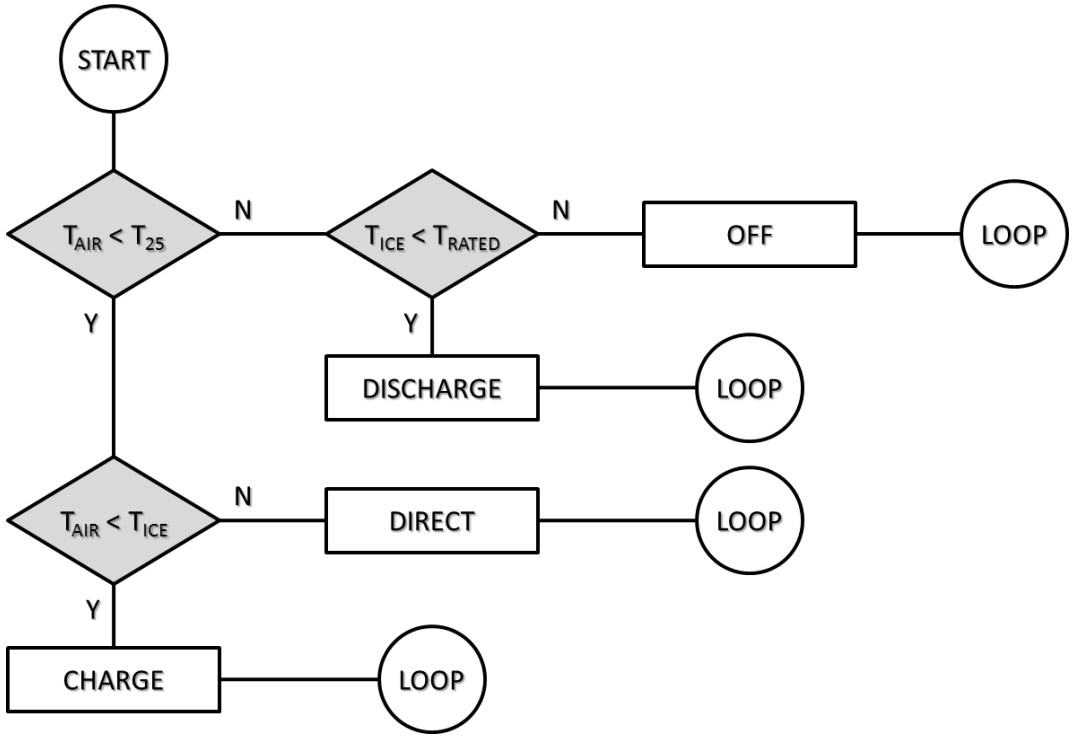

Fig. 5A-4. Control logic for operation of glaciothermal engine in conjunction with ice sheet thermal storage.

5-B Year round augmented power

In the event that thermal storage systems within the ice sheet can readily provide both heat source and heat sink capabilities, then year round glaciothermal power generation at many sites is all but guaranteed, Fig. 5.1. Integration of glaciothermal energy within hybrid diesel-wind-solar power systems becomes a moot point.

If ambient conditions are cold enough to run a glaciothermal engine for 3 months of the year or more, then they are also able to charge ground source thermal storage for year round operation. Operation at coastal oases sites is a likely exception, however, because ground source thermal storage is not affordable if vents need to be excavated within rock. In this case, however, winter temperatures are not typically cold enough to permit economic operation of glaciothermal plant anyway.

Interior sites

Using solar concentrators to raise steam for meltwater production during summer is not difficult at most high elevation interior sites due to the exceptional 24 hour summer-time insolation, Fig. 5.1. The extreme cold winter temperatures guarantee efficient operation of the glaciothermal engine and ensure that meltwater demand is not excessive. Potential for affordable year round glaciothermal power output is excellent.

Ross Ice Shelf

Cloudy conditions do not pose a problem for glaciothermal plant located on Ross Ice Shelf because the availability of seawater immediately below means there is no requirement to produce meltwater, Fig. 5B-1. Our analysis has demonstrated that performance of the stand-alone basic glaciothermal engine will be satisfactory for at least six months of the year. Whether or not glaciothermal power can be provided year round though depends on the availability of suitable ice conditions for the construction of GSHX. Stable blue ice areas on the icesheet are ideal, but there is some question about the structural integrity and dynamic stability of ice shelf material. It may not be possible to safely drill or excavate a stable GSHX installation.

If it is possible to install ground source heat exchange at a suitable location then year round operation may be feasible providing the installation is large enough. Slightly warmer winter temperatures on the ice shelf compared to the plateau mean that the basic glaciothermal engine will be less efficient and thus require larger condensers and greater GSHX capacity.

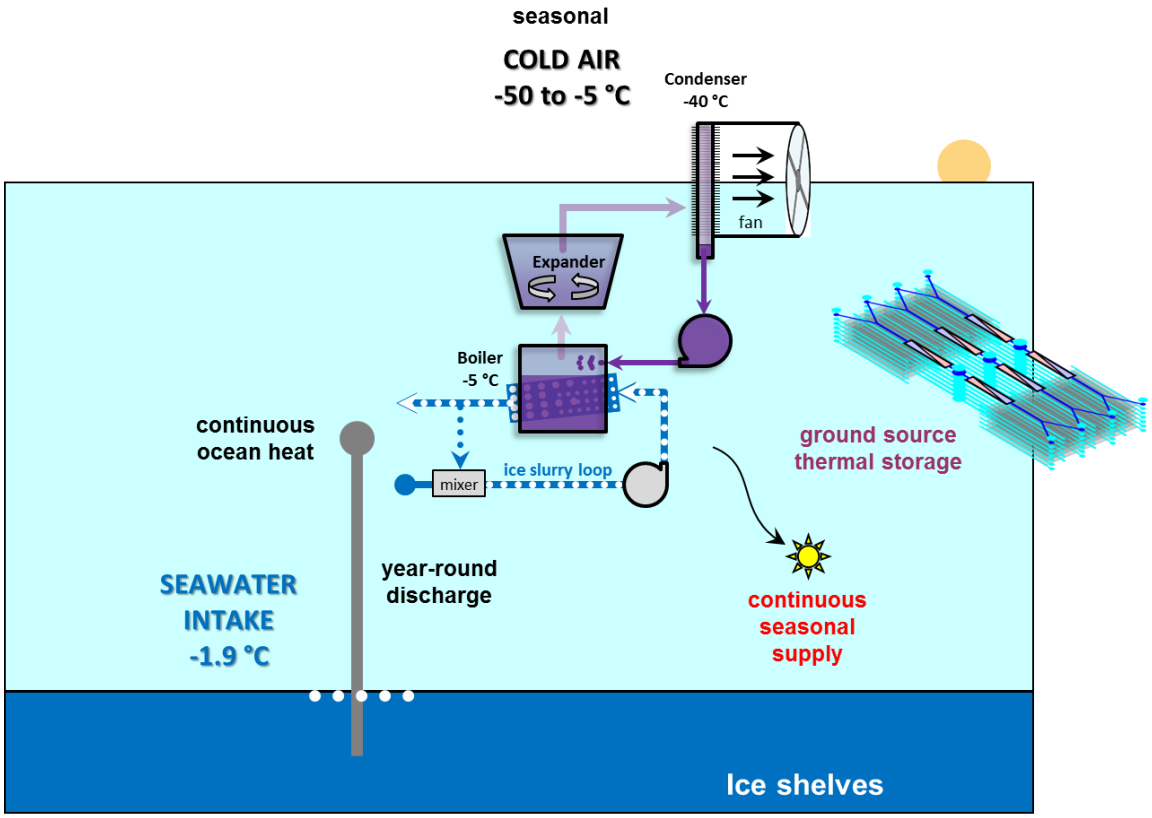

Fig. 5B-1. Seawater and ground source thermal storage for ice shelf sites.

Oasis sites

Mild winter temperatures seriously constrain the operation of glaciothermal power systems at coastal oasis sites, however, colder temperatures are often available a short distance up on the ice sheet. Low thermal efficiency means that less power output is possible for a given glaciothermal engine. Engine components thus need to be scaled up or replicated in order to maintain a given nominal output. This means large expanders, multiple boilers and condensers, and additional meltwater supply and heat sink capacity, Fig. 5B-2 (a) and (b).

Parasitic losses from ice slurry pumps and condenser and ground source fans become a critical limiting factor. An increasingly large mass of air needs to be pumped through the ice sheet heat

exchanger and this dictates low velocity air flow in order to minimise fan losses. Decreasing the flow velocity means that ice tunnel cross-sectional areas must also increase in proportion to maintain overall mass flow. The systems quickly grow in size and become less economic.

The supply of meltwater is doubly affected. Low engine efficiency increases the meltwater consumption for a given power output thus increasing the demand for steam from solar concentrators over summer. Solar thermal heat availability (as steam or hot water) is excellent on the high plateau due to the extraordinarily clear air, cloud free conditions and 24 hour continual sunshine. Shorter days and cloudy conditions at coastal sites substantially reduce the output of individual solar collectors.

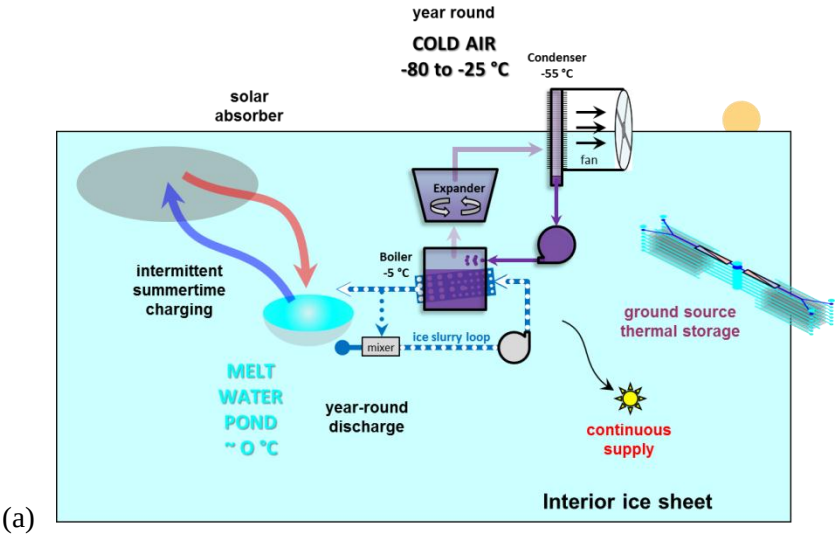

(a)

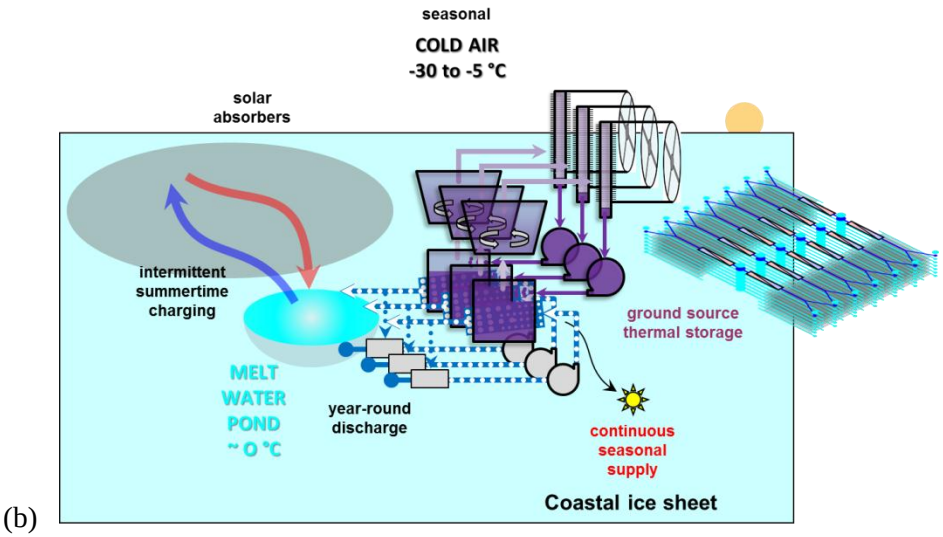

(b)

Fig. 5B-2. Exponential growth in size of glaciothermal engine components, feedwater and thermal storage devices with mild ambient temperatures at coastal sites (b) compared to frigid interior sites (a).

5-C Potential large scale augmentation methods

Direct contact glaciothermal boilers

In much the same way that droplet sprays can potentially replace expensive copper tube fin condensers, direct contact glaciothermal boilers can potentially do away with expensive copper boiler tubes (although glaciothermal boilers use much less copper tube than tube fin condensers).

Multi-component, multi-phase flows involve exceedingly complex dynamic heat and mass flows and similar systems are beginning to be modelled using CFD [77]. Earlier empirical research suggests that feed water to working fluid MTD's are less than 1 K for direct contact evaporators [117].

Two modes of operation are envisaged:

1. Ice injection method
2. Mixture injection method

The *ice injection method* is essentially the same mass flow regime as the ice slurry loop for an ice-in-tube glaciothermal boiler, but without the copper tube. The seeded ice slurry mixture is roughly blended with incoming preheated condensate and allowed to flash boil as it rises upwards through a vertical flash chamber. Condensers at the top maintain low exhaust pressure as normal.

For the *clathrate injection method* an ice slurry loop is not employed at all. Instead, the feed water and working fluid phases are mixed much more vigorously to form a fine emulsion. Heat transfer occurs by diffusion of working fluid molecules into a solid clathrate host at the water-fluid interface. The clathrate crystallises at the high temperature Q_2 point, a few degrees warmer than ice at the Q_1 point, Fig. 5C-1 and Table 2.1. This potentially raises the boiling point temperature of working fluid and thus improves the thermal efficiency of the resulting augmented glaciothermal engine cycle.

Much more clathrate is formed by the clathrate injection method than is formed by the ice injection method. The key challenge with either method is to dissociate all the clathrate prior to discharging the spent ice slush into the ambient environment. This problem is potentially much

simpler to solve if the power generation cycle is run in conjunction with a BPMED [151] or DAC [152-156] loop which has the intrinsic capability to remove CO_2 dissolved in water. The feasibility depends upon the nett energy balance of the combined processes.

Preliminary calculations suggest that the above direct contact methods have potential application for large scale power generation and CO_2 capture systems, however, the concept remains speculative until sufficient research is carried out. Clathrate ices formed during the heat transfer process need to be separated by vacuum pumping. It is possible that the phase separation challenges may prove unworkable and thwart the concept.

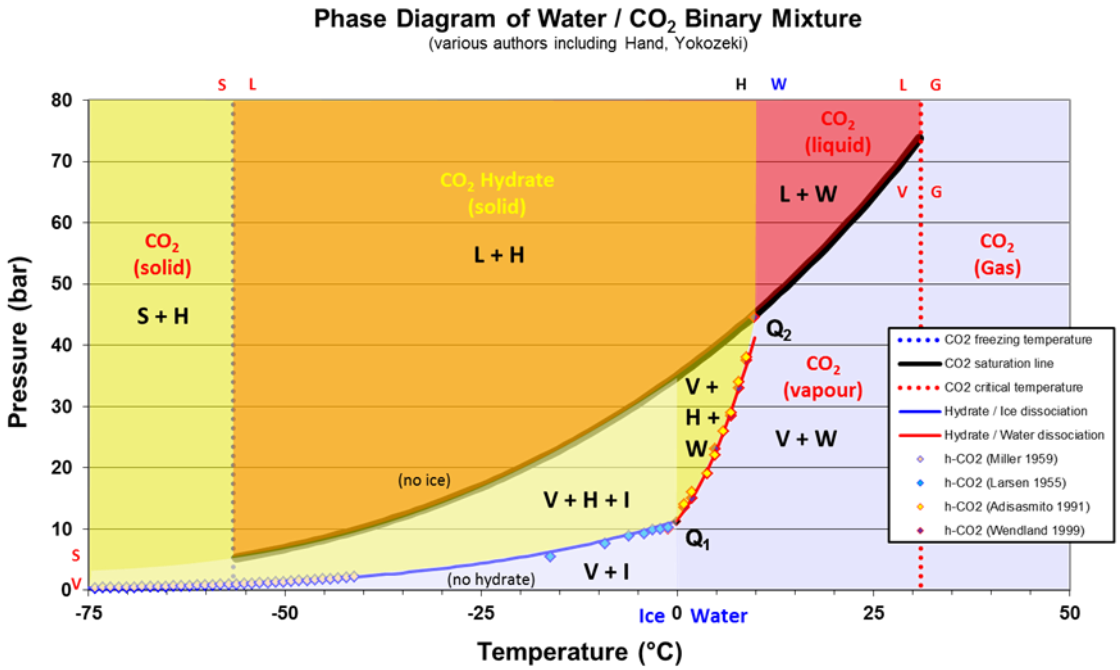

Fig. 5C-1 Phase diagram for CO_2 clathrate hydrates (note that CO_2 is immiscible with water, and there are two invariant T-P points Q_1 & Q_2 [157-165])

Dual phase expanders

In the case of a vaporjet expander, the shaft above the flash chamber is very tall (2—3 km) and the liquid condensate passes through Pelton wheel turbines to generate power as it returns to the base of the shaft to start the cycle over again, Fig. 5C-2 [68, 166]. Other two phase vapour expanders are possible but the flash chamber is the essential element of the direct contact boiler. All shafts and chambers are at negative pressure with respect to the weight of the overlying strata. Unlike rock, tunnels constructed at sufficient depth within the ice will form natural air tight seals.

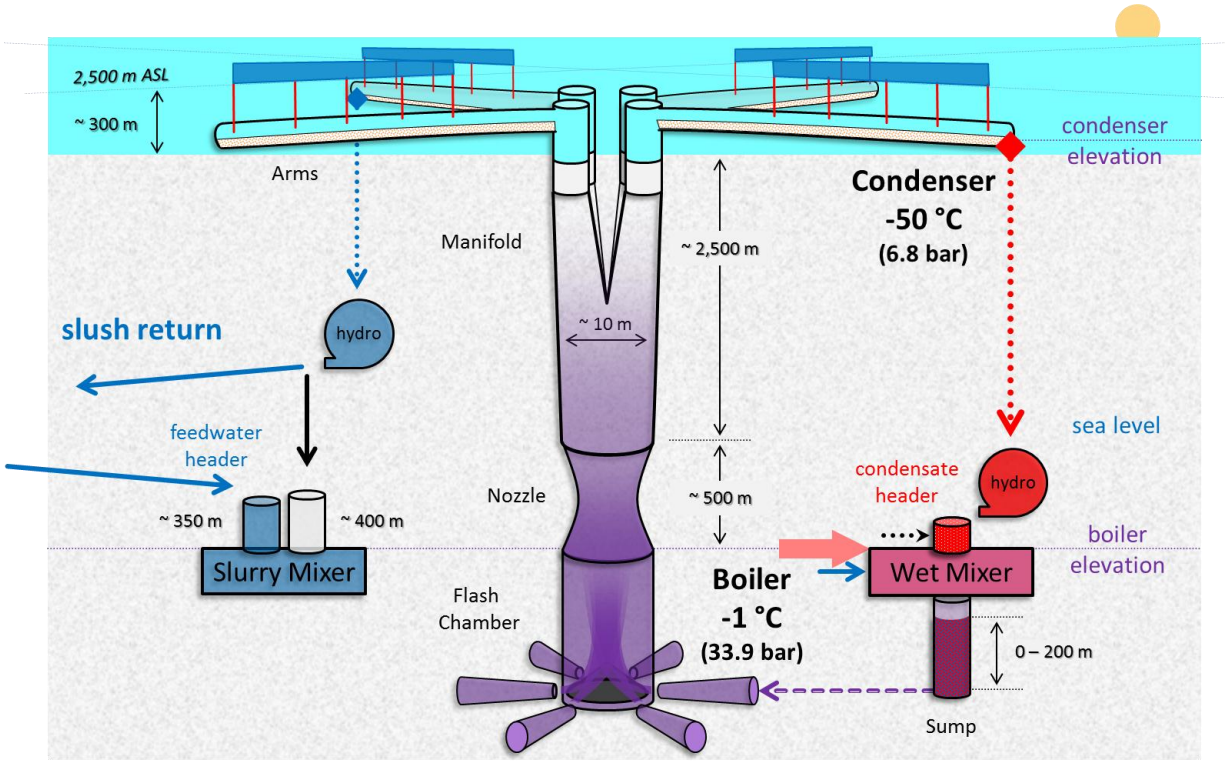

Fig. 5C-2 Illustration of potential 10,000+ MW vaporjet expander / glaciothermal hydro concept.

Preliminary qualitative modelling suggests that a vaporjet expander powered by an appropriate meltwater-brine feed and running CO_2 has the capacity to generate massive amounts of glaciothermal hydro power, Fig. 5C-3. Several issues including fluid flow stability and electrodynamic effects need to be investigated and safety issues addressed for such a large high pressure device.

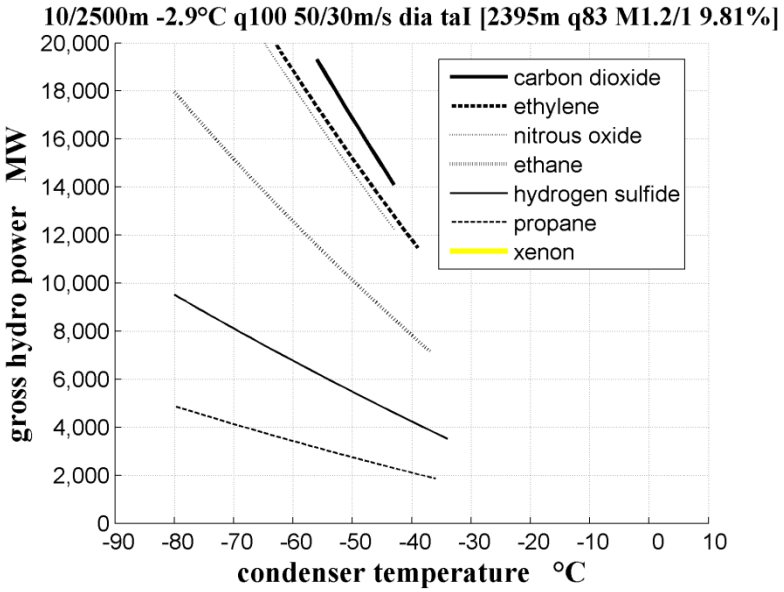

Fig. 5C-3 Qualitative model of power output from vaporjet expander. Losses due to wall friction are ignored.

We assert that a system comprising little more than water, cold-air, liquid CO_2 and ethane, fan-forced or droplet spray condensers, and hydro-turbines can be rapidly constructed on the ice caps to generate massive amounts of electrical power. This might be used to power capture of global CO_2 emissions and drive the subsequent manufacture of synthetic fuels from CO_2 slush or clathrate stored within the icesheet [167] and hydrogen obtained by electrolysis of glacial meltwater. The potential applications for such a large scale power system warrant urgent investigation.

Optimum conditions for year round glaciothermal power generation occur at icesheet sites subject to extreme cold ambient temperatures. An estimated 5,000,000 km^2 of East Antarctic Plateau is subject to mean annual temperatures colder than -40 °C, Fig. 5C-4. Ideal sites exist there for solar meltwater production and ground source thermal storage. Small scale glaciothermal power systems are self-starting and provide continuous power without any need for diesel generator backup. Glaciothermal power thus potentially provides a clean, affordable, renewable energy alternative to fossil fuels over a large area of the Earth's icecaps.

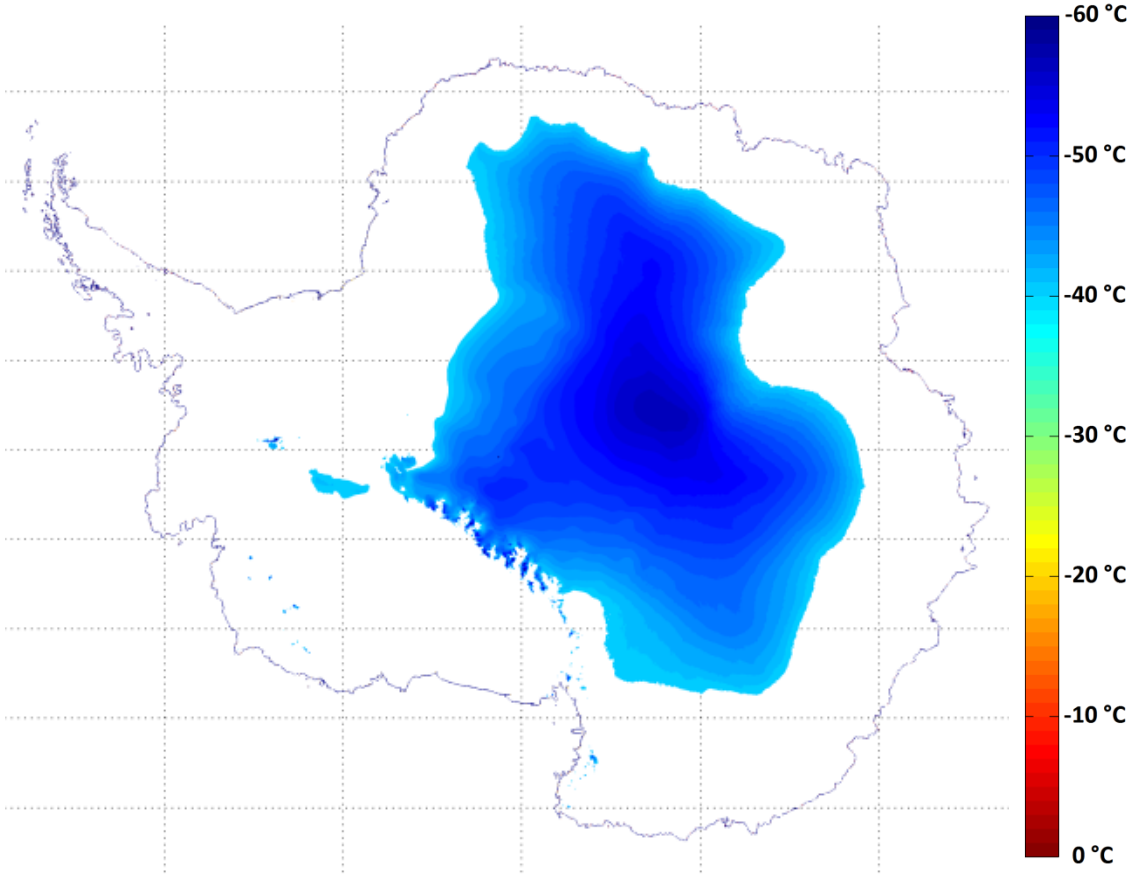

Fig. 5C-4. An estimated 5 million km^3 of Antarctica has mean annual surface temperatures colder than -40 °C.

5-D Minor findings

Minor research findings of this project include the following:

- An ice blender may be adequate to manage ice particle size distribution within ice slurry
- Technological solutions are sought regarding nano-scale enhanced boiling surfaces
- Optimal operation of the ice-in-tube glaciothermal boiler is achieved with short temperature glides and high velocity flow of low salinity ice slurry in thin boiler tubes
- Feed water salinity is a key factor affecting the suitability of a potential glaciothermal heat source.

Potential for year round power generation at various sites:

- Coastal oasis sites are not cold enough at any time of the year for glaciothermal power
- Icesheet sites close to the coast may permit glaciothermal power during the depths of winter but low thermal efficiency means they require large boilers and condensers
- Conditions on the East Antarctic Plateau and on Ross Ice Shelf both permit glaciothermal power production from seawater feed throughout the six months of winter
- Extended temperature glides of at least 5 K are needed when pumping seawater inland to maximise the proportion of ice formed from freezing seawater

Full analysis of specific thermal augmentation methods have not been completed so the thesis cannot claim any specific findings related to augmented cycles. The following points are noted, however, regarding the siting requirements for augmented systems:

- High proportion of cloud free days and a suitable icesheet location are the essential requirements for meltwater production
- At least 3 months per year of cold ambient temperatures and good icesheet ground conditions are required for construction of an effective ground source heat exchanger
- Structural integrity and dynamic stability of shelf ice may limit GSHX

5-E Miscellaneous future work

A number of potential enhancements and modifications can be made to improve the performance of the basic glaciothermal engine.

Thermal storage methods offer the potential for year round power generation at icesheet sites which represents a fundamental improvement to the intermittent seasonal capability of the basic glaciothermal engine (BGE). Specific tasks include:

- Finite element analysis of solar absorber and meltwater pond heat and mass flows
- Numerical modelling of salinity changes as meltwater storage is depleted
- Complete current finite element analysis of ground source heat exchanger
- Integration of meltwater, GSHX and BGE models

Although feasibility modelling of the basic glaciothermal engine is largely complete, there are a number of component performance issues that require further investigation to determine potential efficiency gains:

- Identify or develop a power output model for twin screw expander to enable comparative modelling of synchronous generators with doubly fed induction and permanent magnet generators given fixed speed or variable working fluid mass flows
- Numerical optimisation of boiler and condenser dimensions and operational settings based on statistical models
- Research potential high performance enhanced boiling surfaces for evaporator including nano-scale surface treatment technologies

Similar modelling is needed at the engine design stage to maximise performance at specific sites:

- Nominate fixed engine dimensions and estimate capacity factors at type locations
- Research protective surface coatings (electroless nickel) for boiler tubes
- Construct 20 kW pilot plant to simulate operational performance of BGE

Investigating the potential for large scale glaciothermal power generation is important. A qualitative model has been programmed in MATLAB to simulate the steady state fluid flow processes and estimate power output. This work needs to be put on a more substantial footing:

- CFD modelling of multiphase quasi-isothermal expansion for flash chamber
- Heat transfer rate experiment for multiphase clathrate mixture using piston expander to provide base line data to support CFD model
- Comparative study of large two phase expanders including vaporjet and reaction turbines
- Investigate BPMED for potential CO_2 capture from seawater, meltwater or eutectic brines exposed to the atmosphere at high elevation interior sites
- Heat transfer modelling of eutectic brine droplet sprays as an alternative to the tube fin condenser (may be more affordable and also complement direct air capture of CO_2).

Miscellaneous housekeeping tasks include:

- Further benchmark testing of existing MATLAB engine model against known device prototypes (including shell-and-tube flooded evaporator using ammonia)
- Upgrade regression analysis model for mean annual Antarctic surface temperature map (fully normalised predictors plus Kriging to pre-process clumpy meteorological data)
- Research station energy demand cycles (needed after loss of discretionary thermal loads for snow melting due to potable water being directly available from meltwater bells)